

SEISMIC PERFORMANCE AND FRAGILITY CURVES FOR
REINFORCED CONCRETE FRAMED BUILDINGS IN
KLANG VALLEY

TAN KOK TONG

INSTITUTE OF GRADUATE STUDIES

UNIVERSITY OF MALAYA

KUALA LUMPUR

2016

SEISMIC PERFORMANCE AND FRAGILITY CURVES FOR
REINFORCED CONCRETE FRAMED BUILDINGS IN KLANG
VALLEY

TAN KOK TONG

THESIS SUBMITTED IN FULFILMENT OF THE REQUIREMENTS
FOR THE DEGREE OF DOCTOR OF PHILOSOPHY

INSTITUTE OF GRADUATE STUDIES
UNIVERSITY OF MALAYA
KUALA LUMPUR

2016

UNIVERSITY OF MALAYA
ORIGINAL LITERARY WORK DECLARATION

Name of Candidate: **TAN KOK TONG**

Registration/Matric No: **KHA100060**

Name of Degree: **Doctor of Philosophy**

Title of Thesis: **Seismic performance and fragility curves for reinforced concrete framed buildings in Klang Valley**

Field of Study: **Earthquake and Structural Engineering**

I do solemnly and sincerely declare that:

- 1) I am the sole author/writer of this Work;
- 2) This Work is original;
- 3) Any use of any work in which copyright exists was done by way of fair dealing and for permitted purposes and any excerpt or extract from, or reference to or reproduction of any copyright work has been disclosed expressly and sufficiently and the title of the Work and its authorship have been acknowledged in this Work;
- 4) I do not have any actual knowledge nor ought I reasonably to know that the making of this work constitutes an infringement of any copyright work;
- 5) I hereby assign all and every rights in the copyright to this Work to the University of Malaya (UM), who henceforth shall be owner of the copyright in this Work and that any reproduction or use in any form or by any means whatsoever is prohibited without the written consent of UM having been first had and obtained;
- 6) I am fully aware that if in the course of making this Work I have infringed any copyright whether intentionally or otherwise, I may be subject to legal action or any other action as may be determined by UM.

Candidate's Signature

Date 17.10.2016

Subscribed and solemnly declared before,

Witness's Signature

Date

Name:

Designation:

ABSTRACT

Fragility curves, nowadays are popularly used in earthquake engineering where structural damage due to complex earthquake can be described in terms of probability. In this study, two primary objectives have been defined: (1) to conduct seismic response analyses and (2) to derive computational based fragility curves for reinforced concrete framed structures in Klang Valley. This study is solely based on computational efforts where a series of RC framed building are simulated. Reinforced concrete framed buildings of 3, 7 and 11 story have been selected. A four-story reinforced concrete school building with infill walls was also selected to be investigated. The simulation is based on force-based fiber elements for structural elements and a single equivalent diagonal strut is selected to model the infill walls. The simulation techniques were verified via comparison with shake table test results. This study performed nonlinear time history analyses via an open source OpenSees. Subsequently, fragility curves were generated with respect to PGA and 4 different damage states including slight damage state, moderate damage state, extensive damage state and complete damage levels. The structural damage was measured consistently with HAZUS definition of damage levels. The structural properties for the analyzed systems were selected to be determinate while the uncertainties associated with ground motions were considered to represent the inter-record variability. Finally, using constructed fragility curves, the degree of expected damage of the structures were estimated for expected earthquake magnitude. The seismic analysis shows that the presence of masonry infill walls was significant influence on the global response of the structure. Although the displacement of the structure with infill wall is reduced in the in-plane direction, it was increased in both in-plane and out-of-plane directions when the infill walls experienced loss in serviceability. It is also shown that the seismic fragility of

the 3-story RC framed building is more relied on local site conditions than those of the 7- and 11-story RC framed buildings investigated.

University of Malaya

ABSTRAK

Lengkungan kelemahan adalah alat yang berguna untuk menunjukkan kebarangkalian kerosakan struktur disebabkan oleh gempa bumi sebagai fungsi indeks gerakan tanah. Tujuan kajian ini adalah untuk menjalankan tindak balas dan menyediakan lengkungan kelemahan untuk bangunan konkrit bertetulang di Lembah Klang, yang telah direka mengikut British Standard BS 8110: 1997. Kajian ini adalah berdasarkan kepada simulasi berangka berkenaan dengan perubahan ketinggian bangunan. Contoh tingkat 3, 7 dan 11 bangunan telah dipilih. Selain itu, untuk mengkaji kesan dinding dalam struktur bangunan, empat tingkat bangunan direka dengan dan tanpa dinding telah dipilih. Simulasi bekerja unsur serat berasaskan kuasa untuk rasuk dan tiang, dan tupang pepenjuru bersamaan tunggal untuk mewakili isian batu tersebut. Persekitaran analitikal dan model struktur untuk terisi bingkai RC telah disahkan melalui perbandingan dengan keputusan ujian meja. Tak linear analisis masa sejarah telah dilakukan dengan menggunakan sumber terbuka berdasarkan dua puluh usul tanah. Lengkungan kelemahan telah dibangunkan dari segi puncak mendatar pecutan bumi untuk tahap kerosakan sedikit, sederhana, teruk dan seluruh dengan andaian pengagihan lognormal. Kerosakan pada struktur telah dinilai berdasarkan nisbah pergerakan antara struktur. Sifat-sifat struktur bangunan telah dipilih untuk menjadi boleh tentu manakala ketidaktentuan yang berkaitan dengan usul tanah telah dianggap mewakili kebolehubahan antara rekod. Akhir sekali, dengan menggunakan lengkungan kelemahan yang dibina, tahap kerosakan diharapkan daripada struktur dianggarkan untuk gempa bumi dianggap maksimum. Analisis seismik menunjukkan bahawa kehadiran dinding isian batu mempunyai pengaruh yang besar ke atas tindak balas keseluruhan struktur. Walaupun anjakan struktur dengan isian dinding dikurangkan ke arah selari dengan dinding, ia telah meningkat dalam kedua-dua arah selari dan seranjang dengan dinding apabila dinding mengalami kerosakan. Ia juga menunjukkan bahawa lengkungan seismik 3 tingkat RC bangunan direka adalah lebih

sensitif kepada keadaan tanah tapak tempatan daripada lengkungan seismik bangunan 7-
dan 11 tingkat RC dibingkaikan

University of Malaya

ACKNOWLEDGEMENTS

The work reported in this dissertation was funded by University of Malaya and the Ministry of Education (MOE), Malaysia through research grants PV081/2011A and UM.C /625/1/HIR/MOHE/ENG/55. The visit of the author to Harbin Institute of Technology (HIT) from September 2011 to August 2012 was funded by UNESCO and the People's Republic of China through UNESCO/China (The Great Wall) Co-Sponsored Fellowships Programme. These supports are gratefully acknowledged. Special thanks are due to Dr. Wang Zhen-Yu, Dr. Yu Xiao-Hui and many other graduate students of School of Civil Engineering, HIT, for their guidance and assistance in the shake table tests.

Most importantly, the author wish to express his sincere gratitude and respect towards Professor Dr. Hashim Abdul Razak, Dr. Meldi Suhatriil and Professor Dr. Lu Dagang from HIT for their advise and guidance in the last four years.

TABLE OF CONTENTS

ABSTRACT	iii
ABSTRAK	v
ACKNOWLEDGEMENTS	vii
TABLE OF CONTENTS	viii
LIST OF FIGURES	xi
LIST OF TABLES	xv
LIST OF SYMBOLS AND ABBREVIATIONS	xvi
LIST OF APPENDICES	xxii
CHAPTER 1: INTRODUCTION.....	1
1.1 Background	1
1.2 Earthquake history	4
1.3 Problem statement	7
1.4 Objectives.....	8
1.5 Scope.....	9
1.6 Organization of the dissertation	10
CHAPTER 2: LITERATURE REVIEW	13
2.1 Introduction	13
2.2 Structural modeling method.....	13
2.2.1 Fiber beam-column elements.....	13
2.2.2 Constitutive models.....	14
2.2.2.1 Steel model	15
2.2.2.2 Concrete stress-strain relation	17
2.2.3 Masonry infill walls	19
2.2.3.1 UMW in-plane failure modes.....	21
2.2.3.2 Strut models.....	25
2.2.3.3 Spring models.....	31
2.3 Ground motion selection techniques	33
2.3.1 Record selection with respect to dominated earthquake scenarios	33
2.3.2 Selection with respect to spectrum matching	34
2.3.3 Additional selection techniques	37
2.3.3.1 Soil profile.....	37
2.3.3.2 Ground motion duration.....	40

2.3.3.3 Seismotectonic environment and other seismological parameters	43
2.3.3.4 Ratio of acceleration to velocity (a/v).....	44
2.3.4 Selection based on seismic code - Eurocode 8	45
2.3.5 Selection based on seismic code - FEMA 450	45
2.3.6 Generation of artificial earthquakes	46
2.4 Measures of structural damage.....	48
2.4.1 Local damage indices	49
2.4.2 Global damage indices	53
2.5 Seismic fragility and reliability method.....	60
2.5.1 SAC-FEMA Method	61
2.5.2 Response Surface Method	63
2.5.3 Monte Carlo Simulation	65
2.5.4 Bayesian method.....	66
2.5.5 Ryu's Method	68
2.6 Summary	72
CHAPTER 3: INPUT ACCELERATION GROUND MOTIONS	74
3.1 Introduction.....	74
3.2 Seismic hazard map	74
3.3 Deaggregation	76
3.4 Site response analysis	79
3.4.1 Site description	80
3.4.2 Modelling of soil layers	82
CHAPTER 4: SHAKE TABLE TEST	86
4.1 Introduction.....	86
4.2 Description of the shake table	86
4.3 Similitude relationship and model materials.....	87
4.4 Instrumentation and experimental setup	90
4.5 Construction process.....	96
4.6 Test program	103
4.7 Observed damage of unreinforced masonry infill wall	105
CHAPTER 5: COMPUTATIONAL MODELLING	109
5.1 System definition.....	109
5.2 Finite element model	112
5.3 Nonlinear time history analysis.....	120
5.4 Validation of numerical model.....	121

5.5 Effect of masonry infilled wall.....	126
5.6 Local and global response of RC framed structure	127
CHAPTER 6: SEISMIC FRAGILITY ANALYSIS	135
6.1 Introduction.....	135
6.2 Damage measure.....	138
6.3 Performance levels.....	138
6.4 Construction of fragility curves	140
6.5 Sensitivity analysis	145
6.5.1 Sensitivity to site conditions	145
6.5.2 Sensitivity to number of storey	147
6.7 Prediction of degree of structural damage based on fragility curves	150
CHAPTER 7: CONCLUSIONS.....	153
7.1 Conclusion	153
7.2 Recommendations for future research	155
REFERENCES	157
LIST OF PUBLICATIONS AND PAPER REPRESENTED.....	166
APPENDIX A: LOGNORMAL PROBABILITY PLOT OF MAXIMUM DRIFT RATIO	167
APPENDIX B: PROBABILITY TABULATIONS FOR DIFFERENT EARTHQUAKE LEVELS	171
APPENDIX C: THE LOCAL AND GLOBAL RESPONSES FOR 11-STOREY RC BUILDING.....	173

LIST OF FIGURES

Figure 1.1: Example of fragility curves (FEMA, 2003).	2
Figure 1.2: Major tectonic plates around Malaysia.	5
Figure 1.3: Two largest earthquakes in Sumatran subduction zone caused tremors felt in Peninsular Malaysia (Balendra and Li, 2008).	6
Figure 1.4: Observed damage to the Pantai Dalam flats after the southern Sumatra earthquake, Sept. 30, 2009.	8
Figure 2.1: Fiber element for RC members (Taucer et al., 1991).	14
Figure 2.2: Steel model (Menegotto & Pinto, 1973).	16
Figure 2.3: Parameter of R in the steel model (Taucer et al., 1991).	16
Figure 2.4: Concrete model (Taucer et al., 1991).	18
Figure 2.5: Hysteretic concrete stress-strain relation (Taucer et al., 1991).	19
Figure 2.6: SAT models.	26
Figure 2.7: Infill walls represented by strut and tie model (Hashemi & Mosalam, 2007).	27
Figure 2.8: Infill walls represented by a diagonal member Kadysiewski and Mosalam (2009).	28
Figure 2.9: Infill walls represented by compression-only diagonal struts (Kwon & Kim, 2010).	29
Figure 2.10: Hysteretic behavior of diagonal strut elements.	30
Figure 2.11: Infill walls represented by double equivalent strut model (Uva et al., 2012).	30
Figure 2.12: Infill walls represented by a spring model (Park et al., 2009).	31
Figure 2.13: Different failure pattern (Park et al., 2009).	32
Figure 2.14: Boundary condition for unreinforced masonry pier (Park et al., 2009).	32
Figure 2.15: Duration for bracketed model.	40
Figure 2.16: Duration for uniform model.	41
Figure 2.17: Significant accelerogram duration.	42
Figure 2.18: Significant duration of a ground motion.	43
Figure 2.19: Ground motion with envelope function.	49
Figure 2.20: Definition of stiffness degradation (Banon et al., 1981).	51
Figure 2.21: Damage index defined by Chung et al. (1987).	54
Figure 2.22: Milikan Library fundamental periods (Williams & Sexsmith, 1995).	57
Figure 3.1: Seismic source zones around Malaysian Peninsula (Adnan, 2013).	75

Figure 3.2: Seismic hazard exposure at Kuala Lumpur (Adnan, 2013).....	76
Figure 3.3: Target spectra for Kuala Lumpur for (a) 500 and (b) 2500 YRP (Adnan, 2013).	77
Figure 3.4: Deaggregation hazard result (Adnan, 2013).....	77
Figure 3.5: Dominated earthquake scenarios (a) 10%/50 years and (b) 2%/50 years (Petersen et al. (2004)).	78
Figure 3.6: Soil description and corresponding V_{s30} for (a) Type C site (OUG Park) and (b) Type D site (IIUM campus).	81
Figure 3.7: Soil and shear-wave velocity profile for the Setapak Vocational High School: (a) Soil type E (BH1) and (b) Soil type D (BH2).	81
Figure 3.8: Modulus reduction curves of dynamic soil properties.	82
Figure 3.9: Damping curves of soil properties.	83
Figure 3.10: Maximum acceleration along the soil type C and D for the input motions: (a) Landers scaled at 0.15g, (b) Duzce scaled at 0.75g, (c) Chi-chi scaled at 1g and (d) Duzce scaled at 1.5g.	84
Figure 3.11: Expected ground motions after site response analysis.	85
Figure 4.1: Scaled model on 5mx5m shake table.	89
Figure 4.2: Instrumentation: (a) accelerometer and (b) data recorder.	91
Figure 4.3: Location of accelerometers (A1-A16) and displacement transducers (D1-D14).	92
Figure 4.4: Preparation of experimental setup.	93
Figure 4.5: Installation of accelerometers.	93
Figure 4.6: Installation of data acquisition sensors.	94
Figure 4.7: Testing of LVDTs.	94
Figure 4.8: Installation of LVDTs.	95
Figure 4.9: Testing of the experimental instruments.	95
Figure 4.10: Completion of experimental setups.....	96
Figure 4.11: Construction of RC based beam.	97
Figure 4.12: Formwork for the scaled model.	98
Figure 4.13: Column reinforcement.....	98
Figure 4.14: Slab and beam reinforcement.	99
Figure 4.15: Concrete casting.	99
Figure 4.16: Preparation of concrete test cubes.....	100
Figure 4.17: The scaled model after stripping forms.....	100
Figure 4.18: Cutting solid clay bricks.....	101

Figure 4.19: Transporting the scaled model to the shake table.	101
Figure 4.20: Construction of unreinforced masonry infill walls.	102
Figure 4.21: Preparation of mortar test cubes.	102
Figure 4.22: (a): Kepulauan Mentawai Region earthquake (M6.7) and (b) Sumatra earthquake (M7.5).....	104
Figure 4.23: Wenchuan earthquake (M7.9).	104
Figure 4.24: Crack patterns observed on the scaled model: (a) after 0.06g, (b) after 0.12g, (c) after 0.20g and (d) after 0.34g.	107
Figure 5.1: The layout of the RC office framed buildings.	110
Figure 5.2: The layout of the RC school building (unit: mm).....	111
Figure 5.3: Frame and section modeling.....	113
Figure 5.4: 3-storey RC framed building.	118
Figure 5.5: 4-story infilled RC framed building.....	119
Figure 5.6: 7-storey RC framed building.	119
Figure 5.7: 11-storey RC framed building.	120
Figure 5.8: A concatenation of table motion for simulation.	122
Figure 5.9: Roof acceleration time histories of the infilled system: (a) 0.06g (b) 0.12g (c) 0.34g.	124
Figure 5.10: Roof displacement time histories of the infilled system: (a) 0.06g (b) 0.12g (c) 0.34g.	125
Figure 5.11: Global responses of four-story RC structure: (a) base shear, (b) stiffness and (c) displacement.	128
Figure 5.12: Comparison of predicted hysteresis curves of the four-storey school building with and without masonry infill for in-plane direction: (a) 0.06g and (b) 0.20g.	129
Figure 5.13: Comparison of predicted hysteresis curves of the four-storey school building with and without masonry infill for out-of-plane direction: (a) 0.06g and (b) 0.20g.....	129
Figure 5.14: Comparison of peak lateral displacement for 11-story RC building at soil types C and D: (a) Chi-chi NS, (b) Chi-chi EW, (c) Northern California and (d) Landers NS.	130
Figure 5.15: Comparison of displacement time history for 11-story RC building at soil types C and D: (a) Chi-chi NS, (b) Chi-chi EW, (c) Northern California EW and (d) Landers NS.	132

Figure 5.16: Comparison of maximum interstory drift ratio for 11-story RC building at soil type C and D: (a) Chi-chi NS, (b) Chi-chi EW, (c) Northern California EW and (d) Landers NS.	133
Figure 5.17: Assumed stress strain curves for (a) Kent and Park model for unconfined concrete sections and (b) Menegotto and Pinto model for steel rebars.	134
Figure 5.18: Strain and stress distribution through the depth of section.	134
Figure 6.1: Concept of fragility curve (Park et al., 2009)	135
Figure 6.2: Fragility curves of the 3-storey RC framed building.	142
Figure 6.3: Lognormal probability plot of maximum drift ratio for 3-storey RC framed building.	144
Figure 6.4: Fitted fragility curves of the 3-storey RC framed building.	145
Figure 6.5: Seismic fragility curves for the RC framed buildings at the study sites. ...	148
Figure 6.6: Seismic fragility curves for the 4-story infilled RC framed building at the study sites.	149
Figure 6.7: Seismic fragility curves for RC framed buildings at (a) soil type C, and (b) soil type D.	151

LIST OF TABLES

Table 2.1: In-plane modes of failure and their corresponding estimated capacities H_u and joint shear demands V_j of infilled systems (Liauw & Kwan, 1985).	22
Table 2.2: Site classification (NEHRP, 2001).....	38
Table 2.3: Damage threshold (Park et al., 1987).....	52
Table 3.1: Properties of the selected records.....	79
Table 3.2: Soil density (Brandenberg et al., 2010).	83
Table 4.1: Similitude parameters.	90
Table 4.2: The sequence of loading of the shake table experiment.	106
Table 5.1: Nonlinear force-deflection relations for infill panels (FEMA 356).	116
Table 5.2: Values of λ_2 (FEMA 356).	116
Table 5.3: Error indices, ϵ	126
Table 6.1: The maximum drift ratio for RC moment resisting frames (FEMA, 2003).	140
Table 6.2: The maximum drift ratio for infilled RC frames (FEMA, 2003).....	140
Table 6.3: The distribution of the drift ratio of the 3-storey RC framed building under different earthquake inputs at soil type D.	143
Table 6.4: The lognormal parameters of the drift ratio for the 3-storey RC framed building at soil type D.	143
Table 6.5: The values of probability of exceedance corresponding to slight, moderate, extensive and complete damage of the 3-storey RC framed building at soil type D....	143
Table 6.6: Lognormal parameters for the fitted fragility curves at soil type C except 4-storey RC school building at soil type D.	144
Table 6.7: Lognormal parameters for the fitted fragility curves at soil type D except 4-storey RC school building at soil type E.	144
Table 6.8: The probability of exceeding given damage limit states of the buildings for two site soil conditions in Kuala Lumpur at MCE.	152
Table 6.9: The probability of exceeding given damage limit states of the infilled RC frames for two site soil conditions in Kuala Lumpur at MCE.	152

LIST OF SYMBOLS AND ABBREVIATIONS

$a(t)$	=	Acceleration time history
a/v	=	Maximum acceleration over maximum velocity ratio
a, b	=	regression coefficients for linear regression
A_n	=	Area of net mortared or grouted horizontal section across infill panel
A_{nm}	=	Relative amplitudes of different surface wave modes
A_{wt}	=	Effective cross-sectional area of walls in a given horizontal direction
A_{cw}	=	Total cross-sectional area of reinforced concrete walls in one horizontal direction at base
A_{mw}	=	Cross-sectional area of unreinforced masonry infill walls in one horizontal direction at base
A_{ft}	=	Total floor area above base in a building
A_{ce}	=	Effective cross-sectional area of columns at base
A_{col}	=	Total cross-sectional area of columns above base
B	=	width of a rigid pad foundation
d	=	Peak ground displacement
C	=	capacity variable for structural demand D
\hat{C}	=	median drift capacity
C_A	=	coefficients that reflect architectural features
C_M	=	coefficients that reflect construction quality
C_{AS}	=	soft story feature
C_{ASC}	=	fragility due to presence of short column
C_{AP}	=	effect of plan irregularity that results in horizontal torsion and significant amount of overhangs
C_{AF}	=	vertical and in-plan discontinuity of frames
CI	=	Ratio of effective column cross-sectional areas to the total floor area
d_b	=	longitudinal bar diameter
dE	=	Incremental dissipated hysteretic energy
d_s	=	Damage state
d_b	=	Longitudinal bar diameter
d_m	=	Diagonal strut length
D	=	Drift demand
D_{ms}	=	Maximum softening
D_{ps}	=	Plastic softening

D_{fs}	=	Final softening
D_{rms}	=	Closer matching between the shapes of the record and target spectra
$D_{max-rec}$	=	Maximum displacement response of inelastic single DOF oscillators
DT	=	global damage index
D_i^k	=	Local damage at location I on story k
DT_i	=	global damage index for the ith damage state
\hat{D}	=	median drift demand
E_i	=	Energy dissipated in element i
E_h	=	Hardening modulus
E_i^k	=	Energy dissipated at location i on story k
E_{fe}	=	Modulus of elasticity of frame material
E_{me}	=	Modulus of elasticity of infill material
FS	=	Fourier amplitude spectrum
f_y	=	Resistance of steel
f_c	=	Longitudinal stress in concrete
f'_c	=	Concrete compressive cylinder strength
f_{yh}	=	Yield strength of hoop reinforcement
f_{me}	=	Compressive strength of masonry
f_{ss}	=	First natural frequency of infill wall
f'_{tb}	=	Tension strength brick
f'_{cb}	=	Compression strength of brick
f'_j	=	Compression strength of mortar
f'_m	=	Masonry compression strength for ungrouted clay brick
g	=	Acceleration due to gravity
$g(x)$	=	limit state function
h''	=	Width of concrete core measured to outside of the peripheral hoop
h	=	Story height
h_{col}	=	Column height between centerlines of beams
h_{inf}	=	Height of infill panel
$H(S_a)$	=	hazard function of spectral acceleration, annual probability that intensity S_a at site will equal or exceed S_a
H_u	=	Lateral frame capacity
$H_D(d)$	=	hazard function of drift, mean annual probability that drift demand D exceeds any specific value d
i	=	Indicator of displacement or curvature level
I_{col}	=	Moment inertial of column

IM	=	Earthquake intensity measure
IM _{mi}	=	Median threshold value of the earthquake intensity measure
j	=	Thickness of mortar
k _o , k	=	coefficients for linear regression of hazard H(S _a) on intensity S _a in proximity of limit state probability P _{PL} (region of interest) in logarithmic
k _m	=	Equivalent secant stiffness of the maximum response
k _f	=	Ultimate secant stiffness
k _i	=	In-plane lateral stiffness of infill panel
k _{eq_N}	=	Out-of-plane stiffness of masonry infill
L	=	Span of infilled RC frame
L _{diag}	=	Diagonal length between column centerlines and floor centerlines
I _{eq}	=	Moment of inertia of infill panel
I _k	=	Weighting factor for story k
l _m	=	Length of infill panel
L _v	=	Shear span
L _{pl}	=	Plastic hinge length
m	=	number of ANN training data sets
MMI	=	modified mercalli intensity
MEW	=	Modal effective weight
M _{pb}	=	Plastic moment capacity of beam
M _{pc}	=	Plastic moment capacity of column
M _{pj}	=	Plastic moment capacity of beam-column joint
M _{n0}	=	Out-of-plane yield moment of infill panel
M _i	=	Initial strength at curvature level i
M _{fi}	=	Final strength at curvature level i
M _w	=	Moment magnitude
M _y	=	Yield strength of the longitudinal reinforcement
ΔM _i	=	Strength drop at curvature level i
MCE	=	Maximum considered earthquake
N	=	Vertical load in infill walls
NGA	=	Next generation attenuation
NIDD	=	Median values of normalized inelastic displacement demand
N _f	=	number of simulation cycles
N	=	Total number of simulation cycles
N	=	a random variable representing the number of collapsed structures
n	=	a specific numeric value of N

n_i	=	Number of cycles actually applied at curvature level i
n_t	=	total number of structures
PGA	=	Peak ground acceleration
PHGA	=	Peak horizontal ground acceleration
\overline{PGA}_{ds}	=	mean of value of magnitude given the damage event
PI	=	Priority index
P_{ce}	=	Gravity compressive force on wall
P_{ij}	=	probability of being in a given damage state at specified MMI
P_f	=	Probability of failure
P_{ik}	=	probability of exceeding damage state
P_{PL}	=	annual probability of performance level not being met
Q_s	=	Ratio of volume of hoop reinforcement to volume of concrete core
q_{ine}	=	Out-of-plane strength of infill wall
r_{inf}	=	Diagonal length of infill panel
S	=	Shear strength of interface connection
S_a	=	Spectral acceleration
S_g	=	Value of power spectral density for ground acceleration
SA_s	=	Target spectral acceleration
$S_{d-A.R}$	=	Mean spectral displacement
SI	=	Softening damage index
S_h	=	Center-to-center spacing of hoop sets
S_v	=	spectral velocity
S_d	=	spectral displacement
s_a^d	=	spectral acceleration “corresponding to” drift demand level d
$s_a^{\hat{c}}$	=	spectral acceleration “corresponding to” median drift capacity
SRSA	=	Computed response spectrum from generated non-stationary time history
T	=	Period
T_0	=	Initial period of capacity spectrum
T_j	=	Effective (secant) period at some intermediate spectral displacement
T_f	=	Final natural period of an equivalent linear system
T_{und}	=	Fundamental period of structure before earthquake
T_{dam}	=	Fundamental period of structure after earthquake
T_m	=	Maximum period obtained during earthquake
TRSA	=	Target prescribed response spectrum
t_{nm}^*	=	Arrival time

t_r	=	Total duration of accelerogram
t_w	=	Infill wall thickness
U_u	=	Stress nonuniformity coefficient
U_y	=	Yield displacement
U_m	=	Maximum displacement at peak force
V_{ine}	=	Shear strength of infill panel
V_{te}	=	Bed-joint shear strength
V_y	=	Yield shear force
V_m	=	Maximum shear force
V_{me}	=	Shear strength of masonry infill
V_s	=	Shear-wave velocity
V_{s30}	=	Shear-wave velocity at the uppermost 30m
WI	=	Ratio of effective wall cross-sectional areas to the total floor area
w_{inf}	=	Weight per unit of length of infill panel
z	=	Equivalent strut width
τ_0	=	Cohesive capacity of the mortar beds
β	=	Modal parameter
β_c	=	Dispersion measure for drift capacity
β_D	=	Dispersion measure for earthquake demand
β_{ds}	=	Dispersion measure for damage state definition
β_z	=	hysteretic damping corresponding to vertical
β_x	=	hysteretic damping corresponding to horizontal
β_ϕ	=	hysteretic damping corresponding to rocking
β_{tot}	=	Total lognormal standard deviation
$\beta_{D S_a}$	=	dispersion measure for drift demand D at given S_a level
β_{SPGA}	=	standard deviation of magnitude given the damage event
α_{nm}	=	Scaled factor for determining the final amplitude trough overall Fourier amplitude spectrum
α_i	=	Damage modifier
μ	=	Sliding friction coefficient along the bed joint
μ_θ	=	Ductility ratio in terms of rotation
μ_ϕ	=	Ductility ratio in terms of curvature
μ_δ	=	Ductility ratio in terms of displacement
λ	=	Slenderness parameter
Y	=	ground motion random variable
Φ	=	Standardized cumulative probability function
x_x	=	basic random variables for $C(x)$ and $D(x)$

ε	=	random deviation term with zero-mean
ε_0	=	Strain level corresponding to the maximum stress in compression
ε_c	=	Longitudinal strain in concrete
ε_m	=	Maximum or minimum value of strain during the loading history
ε_m'	=	Masonry compression strain at the maximum compression stress
ε_{cu}	=	ultimate concrete strains
ε_{su}	=	ultimate steel strains
ε_y	=	Yield strain of longitudinal rebars
ω	=	Fundamental frequency of structure after being damaged
ω_e	=	Fundamental frequency of the undamaged or elastic structure
ω_n	=	Center frequency of band
$f'(\theta)$	=	prior density function of the parameter θ
$f''(\theta)$	=	posterior density function of θ
$L(\theta)$	=	product of the density function of X evaluated at x_1, x_2, \dots, x_n
μ	=	sample mean
σ	=	standard deviations
σ_c	=	Crushing stress of panel material
σ_N	=	Vertical compression stress in the infill walls
θ	=	Angle between diagonal of infill panel and horizontal axis
θ_m	=	Maximum rotation
θ_y	=	Yield rotation
θ_u	=	Ultimate rotation capacity
ϕ_m	=	Maximum curvature
ϕ_y	=	Yield curvature
ϕ_u	=	Ultimate curvature
δ	=	Random-effect i.e. the effect of the random factor x_2 , which accounts for the variability in the response due to the seismic action
δ_r	=	Maximum roof deflection under earthquake excitation
δ_f	=	Roof deflection at which the structure is assumed to fail
δ_m	=	Maximum displacement
δ_y	=	Yield displacement
Δ_{Hy0}	=	Lateral deflection of panel at yield
Δ_{Hcp0}	=	Lateral deflection of panel at collapse prevention limit state
Δ_{CP}	=	collapse prevention limit state
Δ_{DC}	=	damage control limit state
l	=	lower bounds on N
u	=	upper bounds on N

\cup	=	union symbol representing logical “or”
\cap	=	union symbol representing logical “and”
n_d	=	total number of damage states excluding nondamage state
j	=	index for the subevents
n_e	=	total number of subevents
T_0	=	initial period of the capacity spectrum
T_j	=	effective (secant) period at some intermediate spectral displacement
Y	=	ground motion random variable
ν	=	soil Poisson’s ratio
V_{yw}	=	yield base shear capacity with infill walls
V_y	=	yield base shear capacity without infill walls
A_w	=	total area of the filler walls
A_{ef}	=	total floor area of the building
V_c	=	concrete shear capacity

University of Malaya

LIST OF APPENDICES

APPENDIX A: LOGNORMAL PROBABILITY PLOT OF MAXIMUM DRIFT RATIO	167
APPENDIX B: PROBABILITY OF EXCEEDING LIMIT STATES FOR DIFFERENT EAARTHQUAKE LEVELS	171
APPENDIX C: THE LOCAL AND GLOBAL RESPONSES FOR 11-STOREY RC BUILDING.....	173

University of Malaya

CHAPTER 1: INTRODUCTION

1.1 Background

Fragility curves, nowadays are popularly used in earthquake engineering where structural damage due to complex earthquake can be described in terms of probability. Various ground motion parameters such as peak ground acceleration (PGA), elastic pseudo spectral acceleration (S_a), and elastic spectral displacement (S_d) (Kircil & Polat, 2006) can be used to represent the complex earthquake intensity. These tools are widely used for retrofitting and damage assesment. A lognormal probability distribution function (FEMA, 2003) is usually used to derive the fragility curves as follows:

$$P_f(ds \geq ds_i | S) = \Phi \left[\frac{1}{\beta_{tot}} \cdot \ln \left(\frac{IM}{IM_{mi}} \right) \right] \quad (1-1)$$

where $P_f(\cdot)$ is the probability of reaching a damage state, ds , by assigning a ground motion intensity level, Φ is the standard cumulative probability function, IM_{mi} is the median threshold value of the earthquake intensity measure, required to cause the i^{th} damage state, and β_{tot} is the total lognormal standard deviation.

As common practice, three primary sources are considered for the lognormal standard deviation (β_{tot}) (FEMA, 2003). It can be represented in the following equation:

$$\beta_{tot} = \sqrt{\beta_{DS}^2 + \beta_C^2 + \beta_D^2}$$

(1-2)

where β_{DS} is the definition of damage states, β_C is the response and resistance of the element and β_D is the earthquake input motion. The first two uncertainties can be defined

based on literature. For example, FEMA (2003) suggests β_{ds} is equal to 0.4 for all types of damage states and building, while β_c is equal to 0.25 for seismically resistant buildings and 0.3 for non-seismically resistant buildings. However, the third uncertainty is represented by standard deviation of the DIs that have been calculated for different input earthquakes (Argyroudis et al., 2013). Figure 1.1 shows a template fragility curves for different damage states and various ground motion intensity levels e.g. weak shaking, medium shaking and strong shaking.

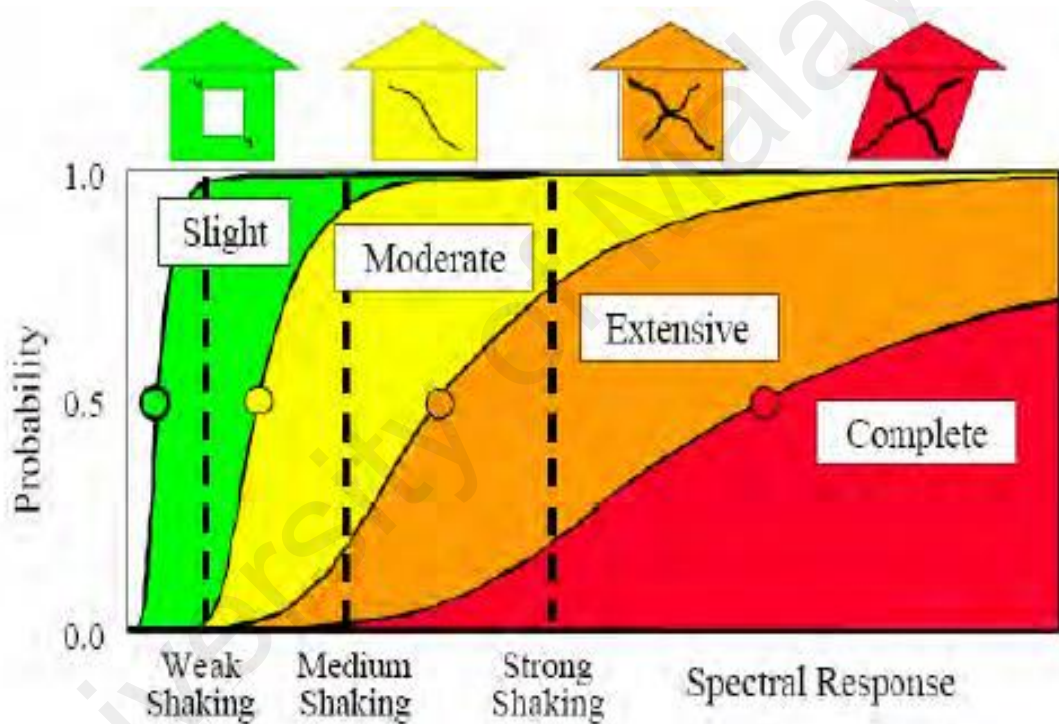


Figure 1.1: Example of fragility curves (FEMA, 2003).

The fragility curves have attracted a large number of researchers for assessing of damage risk due to earthquake ground motions. In the last two decades, the fragility curves have been generated from risk analysis in a particular field such as nuclear power plants. They have advantages of representing the fragility of the power plants in an understanding and easy way. Furthermore, they predict the structural damage level with an earthquake intensity. They illustrate an estimation of economic losses, emergency

planning and recovery efforts and most importantly for determining the need for strengthening vulnerable systems or part of system.

Furthermore, four different approaches have been proposed for fragility curves developments (Kwon & Elnashai, 2006; Rossetto & Elnashai, 2003). They are usually considered to be empirical, judgmental, analytical and hybrid approaches. Empirical based approach, the fragility curves are usually based on survey data as their statistical representation. The resulting curves are more representative because actual site conditions are taken into consideration (Rossetto & Elnashai, 2003). However, a great number of structure of same year of construction or same construction technique are usually employed. Therefore, the difference between building characteristics or construction techniques is not made. Moreover, the field data is dominated by low and medium damage under low levels of ground motion. Damage due to aftershocks may be aggregated. Inexperience engineers may cause errors in building damage classification (Elnashai, 2006).

Judgemental fragility curves are based on information from experts (Rossetto & Elnashai, 2003). Civil engineers can provide damage description for any structure based on their observation. The estimation can be simply made to include all the factors. Eventhough, the judgment based approach can save a lot of time in their derivation, it can only be used to identify the overall estimation because the reliability of the estimation relied on the engineer experiences as different engineers have different opinions and perceptions.

Analytical based approach the fragility curves are developed with respect to computational outcomes either from static or dynamic analyses under earthquake increasing intensity level. This approach has no limitations (Jeong & Elnashai, 2007). But

a large number of analyses usually result in reducing error and increasing statistically reliable to use in future loss assessment studies. Nevertheless, a large computational simulation is usually involved (Rossetto & Elnashai, 2005). Moreover, the method of analysis, structural modelling, earthquake ground motions or target spectrum and damage models can be a challenging task.

Hybrid based approach the fragility curves try to improve the limitation of survey data, engineer opinion, and simulation techniques by compiling results from different methods (Rossetto & Elnashai, 2003). Fragility analysis may be performed based on judgemental opinion, and it also incorporates limited field data (e.g. ATC-40). They may also be performed by combining analytical simulation with observation field data. Analytical simulations provide the statistical data due to insufficient field data. Therefore, consideration of multiple datas can improve the fragility curves.

1.2 Earthquake history

Malaysia is located on the southern edge of the Eurasian Plate and is closed to a seismically active plate boundary i.e. the inter-plate boundary between the Indo-Australian and Eurasian Plates (Figure 1.2). However, strong tremors are frequently felt throughout the region, mainly from several distant earthquakes originating from Sumatra. Between 1909 and 2008, Kuala Lumpur reported 51 felts tremor, while Penang with 35 felts and Kedah has 14 felts. Johor and Perak have only 27 and 20 record felts, respectively. These earthquake felts range from III to VI on the Modified Mercalli Intensity scale (MMI).

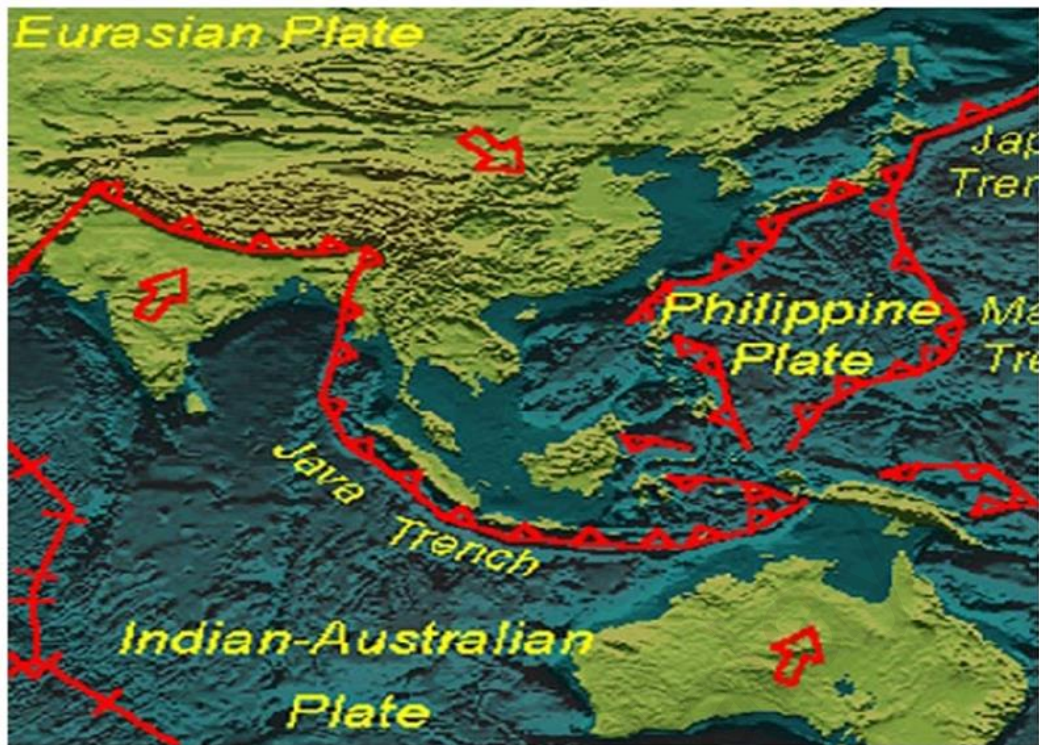


Figure 1.2: Major tectonic plates around Malaysia.

Among these the Northern Sumatra earthquake with a magnitude of 8.6 on 28th March 2005 and Southern Sumatra earthquake with a magnitude of 7.6 and 8.4 on 30th September 2009 and 12th September 2007 caused panic among the occupants in high-rise buildings. The incidents of crack observed on several high-rise buildings were also reported in the local newspapers.

The 26th December 2004 earthquake has generated a tsunami along the west coast of Peninsular Malaysia and caused many buildings to collapse. The casualties were more than any other records in history. The tsunami inflicted tremendous damage to property and caused the loss of 68 lives along the affected coastal regions in Peninsular Malaysia.

According to Rosaidi (2001), the Bengkulu earthquake occurred in Sumatran, Indonesia on 4th June 2000 with a magnitude of 7.8 and the epicentre was about 650km from Johor and about 800km from Kuala Lumpur. It caused several buildings in Johor

and the Klang Valley shaking. This tremor caused hundreds of people to rush out of high-rise buildings down to the ground level. Minor cracks in the building walls were also reported. The maximum earthquake magnitude in Johor and Kuala Lumpur was estimated about VI on the Modified Mercalli Intensity scale (MMI).

Some local earthquakes in Bukit Tinggi with magnitudes of around 3.0 on the Richter scale have also been reported. Tungah (2001) reported that an old façade (Penang Old Market, 1967) collapsed as a result of an earthquake from Sumatra. An induced local earthquake over the Kenyir Dam area in the state of Terengganu from 1984 to 1987 was reported due to the impounding of the dam. Obviously, distant earthquakes in Sumatra had frequently shaken high-rise buildings in Peninsular Malaysia and minor cracks on buildings were reported. Thus, it is necessary to be prepared for such disasters and to mitigate the risk associated with earthquakes. The two recent largest earthquakes in Sumatra caused tremors felt in Peninsular Malaysia are shown in Figure 1.3.

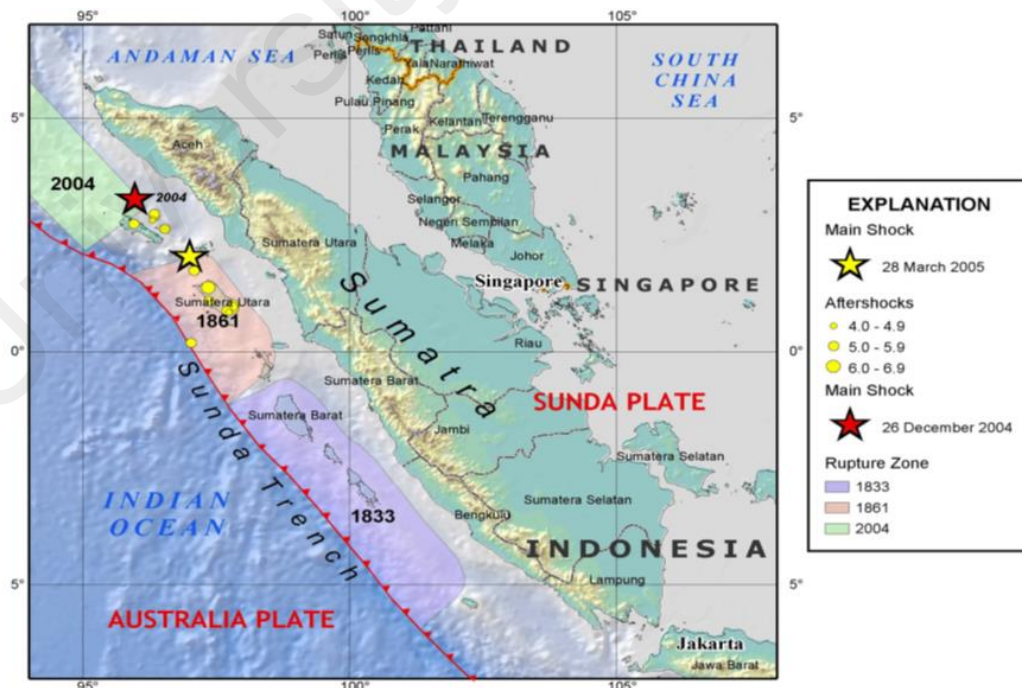


Figure 1.3: Two largest earthquakes in Sumatran subduction zone caused tremors felt in Peninsular Malaysia (Balendra and Li, 2008).

1.3 Problem statement

On September 30, 2009 at 10:16am local time, a powerful events of magnitude M_w 7.6 occurs in southern Sumatra, Indonesia. The epicenter of the earthquake was located at 0.725°S , 99.856°E with a distance of approximately 330km from Kuala Lumpur. Most existing buildings in Malaysia were directly affected. The Ministry of Public Works reported that the earthquake caused slight damage to the worker's quarters of Kuala Lumpur Hospital and the Pantai Dalam flats (Figure 1.4). These damages drew attention to an on-going problem in Malaysia regarding seismic fragility of existing buildings since most of these were designed according to British Standard BS8110:1997.

In Malaysia, few severe low-ground motions are recorded since the Sunda tectonic plate is stable, but the paucity of such information has nevertheless been ultimately detrimental to society. Thus, this dearth of such data has promoted the development of a set of artificial "target" acceleration time histories based on site response analysis. To aid this effort, ground motion data from other parts of the world were selected from the available strong-motion database. One-dimensional (1-D) equivalent linear site response analyses are carried out with increasing levels of seismic intensity. This approach is used to develop a set of time histories at the surfaces of this study. This approach permitted the local soil conditions such as different soil layering and characteristics to be considered in the analysis.



Figure 1.4: Observed damage to the Pantai Dalam flats after the southern Sumatra earthquake, Sept. 30, 2009.

1.4 Objectives

This dissertation focuses on seismic response analyses and development of the fragility curves for typical building stocks in Malaysia, particularly those that had been designed according to the British Standard BS8110:1997. The seismic fragility for such buildings is important due to a great number of buildings throughout Malaysia have been built to this standard. Specifically, the research involves five primary objectives:

1. To develop a set of target acceleration time histories at the ground surface for soil type C (very dense soil and soft rock), D (stiff soil) and E (soil with $> 3\text{m}$ of soft clay) at Kuala Lumpur,
2. To validate analysis model and assumption of infilled RC frames with shake table experimental results,

3. To evaluate the local and global response of a 11-story RC framed building at soft rock and stiff soil,
4. To evaluate the effect of infill in-plane and out-of-plane masonry walls on the seismic response of a four-storey RC school building,
5. To examine the effects of site soil conditions and the number of building storeys on the resulting fragility curves.

1.5 Scope

The scope of this work focuses primarily on reinforced concrete framed buildings that were constructed using two different standard designs done by Ministry of Public Works Malaysia. Four typical heights for the design are considered, i.e. 3-, 4-, 7- and 11-storeys.

A database of actual, recorded earthquake ground motion is formed by selecting ten records from the Consortium of Organizations for Strong Motion Observation Systems (COSMOS) Strong Motion Database according to expected earthquake magnitude, epicentral distance and site soil condition. A site response analysis model is selected and several soil profiles from the soil investigation report are then constructed. The ground motions at the surface as input to time history analysis are computed by propagating selected ground motions via soil column.

Three-dimensional finite element models are analyzed using nonlinear dynamic time history analysis. The modified Kent-Park model (Kent & Park, 1971) is employed to describe the stress-strain relationship of the concrete and the Giuffr -Pinto formulation, implemented later by Menegotto and Pinto (1973) is employed for the steel. The single

equivalent diagonal strut model proposed by Kadysiewski and Mosalam (2009) is adopted for modeling solid infill panels. However, the openings in masonry infill walls are beyond the scope of this study. The finite element model and analysis assumption are compared with shake table test for verification. The comparison is done in terms of global acceleration and displacement time histories but the local stress-strain relationship are not considered.

Four damage states, namely slight, moderate, extensive and complete damage levels defined in HAZUS-MH MR4 (FEMA, 2003) are used and fragility curves are developed accordingly. The fragility curves are constructed based on peak horizontal ground acceleration (PHGA) at the “seismic bedrock”. The material uncertainty is ignored while uncertainties associated with ground motions are taken into account through the record-to-record variability.

1.6 Organization of the dissertation

The research work of this dissertation is organized in seven chapters. Each chapter is summarized as follows:

Chapter 1 starts with a general background of this study and earthquake history recorded in Malaysia. These sections discuss the geographical location and earthquake events in Malaysia over 100 years, providing general knowledges to readers. However, section 1.3 discusses the current problems the author found. The section 1.4 lists five different objectives in line with current research trends and section 1.5 shows the scope for this study.

Chapter 2 focuses on relevant literature to help the author to conduct the research. It starts with structural modeling techniques and then the selection of ground motion accelerations. The measures of structural damage and reliability approaches are discussed in section 2.4 and 2.5 respectively.

Chapter 3 presents the input ground motions for fragility assessments. It start with seismic hazard map and determine the most contributing earthquake scenarios to the study areas. Local site effects will be analysed in section 3.4.

Chapter 4 discusses shake table tests conducted in Harbin Institute of Technology, China. The development of the test structure is explicitly discussed. This aspect includes small-scale design criteria, similitude relationship, construction process, shake table facilities and instrumentations, additional mass arrangement and sequence of loading. The observation of the outcome of the experimental tests will be discussed in the last section of this chapter.

Chapter 5 summarizes the computational modeling of rc frame buildings with and without infill walls. Nonlinear time history analysis and assumption made will be discussed in section 5.3. Next, the verification of the structure model and analysis environment through comparison with shake table tests conducted at Harbin Institute of Technology, China is undertaken. Subsequently, the effects of masonry infilled wall and response of rc frame building will be discussed.

Chapter 6 presents seismic fragility analysis. The damage measure, performance levels and construction of fragility curves will be discussed in section 6.2, 6.3 and 6.4, respectively. Sensitivity analyses are discussed in section 6.5. These include the effects of site conditions and number of story on fragility curves. The prediction of degree of structural damage based on fragility curves is given in the last section of this chapter.

Conclusions are made in chapter 7. The improvements for future study are given in the last section of this chapter. The papers that have been accepted or are being reviewed in a scientific journal are listed in Appendix D.

University of Malaya

CHAPTER 2: LITERATURE REVIEW

2.1 Introduction

Several investigations related to seismic analysis are discussed in this chapter. In particular, the structural modeling approaches, the selection of ground motion acceleration as well as the measures of structural damage. The generation of artificial ground motions is also discussed in Section 2.3.5. Section 2.5 summarizes the seismic fragility and reliability methods including SAC-FEMA method, Response Surface method, Monte Carlo simulation, Bayesian method and Ryu's method.

2.2 Structural modeling method

This section shows the modelling of a complex system using an open source OpenSees (Mazzoni et al., 2007; McKenna & Fenves, 2001). In particular, fiber beam-column elements, constitutive models and infill walls simulation are studied.

2.2.1 Fiber beam-column elements

The response of frame elements can be adequately captured by many different elements. Taucer et al. (1991) demonstrated that any frame member can be accurately modeled as fiber model for calculate the response of structural concrete to cyclic loadings. The cross sections of the beam-column element are divided into unconfined concrete, confined concrete and steel fibers with corresponding material stress-strain relationships as shown in Figure 2.1.

The effects of cover and core concrete were described using stress-strain relationship. However, a large computational effort is generally required when a large

number of fibers are defined. Therefore, an appropriate number of fibers should be defined in order to satisfy a reasonable degree of accuracy and computational efforts.

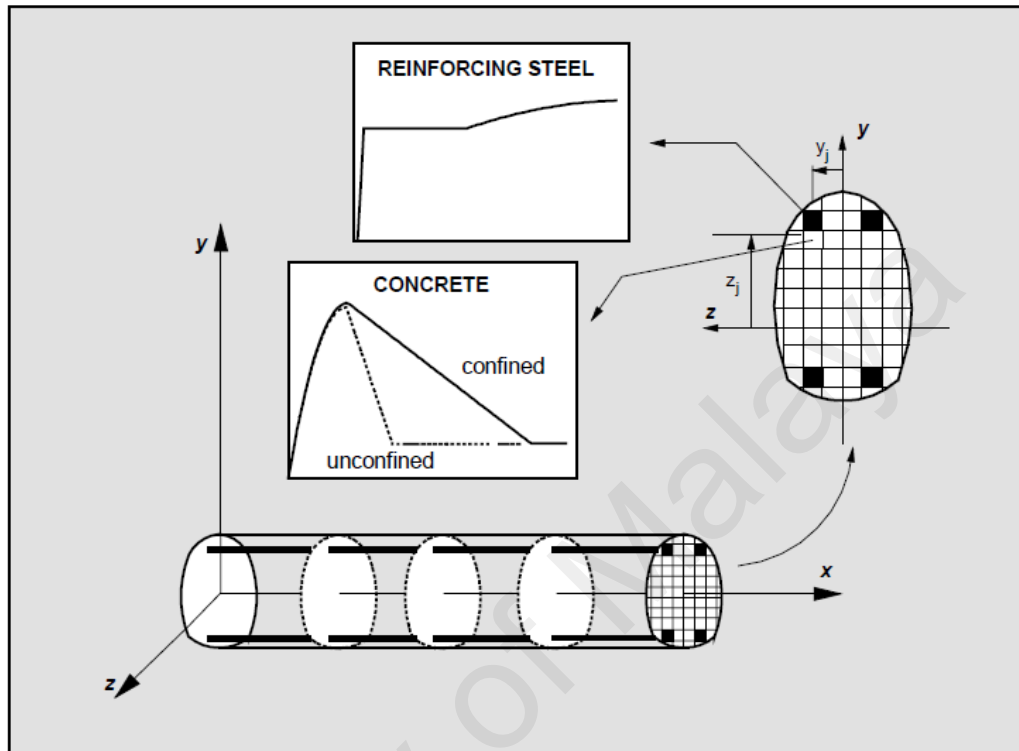


Figure 2.1: Fiber element for RC members (Taucer et al., 1991).

2.2.2 Constitutive models

The plot of stress versus strain for material fibers were required to assign to the fiber beam-column element. An open source, OpenSees (Mazzoni et al., 2007; McKenna & Fennes, 2001) provides several uniaxial material models. Among these, the Menegotto-Pinto model for steel fiber and the modified Kent and Park model for concrete fiber are discussed hereafter.

2.2.2.1 Steel model

The steel model proposed by Menegotto and Pinto (1973) has been popularly used due to earthquake loading. This model is illustrated in Figure 2.2 and it was used by Li and Hatzigeorgiou (2012), Taucer et al. (1991) and among others in examining RC structures under seismic loadings. It shows comparable with experimental test results. The Bauschinger effect was also taken into consideration. The loading and unloading path was defined as follows:

$$\sigma^* = b\varepsilon^* + \frac{(1-b)\varepsilon^*}{(1+\varepsilon^{*R})^{1/R}} \quad (2-1)$$

and

$$\sigma^* = (\sigma - \sigma_r) / (\sigma_0 - \sigma_r) \quad (2-2)$$

$$\varepsilon^* = (\varepsilon - \varepsilon_r) / (\varepsilon_0 - \varepsilon_r) \quad (2-3)$$

$$b = E_h / E_s \quad (2-4)$$

$$R = R_0 - \frac{a_1 \xi}{a_2 + \xi} \quad (2-5)$$

$$\xi = |(\varepsilon_m - \varepsilon_0) / \varepsilon_y| \quad (2-6)$$

and $(\varepsilon_r, \sigma_r)$ is the strain reversal point, $(\varepsilon_0, \sigma_0)$ is the an intersection between elastic and yield point, E_h is modulus of hardening, ε_m is an upper and lower bound of strain. R was the difference of strain as shown in Figure 2.3. R_0 , a_1 and a_2 can be determined by experimental tests. Dhakal and Maekawa (2002) proposed 20 for R_0 , 18.5 for a_1 and 0.15 for a_2 .

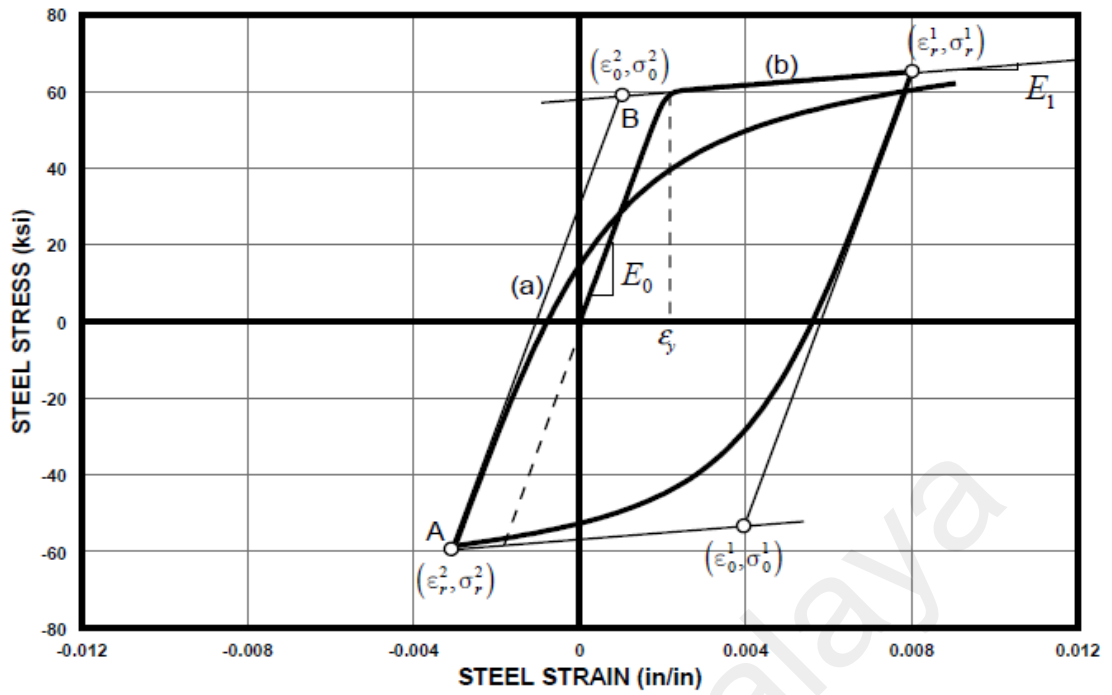


Figure 2.2: Steel model (Menegotto & Pinto, 1973).

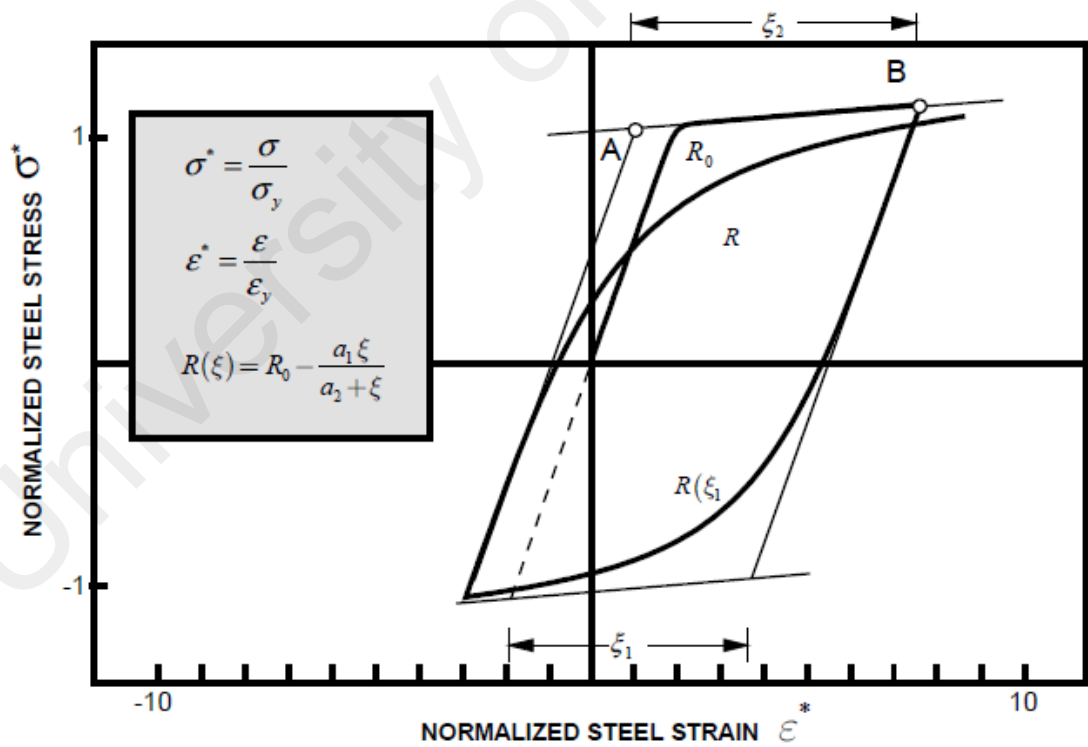


Figure 2.3: Parameter of R in the steel model (Taucer et al., 1991).

2.2.2.2 Concrete stress-strain relation

The Kent and Park model (1971) that was improved by Scott et al. (1982) was popularly employed for earthquake studies as shown in Figure 2.4. The concrete stress-strain relation is expressed as below:

$$f_c = Kf'_c \left[\frac{2\varepsilon_c}{0.002K} - \left(\frac{\varepsilon_c}{0.002K} \right)^2 \right] \quad \text{for } \varepsilon_c \leq 0.002K \quad (2-7)$$

$$f_c = Kf'_c [1 - Z_m(\varepsilon_c - 0.002K)] \quad \text{for } \varepsilon_c > 0.002K \quad (2-8)$$

but not less than $0.2Kf'_c$

where

$$K = 1 + \frac{Q_s f_{yh}}{f'_c} \quad (2-9)$$

and

$$Z_m = \frac{0.5}{\frac{3 + 0.29f'_c}{145f'_c - 1000} + \frac{3}{4} Q_s \sqrt{\frac{h''}{s_h}} - 0.002K} \quad (2-10)$$

ε_c was longitudinal elongation over length in concrete, f_c was longitudinal force over area in concrete (MPa), f'_c is strength of concrete in MPa, f_{yh} is the yield strength of hoop reinforcement in MPa, Q_s is the volume of link bars over volume of core concrete, h'' is the core concrete width in mm, and s_h was spacing of link bars in mm.

For stirrup-tie, Scott et al. (1982) recommended ε_u can be estimated as follows:

$$\varepsilon_u = 0.004 + 0.9Q_s(f_{yh}/300) \quad (2-11)$$

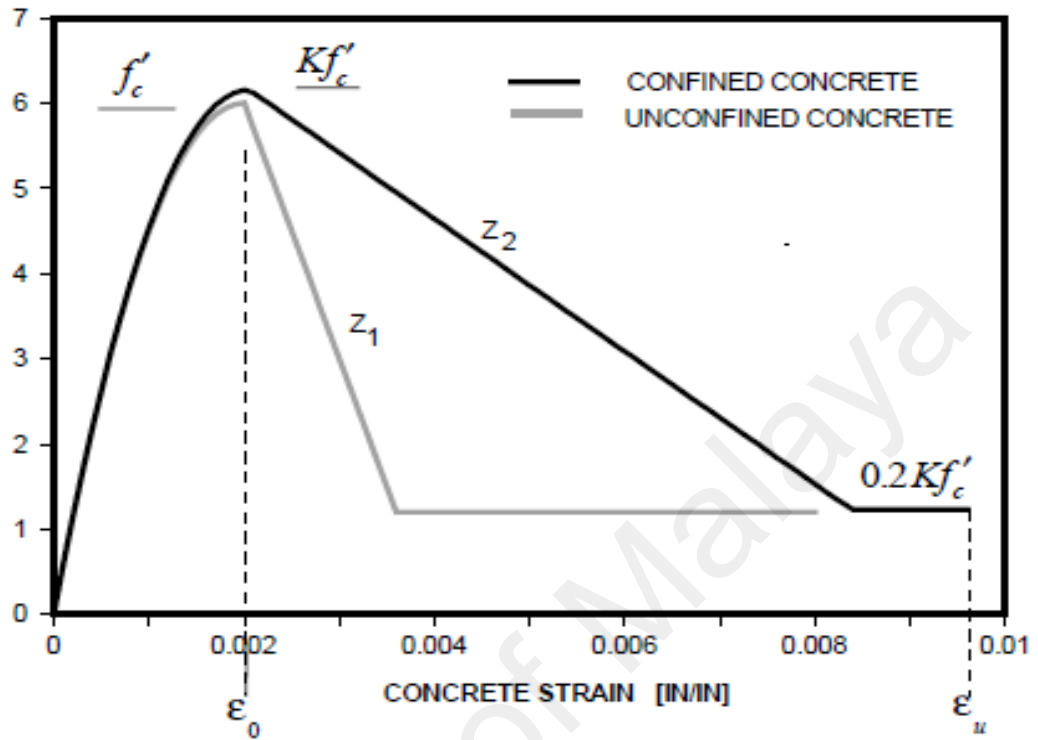


Figure 2.4: Concrete model (Taucer et al., 1991).

To consider concrete cover breaking, the cover strength was decreased to $0.2f'_c$ when ε_u is equal to 0.005 (Taucer et al., 1991). The concrete tensile strength was not included because the section response was only affected before yielding. According to Taucer et al. (1991), some laws govern the concrete stress-strain relationship behavior are as follows:

1. ε_r and ε_p indicated in the curve was expressed as:

$$\frac{\varepsilon_p}{\varepsilon_0} = 0.145 \cdot \left(\frac{\varepsilon_r}{\varepsilon_0} \right)^2 + 0.13 \cdot \left(\frac{\varepsilon_r}{\varepsilon_0} \right) \quad \text{for} \left(\frac{\varepsilon_r}{\varepsilon_0} \right) < 2 \quad (2-12)$$

$$\frac{\varepsilon_p}{\varepsilon_0} = 0.707 \cdot \left(\frac{\varepsilon_r}{\varepsilon_0} - 2 \right) + 0.834 \quad \text{for} \quad \left(\frac{\varepsilon_r}{\varepsilon_0} \right) \geq 2 \quad (2-13)$$

where ε_0 was the level of strain at peak stress.

2. Stress of concrete was taken as 0.
3. The stress is taken as 0 when reloading is in compression. It will continue when concrete strain is high. However, in actual the concrete follow inelasticity. Figure 2.5 shows the illustration of the hysteretic concrete stress-strain relation.

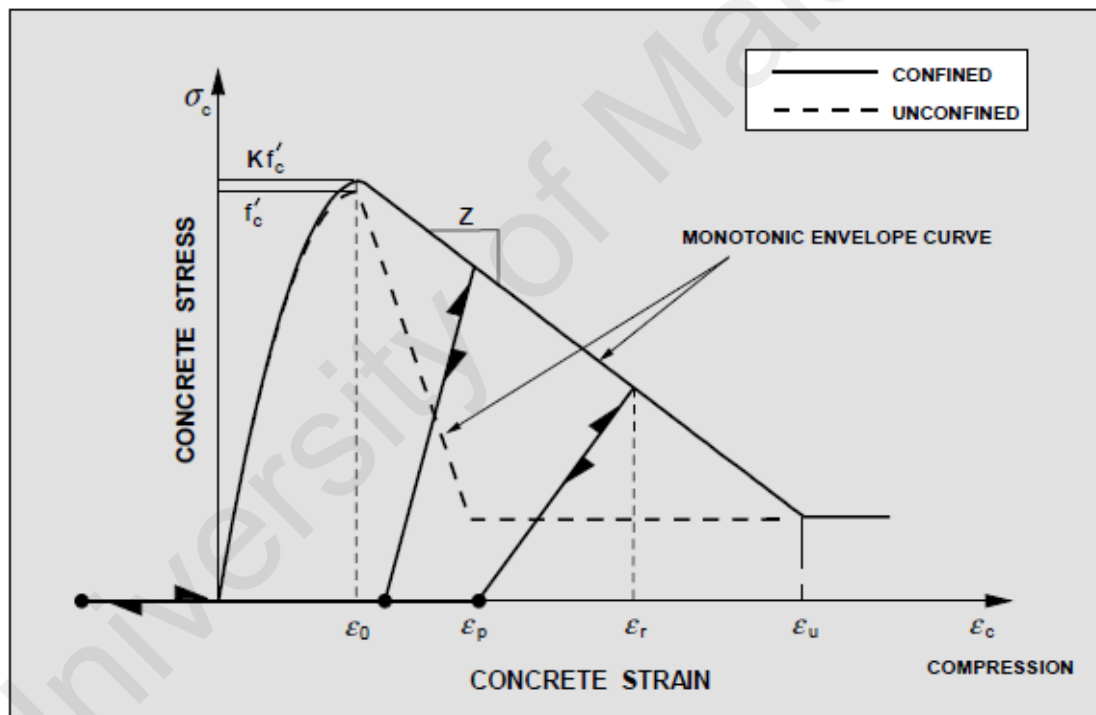


Figure 2.5: Hysteretic concrete stress-strain relation (Taucer et al., 1991).

2.2.3 Masonry infill walls

The response of concrete frame along with brick walls can be broadly categorized in two different types (Chrysostomou & Asteris, 2012; Fiore et al., 2012; Perera, 2005; Su & Shi, 2013). The first is to include micro-modeling models where the masonry panel

and their interaction are separately model and described by appropriate constitutive relations. This model allows the direct implementation of the material properties of each component. To calibrate the properties of a unit cell that can be eliminated. Some localized effects can be detected as well (Rabinovitch & Madah, 2011). However, this model is generally time consuming especially for large and complex buildings under repeated dynamic time-history analyses. On the other hand, a practical and efficient modelling technique is always sought after.

Another type is based on macro-modeling technique. This type of technique does not take into account any distinction between masonry units and joints. The masonry walls are considered as a homogeneous material. This models can be further incorporated out-of-plane behavior of masonry infill through the arching or rocking effects (Kadysiewski & Mosalam, 2009; Roh & Reinhorn, 2009; Tu et al., 2010). In particular, single diagonal struts have some disadvantages of not being able to model the interaction with the bounding frame. The openings in masonry panels (Asteris et al., 2011) needs a special treatment (Asteris et al., 2012). This model, however, more simpler and efficient compared to micro-model. Subsequently, the latter model is more practical in earthquake engineering when complex and full-scale three-dimensional masonry infilled structures are studied.

In this section, several traditional methods for macro simulation will presented below.

2.2.3.1 UMW in-plane failure modes

The wall failures are expressed in sequence of damage among the elements of the infilled RC frames. Such damage can be classified into four different failure modes as follows (Liau & Kwan, 1985).

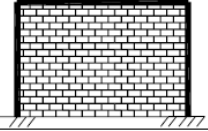
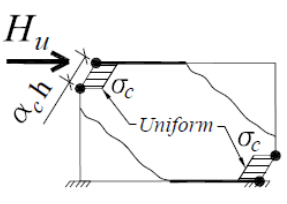
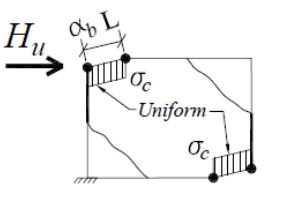
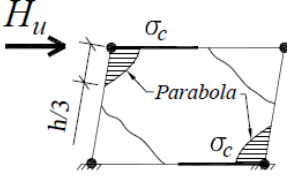
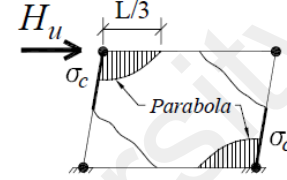
Mode 1, corner crushing: In this mode of failure, the brick walls were crushing especially in corner areas. The corners found plastic hinges near compression zone of the panel where shear connectors and the infill-beam connections are yielded.

Mode 2, crushing was found in corner area while beams and infill-columns connections are failed: In this mode of failure, the compressive corner regions of the infill panels crush.

Mode 3, diagonal crushing: In this mode of failure, all plastic hinges form near connection of beam and column. Shear connectors and infill-beam connections are also yielded.

Mode 4, diagonal crushing with failure in infill-columns joints: In this mode of failure, all plastic hinges form near connection of beam and column where shear connectors and infill-columns connections are yielded. Table 2.1 summarizes the modes of failure observed alongwith plastic capacities H_u and joint shear demands V_j .

Table 2.1: In-plane modes of failure and their corresponding estimated capacities H_u and joint shear demands V_j of infilled systems (Liauw & Kwan, 1985).

Mode		Estimated capacity H_u and joint shear demand V_j (Liauw and Kwan 1985b)
1		$H_u = \sqrt{2 \frac{(M_{pj} + M_{pc})}{\sigma_c t h^2}} \sigma_c t h + s \left(L - \frac{h}{2} \right)$ $V_j = \frac{M_{pj} + M_{pc}}{\alpha_c h} + \sigma_c t \frac{\alpha_c h}{2}$
2		$H_u = \frac{1}{\tan \theta} \sqrt{2 \frac{(M_{pj} + M_{pb})}{\sigma_c t h^2}} \sigma_c t h + s \frac{h}{2} \tan \theta$ $V_j = \frac{M_{pj} + M_{pb}}{\alpha_b L} + \sigma_c t \frac{\alpha_b L}{2}$
3		$H_u = 4 \frac{M_{pj}}{h} + \sigma_c t \frac{h}{6} + s \left(L - \frac{h}{2} \right)$ $V_j = 4 \frac{M_{pj}}{h} + \sigma_c t \frac{h}{6}$
4		$H_u = 4 \frac{M_{pj}}{h} + \sigma_c t \frac{h}{6(\tan \theta)^2} + s \frac{h}{2 \tan \theta}$ $V_j = 4 \frac{M_{pj}}{h} \tan \theta + \sigma_c t \frac{h}{6 \tan \theta} + s \frac{h}{2}$

where

$$\alpha_b = \sqrt{2 \frac{(M_{pj} + M_{pb})}{\sigma_c t h^2}} \tan \theta \quad (2-14)$$

$$\alpha_c = \sqrt{2 \frac{(M_{pj} + M_{pc})}{\sigma_c t h^2}} \quad (2-15)$$

and

H_u is the lateral frame capacity,

M_{pb} is amount of beam moment,

M_{pc} is the amount of column moment,

M_{pj} is amount of beam and column connection moment,

h was story height,

L is the span of infilled concrete structure,

T was wall thickness,

S was shear strength of interface connection,

σ_c is the crushing stress of panel material, and

θ was diagonal degree on wall.

However, masonry infill walls can also be determined based on three possible failure modes (Paulay & Priestley, 1992).

In strut failure, the masonry prism strength, f'_m is a main factor. Estimation of the masonry prism strength is given as:

$$f'_m = f_y = \frac{f'_{cb}(f'_{tb} + \alpha f'_j)}{U_u(f'_{tb} + \alpha f'_{cb})}$$

(2-16)

where α is $j/4.1h$, j is mortar thickness, h is masonry unit height. U_u is coefficient of stress ($U_u=1.5$), f'_{tb} is brick strength of tension ($=0.1f'_{cb}$), f'_{cb} is brick strength, and f'_j is mortar strength.

The capacity of strut in horizontal direction was then given as,

$$V_c = z t_w f'_m \cos \theta \quad (2-17)$$

where

f'_m is the clayed brick strength, and z is the width of strut.

For failure mode sliding, the strength of shear, τ_f , was expressed as follows:

$$\tau_f = \tau_0 + \mu \sigma_N \quad (2-18)$$

where

τ_0 is mortar beds capacity, μ is friction coefficient of sliding, and σ_N is stress in vertical direction. The force is then given as,

$$V_f = \tau_0 t_w l_m + \mu N \quad (2-19)$$

where

t_w is thickness of wall, l_m is wall length, and N is force in vertical direction. Thus N can be estimated as force in vertical direction, $R_c \sin \theta$, where R_c is diagonal compression force, Eq. 2-19 can be rewritten as

$$V_f = \frac{\tau_0 t_w l_m}{1 - \mu \tan \theta} \quad (2-20)$$

2.2.3.2 Strut models

To represent unreinforced masonry infill walls within a larger structural systems, properties of simple equivalent strut or struts replacing the infill wall in each frame have been proposed. Such strut models are proportioned to represent the characteristics of unreinforced masonry walls in concrete structures assembly by matching experimental results, assuming some specific failure mode, or by calibrating the struts from computational simulation.

The struts is arranged based on the expected failure mode of the assembly. For example, to represent the failure modes discussed in Section 2.2.3.1 and based on crack patterns observed in experiments performed on unreinforced masonry infilled RC frames, the Strut and tie (SAT) models shown in Figure 2.6 are proposed. These SAT assemblies can be made more simple. For example, by neglecting the material strength, the tie elements can be omitted in modes 1 and 2. Another possible simplification for modes 3 and 4 is to use the strut model. Simplified representations of the SAT models in Figure 2.6(a) are shown in Figure 2.6 (b).

The choice of the geometric details of the SAT model for infilled RC frames can be adjusted based on the experience of the designer and the balance between the practicality and the accuracy of the model. In general, the material properties of each horizontal strut or tie is then predicted from shear capacity of the interface between the mortar joint and the masonry units. The material properties of the vertical struts and tie can be estimated from the behavior of the masonry prisms in compression and tension. The material properties of the diagonal struts and ties can be obtained from the diagonal compression and tension behavior of masonry assemblies. The area of each strut and tie

can be selected with respect to a step such that the assembly has the same strength and stiffness as predicted by experiments or by finite element analyses.

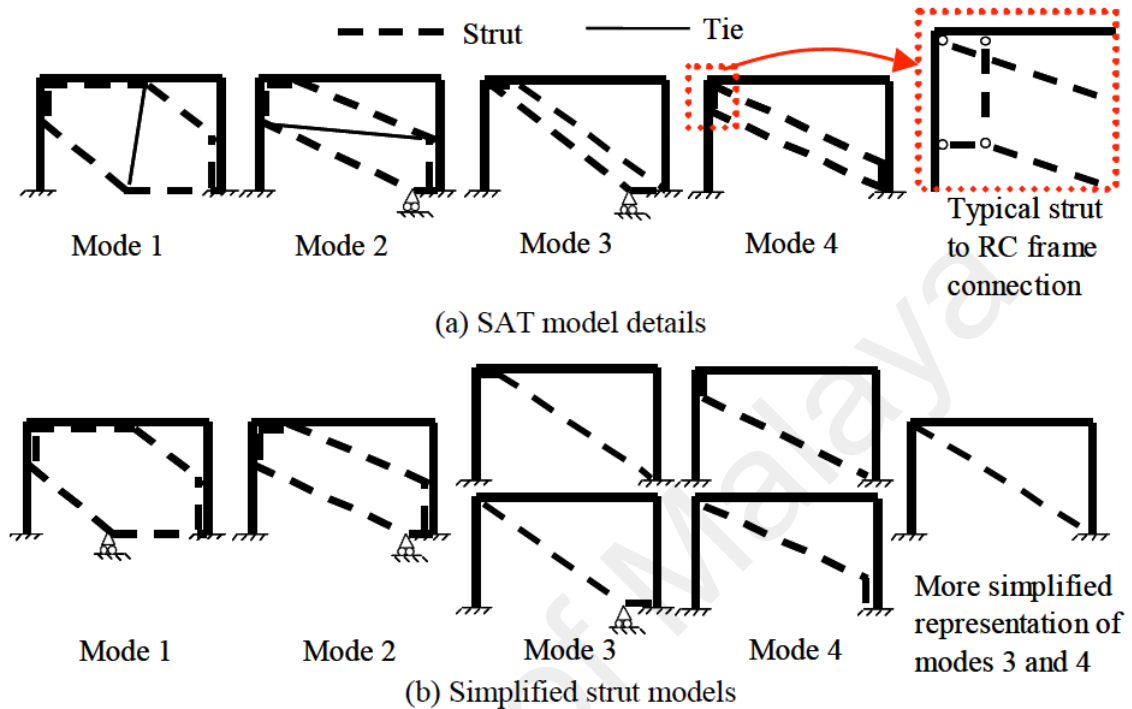


Figure 2.6: SAT models.

Among these, Hashemi and Mosalam (2007) used a three dimensional SAT model for the encountered both failures . An interaction among the horizontal and vertical direction forces is given in Figure 2.7. Eight compression elements connected is included in this model.

The compressive stress-strain relationship for the model is a parabolic from zero to peak stress, while the post-peak is linear down to a constant residual resistance. The model response is estimated on the basic of the finite displacements of the DOF and is thus geometrically and material nonlinearity. Kadysiewski and Mosalam (2009) showed that this model has some problematical behaviors where under certain conditions, the both direction forces in the model may exceed a specified interaction surface, and this model

may be difficult to achieve the elastic properties of the model with those of the actual infill panel.

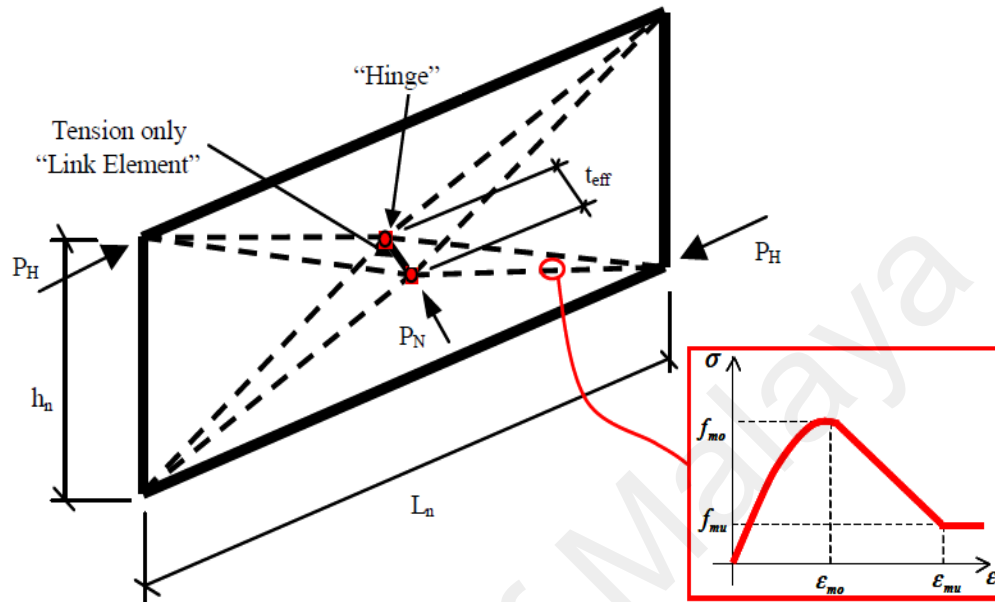


Figure 2.7: Infill walls represented by strut and tie model (Hashemi & Mosalam, 2007).

Kadysiewski and Mosalam (2009) proposed a diagonal member as shown in Figure 2.8. The node was given a lumped mass in out-of-plane direction. The both directional failure properties of wall were estimated according to FEMA 356. This model enables modeling a cross section as an arbitrary collection of nonlinear fiber elements, and satisfies the in-plane and out-of-plane interaction relationship.

It should be noted that this single diagonal member model can cause different loadings distribution in the surrounding building, but when the floor diaphragms are relatively stiff the consequences of this simplification are likely to be minor. The disadvantage of the single diagonal struts is unable to model the interaction with the bounding frame. The openings in infill panels need special skill and adjustment knowledge (Asteris et al., 2011, Asteris et al., 2012).

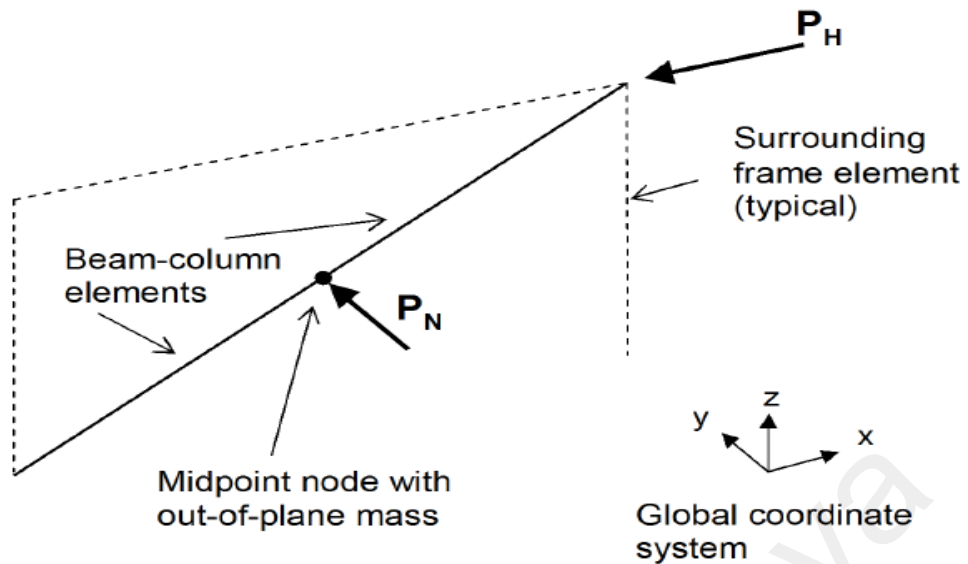


Figure 2.8: Infill walls represented by a diagonal member Kadysiewski and Mosalam (2009).

Kwon and Kim (2010) adopted compression-only diagonal struts for masonry infill walls (Figure 2.9). The strut strength was estimated considering three potential failure modes as discussed in Section 2.2.3.1. The minimum strength of the three failure modes was considered as the ultimate strength.

However, the strength of shear from failure sliding and compression was not exceed 0.83MPa as suggested by ACI 530-05:

$$V_{\max} / t_w l_m = 0.83 \quad (2-21)$$

The resistance against lateral load can be provided by multiple struts of walls. Figure 2.10 shows a compression and zero tension curve that was assumed for a relationship of force and displacement of strut model. The springs proposed at strut was used for hysteretic behavior of diagonal struts. A rigid truss element was used to simulate the strut model. Four different relationships were developed. The ultimate displacement is then calculated as:

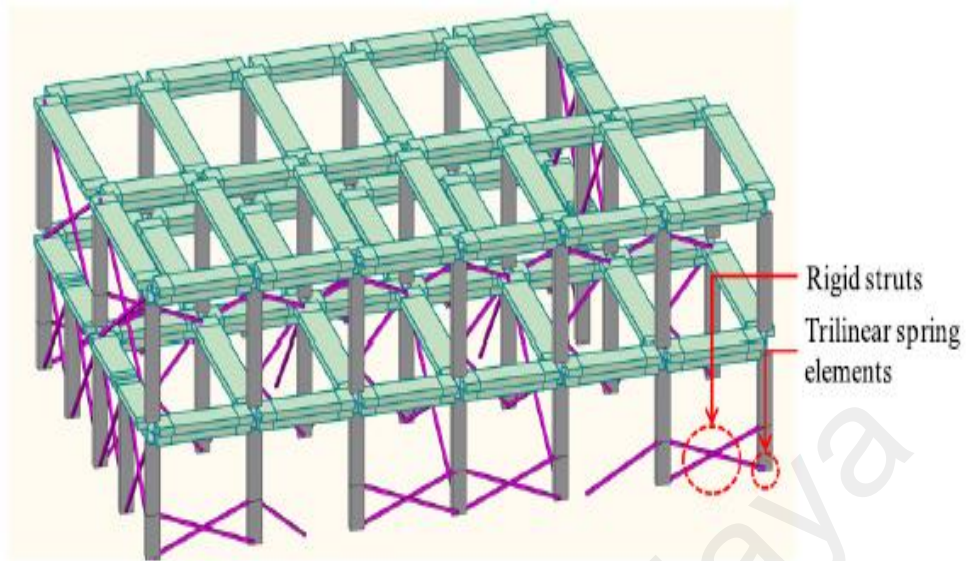


Figure 2.9: Infill walls represented by compression-only diagonal struts (Kwon & Kim, 2010).

$$U_m = \frac{\varepsilon'_m d_m}{\cos\theta} \quad (2-22)$$

where ε'_m is strain of masonry and assumed to be 0.0018 and d_m is length of strut. 0.8% of ultimate drift was given to the U_m/h_m ratio. The initial stiffness K_0 was determined as follows:

$$K_0 = 2(V_m / U_m) \quad (2-23)$$

where V_m is the maximum shear force determined from Eq. 2-21. The stiffness ratio, α , was assumed as 0.2 and U_y and V_y , were estimated based on V_m , K_0 , and α .

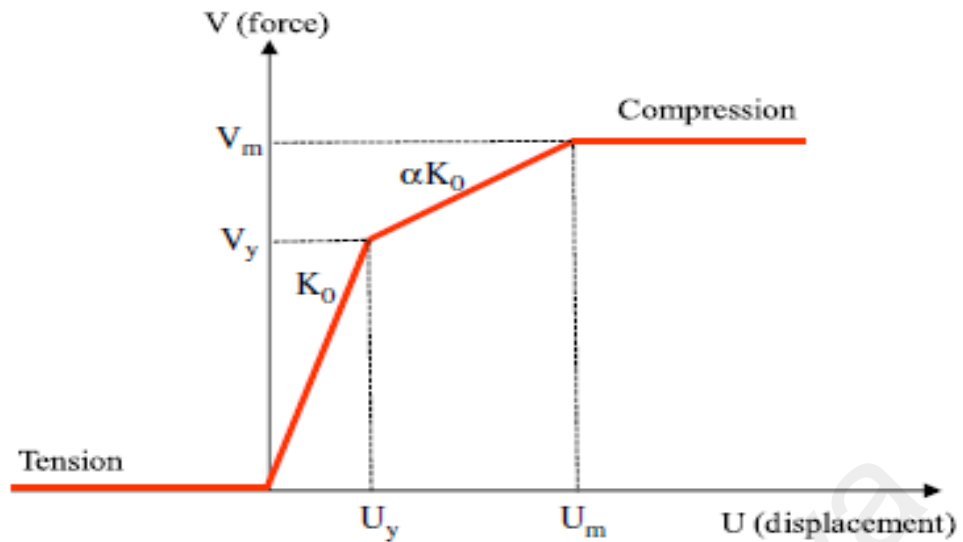


Figure 2.10: Hysteretic behavior of diagonal strut elements.

In addition to these strut models, the wall and structural element interaction was considered using a double equivalent strut as given in Figure 2.11 (Uva et al., 2012). The multiple struts provided by the force-displacement relationship is similar to the case of a single equivalent strut, but the stiffness is shared among them.

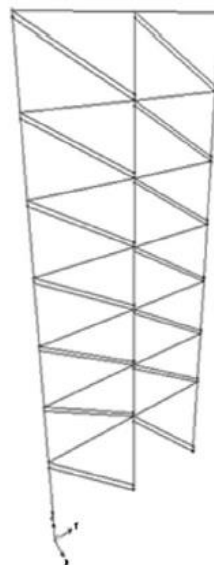


Figure 2.11: Infill walls represented by double equivalent strut model (Uva et al., 2012).

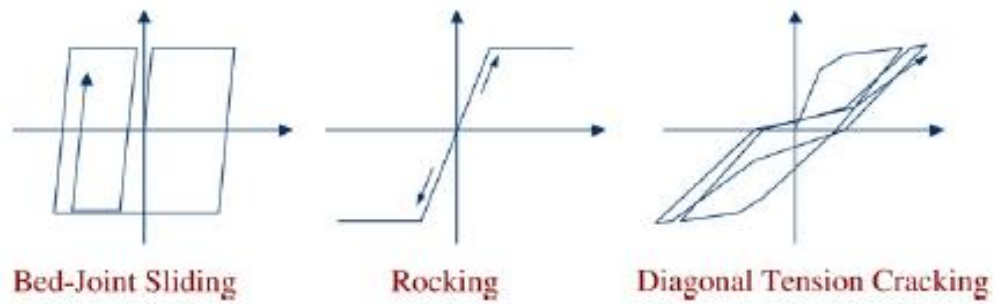


Figure 2.13: Different failure pattern (Park et al., 2009).

For boundary conditions, the pier height is adjusted and fixed end conditions were used as shown in Figure 2.14. This is to reduce the rigid at the end supports. In other words, r is increased creating a different height. More description regarding this approach can be found in literature.

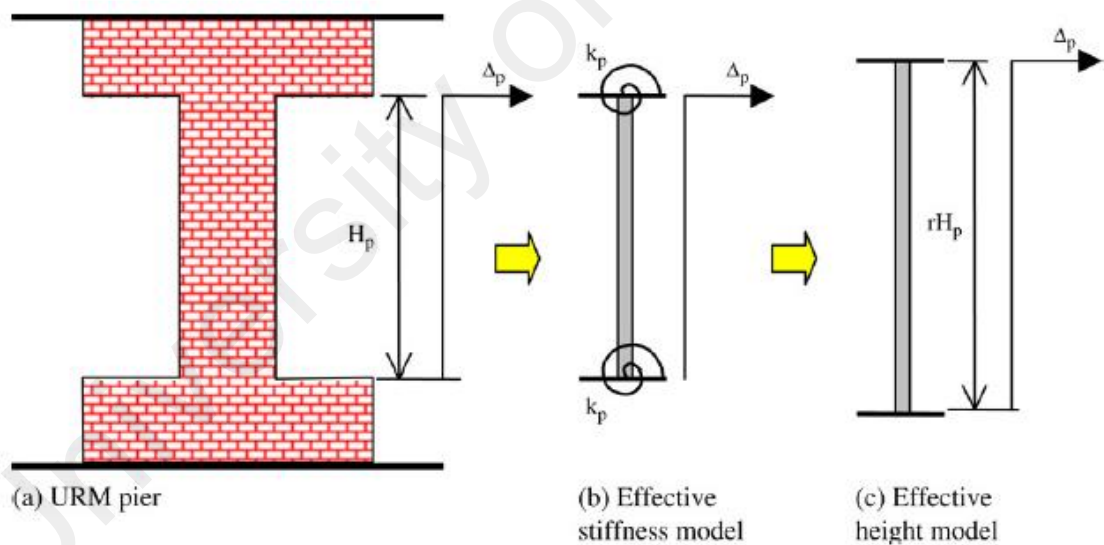


Figure 2.14: Boundary condition for unreinforced masonry pier (Park et al., 2009).

In addition, Park et al. (2009) proposed three different modeling approaches for out-of-plane walls. The first approach is that neglecting the property of the walls. The dynamic analysis of the unreinforced masonry building only considers the mass of the

out-of-plan wall. FEMA (2003) shows a similar technique for modeling the infill wall. A conservative approach can be considered in terms of estimating displacements.

The second approach is that both end of supports were fixed.. A simpler calculation for stiffness in out-of-plane wall is based on bending theory. This configuration was adopted for the walls with a conditional connection.

The third approach is that connection between out-of-plan and in-plane walls and floor were assumed. Thus, giving a higher stiffness of out-of-plane wall. The wall stiffness was determined from computational simulation. Subsequently, the masonry elastic modulus over the degraded building can provide the stiffness in out-of-plane direction of the degraded building.

2.3 Ground motion selection techniques

A crucial role in earthquake studies is the ground motion selection techniques that are expected to be recorded in future. This step has several different methods. These include steps based on dominated earthquake scenarios, spectral matching, and/or other criteria. The record selection based on seismic code recommendations are also briefly summarized in Section 2.3.4 and 2.3.5. A generation of synthetic earthquakes is presented in Section 2.3.6.

2.3.1 Record selection with respect to dominated earthquake scenarios

The dominated earthquake scenarios are the most popular merits employed in the earthquake studies. Among these, Shome et al. (1998) forms sets of recorded ground

motions based on four pairs of different magnitude and distance. This approach allows a controlling in a range value of $(M \pm \Delta M, R \pm \Delta R)$. Papaspiliou et al. (2012) formed a set of real accelerograms in order to performed site response analysis. Record selection was made based on earthquake moment magnitude more than 6.0, epicenter distance less than 100km and other criteria.

However, Stewart et al. (2001) and also Bommer and Acevedo (2004) considered magnitude as a crucial parameter, while the effects of epicenter distance had not been investigated. However, $\pm 0.25M_w$ for magnitude was suggested by Stewart et al. (2001) and $\pm 0.20M_w$ was recommended by Bommer and Acevedo (2004). A search window for earthquake magnitude shall control in a small range while epicenter distance shall kept widened.

Based on recent studies, Iervolino and Cornell (2005) showed that the dominated earthquake scenarios selection technique was not given a much different results. Shome et al. (1998) also highlighted that some structural damages are not sensitive to the selection process. Baker and Cornell (2005) indicated the results of structural analysis is also insensitive to epicenter distance, but it is depend on earthquake magnitude. Therefore, earthquake magnitude is considered as a most weighted factor in the selection process while epicenter distance is only an additional criterio.

2.3.2 Selection with respect to spectrum matching

The spectrum matching is also adopted in the earthquake studies, in particular in earthquake selection. In this case, the target spectrum are usually defined based on seismic code or PSHA This is usually considered as an alternative selection criterion, after

selection based on earthquake magnitude. Along these lines, several formulations to check spectral compatibility of given ground motion with target spectrum have been published. For example, a different between target spectrum and ground motion, D_{rms} has been proposed by Pagliaroli and Lanzo as follows:

$$D_{rms} = \frac{1}{N} \sqrt{\sum_{i=1}^N \left(\frac{SA_0(T_i)}{PGA_0} - \frac{SA_s(T_i)}{PGA_s} \right)^2} \quad (2-24)$$

where N is the period of spectral shape interested, $SA_0(T_i)$ is the acceleration spectral at period T_i , $SA_s(T_i)$ is the expected acceleration spectral, and PGA_0 and PGA_s are respectively maximum ground amplitude and at 0 period expected spectrum. The closer matching between a ground motion shape and target spectrum usually has a small value of D_{rms} . In general, the database size and ground motion determine the value of D_{rms} . The period range of interest is also another criterion that should be considered for this approach. The range of shorter is always the engineer looking for.

Among these, the deviation for spectrum matching can be expressed in three different expressions as follows (Kayhan et al., 2011):

$$\delta = \sqrt{\frac{1}{m} \sum_{i=1}^m \left(\frac{E(T_i) - A(T_i)}{A(T_i)} \right)^2} \quad (2-25)$$

$$MSE = \frac{1}{m} \sum_{i=1}^m (E(T_i) - A(T_i))^2 \quad (2-26)$$

$$MRE = \frac{1}{m} \sum_{i=1}^m \left| \left(\frac{E(T_i) - A(T_i)}{A(T_i)} \right) \right| \quad (2-27)$$

where δ and MRE are estimated based on mean spectra of ground motion deduct the expected spectrum, MSE is determined using absolute values of them, m is the step number depending on ΔT while spectrum was sketched, $E(T_i)$ was pseudo-acceleration ordinate for mean spectrum at interested period T_i , $A(T_i)$ has values of interval spectral of expected spectrum at similar time.

However, Shahrouzi and Sazjini (2012) proposed an equation for the average spectrum deviation $f_{ERROR}(X)$ as

$$f_{ERROR}(X) = \sqrt{\frac{1}{n} \sum_{j=1}^n \left(\frac{\beta \times SA_{mean}(T_j) - SA_{target}(T_j)}{SA_{target}(T_j)} \right)^2} \times 100 \quad (2-28)$$

where

$$\beta = \max \left\{ \frac{SA_{target}(T_j)}{SA_{scaled-mean}(T_j)} \right\} \quad j = 1, 2, \dots, n \quad (2-29)$$

$$SA_{target}(T_j) = 1.4 \times SA_{design}(T_j) \quad (2-30)$$

and $SA_{mean}(T_j)$ is pseudo-acceleration interval of mean spectra at period T_j . $SA_{target}(T_j)$ is spectral ordinate for expected spectrum at similar time, and n is number for pre-defined time frame.

In addition, Shantz (2006) proposed another method of spectral matching. This alternative usually applies in time history analysis. It was conducted on the basic of compatibility between response of displacement ($D_{max-rec}$) of inelastic single degree of freedom oscillators at peak value divide periods (T) and ductilities (μ) interested from a

particular ground motion with target displacement surface. The displacement expected is expressed through a region of interest in the T - μ space as follows:

$$D_{design}(T, \mu) = \mu_{NIDD(T, \mu)} S_{d-A.R.}(T) \quad (2-31)$$

$$NIDD(T, \mu) = \frac{D_{max-rec.}(T, \mu)}{S_{d-A.R.}(T)} = \frac{D_{max-rec.}(T, \mu)}{S_{d-rec.}(T)} \frac{S_{d-rec.}(T)}{S_{d-A.R.}(T)} = C_{\mu}(T, \mu) C_a(T) \quad (2-32)$$

where $S_{d-A.R.}(T)$ was displacement spectral at certain period of structure calculated using empirical formulation with dominated earthquake scenarios. For a larger area in the T - μ space ($0.5 \leq T \leq 5$ and $2 \leq \mu \leq 8$) a regression analysis was adopted to calculate mean values of inelastic structural response $NIDD(T, \mu)$. The Next Generation Attenuation (NGA) dataset was used to select a number of earthquake ground motions. An application of a scaling to fit between two spectrum is then recommended based on both expected response and expected response for original records.

2.3.3 Additional selection techniques

In recent scientific literature, other selection criteria have also been proposed. These include site classification, ground motion duration, seismotectonic condition and seismological factors as well as acceleration to velocity ratio. Next sections summarizes these approaches.

2.3.3.1 Soil profile

In addition to earthquake magnitude and epicenter distance, soil condition S at the site of interest is another factor most engineers use in earthquake studies. It is then leaded

to (M , R , S) selection approach. Therefore, the site of interested and station recording are important. Usually, a suitable metric for categorized soil condition shear-wave velocity at the uppermost 30m is always referred to. An example of site classification based on seismic codes provisions is illustrated in Table 2.2.

Table 2.2: Site classification (NEHRP, 2001).

Soil type NEHRP (2001)	Description	Average shear wave velocity to 30m (m/s)
A	Hard rock	>1500
B	Rock	$760 < V_s \leq 1500$
C	Very dense soil and soft rock	$360 < V_s \leq 760$
D	Stiff soil $15 \leq N \leq 50$ or $50 \text{kPa} \leq S_u \leq 100 \text{kPa}$	$180 \leq V_s \leq 360$
E	Soil or any profile with more than 3m of soft clay defined as soil with $PI > 20$, $w \geq 40\%$, and $S_u < 25 \text{kPa}$	≤ 180
F	Soils requiring site-specific evaluations	

In line with this approach, Rossetto and Elnashai (2005) selected ground motion accelerations based on this approach for fragility analyses. However, Bommer and Scott (2000) showed that the number of ground motions was decreased compared those of earthquake dominated technique. Therefore, a suggestion was made where site classification parameter was excepted in the search window, allowing satisfying a minimum ground motion number.

Alternatively, the effects of soil profile in strong earthquake records was considered by conducting an additional analysis (Papaspiliou et al., 2012). Site response prediction models can be classified into two groups. The first one is empirical amplification factor models that are usually used in attenuation relation models when site effects are accounted for (Boore & Atkinson, 2008). Subsequently, the surface ground motions are estimated by adjusting the BC-boundary reference site ($V_{s30} = 760 \text{m/s}$)

ground motion at bedrock. Therefore, more critical facilities or systems usually adopt this kind of method .

Among the performance of elaborate site response analyses, it is worth mentioning an incremental nonlinear model with a modified Kondnor and Zalasko (MKZ) hyperbolic constitutive law (Matasović & Vucetic, 1993) and an equivalent linear (EQL) model (Idriss & Sun, 1992; Schnabel et al., 1972). The loading and unloading cycles in complex nonlinear soil behavior were estimated. Four Masing rules were assumed. Strain-compatible approximation of soil response was adopted. The EQL model is by far the most popular in practice.

The advantages of EQL model include small computational time and effort and few physically meaningful input parameters (e.g., velocity of shear wave, unit weight, and etc.). No additional site parameters are used in MKZ model. However, the disadvantage of MKZ models is poor guidelines (Papaspiliou et al., 2012).

In addition, the overestimation of damping in MKZ model can increase error and reduce confidence of the ground motion predicted. Assimaki and Li (2012) evaluated the bias of these models relative to MKZ model. They showed that the overall prediction error between MKZ and EQL is no obvious, while the estimation error of empirical amplification factor is site-specific.

Some limitations in these alternative approaches have been reported. The ground motions with very high shear wave velocity are very limited. Therefore, modification are required in the latter analysis. Some assumptions have to be made with regard to the parameters of studied site (Katsanos et al., 2010)

2.3.3.2 Ground motion duration

In addition to soil profile, duration of ground motion has also been used in the selection process. The window of strong motion duration is known to influence the maximum response of a structure when the structure undergoes inelastic deformations (Kwon & Elnashai, 2006). Literature have proposed many different expression of duration in earthquake engineering. About 30 definitions of ground motion duration have been collected by Bommer and Martinez-Pereira (1999). 4 different types are usually referred to:

The first group, bracketed durations, are expressed as a duration between first and last execution for certain acceleration level, a_0 , given by Figure 2.15. The peaks at first and last that across a limit value are considered in this group. The parameters for ground motion are completely ignored. Long durations for low amplitude ground motion after primary shocks can be resulted. Furthermore, Unstable condition is observed when low levels of acceleration are used.

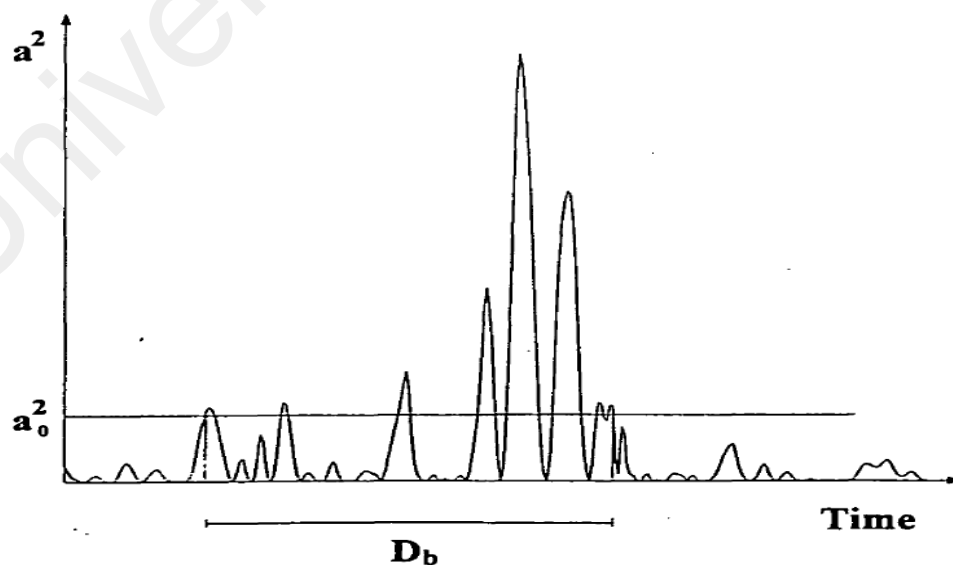


Figure 2.15: Duration for bracketed model.

The second group are uniform durations which are defined based on the sum of the time intervals. Figure 2.16 shows the idea of uniform duration. This approach is insensitive compared to duration for bracketed model. However, the disadvantage of this approach is that not window for continuous time was considered.

The last approach is significant durations that are conducted on the basic of energy accumulation. Acceleration time history can be shown by squaring ground acceleration, velocity or displacement. A quantity was related to energy density if the ground velocity is used. On the other hand, the quantity was related to Arias intensity if ground acceleration was used.

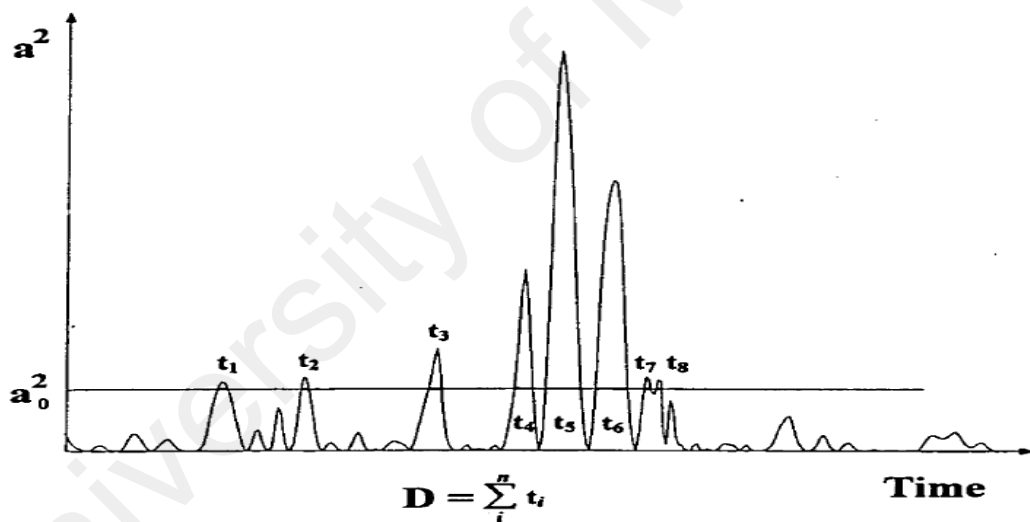


Figure 2.16: Duration for uniform model.

The AI is given as follows:

$$AI = \frac{\pi}{2g} \int_0^{t_r} a^2(t) dt \quad (2-33)$$

where $a(t)$ is ground motion acceleration, t_r is total accelerogram duration and g is 9.81 ms^{-2} . The significant duration is expressed as a total cumulative integration. Figure 2.17

shows an example of Arias intensity from literature. The limitation of this approach is that the characteristics of the whole accelerogram is considered. A stronger ground motion can be considered due to a continuous time window.

Along these lines, Trifunac and Brady (1975) used the squaring acceleration, velocity and displacement in earthquake definition. The range of interval considered for acceleration is start from 5% to 95%. The latter range is powerful in ground motion characterization. However, Kwon and Elnashai (2006) showed that the interval is impractical in seismic analysis. This is because the ground motion accelerations start at a very large value as given in Figure 2.18.

Moreover, the duration starting and ending at the similar margin cannot be accepted since the majority of ground motion energy is shifted to right side. Based on these observation, Kwon and Elnashai (2006) proposed the interval between 0.5% and 95% of the integrals.

The last category of record-based definitions are named structural response based definitions and these are based on ground motion characteristics.

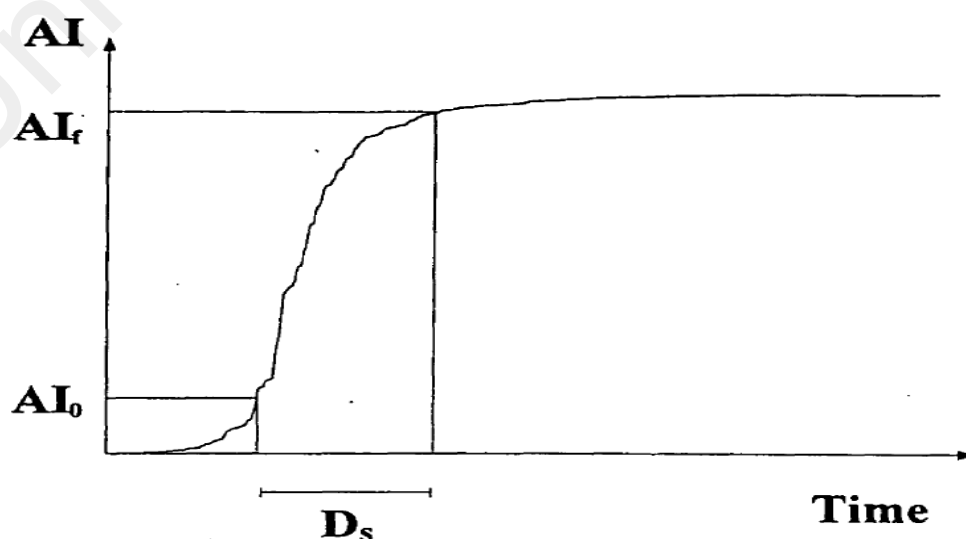


Figure 2.17: Significant accelerogram duration.

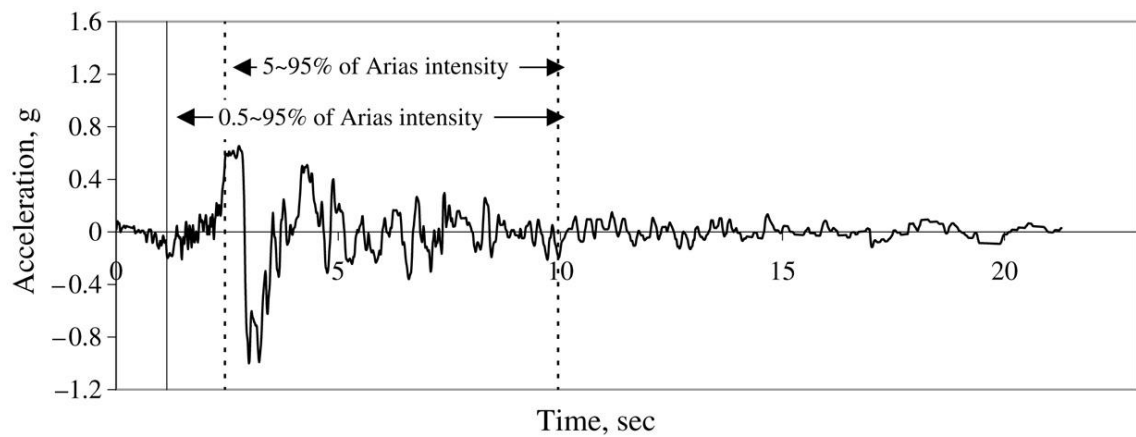


Figure 2.18: Significant duration of a ground motion.

2.3.3.3 Seismotectonic environment and other seismological parameters

The use of regional seismotectonic features has been published in literature. Five different features have been reported in this approach. These criteria have been reviewed by Katsanos et al. (2010). Some are briefly summarized in this section. For example,

The significantly stronger than ground motions caused by surface rupture events is considered as buried rupture based type of earthquake in particular in the period of interesting ranging around one second. The ground motions from shallow stable regions are different in subduction zones. Moreover, the earthquake found on shallow especially for high risk country are generally stronger than the ground motions from subduction zone. Ground motions from reverse faulting earthquakes have similar characteristics with earthquakes from reverse-oblique mechanism.

Based on these observations, a selection process based on seismotectonic environments had been used in many studies. Among these, Sorabella et al. (2006) used this proposal to select a set of strong ground motions for earthquake investigation. Moreover, some specific criteria including dominated earthquake scenario and site conditions were adopted by Dhakal et al. (2006) for a search window. A balance for the

overall selection process was recommended, since the number of ground motion may be reduced significantly if the seismotectonic environment features are adopted (Bommer & Acevedo, 2004). Furthermore, the more criteria selection are considered the less ground motions are selected (Katsanos et al., 2010).

2.3.3.4 Ratio of acceleration to velocity (a/v)

Certain case used this proposal in the search window e.g. (Güneyisi and Altay (2008); Kwon & Elnashai, 2006) to carry out seismic fragility analysis. Sawada et al. (1992) summarized that it is related to dominated earthquake scenarios and frequency of ground motion. In particular, earthquakes with low predominant frequencies, broader response spectra, longer durations and medium-to-high magnitudes, longer epicenter distances and site periods is represented as low a/v ratios. On the other hand, high predominant frequencies, narrow band spectra, short duration and small-medium magnitudes, short epicenter distances and site periods is represented as high a/v ratios. These ratios are divided into three different range (Sawada et al., 1992) as follows:

$$a/v < 0.8g/ms^{-1} \text{ is low} \quad (2-34)$$

$$0.8g/ms^{-1} \leq a/v \leq 1.2g/ms^{-1} \text{ is intermediate} \quad (2-35)$$

$$a/v > 1.2g/ms^{-1} \text{ is high} \quad (2-36)$$

However, the selection of ground motions cannot be solely depend on this particular guideline. It was suggested rather as an upper bound of the ground motions (Katsanos et al., 2010).

2.3.4 Selection based on seismic code - Eurocode 8

Eurocode 8, Part 1, states that seismic design and analysis can be conducted on the basis of ground motion time histories. It depends on records availability. Artificial accelerogram is an alternative approach in Eurocode 8. The use of accelerogram should satisfy four different rules as below:

- a) At least of three accelerograms are applied.
- b) The mean response spectrum at the beginning should be larger than the value of $a_g S$ for interested site. This is particularly applicable to single ground motion.
- c) No mean ground motion spectrum for a period range from $0.2T_1$ and $2T_1$ is less than 90% of the corresponding expected spectrum where T_1 is the fundamental period of the structure where ground motion will be applied.
- d) The mean results from either static pushover or time history analyses can be used if a minimum of 7 ground motion accelerogram are adopted; if not, the maximum results would be preferable.

All these rules are not used for single record selection. If tri-directional analysis is study, three accelerograms should be used. Moreover, No records are used more than once. a_{vg} , should be larger than 0.25g if vertical ground motion for type A site is investigated or slender members and base-isolation is investigated.

2.3.5 Selection based on seismic code - FEMA 450

FEMA 450 also summarizes some requirement for record selection as below:

- a) A minimum of three diferent records are used.

- b) For site response analysis at least 4 different ground motions recorded at rock should be used. The ground motion accelerograms shall be selected based on dominated earthquake scenarios.
- c) In interested period range the spectrum of each time history or the average response spectra should be closed to expected spectrum recorded at rock sites. This can be done by scaling the time history.

2.3.6 Generation of artificial earthquakes

An ideal solution for seismic analysis was applying a sufficient number of actual ground motions. Unfortunately, the number of available records in Malaysia is limited. It is because strong motion recording systems were installed in Malaysia only after the 2004 Andaman earthquake. Therefore, artificially generated ground motions is an alternative to carry out seismic analysis for Malaysian stocks. Eurocode-8 also permits to use artificial accelerograms for any analysis as long as the above approaches are complied.

Artificial ground motions have been widely investigated in the past. Different method have also been reported. Among these, Trifunac (1971) proposed a method for synthesizing realistic strong motion. Parallel layers was used to model the base. The synthetic accelerogram is expressed as follows:

$$a(t) = \sum_{n=1}^N \alpha_n \sum_{m=1}^M A_{nm} \frac{\sin \Delta\omega_n (t - t_{nm}^*)}{(t - t_{nm}^*)} \cos(\omega_n t + \phi_n) \quad (2-37)$$

where A_{nm} represents different amplitude with respect to modes of surface wave, α_{nm} is a factor of scaling where a final amplitude trough overall Fourier amplitude spectrum $FS(\omega_n)$ can be determined, ω_n the frequency of the band $\Delta\omega$ at center, t_{nm}^* a time of m^{th} mode reached at ω_n , was defined based on dispersion curves from site interested.

The scaling factor α_n is defined via specified Fourier spectra $FS(\omega_n)$:

$$\alpha_n = \frac{2\Delta\omega_n FS(\omega_n)}{\frac{\pi}{2} \int_{\omega_n - \Delta\omega}^{\omega_n + \Delta\omega} \left| \sum_{m=1}^M A_{nm} e^{-i((\omega - \omega_n)t_{nm}^* - \phi_n)} \right| d\omega} \quad (2-38)$$

Deodatis (1999) used a stochastic engineering approach to define synthetic accelerations. The step by step to define synthetic acceleration are summarized as below:

Firstly, a pre-defined velocity of wave propagation matching the stationary ground motion acceleration, without pre-defined response spectrum is formulated as follows:

$$g(t) = \sum_{n=1}^N \sqrt{2S_g(w_n)\Delta w} \cos(w_n t + \phi_n) \quad (2-39)$$

where $S_g(w_n)$ is value of power spectral density value determined at w_n frequency corresponding to power spectral density function ordinate with $n= 1, 2, \dots, N$ is frequency number.

$$\Delta w = w_n - w_{n-1} \quad (2-40)$$

ϕ_n is an angle for uniformly distributed phase ranging from 0 to 2π .

The ground motion was then multiplied with an appropriate function to model time varying intensity of a typical earthquake. A common equation for this function $A(t)$ was then given by following equation:

$$\begin{aligned}
&= (t/t_1)^2; (0 < t < t_1) \\
A(t) &= 1; (t_1 \leq t \leq t_2) \quad (2) \\
&= e^{-c(t-t_2)}; (t < t_2)
\end{aligned}
\tag{2-41}$$

where t_1 and t_2 are ground motion's rise and decay times. (t_2-t_1) is duration for ground motion and c is a factor of decay. Figure 2.19 illustrates an envelope function for a ground motion.

To compute corresponding response spectra the resulting nonstationary time history is adopted. After this step a checking with expected spectrum is conducted. A new function is then given if the checking is not satisfied:

$$S'_g(\omega) = S_g(\omega) \left[\frac{TRSA(\omega)}{SRSA(\omega)} \right]^2 \tag{2-42}$$

where $S'_g(\omega)$ is a new function for power spectral density, $TRSA(\omega)$ is expected spectrum, and $SRSA(\omega)$ is spectrum calculated from equation above. New ground motion time history is then constructed, and the ground motion is introduced by multiplying the new function with envelope function. This step is repeated until ground motions matching or satisfying the expected spectrum.

2.4 Measures of structural damage

Different damage measures have been published. Two groups have been introduced (Williams & Sexsmith, 1995). The first one is usually defined as damage index for individual structural members. The second group is defined as global damage indices used to define the state of all or a large part of a structure. Several local damage indices

are briefly summarized in Section 2.4.1 and the global damage indices are discussed in Section 2.4.2.

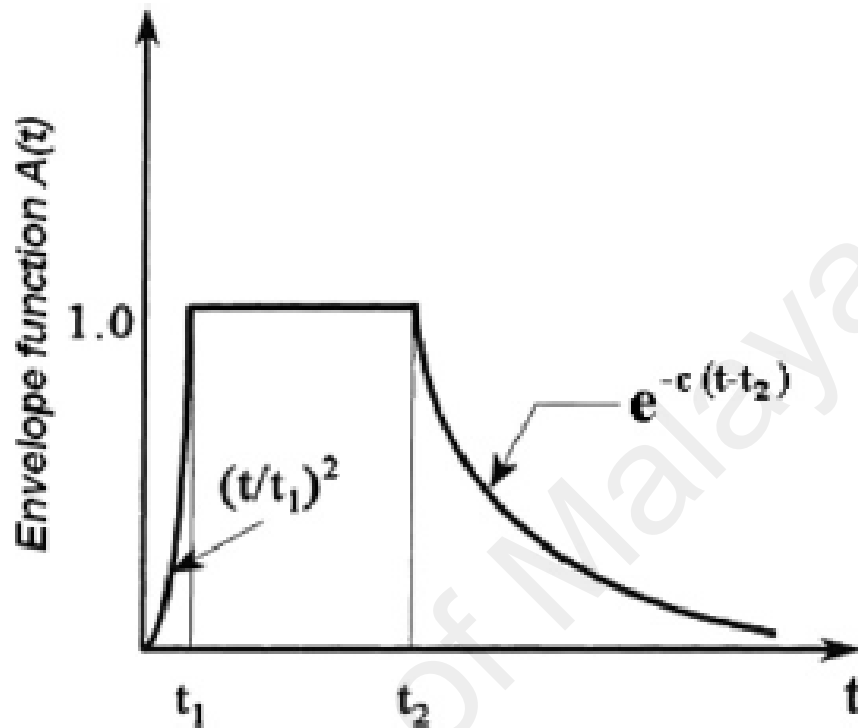


Figure 2.19: Ground motion with envelope function.

2.4.1 Local damage indices

The damage sustained by individual members is expressed by local indices. It commonly uses the ideas of energy dissipated or ductility. Ductility or inter-story drift were two earliest and simplest forms of damage index. They are also very popular due to easier understanding. The ductility ratio can be introduced either using rotation μ_θ , curvature μ_ϕ or displacement μ_δ using Eqs. (2-32), (2-33) and (2-34), respectively:

$$\mu_{\theta} = \frac{\theta_m}{\theta_y} \quad (2-43)$$

$$\mu_{\phi} = \frac{\phi_m}{\phi_y} \quad (2-44)$$

$$\mu_{\delta} = \frac{\delta_m}{\delta_y} \quad (2-45)$$

where θ_m , ϕ_m and δ_m are maximum rotation, maximum curvature and maximum displacement at the end of a member, respectively. θ_y , ϕ_y and δ_y are yield rotation, yield curvature and yield displacement, respectively.

Banon et al. (1981) presented an improvement on the ductility ratio that considers the fundamental structural parameters under cyclic loading as given in Figure 2.20. The flexural damage ratio is defined as:

$$FDR = \frac{k_0}{k_m} \quad (2-46)$$

where k_0 is initial secant stiffness, k_m is the equivalent secant stiffness of the maximum response experienced, and k_f is the ultimate secant stiffness.

As compared with test data, it was found that neither ductility ratios nor the FDR show a consistent indication of failure.

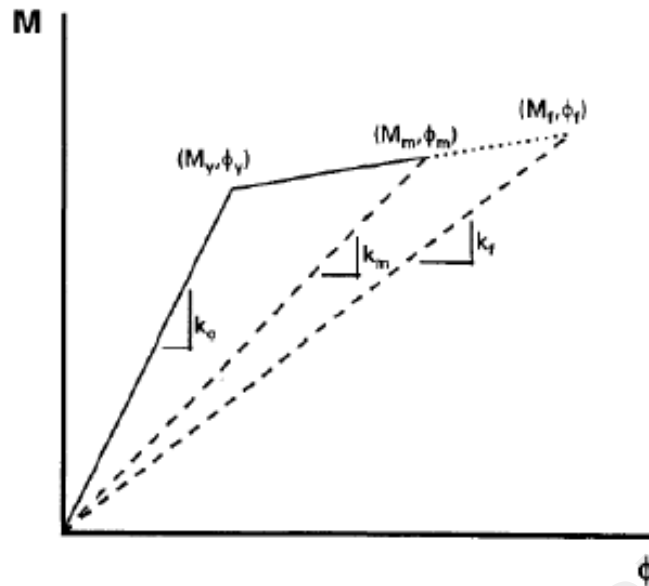


Figure 2.20: Definition of stiffness degradation (Banon et al., 1981).

Another popular damage indicator is the inter-story drift. It has been popularly reported that the interstory drift can be used to measure structural damage. FEMA (2003) adopts interstory drift as centerpiece of earthquakes induced damage estimation.

However, Park and Ang (1985a) combined damage from deformation and loading, unloading and reloading effects to propose a damage index. The index was calibrated based on survey data from various buildings. The damage index is then expressed as follows:

$$D = \frac{\theta_m}{\theta_u} + \frac{\beta}{M_y \theta_u} \int dE \quad (2-47)$$

where θ_m is + or - plastic hinge rotation at maximum value, θ_u is rotation of plastic hinge capacity under monotonic force, β is a parameter for model, M_y was calculated yield strength of longitudinal reinforcement, dE was incremental energy dissipated.

The damage from loading, unloading and reloading is expressed in the first term of Eq. 2-47. However, the damage caused by cumulative hysteretic energy dissipation is presented in the second term. Cosenza et al. (1990) found that the parameter of β well correlated is approximately 0.15. Table 2.3 summarizes the damage threshold from no damage to collapse. When there is no damage, D is zero and there was collapse the index, D is 1.0.

Table 2.3: Damage threshold (Park et al., 1987).

$D < 0.1$	No damage or localized minor cracking
$0.1 \leq D < 0.25$	Minor damage-light cracking throughout
$0.25 \leq D < 0.4$	Moderate damage-severe cracking, localized spalling
$0.4 \leq D < 1.0$	Severe damage-crushing of concrete, reinforcement exposed
$D \geq 1.0$	Totally collapsed, the building is not safe to reoccupy.

Chung et al. (1987) presented an index where a modified version of Miner's Hypothesis is combined with a modifier as shown in Figure 2.21. The response of structural systems is then given as follows:

$$D_e = i \sum \left(\alpha_i^+ \frac{n_i^+}{N_i^+} + \alpha_i^- \frac{n_i^-}{N_i^-} \right) \quad (2-48)$$

where i is response indicator, $N_i = (M_i - M_{fi})/\Delta M_i =$ number of cycles to cause failure at a level of curvature i , $n_i =$ cycle number actually applied at level of curvature i , α_i is modifier for a damage, $M_i =$ initial strength at curvature level i , $M_{fi} =$ final strength at curvature level i , $\Delta M_i =$ strength drop at curvature level i , in a loading and unloading cycle, and $+$, $- =$ loading and unloading, respectively.

The effect of loading history is considered through damage modifier, α_i , which is defined in Eq. 2-48 for positive moment loading.

$$\alpha_i^+ = \frac{\sum k_{ij}^+}{n_i^+ \bar{k}_i^+} \cdot \frac{\phi_i^+ + \phi_{i-1}^+}{2\phi_i^+} \quad (2-49)$$

where:

$$k_{ij}^+ = \frac{M_{ij}^+}{\phi_i^+} = j^{\text{th}} \text{ cycle stiffness up to load level } i,$$

$$\bar{k}_i^+ = \frac{1}{N_i^+} \sum_{j=1}^{N_i^+} k_{ij}^+ = N_i^+ \text{ cycles stiffness up to load level } i, \text{ and}$$

$$M_{ij}^+ = M_{i1}^+ - (j-1)\Delta M_i^+ = j \text{ cycles moment up to load level } i.$$

The modifier was then expressed in a same manner especially for reverse loading. However, the damage due by maximum deformation was not included in the Chung model.

2.4.2 Global damage indices

The building damage or performance level was usually expressed with respect to global damage index. A weighted average of damage for all structural members can be determined or by considering some overall structural characteristic like the modal periods. Several global damage index are discussed below.

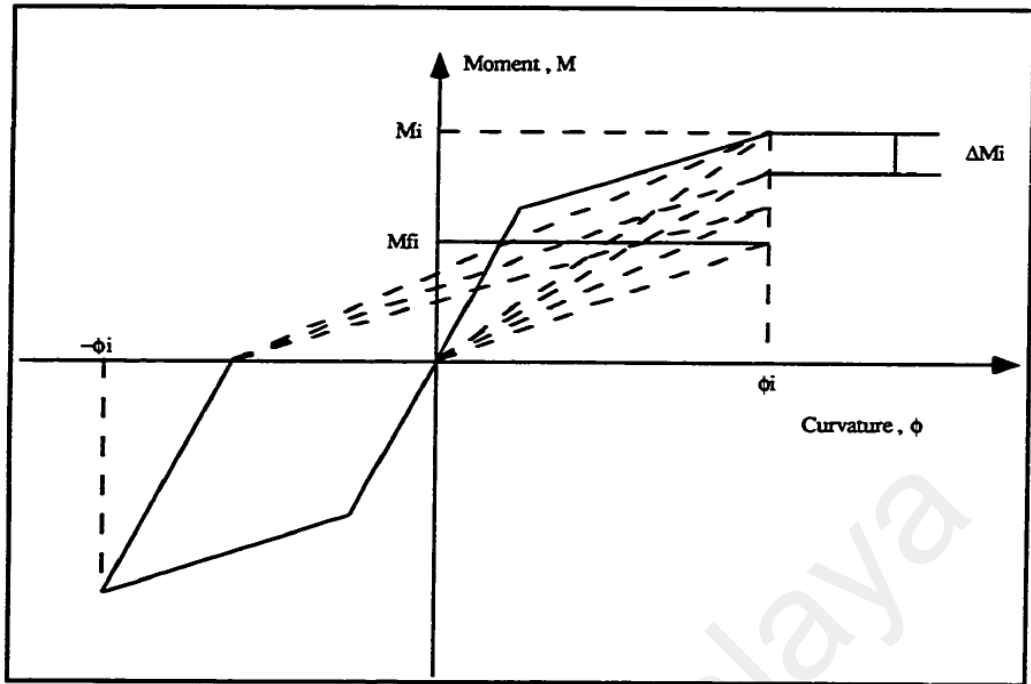


Figure 2.21: Damage index defined by Chung et al. (1987).

Park and Ang (1985b)'s index was presented as an average of individual structural damage. A function for individual structural member was proportional to dissipated energy found in member. The model is then presented as follows:

$$D_T = \sum_{i=1}^N \lambda_i D_i \quad (2-50)$$

where

$$\lambda_i = \frac{E_i}{\sum_{i=1}^N E_i} \quad (2-51)$$

and N = number of element, and E_i = energy dissipated in element i . A focus of individual member damage does not included in the global damage model.

Chung et al. (1987)'s new damage model is presented as an average of story damage using a triangular weighting function with the maximum at the base. The global damage index is given as follows:

$$D_g = \sum_{k=1}^N D_{sk} I_k \quad (2-52)$$

where:

$$D_{sk} = \frac{\sum_{i=1}^n D_i^k E_i^k}{\sum_{i=1}^n E_i^k} \quad (2-53)$$

$I_k = \frac{N+1-k}{N}$ = weighting factor for story k, N = number of stories, D_i^k = local damage at location i on story k, E_i^k is dissipated energy at location i for floor k, and n is floor locations where damage is calculated.

In addition to the above damage models, the softening models relate to the initially few natural period. Erberik (2008) proposed a softening damage index as follows:

$$SI = 1 - \frac{T_0}{T_j} \quad (2-54)$$

where T_0 is a capacity spectrum period and T_j is period effectively found at spectral displacement. When $T_0=T_j$ the index is 0. The index is taken values between 0 and 1 for period elongation due to nonlinear response.

DiPasquale and Cakmak (1990) defined another softening damage index as:

$$SI = 1 - \frac{T_0^2}{T_f^2} \quad (2-55)$$

where T_f is final period of nature of a system.

These softening indices provide limited information about the distribution of damage sustained by different members within the structure. Mork (1992) improved this aspect by extending Eq. 2-55 to include the second mode as shown in the following two equations:

$$SI_1 = 1 - \sqrt{\frac{k_{1,\max}}{k_{1,0}}} \quad (2-56)$$

and

$$SI_2 = 1 - \sqrt{\frac{k_{2,\max}}{k_{2,0}}} \quad (2-57)$$

where SI_1 is the maximum softening index corresponding to the first mode, SI_2 is the maximum softening index corresponding to the second mode, $k_{1,0}$ is stiffness for an equivalent linear model at first mode, $k_{2,0}$ is stiffness for an equivalent linear model at second mode, $k_{1,\max}$ is peak stiffness of an equivalent system for the first mode, and $k_{2,\max}$ is the maximum stiffness of an equivalent linear system for the second mode. The damage measures SI_1 and SI_2 represent the damage of the structure for upper and lower value, respectively.

Roufaiel and Meyer (1987) proposed a softening index in terms of deflections at the roof floor of a system. The change in fundamental frequency of a structure is given as follows:

$$D = \frac{\delta_r - \delta_y}{\delta_f - \delta_y} = \frac{14.28\delta_y(\sqrt{\omega_e/\omega} - 1)}{\delta_f - \delta_y} \quad (2-58)$$

where δ_r is the maximum roof deflection under earthquake excitation, δ_y is the roof displacement at which the first structural element of a building reaches yield strength. It assumed first mode displacement only. δ_f is deflection at roof, ω_e is the fundamental frequency of the undamaged or elastic system, and ω was fundamental frequency of a system after being damaged. A number of different softening indices are then presented in the following Eq. 2-59, which can be expressed as 3 natural periods as given in Figure 2.22.

$$D_{ms} = 1 - \frac{T_{und}}{T_m}; \quad D_{ps} = 1 - \frac{T_{dam}^2}{T_m^2}; \quad D_{fs} = 1 - \frac{T_{und}^2}{T_{dam}^2}; \quad (2-59)$$

where T_{und} and T_{dam} are natural period of a system before and after an event and T_m is peak period observed during an event.

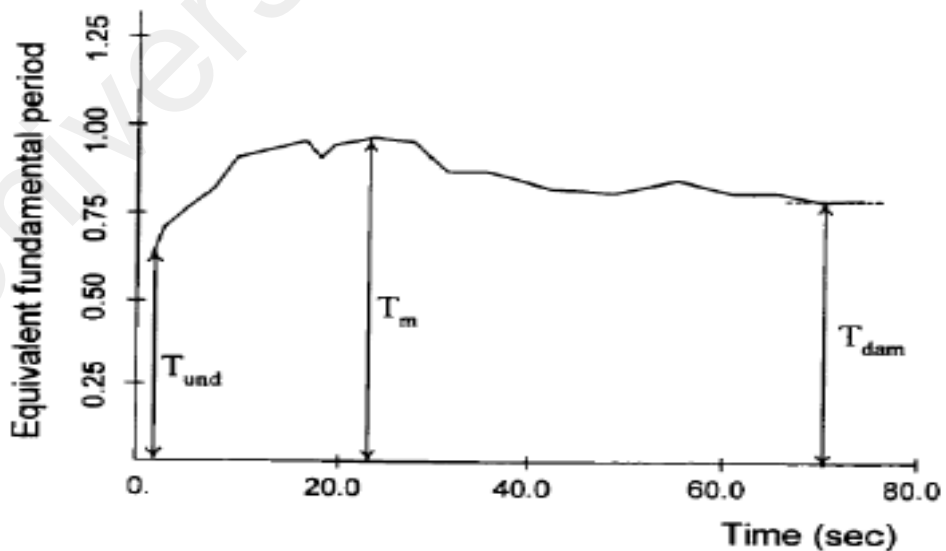


Figure 2.22: Milikan Library fundamental periods (Williams & Sexsmith, 1995).

To quantify buildings with or without reinforced concrete walls especially used in seismic fragility analysis Hassan and Sozen (1997) presented a priority index. This index was proposed as effective column and wall areas divide total floor area of building as follows:

$$PI = WI + CI \quad (2-60)$$

where

$$WI = \frac{A_{wt}}{A_{ft}} \times 100 \quad (2-61)$$

$$CI = \frac{A_{ce}}{A_{ft}} \times 100 \quad (2-62)$$

$A_{wt} = A_{cw} + \frac{A_{mw}}{10}$ is area of walls effectively in x-direction, A_{cw} is total area of walls in one x-direction at base, A_{mw} is area of brick walls in one x-direction at base, A_{ft} is total area of story above base for a system, $A_{ce} = \frac{A_{col}}{2}$ is area of columns effectively found at base, A_{col} is total area of columns excluding ground floor. The lower of the two priority damage indices for a building is then selected.

Kwon and Elnashai (2006) proposed a global damage model using engineering parameter e.g. inter-story drift ratio. The serviceability damage state is defined at first yielding of steel, while the damage control damage state is defined at maximum moment strength and the collapse prevention damage state is defined at confined concrete strain equal to 0.01.

Borzi et al. (2008) defined a damage index using column chord rotation. Four different limit states are presented as below:

Damage limit state for non-structural element: inter-storey rotation capacity for drift sensitive partition walls is taken values between 0.1% and 0.3%.

Light damage structural limit state: The rotation capacity was controlled by the chord rotation corresponding to yielding θ_y as follows:

$$\theta_y = \phi_y \frac{L_v}{3} + 0.0013 \left(1 + 1.5 \frac{h}{L_v} \right) + 0.13 \phi_y \frac{d_b f_y}{\sqrt{f_c}} \quad (2-63)$$

where ϕ_y is the yield curvature of the section, h is the section height, d_b is the longitudinal bar diameter, f_y and f_c are the resistance of steel and concrete in MPa, respectively, and L_v is the shear span (equal to the ratio between bending moment and shear). A double bending distribution was assumed for columns, and therefore L_v is half of the inter-storey height. The yield curvature was then given as:

$$\phi_y = 2.14 \frac{\varepsilon_y}{h} \quad (2-64)$$

where ε_y is the yield strain of longitudinal rebars.

Significant damage limit state: The chord rotation capacity is controlled by 3/4 of the ultimate rotation capacity θ_u as below:

$$\theta_u = \frac{1}{\gamma_{el}} \left(\theta_y + (\phi_u - \phi_y) L_{pl} \left(1 - \frac{0.5 L_{pl}}{L_v} \right) \right) \quad (2-65)$$

where the main structural members γ_{el} is taken as 1.5 and all others γ_{el} is taken as 1. ϕ_u is the ultimate curvature and L_{pl} is the plastic hinge length. The plastic hinge length can be estimated as the following equation:

$$L_{pl} = 0.1L_v + 0.17h + 0.24 \frac{d_b f_y}{\sqrt{f_c}} \quad (2-66)$$

whilst the ultimate curvature is assumed to be

$$\phi_u = \frac{\varepsilon_{cu} + \varepsilon_{su}}{h} \quad (2-67)$$

where ε_{cu} and ε_{su} are the ultimate concrete and steel strains, respectively. The ranges for the ultimate strain capacity are recommended by Calvi (1999) as follows:

$\varepsilon_{cu} = 0.5\%-1\%$; $\varepsilon_{su} = 1.5\%-3\%$ for poorly confined RC elements

$\varepsilon_{cu} = 1\%-2\%$; $\varepsilon_{su} = 4\%-6\%$ for well confined RC elements

Collapse limit condition: The chord rotation capacity is controlled by the ultimate rotation capacity ϕ_u .

2.5 Seismic fragility and reliability method

This section presents several methods that have been used to increase the reliability of seismic fragility estimate. The methods discussed herein are the SAC-FEMA, Response Surface, Monte Carlo Simulation, Bayesian and Ryu's method. Some advantages and disadvantages of these methods are also discussed.

2.5.1 SAC-FEMA Method

The SAC-FEMA method was published by Cornell et al. (2002) for seismic design and analysis of steel moment-resisting frame buildings. In this approach, the ground motion intensity is characterized by the level of spectral acceleration S_a . To define drift hazard $H_D(d)$ seismic hazard S_a is combined with drift demand D as given in the following equation:

In discrete form,

$$H_D(d) = P[D \geq d] = \sum_{all\ x_i} P[D \geq d | S_a = x_i] P[S_a = x_i] \quad (2-68)$$

In continuous, integral form Eq. 2-68 is given as

$$H_D(d) = \int P[D \geq d | S_a = x] |dH(x)| \quad (2-69)$$

where $|dH(x)|$ meant the absolute value of the derivative of the site's spectral acceleration hazard curve times dx , i.e., loosely the likelihood that $S_a = x$. The site hazard curve $H(S_a)$ is expressed as:

$$H(S_a) = P[S_a \geq s_a] = k_o s_a^{-k} \quad (2-70)$$

Drift demand \hat{D} is related to seismic hazard S_a in the form of the following equation:

$$\hat{D} = a(S_a)^b \quad (2-71)$$

where drift demands distribute log-normally about the median with the standard deviation of the natural logarithm, $\beta_{D|S_a}$. The constants, a and b determine from a regression

analysis of $\ln D$ on $\ln S_a$. For a given intensity level, the probability of drift demand D exceeding any specified value d is given as follows:

$$P[D \geq d | S_a = x] = 1 - \Phi(\ln[d/ax^b]/\beta_{D|S_a}) \quad (2-72)$$

In which Φ = widely tabulated “standardized” Gaussian distribution function. Based on this outcome and Eq. 2-69, Eq. 2-70 for the drift hazard become, upon integration

$$H_D(d) = P[D \geq d] = H(s_a^d) \exp\left[\frac{1}{2} \frac{k^2}{b^2} \beta_{D|S_a}^2\right] \quad (2-73)$$

In which s_a^d defines as the spectral acceleration “corresponding to” the drift level d , that is the inverse of Eq. 2-71.

$$s_a^d = (d/a)^{1/b} \quad (2-74)$$

Next, to produce the annual probability of the performance level not being met the drift hazard is combined with drift capacity, C , P_{PL} is given in the following equation and in discrete form,

$$P_{PL} = P[C \leq D] = \sum_{all\ d_i} P[C \leq D | D = d_i] P[D = d_i] \quad (2-75)$$

The continuous form is given as

$$P_{PL} = \int P[C \leq d] dH_D(d) \quad (2-76)$$

The drift capacity C , is assumed to have a median value of \hat{C} and to be log-normally distributed with dispersion β_C . Thus, the probability of capacity C to be smaller than a specified value d is presented as follow:

$$P[C \leq d] = \Phi(\ln[d/\hat{C}]/\beta_C) \quad (2-77)$$

Substituting and carrying out the integration the researchers can observe this main result,

$$P_{PL} = H(s_a^{\hat{C}}) \exp\left[\frac{1}{2} \frac{k^2}{b^2} (\beta_{D|s_a}^2 + \beta_C^2)\right] \quad (2-78)$$

where $s_a^{\hat{C}}$ is the spectral acceleration “corresponding to” the median drift capacity as given by,

$$s_a^{\hat{C}} = (\hat{C}/a)^{1/b} \quad (2-79)$$

2.5.2 Response Surface Method

To represent the capacity in the form of an analytical limit-state function as input for First-Order Reliability Method (FORM) analysis for calculating the fragility function of the system Schotanus et al. (2004) used response surface. Limit state function formulates based on capacity minus demand is given as,

$$g(x) = C(x) - D(x) \quad (2-80)$$

where $C(x)$ and $D(x)$ are the capacity and demand terms. The capacity is assumed to be constant in time-dependent proble. The maximum of the seismic demand over time interval was used in the limit state function. If both the capacity and demand varies with time, the limit state function is formulated as the minimum of the difference $C(x, t) - D(x, t)$.

Alternatively, the capacity expresses in terms of spectral acceleration as:

$$g(x) = S_{af}(x) - S_a \quad (2-81)$$

The spectral acceleration S_a was considered as a demand parameter in the above equation. When $S_{af}(x)$ was established by some form of simulation, the entire fragility can generate by solving repeatedly the analytical problem above by changing the value of S_a .

To estimate failure probabilities, the capacity and seismic demand variable x_1 and x_2 are presented. For instance, random variables such as soil mechanical properties, material strengths and structural geometry were considered as uncertainty on capacity, denoted as x_1 . Moreover, the seismic intensity levels consider as the random variables for seismic demand, denoted as x_2 . Therefore, a response surface is then modeled as a function of x_1 and x_2 :

$$y(x_1, x_2) = z(x_1)\beta + \delta + \varepsilon \quad (2-82)$$

where x_1 and x_2 are basic random variables for $C(x)$ and $D(x)$. The fixed-effect part of the model is represented by $z(x_1)\beta$, ε is a random deviation term with zero-mean, while δ is the random-effect, i.e. the effect of the random factor x_2 , that considers the changes in the response due to seismic loadings.

According to Schotanus et al. (2004), one of the advantages of this procedure is that the step is simpler. It can use in conjunction with state-of-the-art mechanical models, and that the variability in the response due to ground motion uncertainty was realistically represented. In addition, the method regards as low computational time consuming. Moreover, a second order polynomial is presented with reasonable accuracy.

2.5.3 Monte Carlo Simulation

The Monte Carlo Simulation (MCS) was a popular approach especially use in reliability analysis of seismic risk assessments. Koji (2002) used Monte Carlo simulation to generate fragility curve of gravity type quay walls in terms of normalized seaward displacement. Based on the MCS Method, all basic random variables are randomly constructed based on joint density function. The probability of failure is given as follows:

$$P_f = \frac{N_f}{N} \quad (2-83)$$

where N_f is the number of simulation cycles with a condition of $g(.) < 0$. N is the total number of simulation cycles. In most of the studies, Latin Hypercube Sampling (LHS) is applied with Monte Carlo Simulation.

The advantages of Monte Carlo Simulation are straightforward and simple. However, it needs a large numbers of sample to estimate the probability of failure. It also needs a large computational time. But these disadvantages can be improved by incorporating artificial neural networks (ANN) into Monte Carlo Simulation based fragility analysis framework. This approach, however, has been presented by Lagaros et al. (2009) to estimate geo-structure failures. To develop fragility curves and replaced the repeated numerical analyses the ANN was performed. The correlation coefficient of ANN is given as follows,

$$r = \frac{\sum_{i=1}^m (x_i - \bar{x})(y_i - \bar{y})}{\sqrt{\sum_{i=1}^m (x_i - \bar{x})^2 \sum_{i=1}^m (y_i - \bar{y})^2}} \quad (2-84)$$

where x_i and \bar{x} are the numerical and the averaged response values, while y_i and \bar{y} are calculated from ANN. m denotes the number of ANN training data sets. The advantages

of ANN prediction are that the sample size of MCS can be increased and more accurate prediction can be easily obtain as compare with conventional procedures.

2.5.4 Bayesian method

Bayesian approaches are used to obtain a balanced estimation where expert or engineer perspective can be systematically incorporated with experimental outcomes. Singhal and Kiremidjian (1998) applied the Bayesian method to improve fragility curves. If the experimental outcome x_i is a set of observed values x_1, x_2, \dots, x_n , representing a random sample from a population X with underlying density function $f_X(x_i|\theta)$, the parameter of the distribution θ , revises in light of the experimental outcomes based on following equation:

$$f''(\theta) = \frac{[\prod_{i=1}^n f_X(x_i|\theta) dx \theta] f'(\theta)}{\int_{-\infty}^{\infty} [\prod_{i=1}^n f_X(x_i|\theta) dx] f'(\theta) d\theta} = kL(\theta)f'(\theta) \quad (2-85)$$

where $f'(\theta)$ is prior density function of the parameter θ , while $f''(\theta)$ is posterior density function of θ , and $f_X(x_i|\theta)$ is probability distribution function of the basic random variable x . The normalizing constant was expressed as

$$k = [\int_{-\infty}^{\infty} (\prod_{i=1}^n f_X(x_i|\theta)) f'(\theta) d\theta]^{-1} \quad (2-86)$$

whereas the likelihood function $L(\theta)$ is the product of the density function of X evaluated at x_1, x_2, \dots, x_n and is expressed as

$$L(\theta) = \prod_{i=1}^n f_X(x_i|\theta) \quad (2-87)$$

In the case of a Gaussian population with known standard deviation σ , the likelihood function for the parameter μ , according to Eq. 2-87 is expressed as:

$$L(\mu) = \prod_{i=1}^n \frac{1}{\sqrt{2\pi}\sigma} \exp\left[-\frac{1}{2}\left(\frac{x_i-\mu}{\sigma}\right)^2\right] = \prod_{i=1}^n N_{\mu}(x_i, \sigma) \quad (2-88)$$

where $N_{\mu}(x_i, \sigma)$ is the density function of μ with mean value x_i and standard deviation σ . A normal density function with mean μ^* and standard deviation σ^* is also the product of m normal density functions, with respective means μ_i and standard deviations σ_i given by:

$$\mu^* = \frac{\sum_{i=1}^m (\mu_i/\sigma_i^2)}{\sum_{i=1}^m 1/\sigma_i^2} \quad \text{and} \quad (\sigma^*)^2 = \frac{1}{\sum_{i=1}^m 1/\sigma_i^2} \quad (2-89)$$

Therefore the likelihood function $L(\mu)$ becomes

$$\begin{aligned} L(\mu) &= N_{\mu}\left(\frac{\sum_{i=1}^n (x_i/\sigma^2)}{\sum_{i=1}^n (1/\sigma^2)}, \frac{1}{\sqrt{\sum_{i=1}^n (1/\sigma^2)}}\right) \\ &= N_{\mu}\left(\frac{(1/\sigma^2)\sum_{i=1}^n x_i}{n/\sigma^2}, \frac{1}{\sqrt{n/\sigma^2}}\right) = N_{\mu}\left(\bar{x}, \frac{\sigma}{\sqrt{n}}\right) \end{aligned} \quad (2-90)$$

where \bar{x} is the sample mean.

Suppose that $f'(\mu)$ is $N(\mu', \sigma')$ thus, with likelihood function of Eq. 2-85, the posterior distribution of μ becomes

$$f''(\mu) = kL(\mu)f'(\mu) = kN_{\mu}\left(\bar{x}, \frac{\sigma}{\sqrt{n}}\right)N_{\mu}(\mu', \sigma') \quad (2-91)$$

where posterior mean and standard deviation are expressed by the following two equations, respectively,

$$\mu'' = \frac{\bar{x}(\sigma')^2 + \mu'(\sigma^2/n)}{(\sigma')^2 + (\sigma^2/n)} \quad (2-92)$$

$$\sigma'' = \sqrt{\frac{(\sigma')^2(\sigma^2/n)}{(\sigma')^2 + (\sigma^2/n)}} \quad (2-93)$$

The advantages of the Bayesian approach are summarized as that the formal framework for incorporating engineering judgment with observational data is provided. The uncertainties associated with randomness and those arising from errors of estimation and prediction systematically combined, as well as a formal procedure for systematic updating of information is provided.

2.5.5 Ryu's Method

To estimate the magnitude of a historical earthquake by using fragility functions Ryu et al. (2009) published a probabilistic method. It may be the case that the proposed method focuses on the magnitude estimation of historical earthquake, but the procedure for structural fragility function generation is well presented. This section, however, only focuses on the procedure for fragility function generation defined in the probabilistic method.

The probability of the occurrence of the damage event, E (i.e., n collapses out of n_t total buildings) given a ground motion intensity measure IM , magnitude M , and distance R is computed using the multinomial distribution as:

$$\begin{aligned}
 P(E|IM = im, M = m, R = r) &= P(N = n|im, m, r) && 0 \leq n \leq n_t \\
 &= \frac{n_t!}{n!(n_t - n)!} \times P(DM = collapse|im, m, r)^n \times \\
 &P(DM = noncollapse|im, m, r)^{n_t - n} && (2-94)
 \end{aligned}$$

where N is a random variable representing the number of collapsed structures, n was a specific numeric value of N , and n_t is total number of structures. Specified bounds for the number of collapsed structures are proposed instead of assigning a single value for N .

$$\begin{aligned}
 P(E|IM = im, M = m, R = r) &&& 0 \leq l \leq n \leq u \leq n_t \\
 &= P(l \leq N \leq u|im, m, r) \\
 &= P[\cup_{n=l}^u (N = n)|im, m, r] \\
 &= \sum_{n=l}^u \frac{n_t!}{n!(n_t - n)!} \times P(DM = collapse|im, m, r)^n \\
 &\times P(DM = noncollapse|im, m, r)^{n_t - n} && (2-95)
 \end{aligned}$$

where l and u are lower and upper limits on N , respectively, and \cup is the union symbol representing logical “or”.

Likewise, instead of considering a single damage state, the multiple damage state is defined as:

$$P(E|IM = im, M = m, R = r) \qquad 0 \leq n_k \leq n_t$$

$$\begin{aligned}
&= P\left[\bigcap_{k=0}^{n_d} (N_k = n_k) \mid im, m, r\right] \\
&= \frac{n_t!}{\prod_{k=0}^{n_d} n_k!} \times \prod_{k=0}^{n_d} P(DM = dm_k \mid im, m, r)^{n_k} \tag{2-96}
\end{aligned}$$

where k is the index for the damage state, n_d is the total number of damage states excluding no damage state ($k = 0$), \cap is the intersection symbol representing logical “and”, N_k is the number of structures in the k th damage state, and n_k is a specific numeric value of N_k . When bounds are assigned for the number of structures in multiple damage states, the damage event is expressed as follows,

$$\begin{aligned}
&P(E \mid IM = im, M = m, R = r) \qquad 0 \leq {}^j n_k \leq n_t \\
&= P\left\{\bigcup_{j=1}^{n_e} \left[\bigcap_{k=0}^{n_d} ({}^j N_k = {}^j n_k)\right] \mid m, m, r\right\} \\
&= \sum_{j=1}^{n_e} \frac{n_t!}{\prod_{k=0}^{n_d} {}^j n_k!} \times \prod_{k=0}^{n_d} P(DM = dm_k \mid im, m, r)^{{}^j n_k} \tag{2-97}
\end{aligned}$$

where j is index for the subevents, n_e is the total number of subevents, ${}^j N_k$ is the number of structures in the k th damage state of the j th subevent, and ${}^j n_k$ is a specific numeric value of ${}^j N_k$.

The number of multiple types of structures in multiple damage states are then expressed as:

$$\begin{aligned}
&P(E \mid IM = im, M = m, R = r) \qquad 0 \leq {}^j n_k^i \leq n_t^i \\
&= P\left(\bigcap_{i=1}^{n_s} \left\{\bigcup_{j=1}^{n_e^i} \left[\bigcap_{k=0}^{n_d^i} ({}^j N_k^i = {}^j n_k^i)\right]\right\} \mid im, m, r\right)
\end{aligned}$$

$$= \prod_{i=1}^{n_s} \left[\sum_{j=1}^{n_e^i} \frac{n_t^i!}{\prod_{k=0}^{n_d^i} j n_k^i!} \times \prod_{k=0}^{n_d^i} P(DM = dm_k^i | im, m, r)^{j n_k^i} \right] \quad (2-98)$$

where i is the index for the structure type, n_s is the total number of structure types, n_e^i and n_d^i are the total number of subevents and damage states of type i structure, respectively, ${}^j N_k^i$ is the number of type i structures in the k th damage state of the j th subevent, ${}^j n_k^i$ is a specific numeric value of ${}^j N_k^i$ and n_t^i is the total number of type i structures. While, dm_k^i is the k th damage state of type i structure.

The probability of occurrence of the damage event given the magnitude is expressed as:

$$P(E|m) = \iint P(E|im, m, r) \times f_{im|M,R}(im|m, r) \times f_R(r) \dim dr. \quad (2-99)$$

where $f_{im|M,R}(im|m, r)$ is a probability density function (PDF) of a ground motion intensity given M and R , and $f_R(r)$ is a prior probability distribution of distance.

The posterior distribution of magnitude given the damage event is then computed by applying Baye's theorem as follow,

$$\begin{aligned} f_{M|E}(m|E) &= \frac{P(E|M = m) \times f_M(m)}{P(E)} \\ &= \frac{P(E|M = m) \times f_M(m)}{\int P(E|M = m) \times f_m(m) dm} \end{aligned} \quad (2-100)$$

Thus, the fragility functions are defined with two parameters as:

$$P(DS \geq ds | PGA = x) = \Phi \left(\frac{\ln x - \ln \overline{PGA}_{ds}}{\beta_{SPGA}} \right) \quad (2-101)$$

where \overline{PGA}_{ds} denotes the mean of value of magnitude given the damage event and β_{SPGA} is standard deviation of magnitude given the damage event.

The advantages of this approach are summarized as that this approach is a probabilistic procedure that can explicitly incorporate various sources of uncertainty. However, this approach is a modular procedure and thus easily extended to take into account other issues. In spite of that by virtue of Bayes' theorem, this approach incorporates the subjective judgments and utilize previous research results with prior distributions of magnitude and distance.

2.6 Summary

The first part of this chapter reviewed the various structural modelling techniques used to characterize structural model. In this study, the beam and column structural elements are chosen to be characterized by fiber beam-column elements. However, the unreinforced masonry infill walls are characterized by a single equivalent diagonal strut as it enables modelling a cross section as an arbitrary collection of nonlinear fiber elements, and satisfies the in-plane and out-of-plane interaction relationship.

The second part of this chapter described the various ground motions selection approaches used in the development of fragility curves in Chapter 6. The ground motions are selected from international ground motion database based on the contributing sources such as magnitude and distance. Since the use of recorded ground motions is the most realistic, the number of ground motions recorded in Malaysia are limited. Thus, the selection of ground motion in terms of magnitude and distance is the most appropriate

approach for the current study. Peak ground acceleration is chosen to characterize the ground motion as it is a simple parameter and can be easily used in regional damage evaluation.

The third part of this chapter reviewed the different damage measure for reinforced concrete frames with and without unreinforced masonry infill walls. This study adopts interstory drift ratio to represent structural damage while damage states are defined based on those described in HAZUS.

University of Malaya

CHAPTER 3: INPUT ACCELERATION GROUND MOTIONS

3.1 Introduction

In earthquake engineering studies the input acceleration ground motions are known as an important step. As discussed in chapter 2, a lots of selection method have been published. An available international database named COSMOS was used to select a number of ground motion with respect to dominated earthquake scenarios. The ground motions at the surface for different soil conditions were generated from one-dimensionaal equivalent linear analyses. Next, the details of these aspects will be presented.

3.2 Seismic hazard map

A study of PSHA conducted by Adnan (2013) was adopted in this study. The earthquake magnitude and hypocenter distance are assumed where these factors are considered independently. The studied will not be presented here (please refer to Adnan (2013) for detailed discussion). The general steps necessary to apply the model are listed below.

1. Modeling of seismic sources using built in tools.
2. For each source the frequency of occurences will be determined.
3. An empirical relationship was then adopted to derive expected spectrum.

The area sources were used to simulate the seismicity of the region. The attenuation relationship to be used including models proposed by Youngs (1997) and Atkinson-Boore (2003) for predicting PGA from Sumatra Subduction Zone, and attenuation proposed by several researchers such as Boore-Atkinson NGA (2008) and

Campbell-Bozorgnia NGA (2008) for Sumatra Fault Zone. These attenuations were selected because the functions can cover distant earthquakes more than 300km.

The acceleration contours were computed using Ez-Frisk version 7.6.2 (Risk Engineering, 2013). The seismic source was investigated by plotting the spatial distribution of earthquakes using the regional seismicity data recorded since 1900 and then combining with the seismotectonic setting to develop seismic sources for Malaysian Peninsula. To simplify the analysis, both of seismic source zones were segmented into seven sub zones as shown in Figure 3.1.

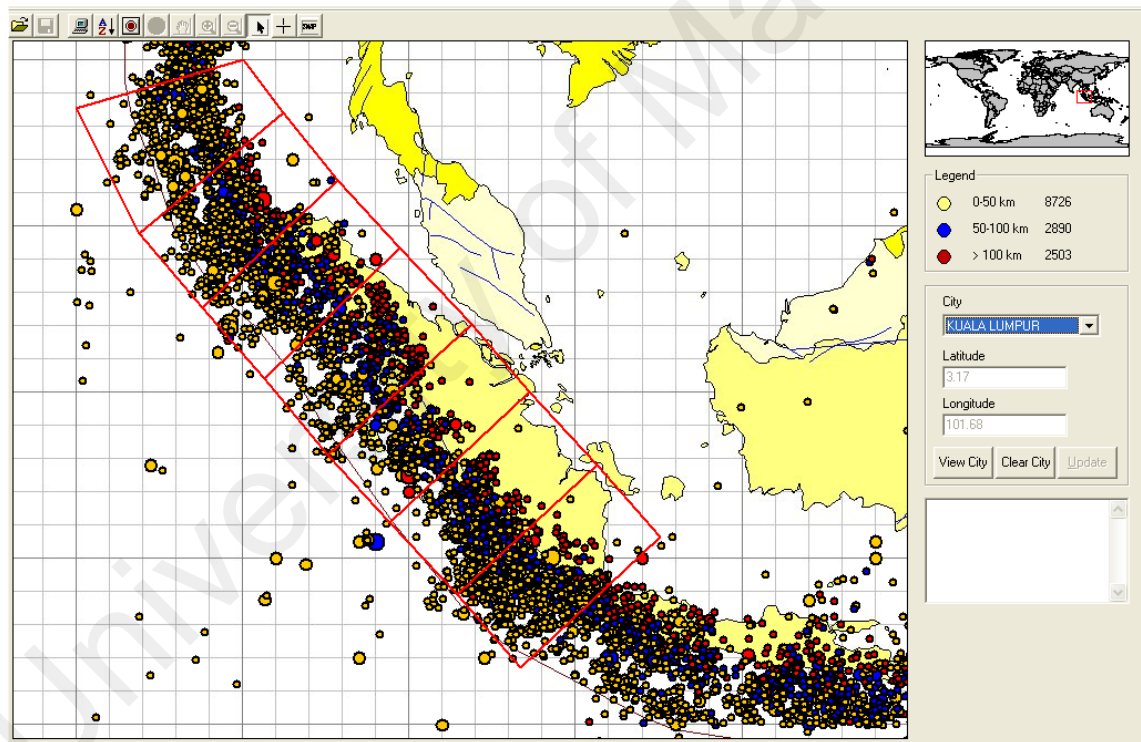


Figure 3.1: Seismic source zones around Malaysian Peninsula (Adnan, 2013).

Two separate maps had been developed for 500 and 2500 years of return period and 10% and 2% chance of exceeding the peak ground acceleration value specified at Kuala Lumpur.

Figure 3.2 shows the relationship between PGA and return period for Kuala Lumpur. It shows that the PGA for Kuala Lumpur are estimated to be 0.086g and 0.192g for 500 and 2500 year return period of earthquake, respectively. The target spectra for Kuala Lumpur is shown in Figure 3.3.

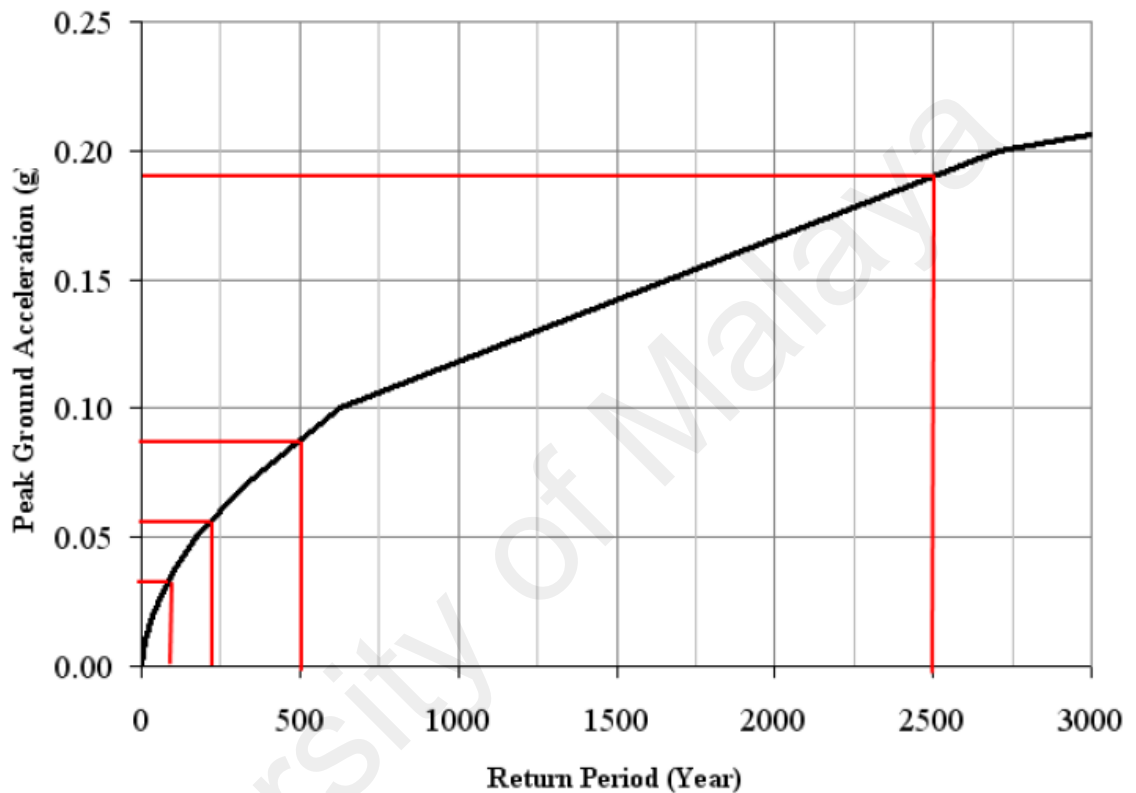


Figure 3.2: Seismic hazard exposure at Kuala Lumpur (Adnan, 2013).

3.3 Deaggregation

Dominated earthquake at 10% and 2% PE in 50 years were deaggregated in this study. Figure 3.4 shows earthquakes along Sumatra fault zone and Benioff zones are contributed to the studied site (Kuala Lumpur) with magnitude M_w of 7.8 and source to site-distance of 300km.

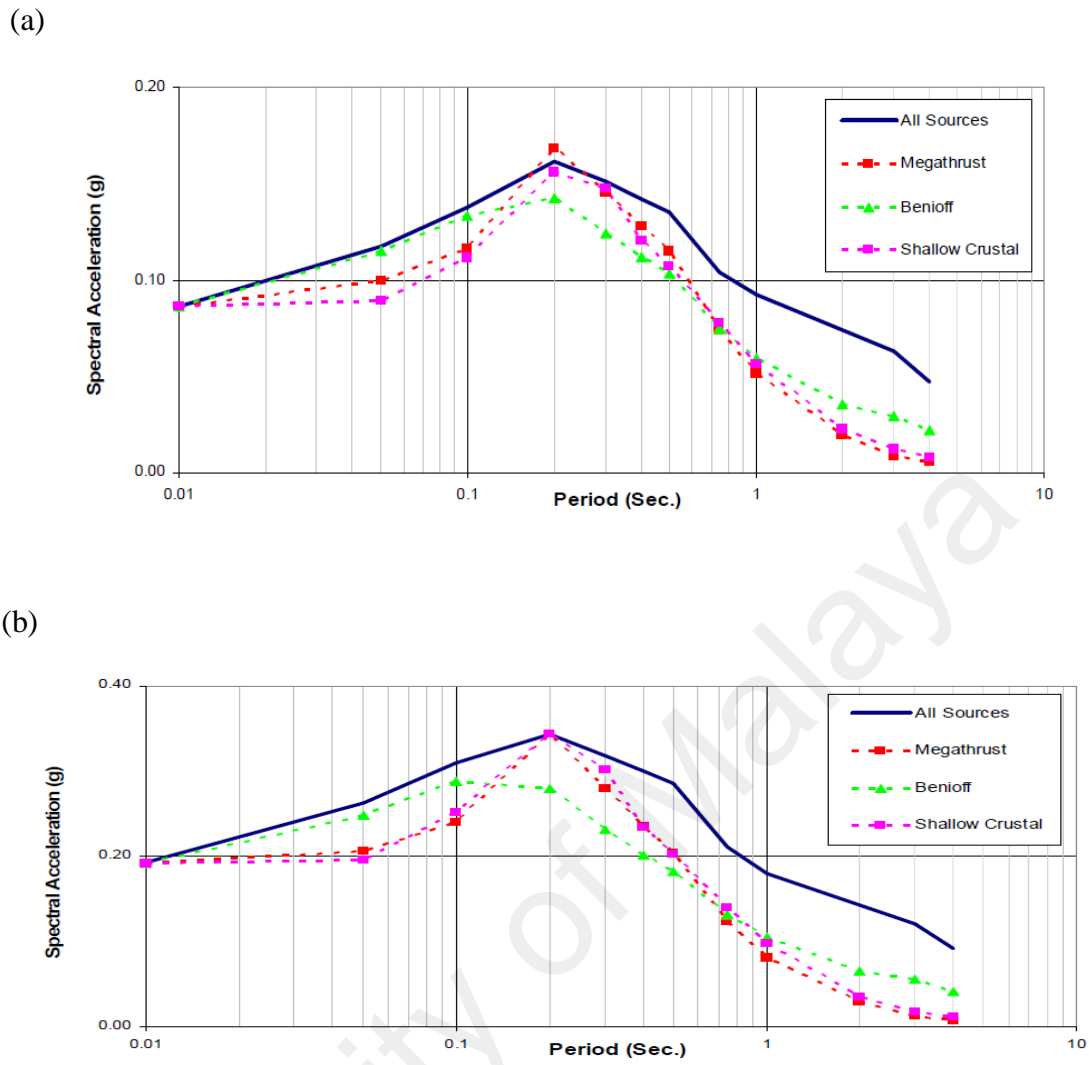


Figure 3.3: Target spectra for Kuala Lumpur for (a) 500 and (b) 2500 YRP (Adnan, 2013).

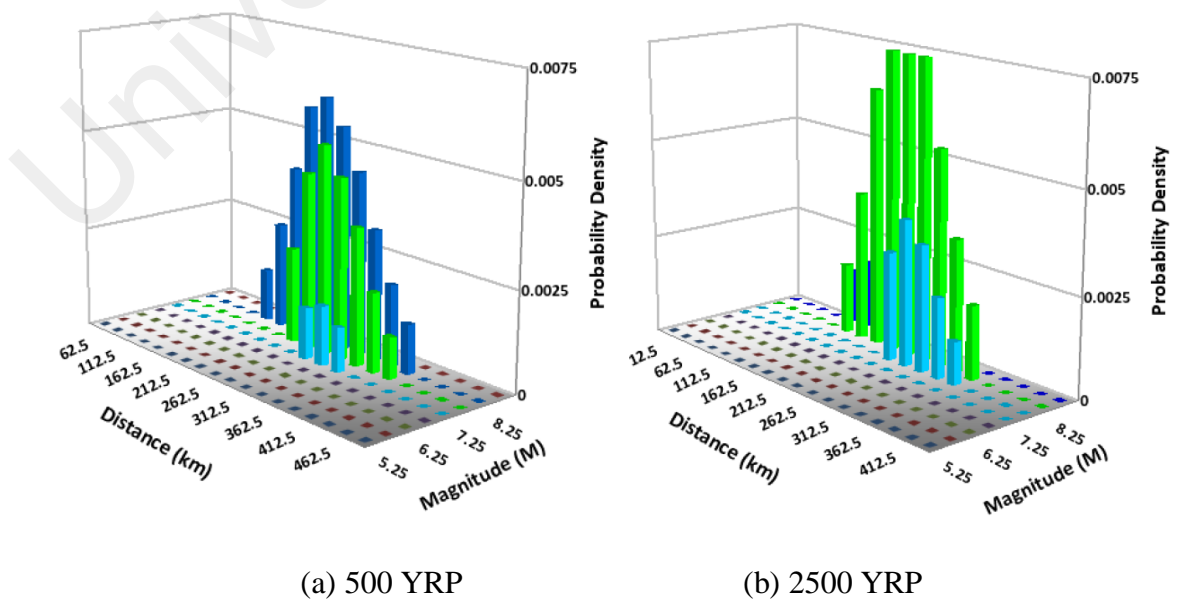


Figure 3.4: Deaggregation hazard result (Adnan, 2013).

Furthermore, Petersen et al. (2004) summarized that the dominated earthquake amplitude in terms of PGA were estimated to be 0.14 and 0.08g for 2% and 10% PE in 50 years. The most contribution earthquake are those occurring along the Sumatran fault with magnitude M_w of 7.7 and epicenter distance of 323km as shown in Figure 3.5

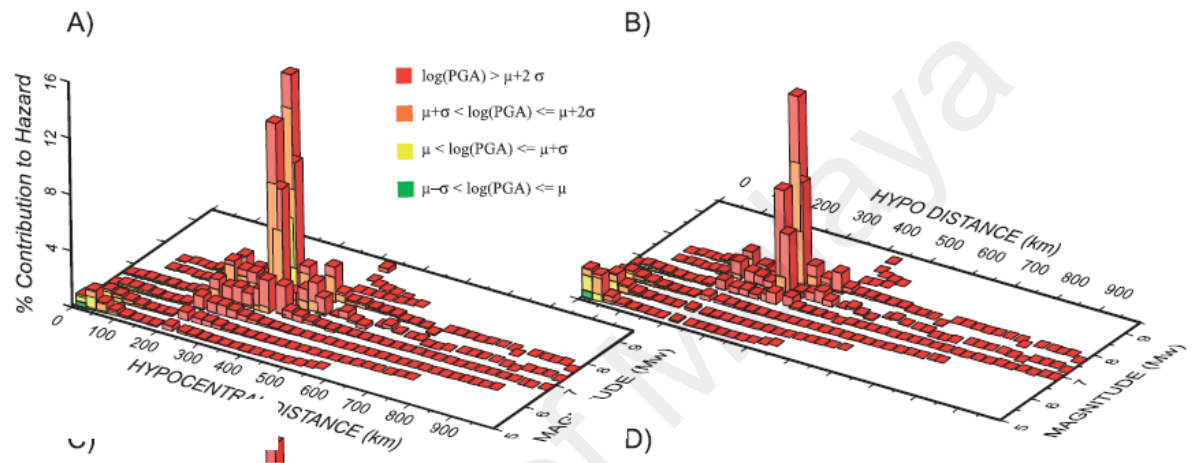


Figure 3.5: Dominated earthquake scenarios (a) 10%/50 years and (b) 2%/50 years (Petersen et al. (2004)).

Therefore, the above magnitude and epicenter distance were employed for an initial step the search window reference. Ten horizontal acceleration time histories from five different earthquake records were chosen from an international database, COSMOS, using guidance from literature as follows:

- a) Magnitude of earthquake should be in the range of $M_w \pm 0.2M_w$ (Bommer & Acevedo, 2004),
- b) The epicenter distance should be more than 100km and
- c) To minimize the site effects, the ground motions recorded at rock of stiff sites are considered.

Only the horizontal components of the records were considered. No rupture directivity effect was taken into account. Table 3.1 summarized the details of the selected records from COSMOS Database. As can be seen that a magnitude of M_w between 6.76 and 7.30 and a distance of 110 to 350km from the recording stations to the ruptured area were chosen. Uncertainty related to earthquakes were also taken into consideration.

Table 3.1: Properties of the selected records.

Earthquake event	Origin time	Magnitude (M_w)	Depth (km)	PGA (g)		Station code	Site condition / V_{s30}	Rupture distance (km)
				NS	EW			
Chi-chi	20/09/1999	7.6	6.8	0.0099	0.0199	KAU003	Rock	118.1
Northern California	15/06/2005	7.2	10	0.0054	0.0033	USGS1584	Rock	134.5
Duzce	12/11/1999	7.1	10	0.0045	0.0057	KOER769	Rock	183.5
Landers	28/06/1992	7.3	7	0.0384	0.0478	CSMIP23590	Rock	121.1
India-Burma Border	06/08/1988	7.2	90	0.0521	0.0547	CHER	Rock	353.0

3.4 Site response analysis

Three main steps to carry out site response analysis are listed below:

- a) Select typical site condition for study.
- b) Select an analysis method and define a soil column based on site investigation data.
- c) Compute the ground motions at the surface based on an analysis method.

3.41 Site description

Three different site conditions were considered in this study as shown in Figure 3.6 and Figure 3.7. The first site is OUG Park Secondary School Figure 3.6(a), a stiff sandy site in Kuala Lumpur. The site comprised of a silt layer with 2.5m thick on top of sand. The level of ground water for OUG Park was observed at 2.5m below the ground surface. To calculate shear wave velocities of the site the Standard Penetration Test (SPT) data and the empirical correlation of Seed and Idriss (1981) are used as follows:

$$V_s = 61.4N^{0.5} \quad (3-1)$$

The second site under investigation is campus of the International Islamic University Malaysia (IIUM) Figure 3.6(b), a relatively soft site comprised largely of clay located in Kuala Lumpur. At 13.5 below existing ground level, it found several 4.5m thick sand layers. Water level for this site was found at 6.0m below the surface. This site is classified to have 280m/s and therefore it was known as type D in site categories.

The third site considered was Setapak Vocational High School, Kuala Lumpur. But two different boring logs, namely BH1 and BH2, were selected as shown in Figure 3.7. At 16.5m below ground surface, BH1 consists of a 3m thick sand layer. The level of ground water was found at 2m below earth and a total depth of 25.5m to bedrock was reported. BH2 is mainly with clay layers. Water table for BH2 is located at 2m below earth and a total depth of 22.5m was reported. The V_{s30} of BH1 is computed to be 171m/s and classified as NEHRP (2001) class E, whereas the V_{s30} of BH2 is calculated to be 238m/s and classified as NEHRP (2001) class D.

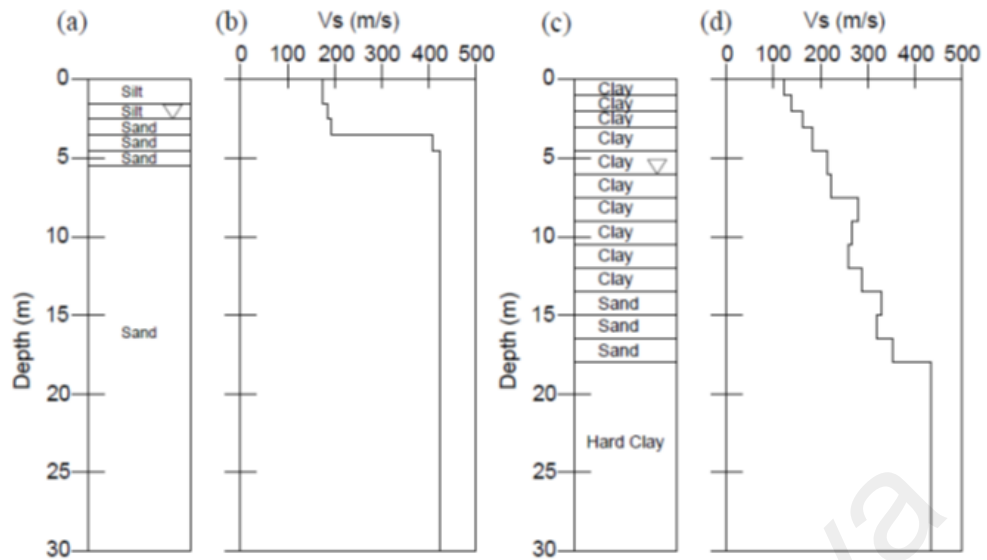


Figure 3.6: Soil description and corresponding Vs30 for (a) Type C site (OUG Park) and (b) Type D site (IIUM campus).

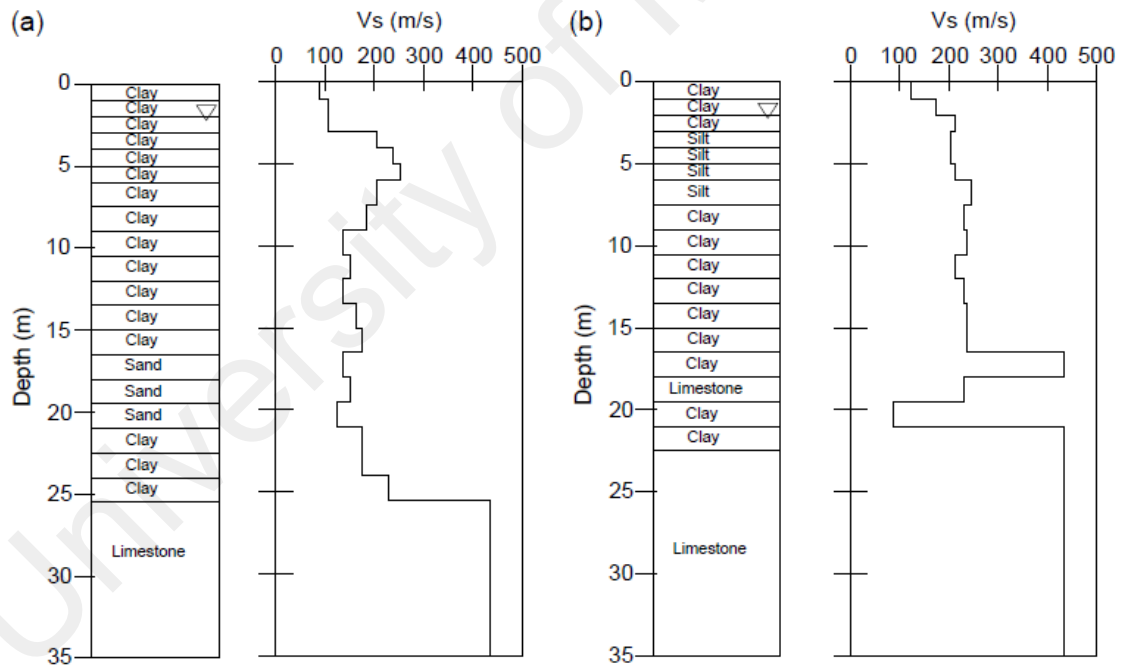


Figure 3.7: Soil and shear-wave velocity profile for the Setapak Vocational High

School: (a) Soil type E (BH1) and (b) Soil type D (BH2).

3.42 Modelling of soil layers

In this study, the various soil conditions studied were investigated using a one-dimensional equivalent linear analysis through a package of SHAKE91 (Idriss & Sun, 1992). It assumes seismic waves propagating in vertical direction via horizontal soil layering. Four parameters need to be carefully identified. Many different soil dynamic property relationships are available from the literature. Specifically, the model from Darendeli (2001) are adopted. The curves proposed by Schnabel et al. (1972) for bedrock are used as given in Figure 3.8 and Figure 3.9.

However, the density of soil were selected from Brandenberg et al. (2010) where position of soil and water table are taken into consideration. Table 3.2 summarizes the density of soil. The soil profiles were separated into layers that ranged between 0.5 and 1.5m in thickness based on the profiles. The effective over maximum shear strain was taken as 0.65, and the critical damping was assumed to be 5%, as suggested by Idriss and Sun (1992).

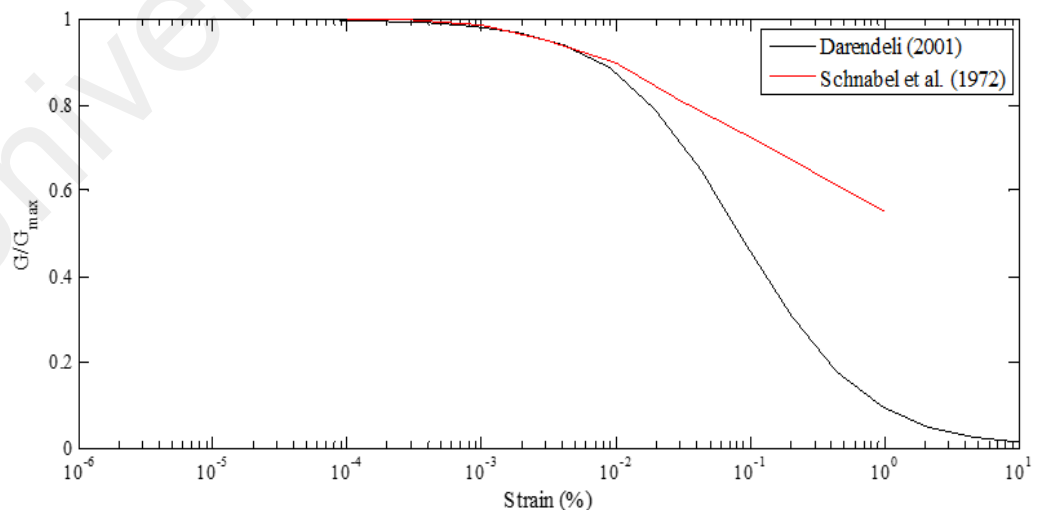


Figure 3.8: Modulus reduction curves of dynamic soil properties.

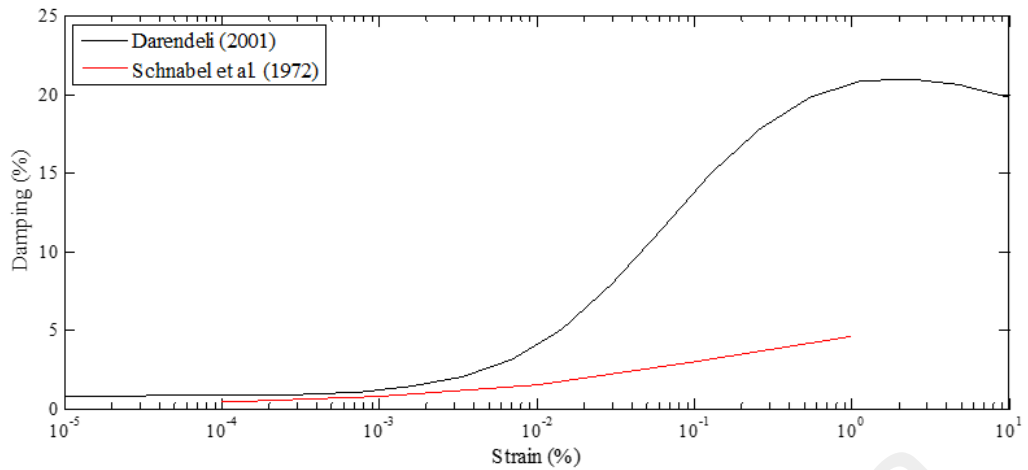


Figure 3.9: Damping curves of soil properties.

Table 3.2: Soil density (Brandenberg et al., 2010).

Soil type	Unit weight above water table (kN/m ³)	Unit weight below water table (kN/m ³)
Sand	18	20
Silt	19	17
Clay	16	18
Gravel	19	17

Figure 3.10 shows the ground response at varying depths from bedrock to surface of two selected soil profiles. It can be seen that, when the acceleration at bedrock is smaller than 0.75g, the surface acceleration is amplified due to dynamic motion effect of layered soils. On the other hand, the surface accelerations are reduced relative to bedrock when bedrock PGAs are larger than 1g.

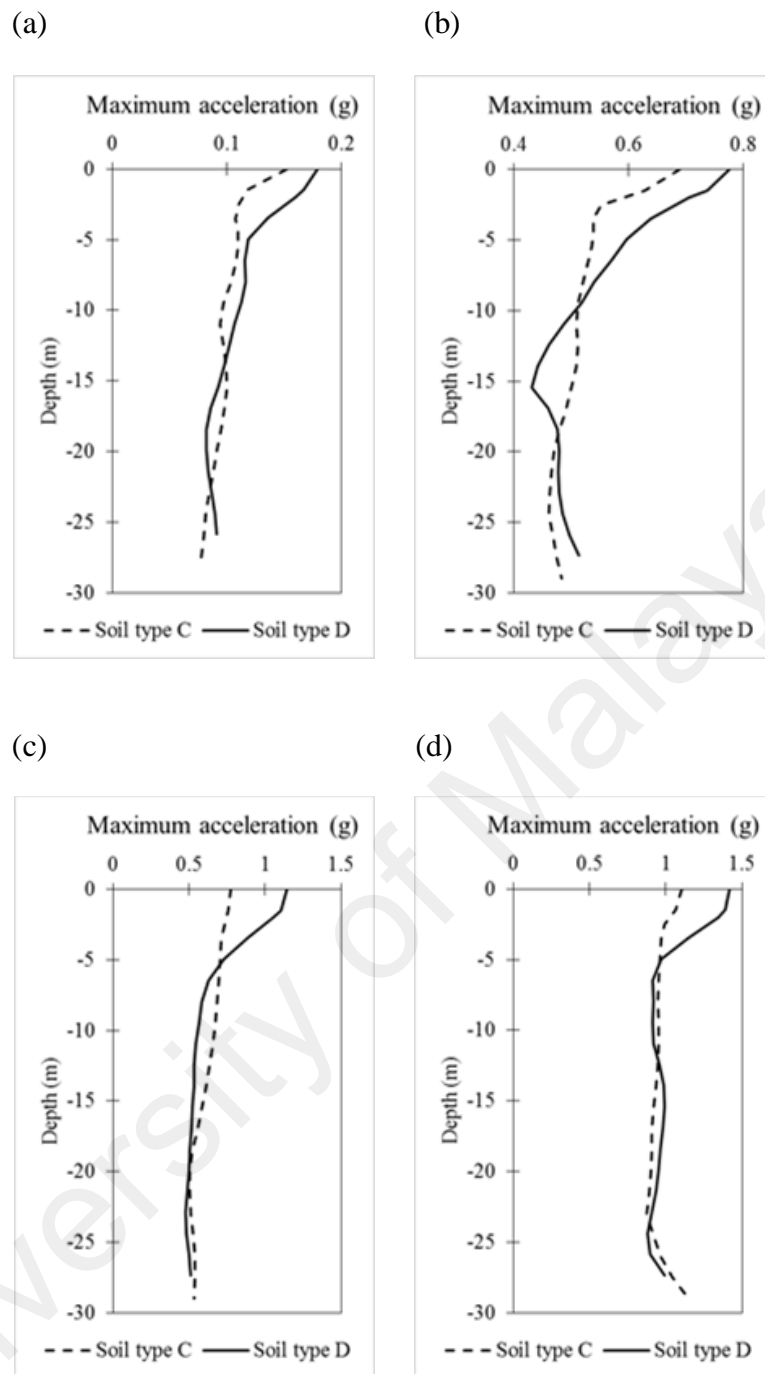


Figure 3.10: Maximum acceleration along the soil type C and D for the input motions: (a) Landers scaled at 0.15g, (b) Duzce scaled at 0.75g, (c) Chi-chi scaled at 1g and (d) Duzce scaled at 1.5g.

The shear modulus of the soil remains linear at small amplitude of ground motion while larger excitation of bedrock will cause soil properties to become nonlinear. Therefore, the dynamic responses of layered soils are affected by the magnitude of

simulated earthquake. Based on this observation, quantitative free field analysis should be performed prior to seismic analysis to identify the ground acceleration amplification effect.

Figure 3.11 shows the surface acceleration ground motions for type C and D soil categories. It was observed that the PGAs at ground surface for type D soil category are greater than that type C soil category. In particular, the maximum accelerations of soil type D are between 13% and 48% higher than those at the surface of soil type C, depending on the ground motions. These results highlight that the soil conditions should not be ignored in earthquake studies. Moreover, the buildings on firm or stiff soil are expected to be less vulnerability than those on weak site.

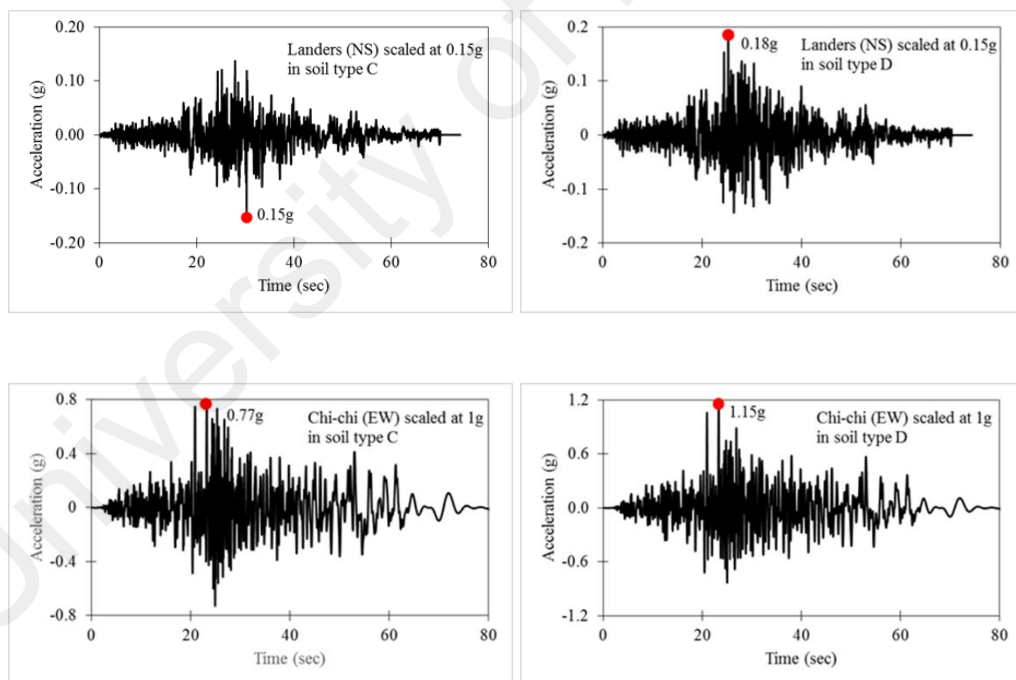


Figure 3.11: Expected ground motions after site response analysis.

CHAPTER 4: SHAKE TABLE TEST

4.1 Introduction

Details for shake table tests conducted, including the construction details and final dimensions of the test structure are discussed hereafter. The characteristics and limitations experimental tests are also presented. The construction sequence, the arrangement of additional masses and the instrumentation of the test structure are also described in detail.

A four-storey two-bay by one-bay reinforced concrete building with URM infill walls is defined as the prototype structure of the experimental test. The details of this structure is discussed in next chapter. It was conducted at the laboratory of Institute of Engineering Mechanics, China Earthquake Administration, Harbin, China. All physical aspects of the proposed model are designed with respect to its prototype. Similar materials from the prototype are used in the proposed model. Thus, the materials of reinforced concrete specimens are fabricated using micro-concrete in order to achieve similitude requirements, while the strength of the concrete was similarly maintained.

4.2 Description of the shake table

The following description of the shake table facility at the laboratory of Institute of Engineering Mechanics (IEM), Earthquake Administration in China, is extracted from Harbin Institute of Technology, China. The shake table has a size of 5m x 5m. It is configured to produce six degree of freedom motions. These six degrees of freedom (DOF) can be programmed to reproduce any waveform within the capacities of force, velocity, displacement and frequency of the system. In this study, only unidirectional horizontal response in line with URM infill walls is considered.

The shake table can test structures weighing up to 30ton and the maximum overturning moment is 75 ton-m. The table can shake with a maximum acceleration value of 1.0g in both horizontal directions and 0.7g in vertical direction. The maximum displacement of the shake table in the horizontal directions is limited to the gap that separates the shake table from the laboratory floor (80mm). The maximum vertical displacement is limited to the stroke of the vertical actuators (50mm). The table frequency ranges from 0.5Hz to 40Hz and 96 channels are available for data acquisition during the experiment.

4.3 Similitude relationship and model materials

Given the table size and capacity of bearing, the test structure is designed to 1:2 scale. In this study the ratio of length (l_r) is 0.5. Only a four-storey two-bay by one-bay RC system with UMR infill walls was investigated. Clay brick walls were only constructed in the central frame. Size of aggregate of 10mm was adopted in concrete batching to construct the scaled model. The total height of the scaled model was reduced to 7.2m excluding the base. The stress-strain relationships between the prototype and the scaled model were assumed to be equal. Ideally, the mass scale factor is expressed as:

$$\frac{(m_m)_{total}}{(m_p)_{total}} = E_r l_r^2 \quad (4-1)$$

where $(m_m)_{total}$ was scale model total weight and $(m_p)_{total}$ was prototype structure total weight. Using Eq. 3-1, the extra weight to be added to the scaled model is 31ton. The extra weight is more than the allowable bearing capacity (30ton) of the shake table. Therefore, the ratio of mass of scale model to prototype structure is given as:

$$\frac{(m_m)_{approx}}{(m_p)_{approx}} = \rho_r l_r^3 \quad (4-2)$$

where $(m_m)_{approx}$ was scaled model total weight, $(m_p)_{approx}$ was prototype building total weight and ρ_r was an equivalent mass density ratio.

In this study, the prototype of the building was calculated to have 124.3ton weight. However, the similitude law reduces the mass of the scaled model from 124.2ton to 22.2ton. The weight of the scaled model was increased from 15.5 ton to 22.2ton. Therefore, an extra weight of 6.7ton was required. This extral weight can be applied using many different methods such as applying concrete block, steel plates and sand bags to the structure. In this study, steel plates were used since they are available in the laboratory.

The ground motion parameters were also need to be scaled because the density of mass ratio was adjusted. Table 4.1 summarizes the main variables to be scaled accordingly.

Concrete for scaled model was fabricated using micro-concrete. The mix design for the micro-concrete was cement: sand: aggregates in the ratio of 2.5: 1.0: 1.5. In this study, 0.48 was taken for water over cement ratio. The concrete strength was measured to be 29MPa based on mean statistic. Two type of reinforcement were used with longitudinal and transverse strength measured to be 450MPa and 250MPa, respectively. The reinforcement lapping in the column and column starter bars was 400mm. No links provided in beam column joints but the reinforcement bars in beam was bent 90° insert into column.

For infill panels, a nominal dimension of 240mm x 115mm x 90mm for soild clay bricks was used. They were proportionally cut into halves. The ratio of cross sectional

area of walls to the total floor area of the scaled model is estimated to be 0.48% according to Pujol and Fick (2010). The compressive and shear strength of masonry were measured to be 4.48MPa and 0.15MPa respectively on the day of testing. The masonry unit strength was measured as 10MPa and the compressive strength of mortar was tested to be 6.4MPa. Figure 4.1 shows the constructed scaled model on the shake table.



Figure 4.1: Scaled model on 5mx5m shake table.

Table 4.1: Similitude parameters.

Properties	Physical quantity	Dimension	Similitude equation	True replica model	Modified replica model	Remark
Material	Strain ε		$S_\varepsilon = 1$	1	1	
properties	Stress σ	FL^{-2}	$S_\sigma = S_E$	1	0.350625	Control factor
	Elastic modulus E	FL^{-2}	$S_E = S_\sigma$	1	0.350625	
	Poisson ratio μ		$S_\mu = 1$	1	1	
	Density ρ	$FT^2 L^{-4}$	$S_\rho = S_\sigma / S_L$	0.50	0.70	Control factor
Geometric properties	Length L	L	S_L	2	2	Control factor
	Linear displacement X	L	$S_X = S_L$	2	2	
	Angular displacement β		$S_\beta = 1$	1	1	
Load	Concentrated force P	F	$S_P = S_E S_L^2$	4	1.4025	
	Linear load W	FL^{-1}	$S_W = S_\sigma S_L$	2	0.70125	
	Surface load Q	FL^{-2}	$S_Q = S_\sigma$	1	0.350625	
	Moment M	FL	$S_M = S_\sigma S_L^3$	8	2.805	
Dynamic properties	Mass m	$FT^2 L^{-1}$	$S_m = S_\rho S_L^3$	4	5.61	Control factor
	Stiffness K	FL^{-1}	$S_K = S_E S_L$	2	0.70125	
	Damping C	FTL^{-2}	$S_C = S_m / S_T$	2.83	1.98	
	Period T	T	$S_T = (S_m / S_K)^{0.5}$	1.41	2.83	Control factor loading
	Frequency f	T^{-1}	$S_f = 1 / S_T$	0.71	0.35	
	Velocity V	LT^{-1}	$S_V = S_X / S_T$	1.41	0.71	
	Acceleration a	LT^{-2}	$S_a = S_X / S_T^2$	1	0.25	Control factor loading
Acceleration of gravity g	LT^{-2}	$S_g = 1$	1	1	Gravity distortion if $S_\sigma \neq S_g$	

4.4 Instrumentation and experimental setup

Two measurement tools were employed in this study to evaluate the response of the scaled model: (1) accelerometers, and (2) displacement transducers (LVDTs). Two reference steel frames are also used as supports of LVDTs. The accelerometers and data recorder used are shown in Figure 4.2 **Error! Reference source not found.** A frequency response of 0-80Hz was measured for accelerometers. The acceleration was measured in range of $\pm 5g$ for accelerometers. The displacement for LVDTs can be measured up to 100mm.

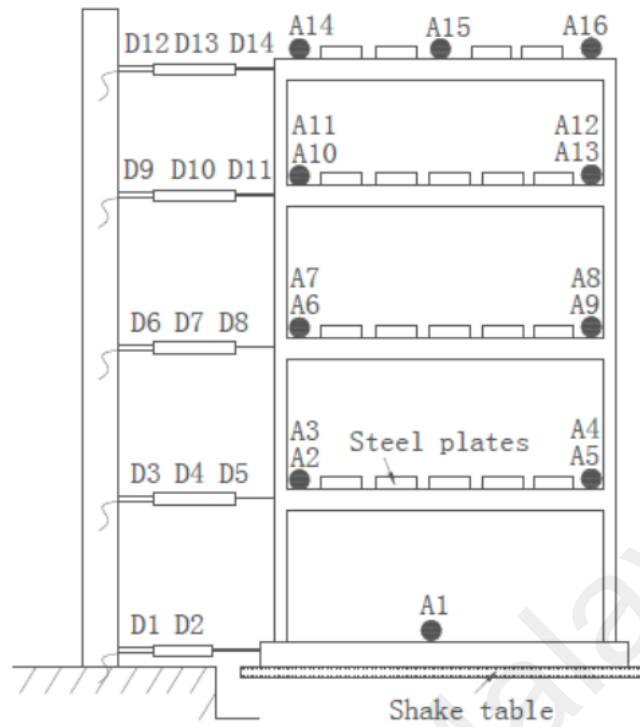
Sixteen accelerometers are located at level of story used to measure floor acceleration especially in longitudinal direction (y-direction). Each floor corner has an accelerometers while the roof is arranged on one of the diagonals on opposite corners and at the center. These are because the accelerometers provided are not enough. In addition, to measure actual base excitations from input ground motions an accelerometer was placed at the center of the foundation beam.

The displacement of the shake table and scaled model was measured with respect to a rigid steel frame. In this study, a total of fourteen displacement transducers are used. Twelve of these measured the displacement of the floor and the remaining two measured the displacements of the shake table.

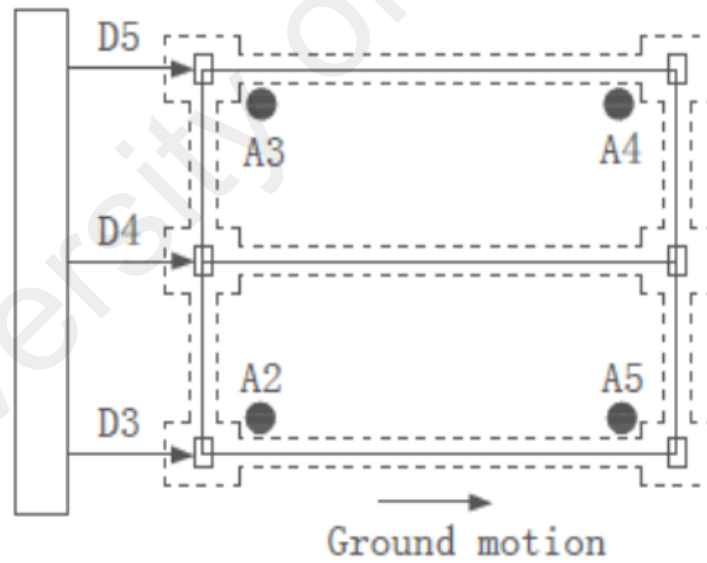
Figure 4.3 depicts the detailed drawings for the exact locations and configurations of all instruments. The letters 'A' and 'D' are referred to accelerometers and displacement transducers, respectively. All data are recorded simultaneously at a sampling rate of 200Hz on 30 channels. The preparations for the experimental setup are shown in Figure 4.4 to Figure 4.10.



Figure 4.2: Instrumentation: (a) accelerometer and (b) data recorder.



(a) Side view



(b) Plan view

Figure 4.3: Location of accelerometers (A1-A16) and displacement transducers (D1-D14).



Figure 4.4: Preparation of experimental setup.



Figure 4.5: Installation of accelerometers.



Figure 4.6: Installation of data acquisition sensors.

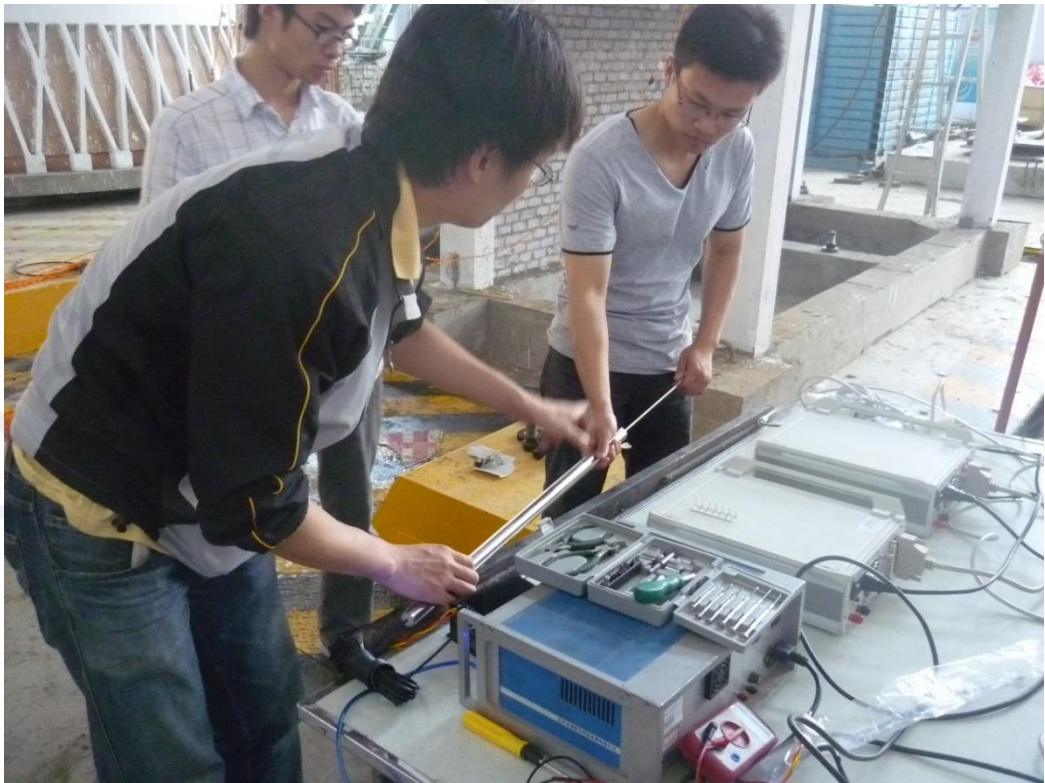


Figure 4.7: Testing of LVDTs.



Figure 4.8: Installation of LVDTs.

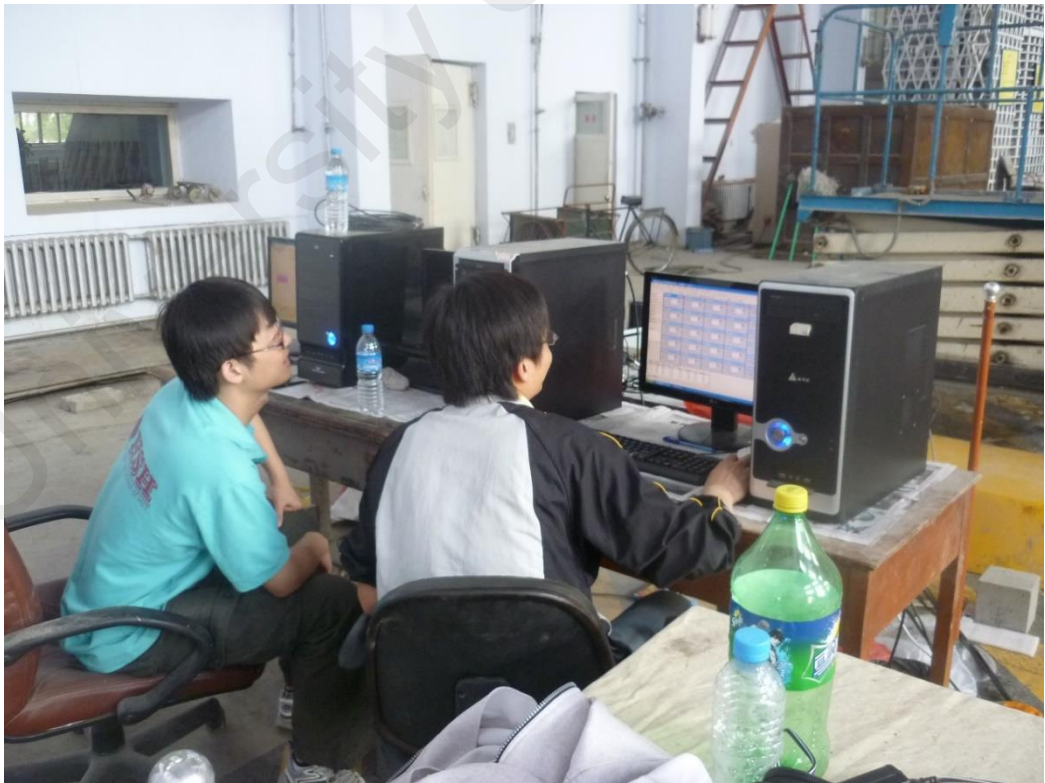


Figure 4.9: Testing of the experimental instruments.



Figure 4.10: Completion of experimental setups.

4.5 Construction process

The scaled model was constructed at the site adjacent to the shake table by several professional contractors. The base of the scaled model was constructed with a rigid RC beam. No interaction between soil and scaled model was assumed. The concrete was placed in four stages. A total of thirty concrete test cubes, twenty-four mortar test cubes and four masonry prisms were prepared during each phase of construction to be tested during various stages of the project.

After completion of the test structure, it was then moved to the shake table using a lifting machine with a capacity of 30ton. The test structure was then fastened to the shake table using several high-strength 30mm diameter steel long rods.

Once the test structure was secured to the shake table, the UMR infill walls were constructed. The work sequence described was designed to avoid moving the structure

with the unreinforced masonry infill wall to eliminate any possibility for micro-cracks to develop in the brittle wall. Upon completion of the construction of the unreinforced masonry infill wall, a month of curing time was allowed before the start of the experiment. This time was used to install instruments and additional masses. Steel plates were grouted on the model for addition mass. Figure 4.11 to Figure 4.21 show the photographs of different stages of the construction process of the model.



Figure 4.11: Construction of RC based beam.



Figure 4.12: Formwork for the scaled model.



Figure 4.13: Column reinforcement.



Figure 4.14: Slab and beam reinforcement.

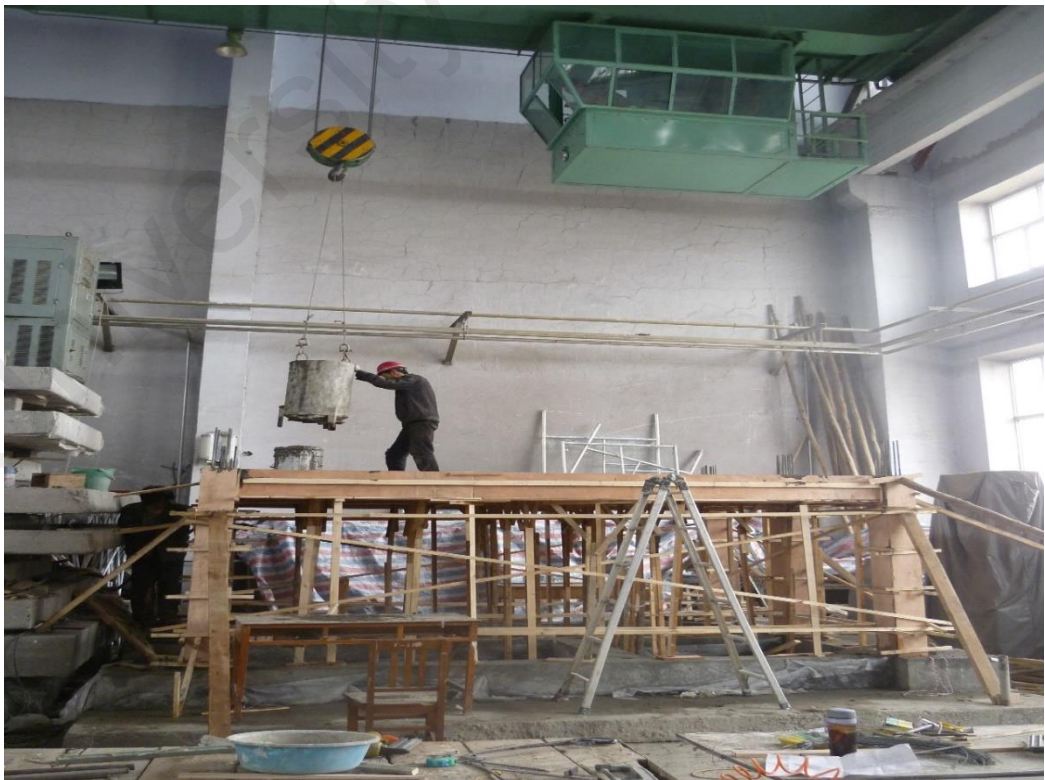


Figure 4.15: Concrete casting.



Figure 4.16: Preparation of concrete test cubes.



Figure 4.17: The scaled model after stripping forms.



Figure 4.18: Cutting solid clay bricks.



Figure 4.19: Transporting the scaled model to the shake table.



Figure 4.20: Construction of unreinforced masonry infill walls.



Figure 4.21: Preparation of mortar test cubes.

4.6 Test program

The test program for the shake table experiments is outlined in this section. Furthermore, three different acceleration time histories were inputted to the shake table control system. These ground motions correspond to Kepulauan Mentawai Region earthquake M6.7 on April 10, 2005, Sumatra earthquake M7.5 on September 30, 2009 and Wenchuan earthquake M7.9 on May 12, 2008. The first and second ground motions are obtained from the Malaysian Meteorological department (Figure 4.22) whereas the earthquake recorded in China is given by Institute of Engineering Mechanics, China Earthquake Administration (Figure 4.23) as they are well recorded.

A gradually increasing amplitudes of acceleration was applied to the scaled model. The selected ground motions were applied as unidirectional motions in y-direction of the scaled model. The similitude laws required time in x-axis compressed by a factor of 0.5. The ground motion signals were also filtered using a trapezoidal band-pass filter.

To generate the different levels of intensity the ground motions were adjusted. However, the peak displacement, velocity and acceleration of adjusted ground motions do not exceed the gap allow in between table and floor. However, an actual output of the shake table was measured at the base beam. Therefore, the output motions at the test structure footings were recorded as input motions to the finite element model.

The shake table experiments were performed in nine distinct phases as shown in Table 4.2. For Phase 1, the test model was subjected to white noise. The white noise test is performed before the earthquake simulation tests in order to capture an initial condition of the fundamental parameters of the scaled model.

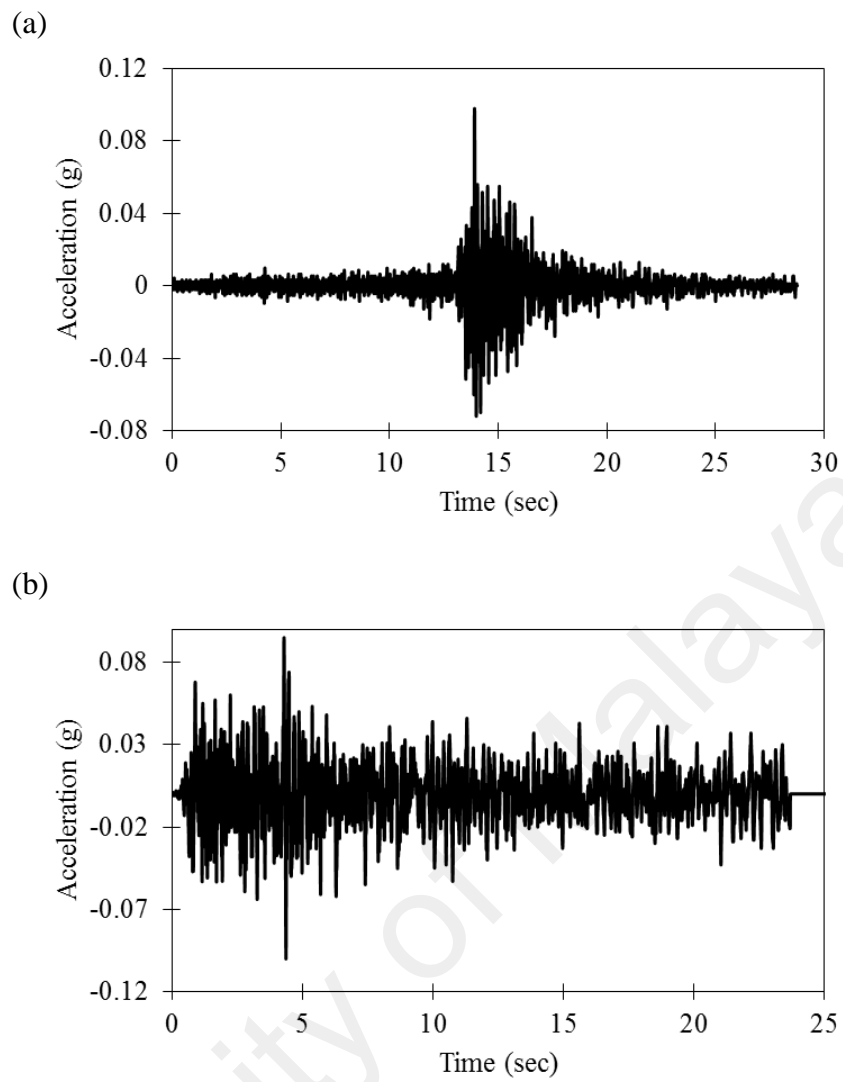


Figure 4.22: (a): Kepulauan Mentawai Region earthquake (M6.7) and (b) Sumatra earthquake (M7.5).

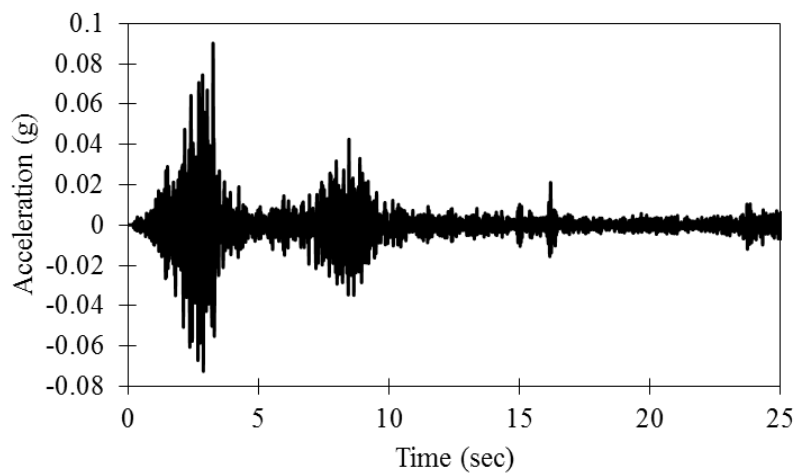


Figure 4.23: Wenchuan earthquake (M7.9).

This can also do a testing on all adopted measurement tools. Make sure they are properly connected. The test was then started from Wenchuan earthquake, Kepulauan Mentawai Region earthquake and lastly Sumatra earthquake.

The white noise excitations were performed after each phase of analysis to monitor the structural parameters due to damage accumulated on the test structure. In addition, Kepulauan Mentawai Region earthquake and Sumatra earthquake have to be terminated at Phase 8 as they have reached the shake table displacement limit. Therefore, Phases 8 and 9, the test structure is subjected only to the Wenchuan earthquake with an amplitude of 0.8g and 0.9g, respectively.

4.7 Observed damage of unreinforced masonry infill wall

Observation of crack pattern of the model after each ground motion input was made in Figure 4.24. In Figure 4.24(a), no damage was found after ground motion of amplitude 0.06g. However, the wall frame interfaces were observed with small visible cracks as shown Figure 4.24(b), after 0.12g. Most of these cracks were happened at the first and second floor especially focusing in the corner areas.

In Figure 4.24(c), after 0.20g, a significant damage to masonry infill walls is apparent and concentrated in the first and second floor of the scaled model was observed with a significant crack on masonry infill walls. It show large cracks at an inclination of about 60° from corners of the upper part to horizontal direction. The cracks also formed a 45 degree diagonal crack on walls of the first and second floor. However, the corners of the first and second floor were crushed. These signs were also observed at the top panel of the second floor.

Table 4.2: The sequence of loading of the shake table experiment.

Phase	Ground motions	Input PGA (g)
1	White noise	0.050
2	Wenchuan earthquake	0.059
	Kepulauan Mentawai Region	0.064
	Sumatra earthquake	0.050
	White noise	0.050
3	Wenchuan earthquake	0.120
	Kepulauan Mentawai Region	0.130
	Sumatra earthquake	0.178
	White noise	0.050
4	Wenchuan earthquake	0.203
	Kepulauan Mentawai Region	0.217
	Sumatra earthquake	0.248
	White noise	0.050
5	Wenchuan earthquake	0.341
	Kepulauan Mentawai Region	0.321
	Sumatra earthquake	0.326
	White noise	0.050
6	Wenchuan earthquake	0.477
	Kepulauan Mentawai Region	0.500
	Sumatra earthquake	0.475
	White noise	0.050
7	Wenchuan earthquake	0.571
	Kepulauan Mentawai Region	0.701*
	Sumatra earthquake	0.700*
	White noise	0.050
8	Wenchuan earthquake	0.779
	White noise	0.050
9	Wenchuan earthquake	0.904
	White noise	0.050

* Shake table automatically shuts off when it reaches allowable displacement limit.

Therefore, a obvious pattern of crack was defined along the diagonal direction. The masonry wall was then divided into two was also observed on third floor. These crack patterns may be due to weak bond strength between mortar joint and masonry unit.

In Figure 4.24(d), after 0.34g, the corners from most upper part of the panel at the 1st and 2nd floors is found with partial collapse. The cracks at the panel of the third floor are extended and widened. Minor cracks were also observed at the connection of beam and column. The URM wall was lost of serviability. The RC frames start to absorb the displacement of the ground motions after 0.34g.

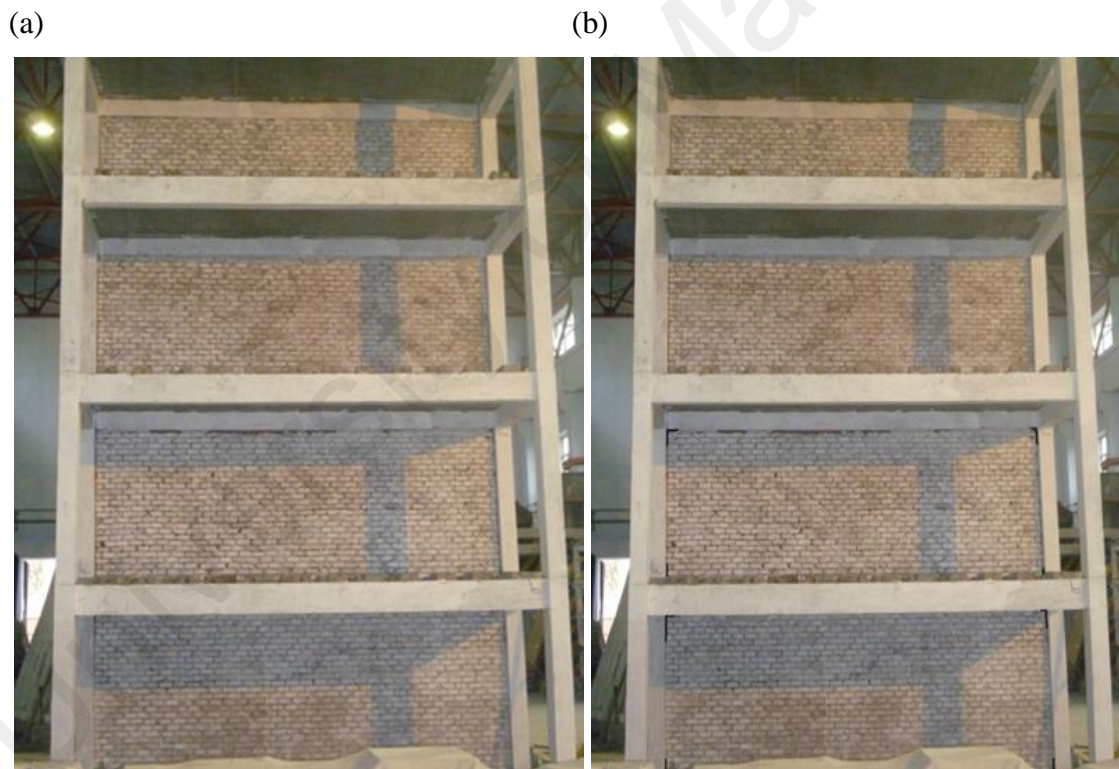


Figure 4.24: Crack patterns observed on the scaled model: (a) after 0.06g, (b) after 0.12g, (c) after 0.20g and (d) after 0.34g.

(c)



(d)



'Figure 4.24, continued'

University of

CHAPTER 5: COMPUTATIONAL MODELLING

5.1 System definition

In Malaysia, the standard designs were designed and prepared by Public Work Department or Jabatan Kerja Raya. The designs are mainly used for government buildings. The It is also an afford to control construction quality. Although some projects may have minor changes from a function to another function, they are similarly in terms of architectural design. Therefore, the seismic fragility for such buildings is essential since Peninsular Malaysia is located near an active fault.

Fragility analyses are performed for RC framed buildings that were constructed from two standard designs. The structural drawings of the standard were collected from Malaysian Public Works Department. The design is symmetrical and simple, ideally meet the current need on research of earthquake engineering. Three typical heights for a typical design were selected, i.e., equal to 3-, 7- and 11-storeys. These buildings were used as the administrative center and were designed according to the British Standard BS8110:1997. Figure 5.1 shows the plan, elevation and beam and column size. The buildings have a rectangular shape with a total of eleven frames. The typical floor area is 2080m^2 (80m x 26m) and the storey height is 4m. Concrete slabs with thicknesses of 15cm are placed at each storey level. The design yield stress of reinforcements in columns and beams is 460MPa, and 30MPa nominal compressive cube strength of concrete for columns and beams was used.

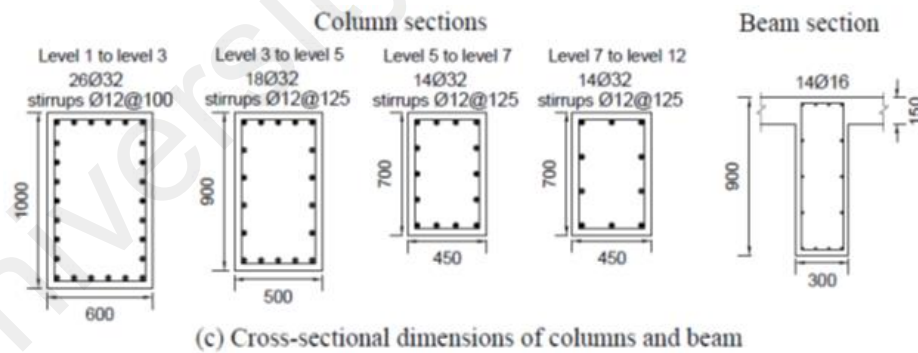
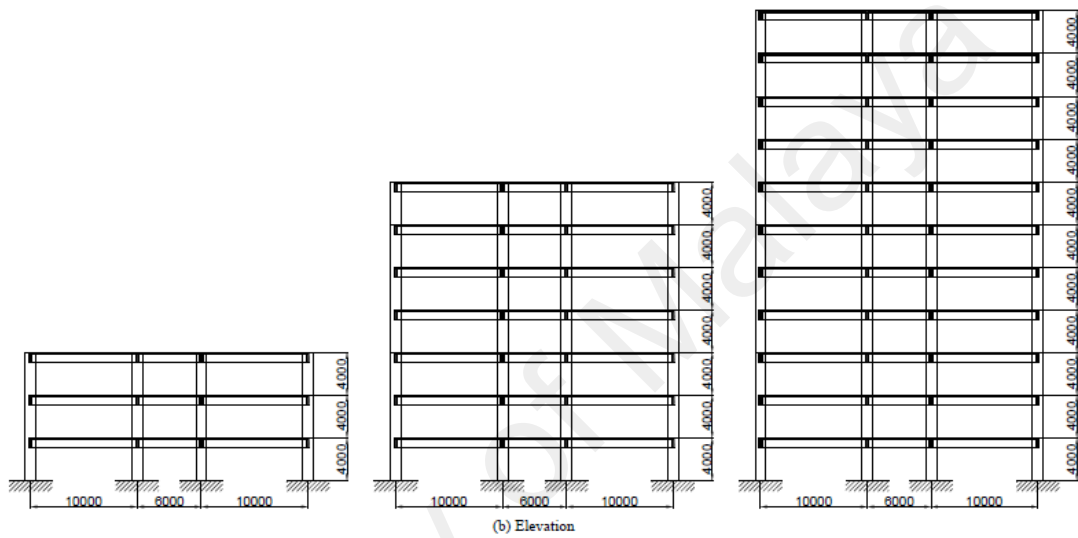
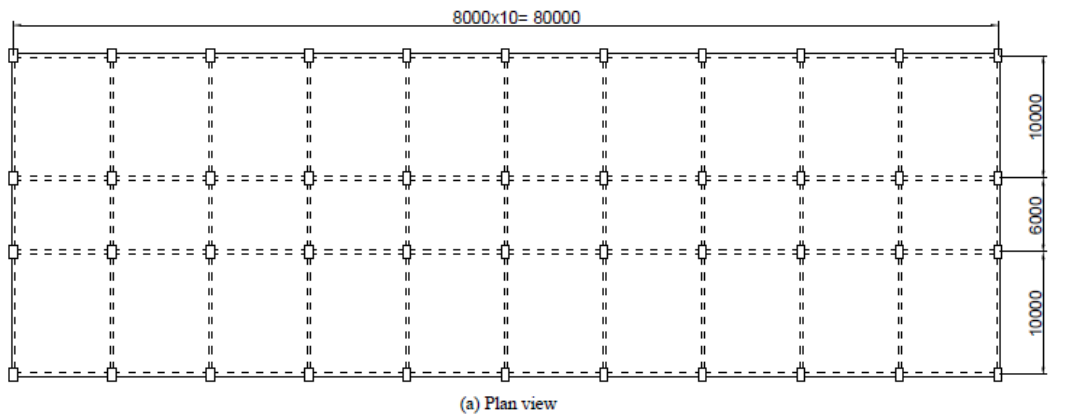


Figure 5.1: The layout of the RC office framed buildings.

Another standard design for reinforced concrete school building was also investigated. It was also designed with respect to British Standard BS8110:1997. It has four story multiple frames with 3.6m constant inter-storey height. Bay widths of 3m and 7.8m in longitudinal and transverse directions were designed. The structural plan and

elevation frames were designed similarly. Solid clay bricks were used to separate the class room.

Slab thickness of 13cm was used for every floor. The concrete covers are followed the code which is 40mm for columns and 30mm for beams. 20mm longitudinal bars with a yield stress of 460MPa were used for column. The column links were used with 10mm reinforcement with a yield stress of 250MPa. The column link spacing is 200mm. No links were provided in the beam and column connection. It was a practice in Malaysia. Concrete strength was 30MPa given in the as-built drawings.

Furthermore, a total of super imposed dead and live load of 1.5kN/m^2 was applied to the structure. This load was taken into consideration for concrete tiles, ceiling, lighting, etc. Figure 5.2 shows the layout and detail for school building.

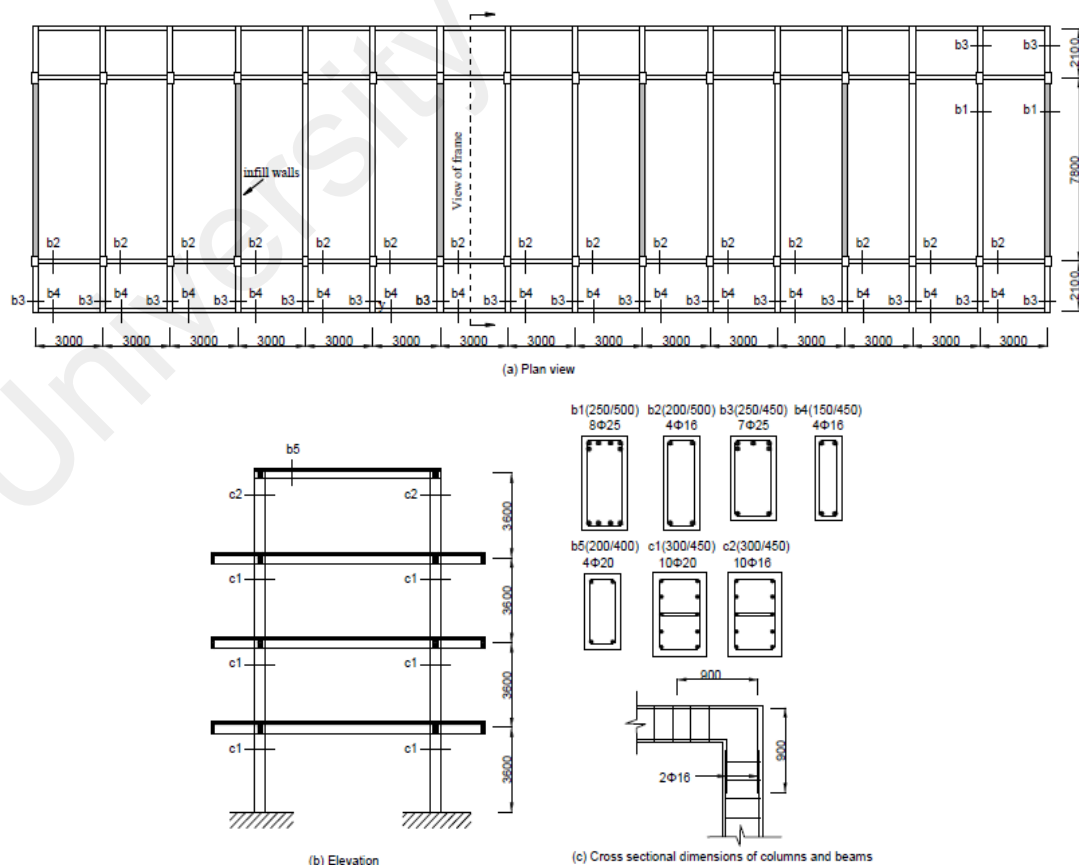


Figure 5.2: The layout of the RC school building (unit: mm).

5.2 Finite element model

Three-dimensional finite-element models for each selected building are constructed in OpenSees platform (Mazzoni et al., 2007; McKenna & Fenves, 2001), which is an open source prepared by PEER. This program is developed primarily to support earthquake simulations with extensive and extensible library of material, section and element objects (Kiureghian et al., 2006). Its adequacy in predicting the seismic response of various RC structures has been validated by many researchers, such as those mentioned in the literature review, through pseudo dynamic and shake table tests.

In this study, frame members are simulated based on distributed plasticity and fiber model. Each element has five Gauss-Lobatto integration points. Cross sections of the beam-column element are divided into unconfined concrete, confined concrete and steel fibers with corresponding material stress-strain relationships.

The modified Kent-Park model (Kent & Park, 1971) is employed to describe the stress-strain relationship of the concrete fibers. This model allows an accurate estimation of the structural demand for flexure-dominated RC members, despite its relatively simple formulation (Lagaros & Papadrakakis, 2012; Mitropoulou & Papadrakakis, 2011). The Giuffré-Pinto formulation, implemented later by Menegotto and Pinto (1973) is employed for the steel fibers. This model has sufficient accuracy to satisfy the requirements of the experimental tests, while also taking into account the Bauschinger effect (Li & Hatzigeorgiou, 2012).

In addition, column bases are assumed to be fixed and no relative rotation at the beam-column joint is considered, i.e., the connection of beam and column are assumed to be rigid in the finite element models. The rigid floor diaphragms are defined based on the degrees-of-freedom coupling feature available in the package (Mazzoni et al., 2007;

McKenna & Fenves, 2001). Shear deformation and bond-slip are neglected. The effects of gravity loads and the second-order effects are included in the analysis through the consideration of geometric nonlinearities. Figure 5.3 shows the frame and section modeling.

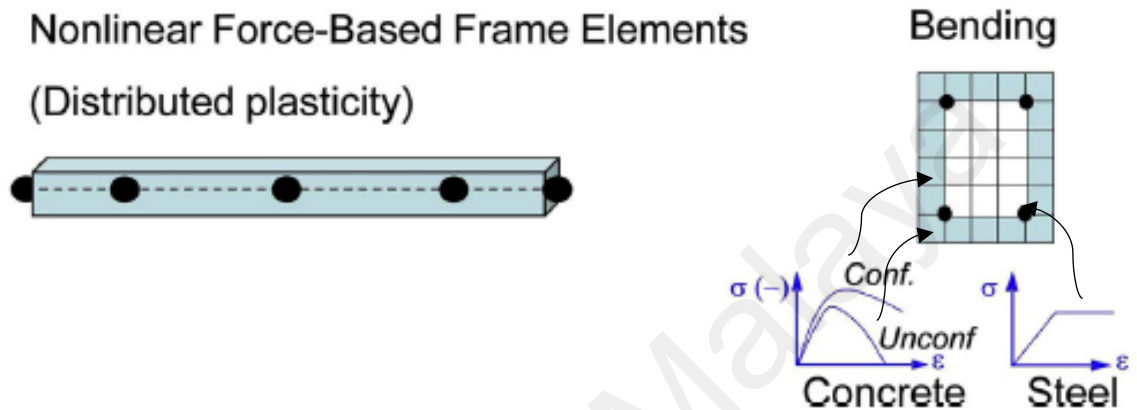


Figure 5.3: Frame and section modeling.

For solid infill panels, a single equivalent diagonal strut proposed by Kadysiewski and Mosalam (2009) is adopted, which is capable of considering in-plane and out-of-plane interaction effect. It is composed of two force-based fiber beam-column elements with a node at midspan, placed between the beam-column joints. The panels do not carry any vertical loads. The out-of-plane behavior of the panels is modeled using the arching mechanism. The effect of partial infill walls for openings is out of scope of this research. Somemore, it is very complicated to capture the behavior of the openings. The mechanical properties of masonry walls considered herein are based on laboratory observations presented in next chapter since in-field tests are costly.

According to Kadysiewski and Mosalam (2009), the thickness of element is same as adopted brick unit, while the length of the model is equal to diagonal length of wall panel. However, the width of the model is determined using equation as follows:

$$a = 0.175(\lambda_1 h_{col})^{-0.4} r_{inf} \quad (5-1)$$

where

$$\lambda_1 = \sqrt[4]{\frac{E_{me} t_{inf} \sin 2\theta}{4E_{fe} I_{col} h_{inf}}} \quad (5-2)$$

and h_{col} is the column height between centerlines of beams, h_{inf} is the height of infill panel, E_{fe} is the expected modulus of elasticity of frame material, E_{me} is the expected modulus of elasticity of infill material, I_{col} is the moment of inertial of column, r_{inf} is the diagonal length of infill panel, t_{inf} is the thickness of infill panel and equivalent strut, and θ is the angle whose tangent is the infill height-to-length aspect ratio. This equation is the lower bound for the equivalent width of infill strut (Chrysostomou & Asteris, 2012).

The lateral stiffness of the infill panel in in-plane direction k_i is defined as:

$$k_i = \frac{a \cdot t_{inf} E_m}{r_{inf}} \quad (5-3)$$

According to FEMA 356, the shear strength of the infill panel V_{ine} is defined as:

$$V_{ine} = A_n v_{me} \quad (5-4)$$

where A_n is net mortared area and v_{me} is shear strength of URM infill expected which should not exceed

$$v_{me} = \frac{0.75(0.75v_{te} + \frac{P_{ce}}{A_n})}{1.5} \quad (5-5)$$

where v_{te} is bed-joint average shear strength and P_{ce} was compressive force in vertical direction applied on the wall. In this study, the URM wall strength, v_{me} is set to be 0.34 MPa (50 psi), as suggested in FEMA 356.

The lateral deflection of the panel at yield Δ_{Hy0} is determined by

$$\Delta_{Hy0} = \frac{v_{ine}}{k_{inf} \cdot (\cos\theta)^2} \quad (5-6)$$

while the lateral deflection of the panel at collapse prevention limit state Δ_{Hcp0} is computed as

$$\Delta_{Hcp0} = d \cdot h_{inf} \quad (5-7)$$

where d is the interstorey drift that is defined as a function of frame divided infill shear strength, β , and aspect ratio, L_{inf}/h_{inf} , listed in Table 5.1. The range of drifts (0.3-1.5%) has been further validated through experimental results.

For URM infill wall in out-of plane direction, the arching mechanism was used.

The strength of the wall q_{ine} was calculated as (FEMA 356):

$$q_{ine} = \frac{0.7 f_{me} \lambda_2}{h_{inf} / t_{inf}} \times 144 \quad (5-8)$$

where f_{me} is masonry strength and λ_2 is a parameter of slenderness listed in Table 5.2.

Table 5.1: Nonlinear force-deflection relations for infill panels (FEMA 356).

$\beta = \frac{V_{fre}}{V_{ine}}$	$\frac{L_{inf}}{h_{inf}}$	d %
$\beta < 0.7$	0.5	0.5
	1.0	0.4
	2.0	0.3
$0.7 \leq \beta \leq 1.3$	0.5	1.0
	1.0	0.8
	2.0	0.6
$\beta \geq 1.3$	0.5	1.5
	1.0	1.2
	2.0	0.9

Table 5.2: Values of λ_2 (FEMA 356).

h_{inf}/t_{inf}	5	10	15	25
λ_2	0.129	0.060	0.034	0.013

The first natural frequency of the panel f_{ss} , spanning in the vertical direction with top and bottom ends simply supported is calculated as:

$$f_{ss} = \frac{\pi}{2 \cdot h_{inf}^2} \sqrt{\frac{E_m \cdot t_{inf} \cdot g}{w_{inf}}} \quad (5-9)$$

where w_{inf} is the weight over wall length.

The stiffness of URM wall in out-of-plane direction k_{eq_N} is calculated as:

$$k_{eq_N} = (2\pi f_{ss})^2 \frac{MEW}{g} \quad (5-10)$$

where MEW is the modal effective weight, taken as 81% of the total infill weight, as recommended in Kadysiewski and Mosalam (2009). This effective weight divided by gravity g was used as the out-of-plane only horizontal mass at the midspan node.

The moment of inertia of the infill panel I_{eq} is calculated as:

$$I_{eq} = \frac{k_{eq-N} \cdot (L_{diag})^2}{48 \cdot E_m} \quad (5-11)$$

where L_{diag} is the diagonal length between column centerlines and floor centerlines.

The out-of-plane yield moment of the infill panel M_{n0} is defined as:

$$M_{n0} = 1.570 \cdot \frac{L_{diag}}{h_{inf}} \cdot M_y \quad (5-12)$$

where M_y is the moment in the infill wall at the time that it reaches its capacity is calculated as:

$$M_y = \frac{q_{in} \cdot L_{inf} \cdot h_{inf}^2}{8} \quad (5-13)$$

For out-of-plane yield displacement, FEMA 356 suggests that the yield displacement corresponding to immediate occupancy limit state is equal to or less than 2% of the out-of-plane storey drift ratio of the infill. According to Kadysiewski and Mosalam (2009), the yield displacement is calculated as:

$$\delta_{Ny0} = \frac{F_{Ny0}}{k_{eq-N}} \quad (5-14)$$

where

$$F_{Ny0} = \frac{4M_{eq-y}}{L_{diag}} \quad (5-15)$$

For out-of-plane ultimate displacement, FEMA 356 suggests that the ultimate displacement corresponding to collapse prevention limit state is equal to or less than 5% of the out-of-plane storey drift ratio of the infill. However, Kadysiewski and Mosalam (2009) defined the ultimate displacement with respect to out-of-plane displacement ductility. A conservative value for ductility of 5 is proposed (Kadysiewski and Mosalam; 2009). Figure 5.4 to Figure 5.7 show the finite element models of the selected buildings.

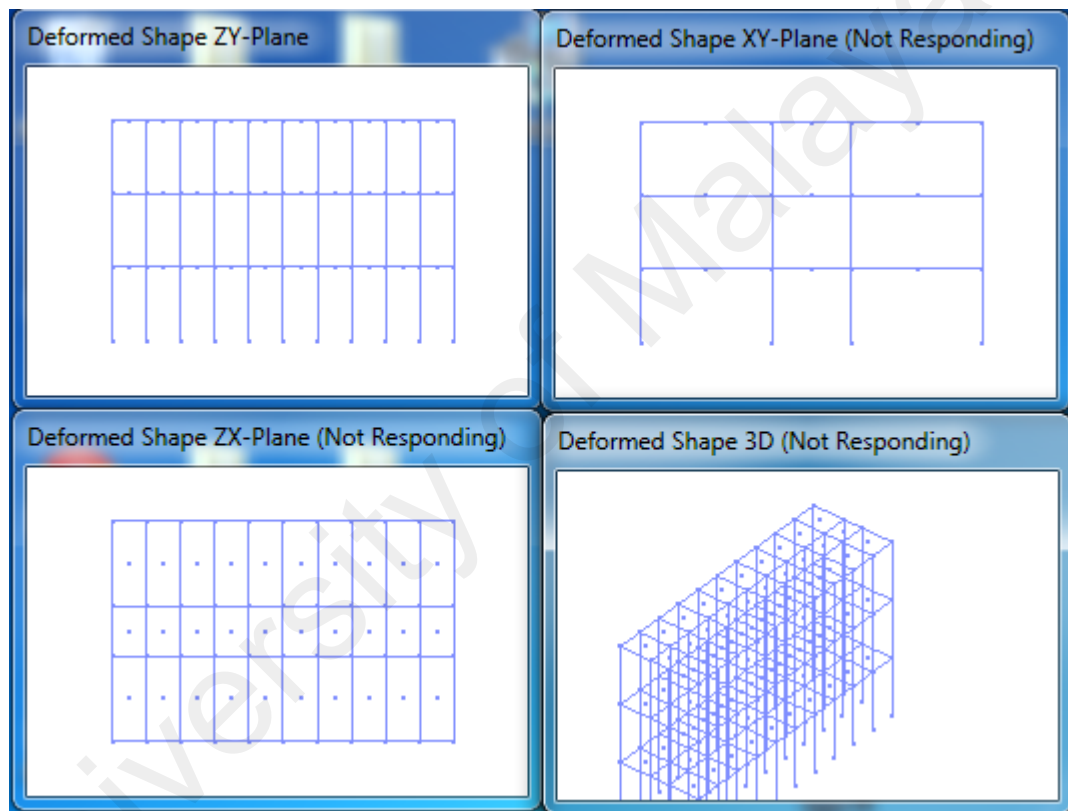


Figure 5.4: 3-storey RC framed building.

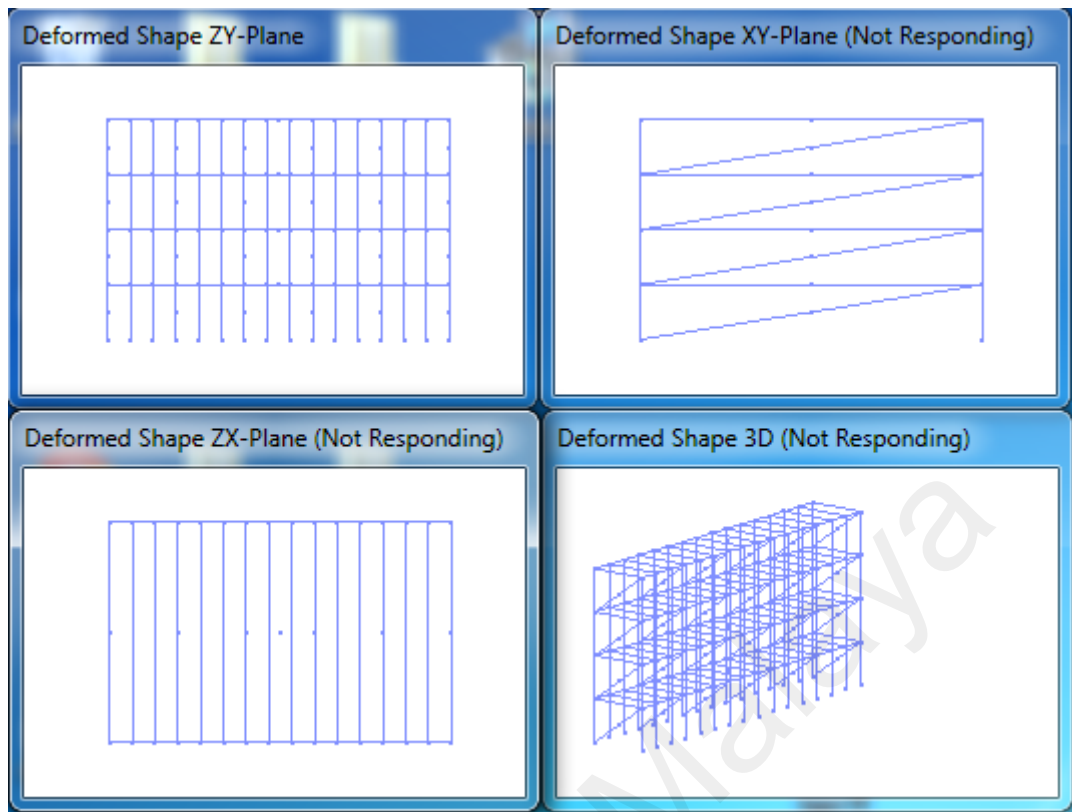


Figure 5.5: 4-story infilled RC framed building.

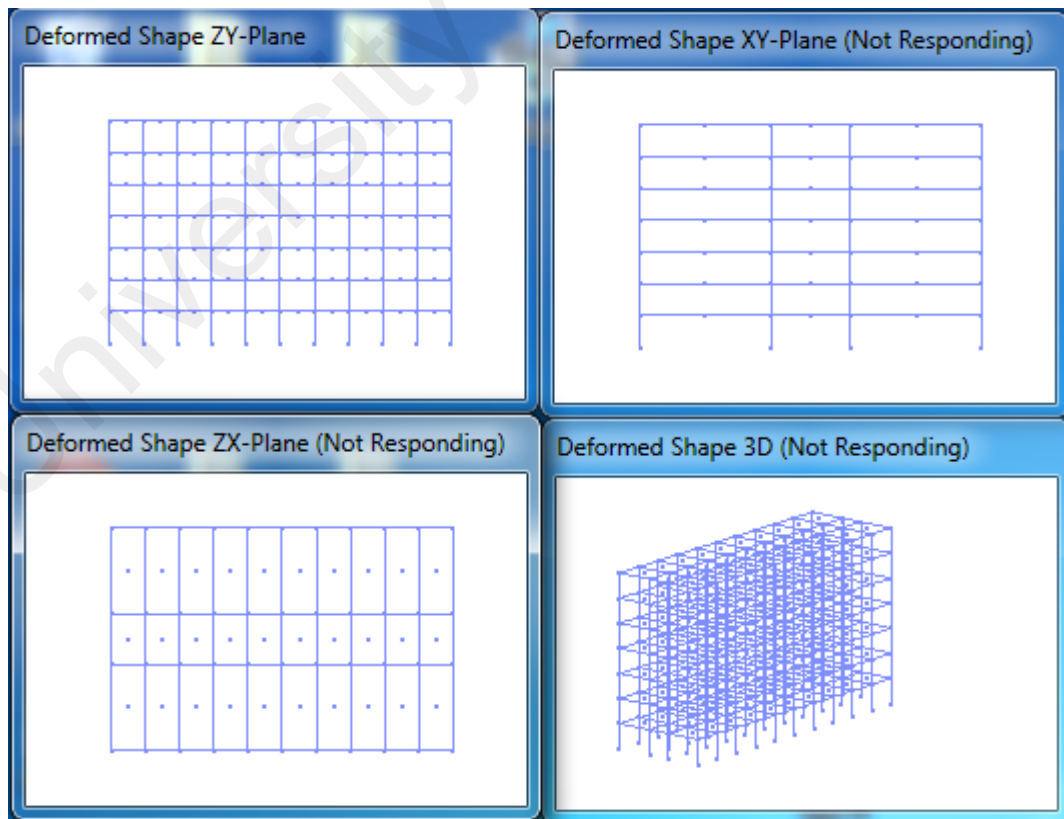


Figure 5.6: 7-storey RC framed building.

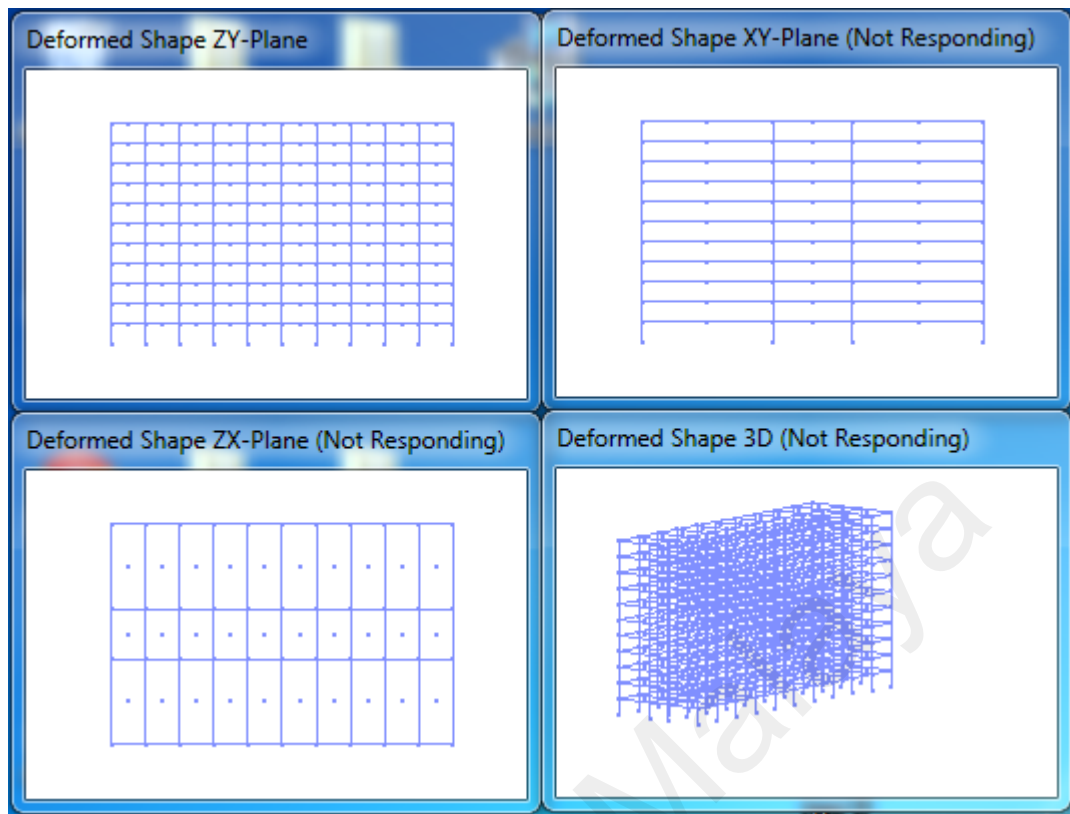


Figure 5.7: 11-storey RC framed building.

5.3 Nonlinear time history analysis

In literature seismic studies or investigations are usually conducted either dynamic or static analysis. Among these the method proposed by ATC-40 is the most popular one. It can provide approximate seismic performance utilizing the structural resistance and seismic demand represented in the acceleration-displacement response spectra format. However, to apply the capacity spectrum method, a structure's pushover curve should be able to represent the global force-deformation relationship. The performance evaluation using capacity spectrum may not be suitable if a structure has very stiff elements such as infill walls.

Since the masonry infill walls are one of the factors considered herein, nonlinear dynamic time history analysis is adopted to evaluate the seismic response of the structure. This approach is the most rigorous and reliable analytical method for developing fragility

curves. However, a high-speed computer was used in order to reduce the computational time. Rayleigh damping is used for the analysis, in which the damping ratio is taken as 2% as suggested by Kwon and Kim (2010). The story displacement demand, inter-story drift ratio and section moment-curvature are evaluated at every time step.

The PHGA at the “seismic bedrock” is selected as an intensity measure to describe the ground motion characteristics. This variable is consistent with modern seismic hazard assessment methods, as applied in recent research, e.g. Fotopoulou and Pitilakis (2013). A total of 230 nonlinear dynamic time history analyses had been performed using the high-speed computer.

Finally, the numerical simulation of the masonry infilled RC frames is verified through comparison of the time history analysis with shake table tests. In this case, the structure is independently analyzed in both the longitudinal (x) and transverse (y) directions since the experimental test is performed only in one direction of loading. Only global responses of the structure, i.e., displacement demand and acceleration demand at story level are evaluated.

5.4 Validation of numerical model

In this section, the verification of the analysis model and environment through comparison with shake table tests are discussed. The analytical model is subjected to the same sequence of ground motions as discussed in test program. These ground motions are measured acceleration time histories recorded at the base of the test structure during the shake table tests.

In order to account for the cumulative damage incurred in each excitation, the validation of the numerical model is carried out based on the base excitations applied sequentially in a single numerical analysis as in the tests. It is an attempt to simulate the actual behavior of the test structure experienced during the shake table tests. A similar approach had been adopted in a study conducted by Koutromanos et al. (2011). Figure 5.8 shows the concatenated input ground motion for simulation. It should be noted that only part of the concatenated input ground motion for simulation is presented due to page width.

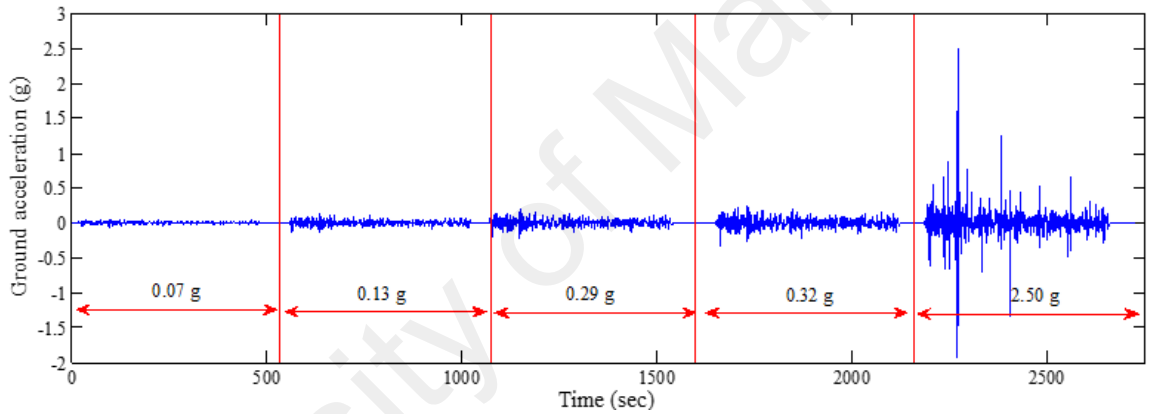


Figure 5.8: A concatenation of table motion for simulation.

The comparisons are also carried out directly from the results of the 1/2 scale model and analysis using a 1/2 scale numerical model. Thus, any influence arising from scaling effects is negligible. An error index ε defined by Yu et al. (2010) is also adopted to quantify the modeling accuracy of the numerical infilled system under different base excitations:

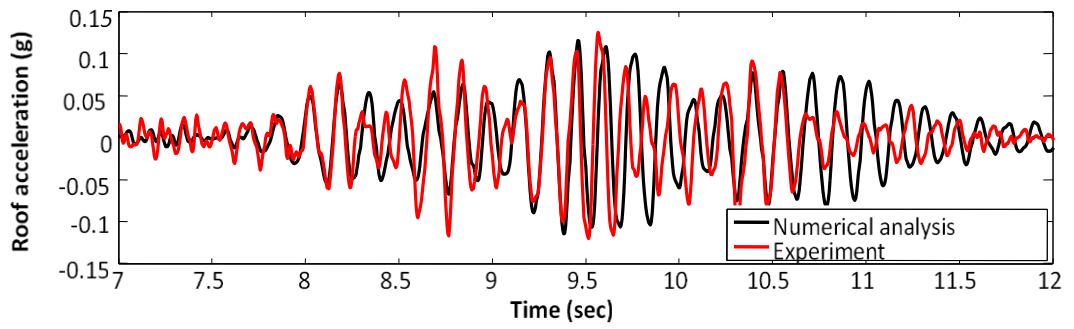
$$\varepsilon = \frac{1}{n} \sum_i \sum_j \left| \frac{ANA_{ij} - EXP_{ij}}{EXP_{ij}} \right| \quad (5-16)$$

where the index i represents four different responses: absolute maximum relative displacements from base, or absolute maximum accelerations, or absolute maximum storey drift angles, or absolute maximum storey shears in both the X and Y directions. The index j varies from the first to the last floor. ANA represents the analytical responses while EXP is associated with the test results. The index n represents the total numbers of responses evaluated. In this study, $n = i \times j = 3 \text{ responses} \times 1 \text{ direction} \times 4 \text{ storeys} = 12$. The error index ϵ roughly suggests the overall prediction error.

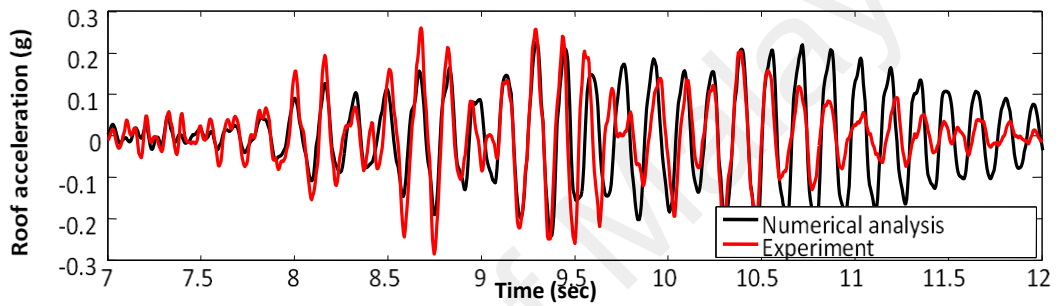
Figure 5.9 and Figure 5.10 compare the numerical and experimental time histories in terms of roof acceleration and displacement of the infilled system. A good agreement between the model predictions and the test results was obtained until about 10.5s. After that the numerical analysis gives considerably larger values of the acceleration and displacement. This discrepancy is probably due to the difference in damping characteristics of the numerical model and the experimental test structure. The damping ratio for the numerical model was assumed to be 2% whilst for the test structure the damping ratio is apparently higher.

Table 5.3 summarizes the overall prediction error of the numerical model for different base excitations. The numerical model shows a good agreement with respect to the experimental model with maximum errors approximations between 10-25%. Based on these observations, it can be concluded that the numerical model replicates well the predicted seismic behavior of the experimental test structure.

(a)



(b)



(c)

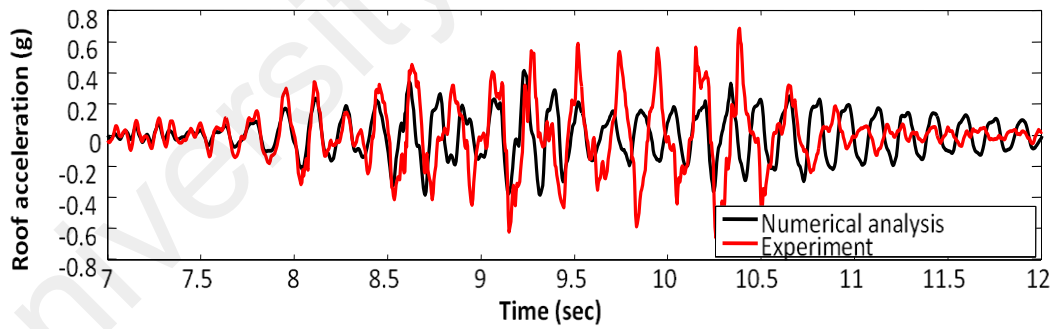
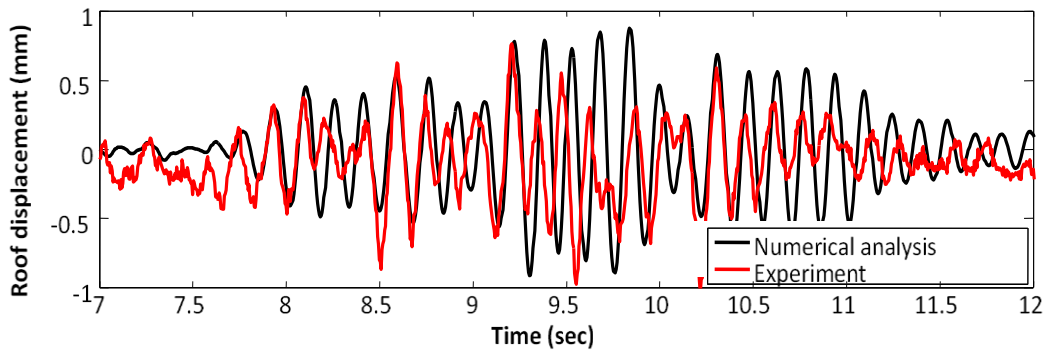


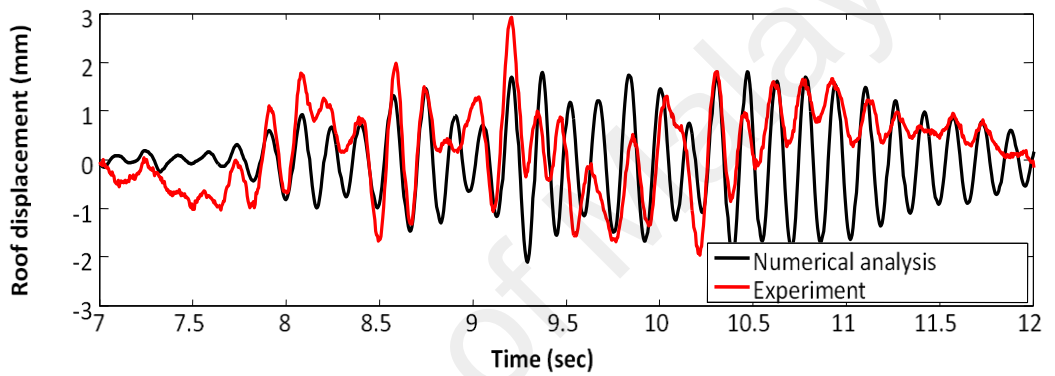
Figure 5.9: Roof acceleration time histories of the infilled system: (a) 0.06g (b) 0.12g

(c) 0.34g.

(a)



(b)



(c)

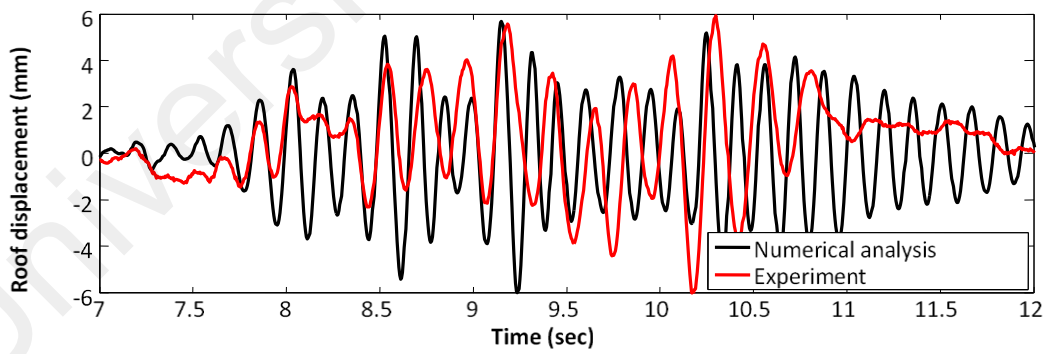


Figure 5.10: Roof displacement time histories of the infilled system: (a) 0.06g (b) 0.12g

(c) 0.34g.

Table 5.3: Error indices, ε .

Base excitation (g)	0.06	0.12	0.20	0.34
ε	-0.15	-0.19	-0.14	-0.24

5.5 Effect of masonry infilled wall

To investigate the effects of infill walls on the RC framed building, the force-deformation behavior of the structure with and without infill walls are discussed. This is represented by the base shear versus the floor displacement relationships. Subsequently, the base shear, stiffness and displacement of the structure with and without infill walls are compared. The effects of ground motions on the RC framed buildings are discussed in terms of story displacement demand, inter-story drift ratio, shear force demand and section moment-curvature response with respect to different soil types. Furthermore, the effects of site soil conditions and the number of storeys on the fragility curves are quantified and discussed.

Figure 5.11 compares the global responses between infilled frame and bare frame of the four-story school building. As shown in Figure 5.11(a), the presence of infill walls increases the base shear of the structure. In the in-plane direction, the base shear at 0.06 g is increased approximately by 80% to 101.43kN in infilled frame from 56.78kN in bare frame. The base shear at 0.20g increased approximately by 100% to 309.43kN in infilled frame from 157.73kN in bare frame. On the other hand, in the out-of-plane direction, the base shear at 0.34g is increased approximately by only 10% to 206.64kN in infilled frame from 183.13kN in bare frame.

In Figure 5.11(b), in the in-plane direction, the infill panels are effective in increasing the stiffness in infilled frame compared to bare frame. The stiffness at 0.06g is increased by nearly 85% to 60.03kN/mm in infilled frame from 32.48kN/mm in bare

frame. The stiffness at 0.34g is increased by 110% to 59.9kN/mm in infilled frame from 29.03kN/mm in bare frame. The infilled frame provides the same stiffness as the bare frame in the out-of-plane direction.

In Figure 5.11(c), in the in-plane direction, the displacement in infilled frame at 0.06g is reduced by 0.07mm, or 4% to 1.71mm, against 1.78mm in bare frame. This is because of the undamaged masonry panels providing additional stiffness in the in-plane direction to the bare frame. However the displacements in infilled frame are unexpectedly increased compared to those in bare frame when the masonry panels suffered some damage. The displacement at 0.20g is increased by 5% from 5.08mm in bare frame to 5.33mm in infilled frame, while the displacement at 0.34g increased by 10% from 5.59mm in bare frame to 6.17mm in infilled frame. Figure 5.12 and Figure 5.13 show the hysteresis curves of the structures with and without infill walls for in-plane and out-of-plane directions for selected ground motion levels.

5.6 Local and global response of RC framed structure

This section discusses the local and global response of an 11-story RC framed building to a single seismic input. Two soil condition were considered (soil types C and D). The global response relates to the response at the overall structural level, e.g. displacements and acceleration at floor levels. Local response relates to the response at the level of the structural component (beams or columns), e.g., inter-story drift ratios, or sub-components (column or beam section), e.g., section curvature.

In this study, the global seismic response of the structure is measured by the floor horizontal displacements relative to the ground at the floor centers of mass in the x-

directions and by the corresponding inter-story drifts. The local seismic response of the structure is quantified by the section curvature at leftmost first story column.

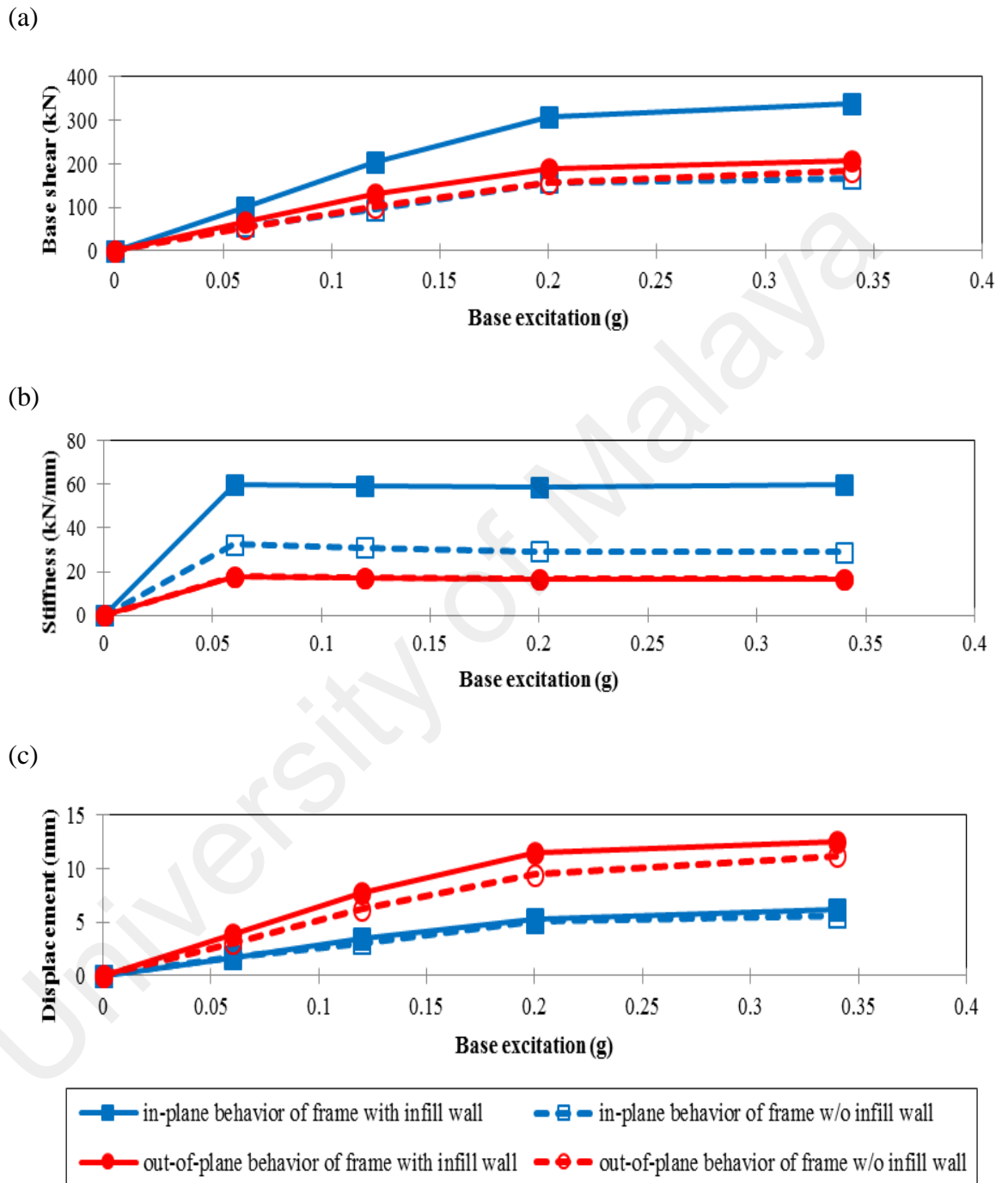


Figure 5.11: Global responses of four-story RC structure: (a) base shear, (b) stiffness and (c) displacement.

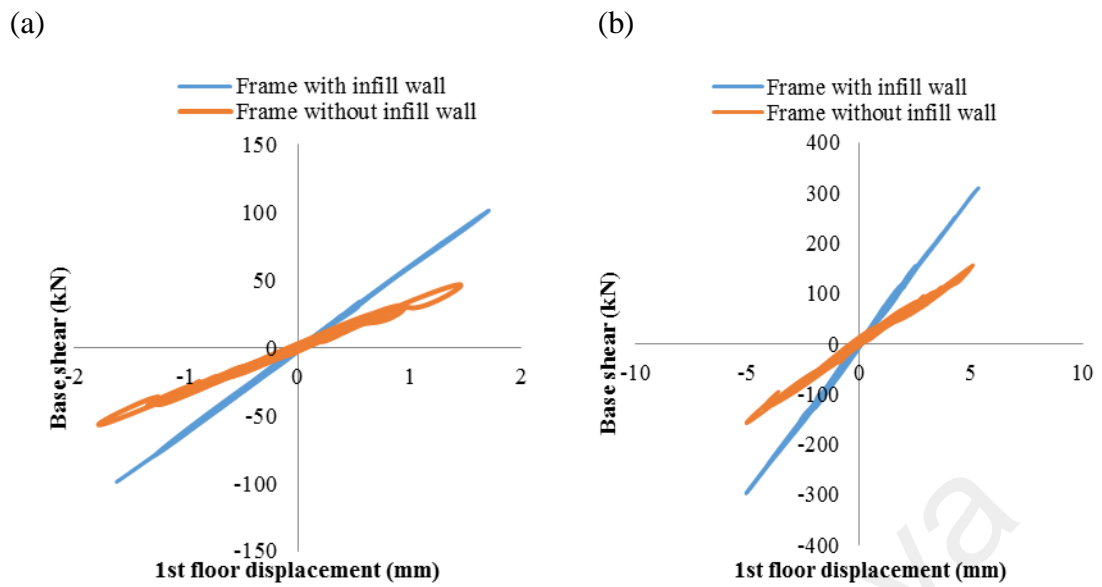


Figure 5.12: Comparison of predicted hysteresis curves of the four-storey school building with and without masonry infill for in-plane direction: (a) 0.06g and (b) 0.20g.

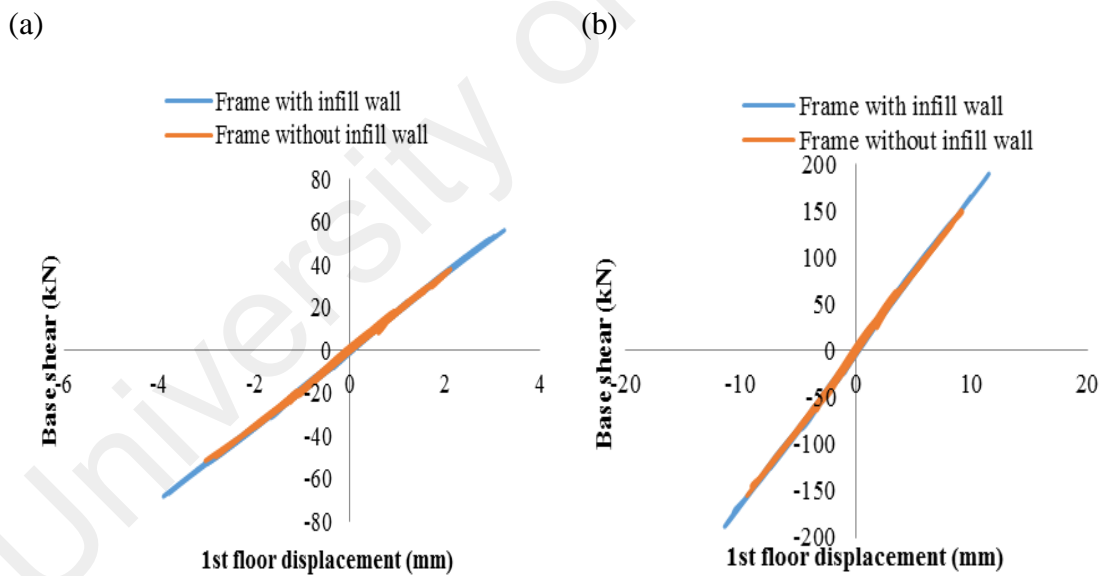


Figure 5.13: Comparison of predicted hysteresis curves of the four-storey school building with and without masonry infill for out-of-plane direction: (a) 0.06g and (b) 0.20g.

The global and local seismic response of the structure subjected to individual ground motion record, Chi-chi NS, Chi-chi EW, Northern California NS and Landers EW are shown in Figure 5.14 to Figure 5.19. As seen in Figure 5.14 the peak roof displacement of the structure at soil type D is slightly higher than at soil type C. At ground motion of Chi-chi NS, the peak roof displacement of the structure is increased approximately by 3% to 90cm at soil type D from 87cm at soil type C. At ground motion of Landers NS, the peak roof displacement of the structure is increased approximately by 5% to 167cm at soil type D from 157cm at soil type C. However, the peak roof displacements are very similar for both ground motions of Chi-chi EW and Northern California EW. Figure 5.15 shows the displacement time histories of the structure for the selected records.

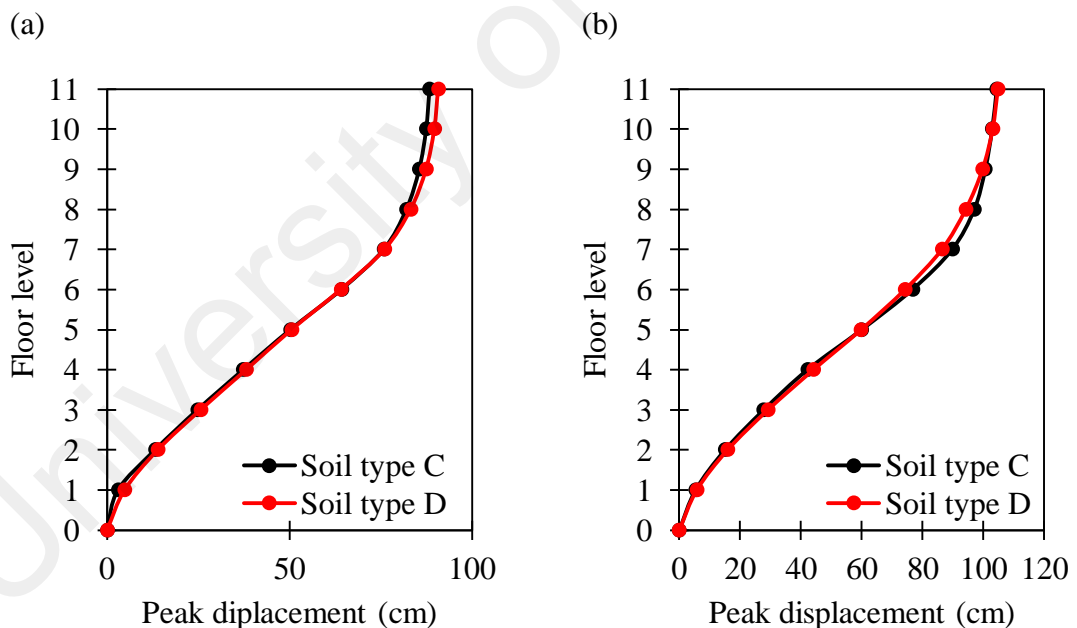
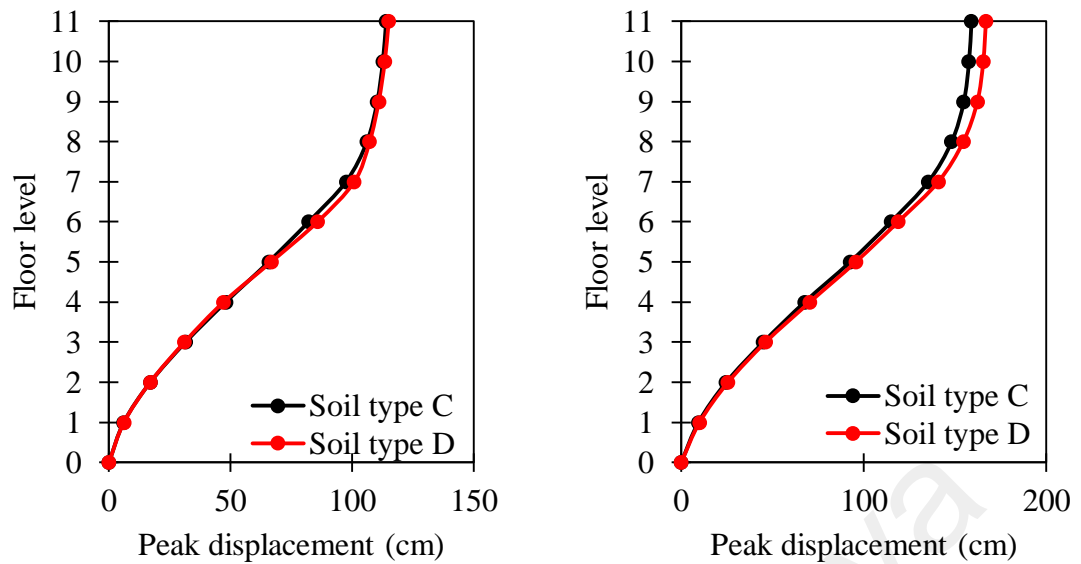


Figure 5.14: Comparison of peak lateral displacement for 11-story RC building at soil types C and D: (a) Chi-chi NS, (b) Chi-chi EW, (c) Northern California EW and (d) Landers NS



'Figure 5.14, continued'

In this study, the damage of the structure is measured in terms of inter-story drift ratio. Therefore, it is important to study the distribution of inter-story drift ratio of the structure. The inter-story drift ratio profiles for the four ground motion records and the two soil types (C and D) for 11-story RC building are provided in Figure 5.16. It is observed that the inter-story drift ratio of the structure at soil type D is greater than at soil type C. This observation is more pronounced especially at higher floor level. The increase in the drift ratio ranges from 1.8% to 44% depending on the floor level and the ground motion. It is also found that the inter-story drift ratio is gradually increased from the ground floor to sixth floor level and then decreased.

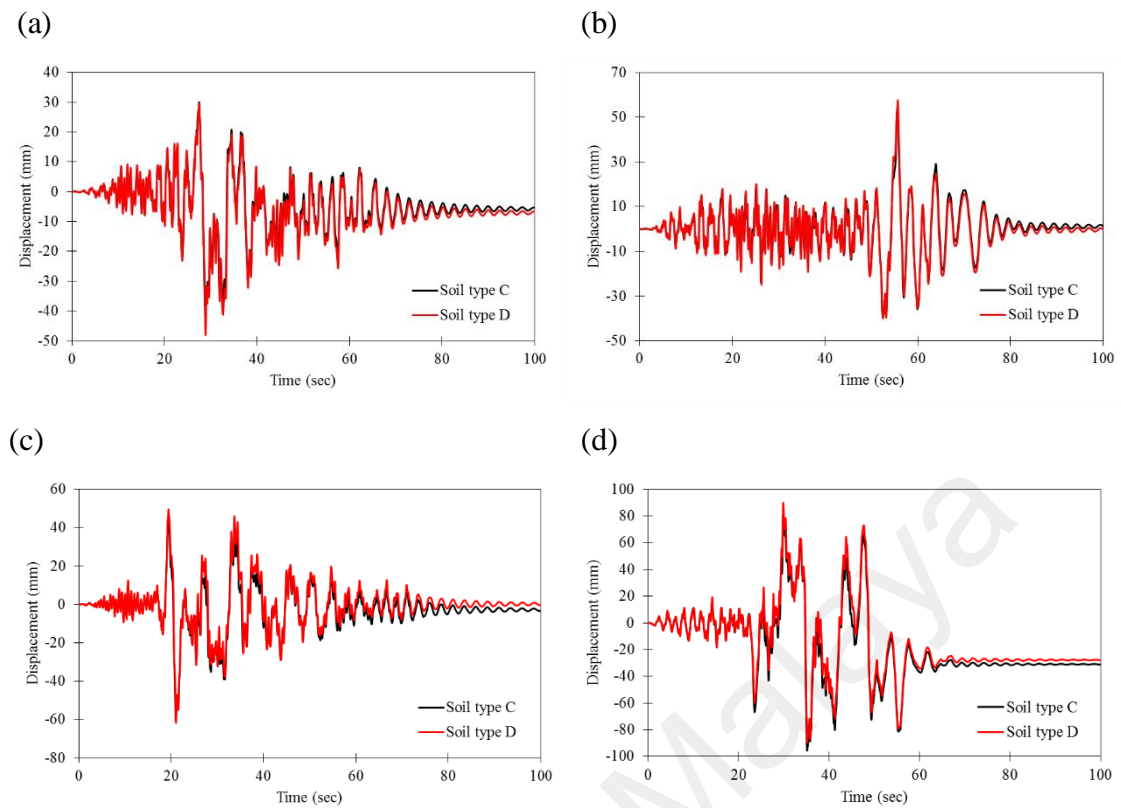


Figure 5.15: Comparison of displacement time history for 11-story RC building at soil types C and D: (a) Chi-chi NS, (b) Chi-chi EW, (c) Northern California EW and (d) Landers NS.

Moment-curvature analysis determines the load-deformation behavior of a concrete section. For computing the moment-curvature of each section it is assumed that concrete stress-strain relationship follows the Kent and Park (1971) curve for an unconfined section and the strain distribution varies linearly with the depth of the section. The steel behavior is modeled using the Menegotto and Pinto (1973) model. Figure 5.17 shows the idealized stress strain curves for concrete and steel rebars.

The moment-curvature curves were obtained by considering equilibrium of the normal stresses on the cross section for increasing values of the extreme fiber concrete strain using nonlinear material stress-strain relationships. Figure 5.18 illustrates the variation of strain and stress through the depth of the section..

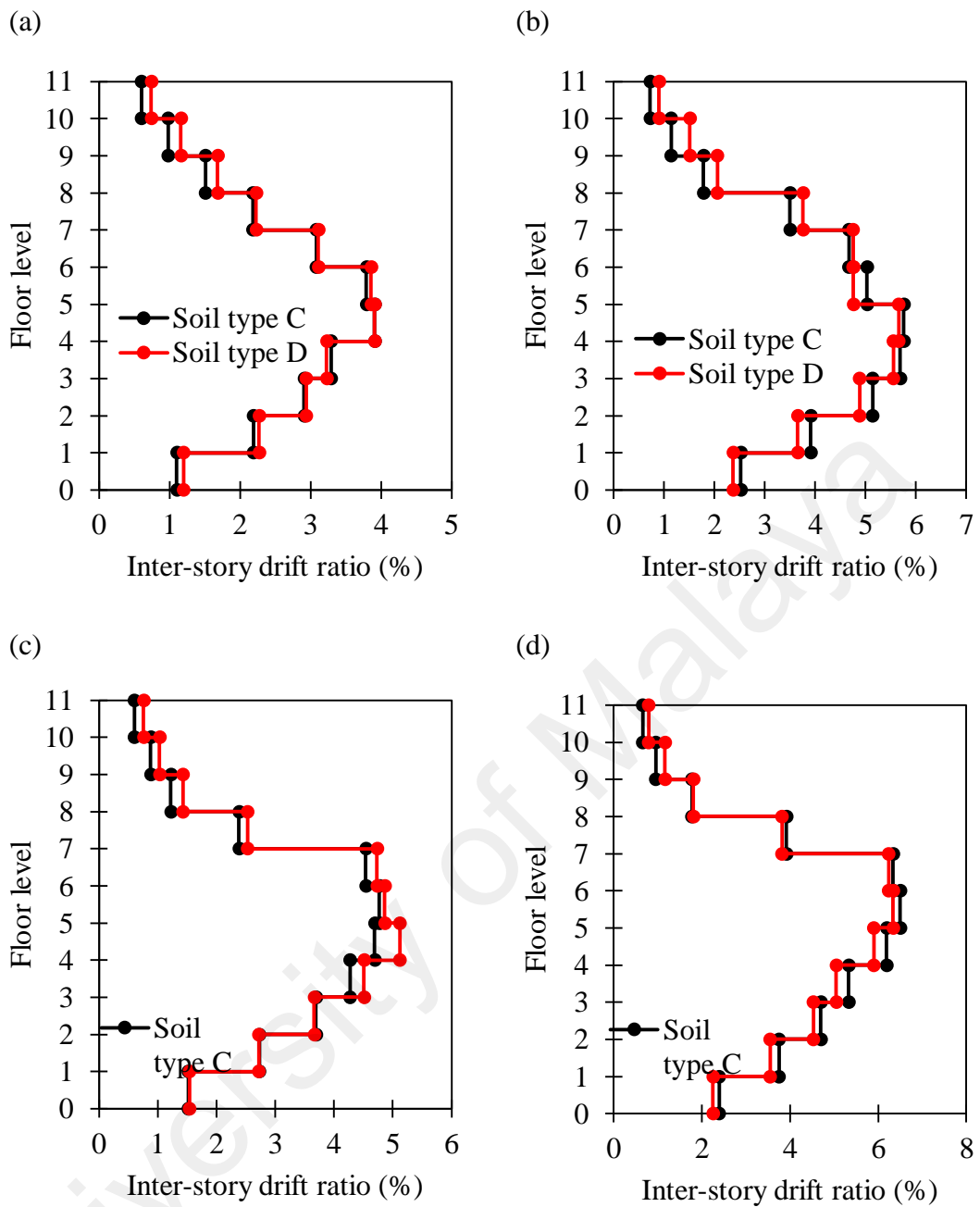


Figure 5.16: Comparison of maximum interstory drift ratio for 11-story RC building at soil type C and D: (a) Chi-chi NS, (b) Chi-chi EW, (c) Northern California EW and (d)

Landers NS.

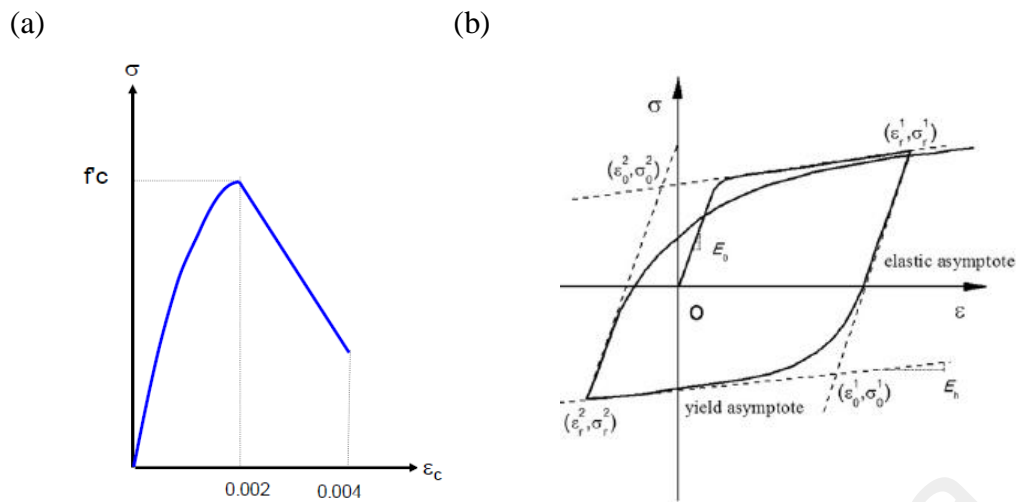


Figure 5.17: Assumed stress strain curves for (a) Kent and Park model for unconfined concrete sections and (b) Menegotto and Pinto model for steel rebars.

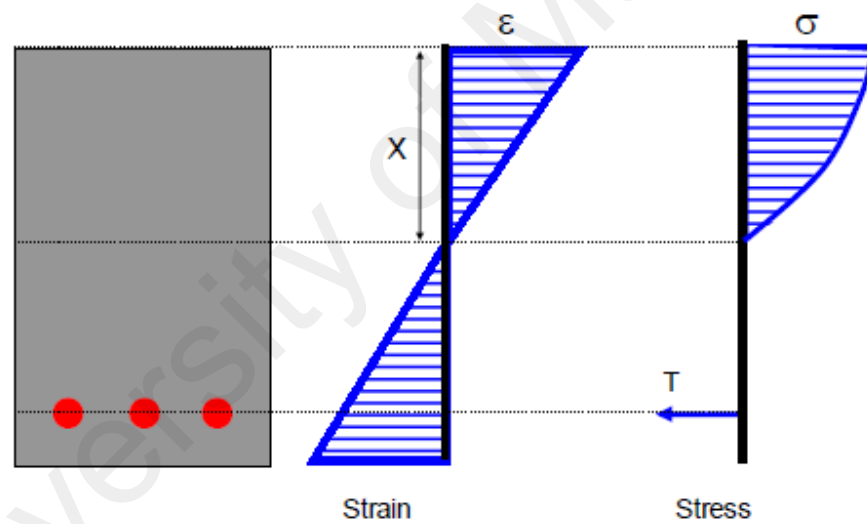


Figure 5.18: Strain and stress distribution through the depth of section.

It is concluded that the peak displacement and inter-story drift ratio of the structure increased from soil type C to soil type D. The section moment-curvature response of the column would move towards the right for soil type D.

CHAPTER 6: SEISMIC FRAGILITY ANALYSIS

6.1 Introduction

Fragility curve is defined as a probability of a structure reaching or exceeding a specified limit state under a given earthquake intensity as shown in Figure 6.1. The shaded area represents a failure domain defined from specific criteria, where a damage measure (some refer to Engineering Demand Parameter, EDP), D , exceeds a specific threshold, d_i . Under a given earthquake intensity $PHGA$, $P[D \geq d_i | PHGA]$ is the probability of the structural response exceeding the i^{th} limit state expressed as a threshold, d_i , and generally increases as the earthquake intensity level increases.

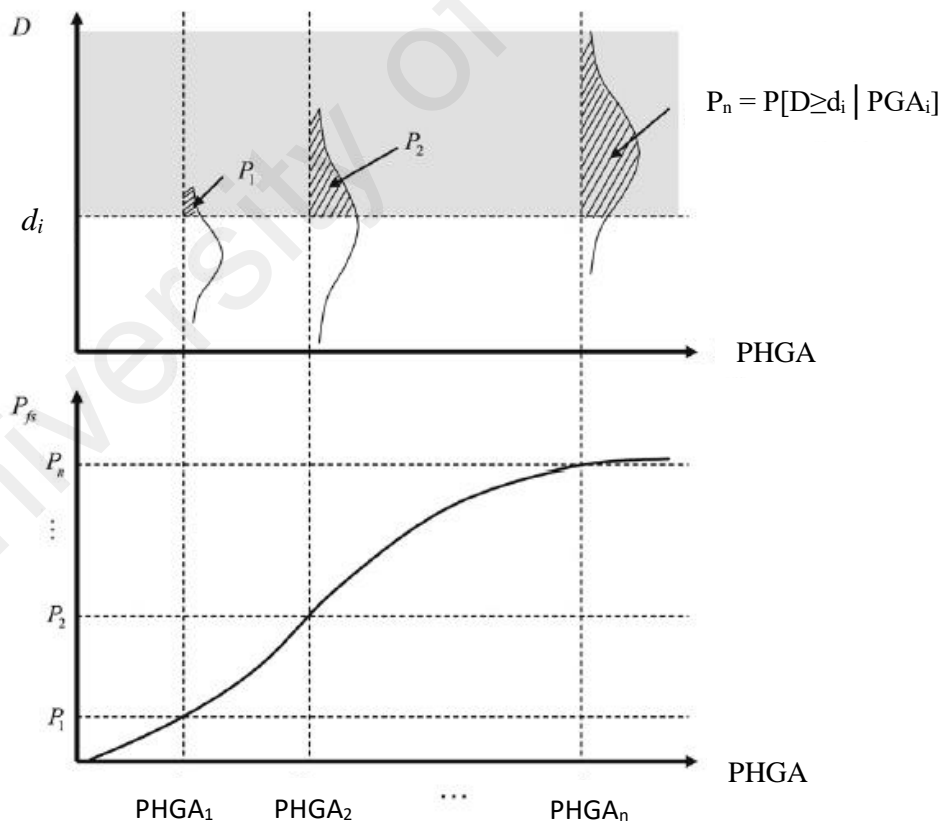


Figure 6.1: Concept of fragility curve (Park et al., 2009)

This probability can be calculated if the probability distribution of the structural damage under a given earthquake level is obtained by accounting for three primary sources of uncertainty, namely the definition of damage states, the response and resistance (capacity) of the element and the earthquake input motion (demand). Consequently, estimation of the probability distribution of the structural damage for different levels of earthquake yields fragility curves.

In this study, the fragility curves of the structures considered are calculated as follows:

$$P[D \geq d_i | PGA] = P[X \geq x_i | PHGA] = 1 - \Phi \left[\frac{\ln(x_i) - \alpha}{\beta} \right] \quad (6-1)$$

$$\alpha = \ln \mu - \frac{1}{2} \beta^2 \quad (6-2)$$

$$\beta = \sqrt{\ln \left[1 + \left(\frac{\sigma}{\mu} \right)^2 \right]} \quad (6-3)$$

where $\Phi(\cdot)$ is the standard normal cumulative distribution function and x_i is the threshold value for d_i (i =slight, moderate, extensive and complete damage). The parameters α and β as defined in Eqs. 6-2 and 6-3 are dependent on the PHGA level. The variables μ and σ are respectively the mean and standard deviation of the seismic demand values in each PHGA level.

As is common practice, the fragility curves are also fitted to the lognormal cumulative distribution functions (lognormal CDF). In this way, the fragility curves is represented with only two parameters, as follows:

$$F_A(a) = \int_0^a \frac{1}{\sqrt{2\pi\xi_A} a} \exp\left[-\frac{1}{2}\left(\frac{\ln a - \ln m_A}{\xi_A}\right)^2\right] da \quad (6-4)$$

where A is the random variable of the PHGA, m_A is the median of A , and ξ_A is the logarithmic standard deviation of A . Eq. 6-4 is related to the standard normal cumulative distribution function with an argument Z , as follows:

$$F_A(a) = \Phi[Z] \quad (6-5)$$

where Z is the standard normal variable, which is defined as $[\ln(a) - \ln(m_A)] / \xi_A$. On the fragility curve, for the fragility probability $F_A(a)$ at a PHGA level of a , the associated normal variable is computed as:

$$Z = \Phi^{-1}[F_A(a)] \quad (6-6)$$

where $\Phi^{-1}(\cdot)$ is the inverse function of the standard normal cumulative distribution. According to the definition of a standard normal variable, for a fragility curve with a lognormal distribution, the relationship of Z vs. $\ln(a)$ is linear. The intercept and slope of the linear relation will be $\ln(m_A)$ and ξ_A , respectively.

Uncertainties associated with the definition of damage states and the response and resistance of the element are assumed to be determinate in this study. However, the last source of uncertainty, associated with seismic demand, is described by the standard deviation of the response that have been calculated for the different input motions at each level of PHGA.

6.2 Damage measure

Many different damage measures for buildings subjected to earthquake loadings have been discussed in the literature. Some used a displacement-based measure such as a maximum roof drift ratio to quantify damage. Some utilized energy-based criteria to relate the amount of hysteretic energy to the level of damage and some combined the two parts. Some others proposed the use of the repair cost ratio, i.e. the ratio between the cost of repair and reinstatement of the structure to the cost of replacing the structure. However, the evaluation of damage in terms of repair cost needs to take into account certain economic factors, i.e., where construction costs vary from place to place and also vary from time to time. Alternatively, FEMA (2003) proposed maximum inter-story drift ratio to assess building performance and levels of damage to structural components.

Considering the purpose of this study, the maximum inter-story drift ratio is used. The inter-story drift is computed as the relative lateral displacement between floors expressed as a percent of the story height at that floor. This damage measure can also be computed directly from the nonlinear time history analysis based on OpenSees without increasing computational time.

6.3 Performance levels

For performance levels the maximum drift limits for the reference buildings are defined based on HAZUS-MH MR4 (FEMA, 2003). In HAZUS-MH MR4, four performance levels are defined including slight damage, moderate damage, extensive damage and complete damage. In particular for reinforced concrete moment resisting frames, the slight damage implies flexural or shear type hairline cracks in some beams and columns near joints or within joints. The moderate damage implies hairline cracks in

most beams and columns, and some of the frame elements, especially in ductile frames, is expected to reach yield capacity indicated by larger flexural cracks and some concrete spalling. The extensive damage shows frame elements reaching their ultimate capacity indicated in ductile frames by large flexural cracks, spalled concrete and buckled main reinforcement. On the other hand, nonductile frame elements may suffer shear failures or bond failures at reinforcement splices, or broken ties or buckled main reinforcement in columns which may result in partial collapse. The complete damage indicates the structure is collapsed or in imminent danger of collapse due to brittle failure of nonductile frame elements or loss of frame stability.

For concrete frame buildings with unreinforced masonry infill walls, the slight damage implies diagonal or sometimes horizontal hairline cracks on most infill walls, and frame infill interface crack. The moderate damage exhibit larger diagonal or horizontal cracks on most infill wall surfaces. Some walls may exhibit crushing of brick around beam-column joints and concrete beams or columns may show diagonal shear cracks. The extensive damage for the infilled frames implies large cracks on most infill walls. Some bricks may dislodge and fall. Some infill walls may bulge out-of-plane. Few walls may fall partially or fully and few concrete columns or beams may fail in shear resulting in partial collapse. Structure may also exhibit permanent lateral deformation. The complete damage shows the structure is collapsed or is in imminent danger of collapse due to a combination of total failure of the infill walls and nonductile failure of concrete beams and columns.

The threshold values of the maximum drift ratio corresponding to the limit states are tabulated in Table 6.1 for the reinforced concrete moment resisting frames, and Table 6.2 for the concrete frame buildings with unreinforced masonry infill walls. The fragility curves are then developed accordingly.

Table 6.1: The maximum drift ratio for RC moment resisting frames (FEMA, 2003).

Damage state	Drift ratio % (Pre-code)		
	Low-rise (1-3 stories)	Mid-rise (4-7 stories)	High-rise (≥ 8 stories)
Slight	0.40	0.27	0.20
Moderate	0.64	0.43	0.32
Extensive	1.60	1.07	0.80
Complete	4.00	2.67	2.00

Table 6.2: The maximum drift ratio for infilled RC frames (FEMA, 2003).

Damage state	Drift ratio % (Pre-code)		
	Low-rise (1-3 stories)	Mid-rise (4-7 stories)	High-rise (≥ 8 stories)
Slight	0.24	0.16	0.12
Moderate	0.48	0.32	0.24
Extensive	1.20	0.80	0.60
Complete	2.80	1.87	1.40

6.4 Construction of fragility curves

Fragility curves are developed for the limit states defined in FEMA (2003) as discussed in the previous section. Note that the limit states defined for “pre code” RC moment resisting frames with and without infill walls in FEMA (2003) are adopted because the reference structures were designed without considering any seismic loadings. A series of nonlinear time history analysis were performed to evaluate the responses of the structures under different earthquakes. Table 6.3 shows the drift response distribution of the 3-storey RC framed building. These data are used here as a sample of developing fragility curves for the structure.

According to Chiou et al. (2011), the statistical description of the building response would follow a lognormal distribution. The lognormal distribution parameters corresponding to PHGA of 0.18g (the lognormal mean (λ) and the standard deviation (ζ)) are calculated as:

$$\delta = \frac{\sigma}{\mu} = \frac{0.000866}{0.00388} = 0.2233$$

$$\begin{aligned}\zeta &= \ln(1 + \delta^2) = \ln(1 + 0.2233^2) \\ &= 0.04866\end{aligned}$$

$$\begin{aligned}\lambda &= \ln(\mu) - 0.5\zeta^2 = \ln(0.00388) - 0.5(0.04866^2) \\ &= -5.5531\end{aligned}$$

The lognormal distribution parameters for the PHGA range are then listed in Table 6.4. The probability of exceedance of the structure corresponding to slight damage (0.40%), is calculated as

$$P[D \geq 0.004 | PHGA = 0.18g] = 1 - \Phi\left[\frac{\ln(0.004) + 5.5531}{0.04866}\right] = 0.2578$$

The values of probability of exceedance corresponding to the moderate, extensive and complete damage are also calculated in a same manner and they are estimated to be 0 in the 3-storey RC framed building as listed in Table 6.5.

The fragility curves of the structure corresponding to different limit states can then be constructed by plotting the input earthquake level represented in terms of PHGA and the probability of exceeding limit states. An example of the fragility curves for the 3-storey RC framed building is shown in Figure 6.2.

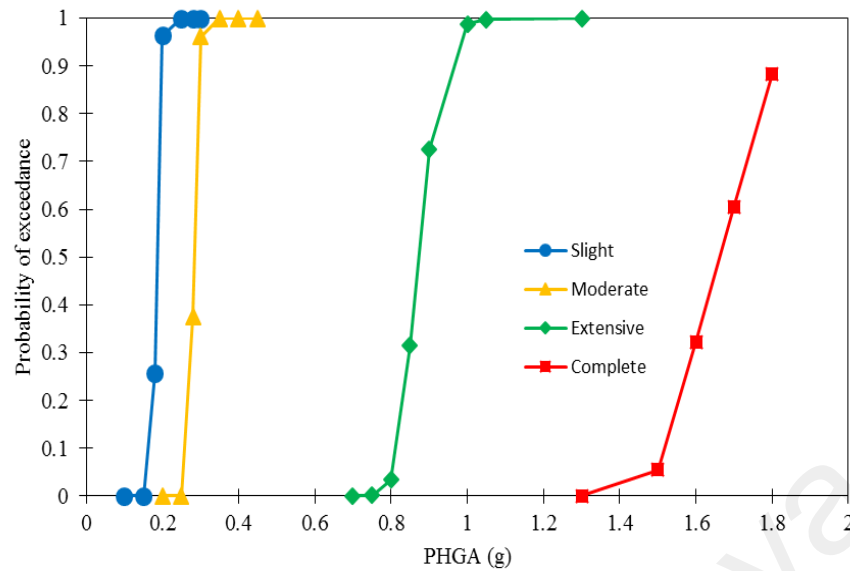


Figure 6.2: Fragility curves of the 3-storey RC framed building.

However, the fragility curves are fitted to the lognormal cumulative distribution functions. In this way, the lognormal parameters are estimated by plotting the calculated values of the probability of exceedance on lognormal probability sheets as shown in Figure 6.3. The lognormal probability plot of maximum drift ratio for the rest of the structures are tabulated in Appendix A. The lognormal parameters, i.e. the lognormal mean (ζ_A) and the standard deviation ($LN(m_A)$) are estimated from the y-intercept and the slope of the fitted line, respectively. Table 6.6 and Table 6.7 summarize the parameters of the fitted lognormal cumulative distribution function.

Finally, the fitted fragility curves for the 3-storey RC framed building are plotted in Figure 6.4 and the corresponding fragility values are tabulated in Appendix B.

Table 6.3: The distribution of the drift ratio of the 3-storey RC framed building under different earthquake inputs at soil type D.

PHGA (g)	0.1	0.15	0.18	0.2	0.25	0.28	0.3	0.35	0.4	0.45	0.5	0.7	0.75	0.8	0.85	0.9	1	1.05	1.3	1.5	1.6	1.7	1.8
Event	Inter-story drift ratio																						
c1	0.0015	0.0023	0.0027	0.003	0.0038	0.0042	0.0045	0.0054	0.0063	0.007	0.0075	0.0104	0.0104	0.0109	0.0117	0.0124	0.0137	0.0145	0.0173	0.0212	0.0241	0.0269	0.0297
c2	0.0022	0.0034	0.0042	0.0047	0.0057	0.0065	0.007	0.0078	0.0083	0.0092	0.0099	0.0129	0.0133	0.0142	0.0149	0.0149	0.0166	0.0168	0.0238	0.0292	0.0353	0.0432	0.0509
i1	0.0017	0.0026	0.0032	0.0035	0.0045	0.0051	0.0056	0.0068	0.0079	0.0089	0.0096	0.0109	0.0116	0.0124	0.0131	0.0136	0.0146	0.0154	0.021	0.025	0.027	0.0313	0.0379
i2	0.0017	0.0027	0.0033	0.0038	0.0052	0.006	0.0064	0.0072	0.0082	0.0096	0.0109	0.0142	0.0148	0.0151	0.0159	0.0163	0.0174	0.019	0.0261	0.0333	0.0371	0.0407	0.0447
u3	0.0021	0.0032	0.0039	0.0044	0.0057	0.0064	0.0068	0.0071	0.008	0.009	0.0097	0.0127	0.0138	0.0146	0.0147	0.0148	0.0158	0.0169	0.023	0.0312	0.0353	0.0399	0.0454
u4	0.0021	0.0032	0.0041	0.0047	0.0062	0.0076	0.0082	0.0088	0.0095	0.0103	0.0107	0.0141	0.0149	0.0159	0.0167	0.0174	0.0186	0.0193	0.0268	0.0332	0.0387	0.0446	0.0511
u9	0.0021	0.0031	0.0038	0.0042	0.0055	0.0061	0.0065	0.0074	0.0081	0.0089	0.0097	0.0122	0.0129	0.0136	0.0143	0.0149	0.0159	0.0162	0.0206	0.0222	0.0261	0.03	0.0335
u10	0.0031	0.0048	0.0058	0.0065	0.0078	0.0084	0.0091	0.0102	0.0111	0.0125	0.0143	0.0206	0.0214	0.0224	0.0237	0.0253	0.029	0.0316	0.0471	0.0664	0.0864	0.0983	0.1046
u11	0.0023	0.0037	0.0045	0.0051	0.0066	0.0073	0.0077	0.0085	0.0093	0.0102	0.0114	0.0146	0.0147	0.0146	0.0152	0.0165	0.0192	0.0202	0.0258	0.0252	0.0274	0.0369	0.0473
u12	0.0017	0.0027	0.0033	0.0038	0.005	0.0057	0.0064	0.008	0.0092	0.0101	0.0106	0.0124	0.0137	0.0151	0.0168	0.0186	0.0212	0.0222	0.0237	0.0291	0.0336	0.0385	0.0473

Table 6.4: The lognormal parameters of the drift ratio for the 3-storey RC framed building at soil type D.

PHGA (g)	0.1	0.15	0.18	0.2	0.25	0.28	0.3	0.35	0.4	0.45	0.5	0.7	0.75	0.8	0.85	0.9	1	1.05	1.3	1.5	1.6	1.7	1.8
σ	0.000455217	0.000708755	0.00086641	0.00097758	0.00111555	0.001223883	0.001301111	0.001290822	0.001271	0.00140479	0.001728	0.002843	0.002925	0.003017	0.003212	0.003589	0.0044	0.004949	0.008114	0.012952	0.018067	0.020271	0.020742
μ	0.00205	0.00317	0.00388	0.00437	0.0056	0.00633	0.00682	0.00772	0.00859	0.00957	0.01043	0.0135	0.01415	0.01488	0.0157	0.01647	0.0182	0.01921	0.02552	0.0316	0.0371	0.04303	0.04924
δ	0.222056915	0.223581948	0.2233016	0.22370299	0.19920477	0.1933464	0.190778686	0.167204962	0.148014	0.14679137	0.165636	0.210587	0.206746	0.202774	0.204594	0.217905	0.241772	0.2576	0.317958	0.409861	0.486992	0.471085	0.421238
ξ	0.048132113	0.048779581	0.04866026	0.04883114	0.03891542	0.036701032	0.035749799	0.027573823	0.021672	0.02131884	0.027066	0.043392	0.041856	0.040295	0.041006	0.04639	0.056809	0.064249	0.096307	0.155281	0.212819	0.200424	0.163344
λ	-6.19107384	-5.75521341	-5.553104	-5.4341845	-5.1857459	-5.06312853	-4.98853483	-4.86432107	-4.75739	-4.64934932	-4.56344	-4.30601	-4.25892	-4.20855	-4.15494	-4.10729	-4.00795	-3.95439	-3.67293	-3.46665	-3.31678	-3.16594	-3.02439

Table 6.5: The values of probability of exceedance corresponding to slight, moderate, extensive and complete damage of the 3-storey RC framed building at soil type D.

PHGA (g)	0.1	0.15	0.18	0.2	0.25	0.28	0.3	0.35	0.4	0.45	0.5	0.7	0.75	0.8	0.85	0.9	1	1.05	1.3	1.5	1.6	1.7	1.8
Slight damage	0	8.25572E-07	0.25775352	0.96305634	1	1	1	1	1	1	1	1	1	1	1	1	1	1	1	1	1	1	1
Moderate damage	0	0	0	2.3315E-15	0.00027948	0.375239276	0.960802761	1	1	1	1	1	1	1	1	1	1	1	1	1	1	1	1
Extensive damage	0	0	0	0	0	0	0	0	0	0	0	4.12E-05	0.001555	0.034292	0.314871	0.726049	0.987436	0.997551	0.999999	0.999992	0.99994	0.999999	1
Complete damage	0	0	0	0	0	0	0	0	0	0	0	0	0	0	0	0	0	0	1.21E-06	0.055281	0.322739	0.604151	0.883106

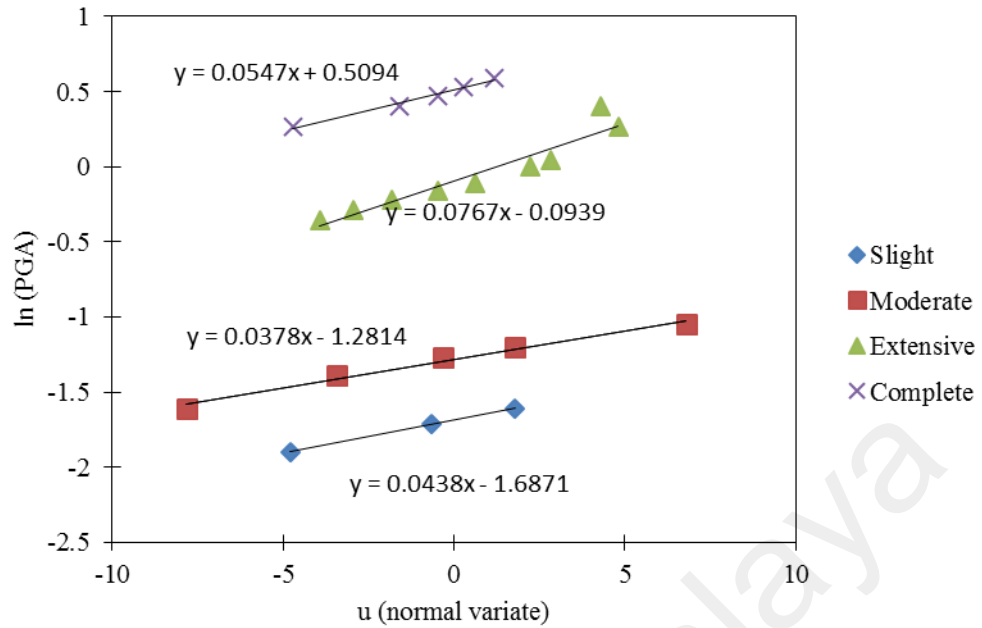


Figure 6.3: Lognormal probability plot of maximum drift ratio for 3-storey RC framed building.

Table 6.6: Lognormal parameters for the fitted fragility curves at soil type C except 4-storey RC school building at soil type D.

	3-storey		4-storey		7-storey		11-storey	
	ζ_A	LN(m_A)	ζ_A	LN(m_A)	ζ_A	LN(m_A)	ζ_A	LN(m_A)
Slight damage	0.0389	-1.4349	0.0234	-1.7492	0.0657	-2.4805	0.0587	-3.208
Moderate damage	0.0411	-0.9934	0.0291	-1.108	0.0701	-1.9798	0.064	-2.7395
Extensive damage	0.0479	0.1135	0.0435	-0.3422	0.069	-0.8845	0.0658	-1.8413
Complete damage	0.0332	1.0296	0.0542	0.3549	0.0764	-0.0891	0.0662	-0.8824

Table 6.7: Lognormal parameters for the fitted fragility curves at soil type D except 4-storey RC school building at soil type E.

	3-storey		4-storey		7-storey		11-storey	
	ζ_A	LN(m_A)	ζ_A	LN(m_A)	ζ_A	LN(m_A)	ζ_A	LN(m_A)
Slight damage	0.0439	-1.6871	0.2391	-2.0737	0.0655	-2.5291	0.0591	-3.2321
Moderate damage	0.0378	-1.2814	0.2261	-1.3272	0.0641	-2.0826	0.064	-2.7596
Extensive damage	0.0767	-0.0939	0.2228	-0.4367	0.0807	-0.9054	0.0634	-1.8582
Complete damage	0.0552	0.5111	0.192	0.2261	0.1021	-0.1854	0.0644	-0.8974

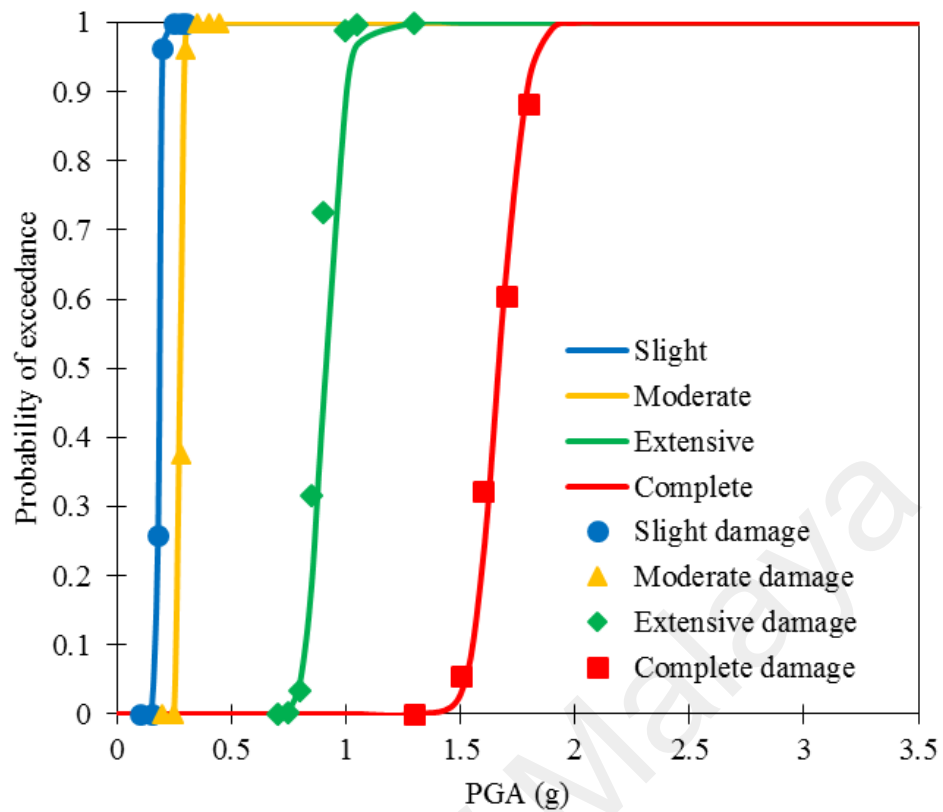


Figure 6.4: Fitted fragility curves of the 3-storey RC framed building.

6.5 Sensitivity analysis

The sensitivity analysis of site conditions and number of story of reinforced concrete framed building was discussed in this section. Three-, seven- and eleven- story building were considered. The fragility curves were constructed in terms of slight, moderate, extensive and complete damage.

6.5.1 Sensitivity to site conditions

Argyroudis et al. (2013) studied the effects of soil conditions underneath bridge abutments with retaining cantilever wall, based on fragility curves. Two different soil

types C and D were considered and the fragility curves were expressed in terms of minor, moderate, extensive damage, based on free field PGA. They concluded that for most of the damage states the fragility of the structure in soil type D is higher than in soil type C.

Goda and Yoshikawa (2013) investigated the effects of site conditions on seismic fragility curves. Two soil conditions were studied with respect to soft and firm soil conditions. They observed that the building portfolio on firm soil has significantly less earthquake risk compared with that on soft soil. This result highlights the importance of classifying local site conditions. The differences between the seismic fragility curves for soft and firm site conditions are contributed by two factors: one is reduced seismic hazard for firm sites and the other is reduced seismic fragility for firm sites. The influence of reduced seismic fragility on overall reduction of seismic loss increases with the probability level. Furthermore, Heidary-Torkamani et al. (2014) evaluated the effect of uncertainties associated with soil parameters on the seismic response of a wharf structure with respect to normalized residual horizontal displacement (NRHD). They found that uncertainties associated with the porosity of loose sand contribute most to the variance of NRHD, while in the case of differential settlement, the friction angle of loose sand contributes most to the variance. Therefore they concluded that for designing similar structure, soil characteristics and friction angle and porosity of loose sand in particular, should be properly be studied.

In this study, the effect of site soil condition on fragility curves for RC framed buildings is investigated. Figure 6.5 shows the fragility curves for 3-, 7- and 11-storey RC framed buildings at the study sites. It was observed that site soil conditions have a significant impact on the seismic performance of the 3-storey RC framed building. However, this effect becomes less critical as the building height increases. The difference of the probability of exceeding the complete damage state obtained for soil type C and D

may reduce approximately from 100% for the 3-storey RC framed building to 4% for the 11-storey RC framed building.

The probability of exceeding slight, moderate and extensive damage for soil type C and D may not change for 7- and 11-storey RC framed buildings. For the 3-storey RC framed building, the fragility at soil type D is anticipated to be higher than that at soil type C. This may be due to the fact that the seismic hazard is reduced for soil type C. For the same soil type, these findings were consistent with those of Goda and Yoshikawa (2013) for wood-frame houses, and those of Argyroudis et al. (2013) for bridge abutments.

Figure 6.6 compares the fragility for 4-storey infilled RC frames at soil type D and E. It was found that for most of the damage states the fragility of the structure in soil type E is higher than in soil type D. The firm soil is anticipated to be significantly less vulnerable than soft soil, indicating the importance of classifying local site conditions e.g. seismic micro zonation map.

6.5.2 Sensitivity to number of storey

Kircil and Polat (2006) showed that the fragility curve parameters, mean and standard deviation, change with respect to the number of stories of the building. The fragility curves were constructed for 3, 5 and 7 story RC framed buildings. The fragility curves for yielding and collapse limit states were defined based on elastic pseudo spectral acceleration, peak ground acceleration and elastic spectral displacement.

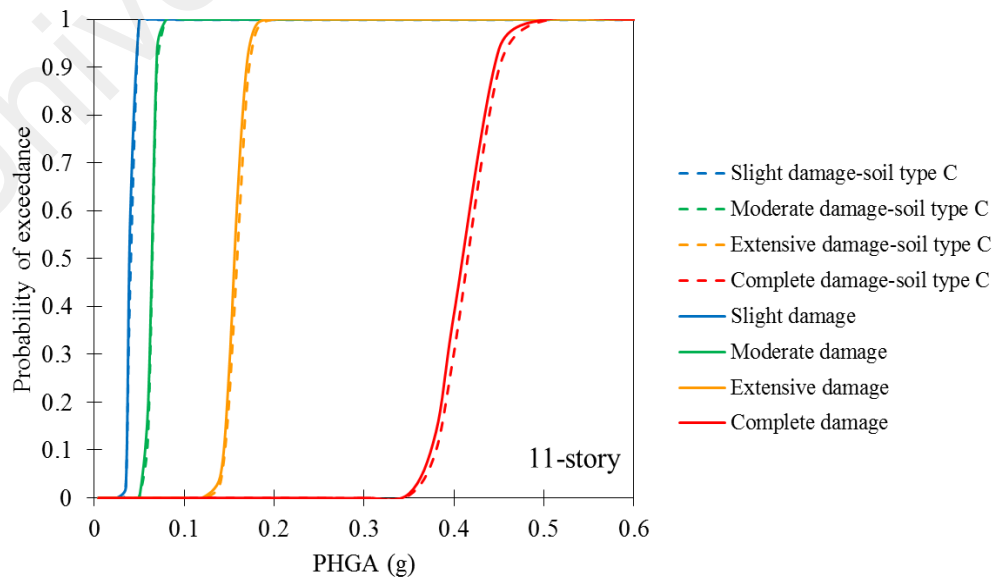
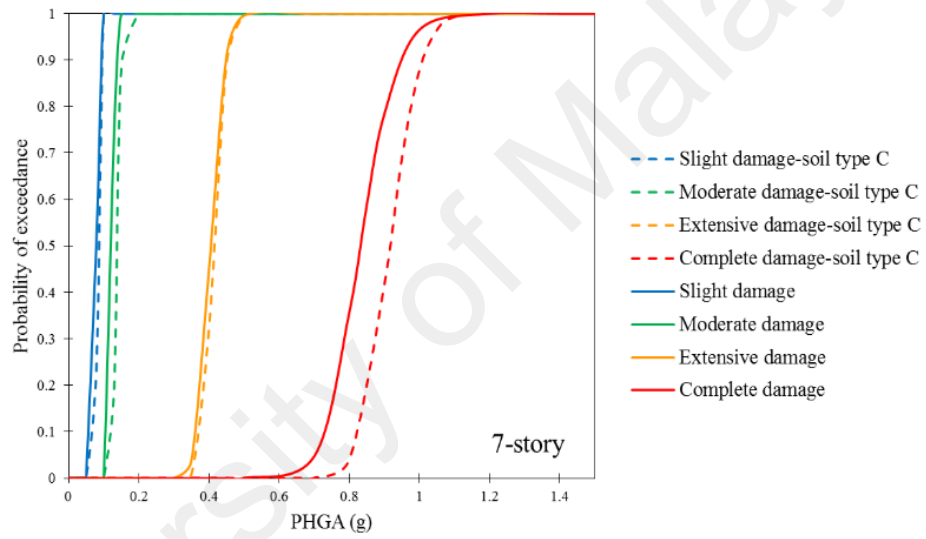
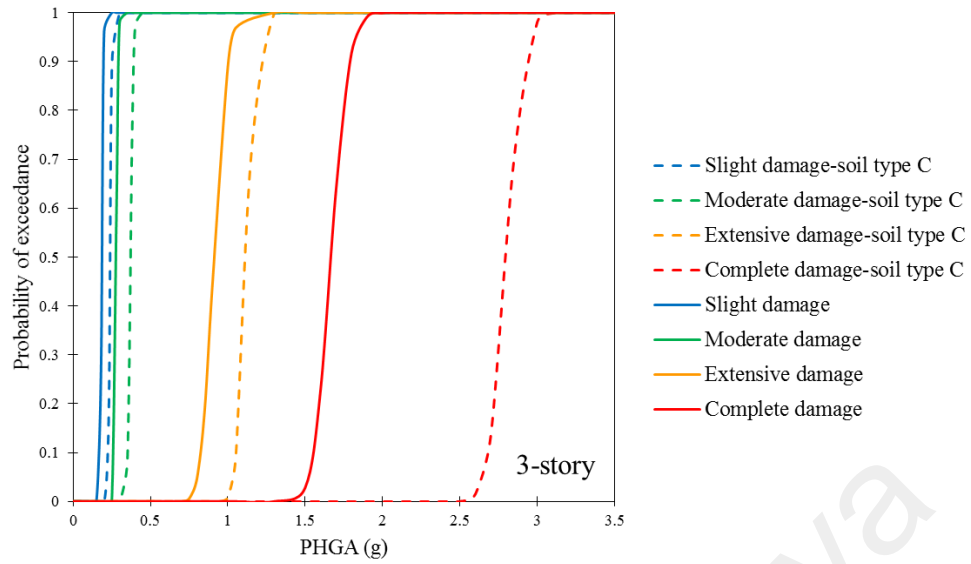


Figure 6.5: Seismic fragility curves for the RC framed buildings at the study sites.

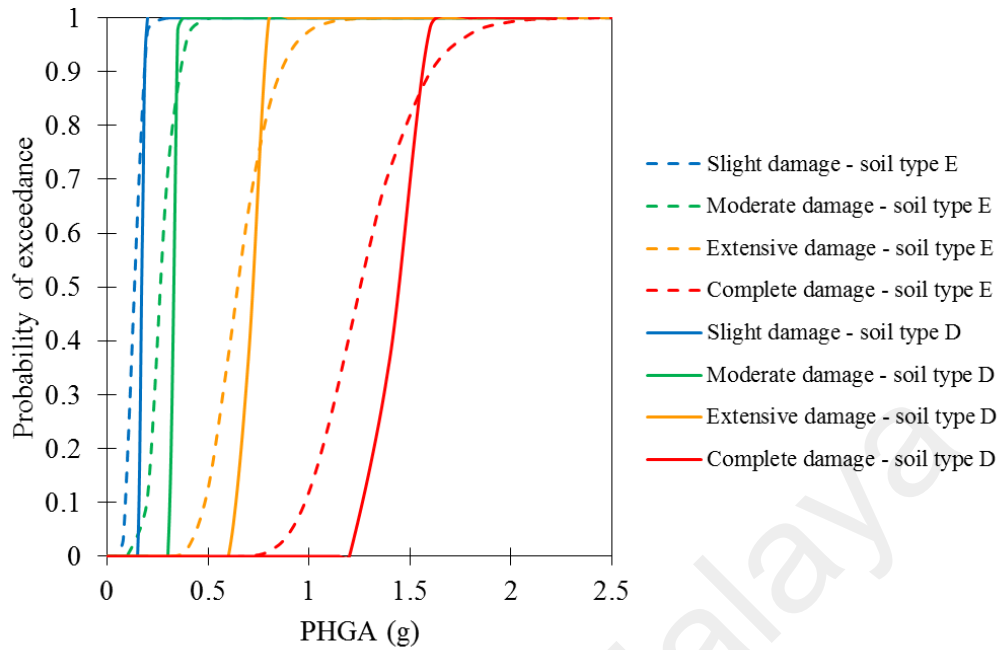


Figure 6.6: Seismic fragility curves for the 4-story infilled RC framed building at the study sites.

Bilgin (2013) investigated the effect of number of stories on the fragility curves based on 3-, 4- and 5-storey template buildings. The fragility curves represent the probability of exceeding the immediate occupancy (slight damage), life safety (moderate damage) and collapse prevention (severe damage) limit states for moment resisting frame and dual system structures to compare damage probabilities. It was observed that the number of stories has a significant effect on the probability of exceeding moderate and severe damage limit states. Moreover, the moderate and severe damage fragility patterns of 4- and 5-storey buildings groups follow a closer trend to each other.

In this study, the effect of number of storeys on the fragility curves is investigated based on damage probability calculation for each building height. 3-, 7- and 11-story of an RC framed building. Figure 6.7 compares the fragility curves in terms of PHGA for the RC framed buildings at the study sites. The number of storeys has a significant impact

on the seismic performance of the RC framed buildings. In particular, at the study sites, the 11-storey RC framed building is much more vulnerable than the other RC framed buildings. For soil type C and a 3-storey RC framed building, the probability of attaining or exceeding a state of complete (100%) damage is expected to be found at 3.2g, whereas for the 7-storey RC framed building it is expected at 1.2g and for the 11-storey RC framed building it is expected to be found at 0.6g. For soil type D and a 3-storey RC framed building, the probability of attaining or exceeding a state of complete (100%) damage is expected to be found at 2.0g, whereas for the 7-storey RC framed building it is expected at 1.2g and for the 11-storey RC framed building it is expected at 0.6g. These findings are consistent with those of Kircil and Polat (2006) and Bilgin (2013).

6.7 Prediction of degree of structural damage based on fragility curves

Given the PHGA from an appropriate seismic hazard analysis or from code prescriptions and local soil conditions, the expected states of damage to the buildings were determined using the proposed fragility curves. The Engineering Seismology and Earthquake Engineering Research (ESEER) has demonstrated that the PHGA at MCE at Kuala Lumpur is approximately 0.2g. Given the MCE event, the 3-storey RC framed building is expected to suffer slight damage with a probability of 96% with soil type D, and is expected to suffer no damage with soil type C. On the other hand, the 7-storey RC framed building is likely to suffer moderate damage with a probability of 100% with soil type C and D, and the 11-storey RC framed building is expected to meet extensive damage with a probability of 100% with soil type C and D.

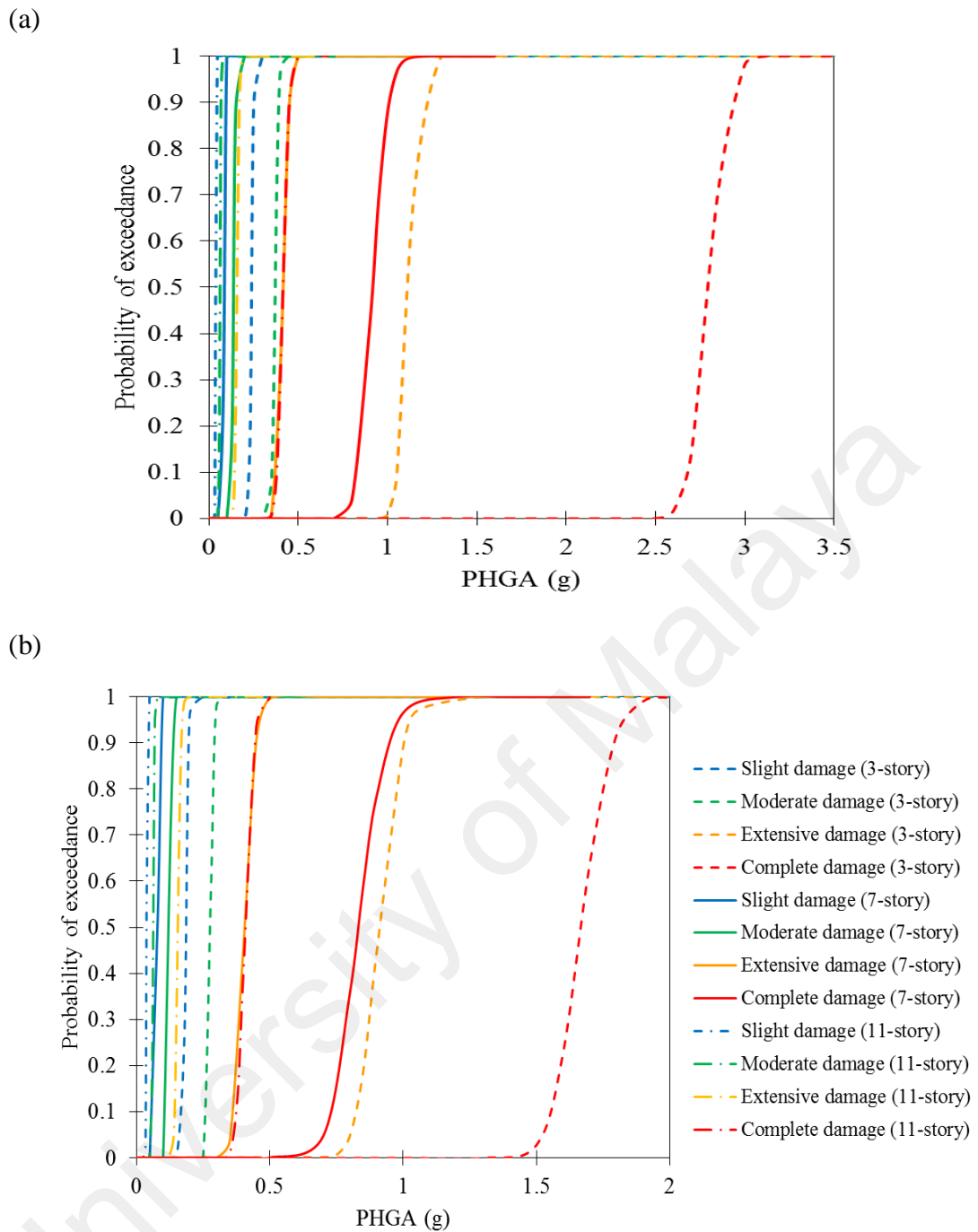


Figure 6.7: Seismic fragility curves for RC framed buildings at (a) soil type C, and (b) soil type D.

The 4-storey infilled RC frames is expected to suffer slight damage with a probability of around 100% with soil type D and E. Table 6.8 summarizes the probabilities of exceeding the damage limit states at the MCE of the RC framed buildings

at soil type C and D. Table 6.9 summarizes the chances of exceeding the damage states at MCE of the infilled RC frames at soil type D and E.

Table 6.8: The probability of exceeding given damage limit states of the buildings for two site soil conditions in Kuala Lumpur at MCE.

Soil type	Slight damage		Moderate damage		Extensive damage		Complete damage	
	C	D	C	D	C	D	C	D
3-storey RC framed building	0	0.96	0	0	0	0	0	0
7-storey RC framed building	1.00	1.00	1.00	1.00	0	0	0	0
11-storey RC framed building	1.00	1.00	1.00	1.00	1.00	1.00	0	0

Table 6.9: The probability of exceeding given damage limit states of the infilled RC frames for two site soil conditions in Kuala Lumpur at MCE.

Soil type	Slight damage		Moderate damage		Extensive damage		Complete damage	
	D	E	D	E	D	E	D	E
4-storey infilled RC frames	1.00	0.97	0	0.10	0	0	0	0

CHAPTER 7: CONCLUSIONS

7.1 Conclusion

Seismic analyses of standard RC Malaysian buildings were investigated in this study. The structural drawings of the standard were collected from Malaysian Public Works Department. Earthquake ground motions were defined based on one-dimensional equivalent linear ground response analysis. Twenty acceleration time histories were selected based on the earthquake magnitudes and distances that predominantly contribute to the seismic hazard at the sites. These time histories were applied to outcrop conditions at the base of the soil models. Finite element models were developed based on force-based, fiber beam-column element. Nonlinear dynamic time history was conducted to evaluate the response of the analytical models. The analysis model and environment were verified through comparison with shake table experiments as discussed in Chapter 4.3.

To evaluate the expected damage of the models, the drift limits proposed by FEMA (2003) were used. Damage of the structures was quantified by a damage index based on the inter-story drift ratio of the structure. The damage states considered were: Slight, Moderate, Extensive and Complete damage. Fragility curves were fitted to the lognormal cumulative distribution function expressed in the form of two parameters (log-median and log-standard deviation). The fragility curves were developed as a function of PHGA. The structural properties were assumed to be determinate while uncertainties associated with ground motions were taken into account through the record-to-record variability. A total of four sets of fragility curves were developed in this study.

A set of twenty target acceleration time histories at the ground surface had been generated for soil type C, D and E. These ground motions were computed using Shake91, one-dimensional equivalent linear analysis. It is concluded that the ground motions at the

surface were modified for different soil types. The peak ground accelerations for soil type D are generally higher than those for soil type C.

The verification of the four-story RC framed building with masonry infill wall was done through comparison of response history analysis with shake table test. It was undertaken in terms of global acceleration and displacement time histories. The finite element model showed a good agreement with respect to the experimental model with maximum errors approximations between 10-25%.

The inter-story drift response of the 11-story RC framed building had been examined based on nonlinear dynamic time history analyses. Two different soil condition, soil type C and D were considered. It showed that the inter-story drift ratio of the structure at soil type D is generally higher than that at soil type C. The same results were obtained even for different ground motions characteristics.

The presence of masonry infill walls in RC frame affects the global response of the structure in terms of base shear, stiffness and displacement. The base shear of the structure with infill walls was increased significantly in both in-plane and out-of-plane directions. However, the stiffness of the structure with infill walls was increased in in-plane direction only but remained almost the same in out-of-plane direction. Although the displacement of the structure with infill wall was reduced in in-plane direction, it was increased in both in-plane and out-of-plane directions when the infill walls suffered some damage.

Seismic fragility curves were developed in terms of slight, moderate, extensive and complete damage. Seismic fragility of the 3-storey RC framed building was seen to be more sensitive to the local site soil conditions than that of the 7- and 11-storey RC framed buildings. Similarly, the fragility of the 4-storey infilled RC frames was modified

for different soil types. Furthermore, the number of storeys in a building had a remarkable effect on the seismic performance of the RC framed buildings. This finding supports the prior literature (Bilgin, 2013; Kircil & Polat, 2006).

7.2 Recommendations for future research

The analytical and experimental investigations described in this study constitute a valuable contribution to the fragility analysis, the issues arise could benefit from further studies. The following are some of the recommendations for future works:

- 1) The experimental studies should be further pursued to consider the effects of bi-directional and tridirectional ground motions.
- 2) The developed finite element models can be used as the basis for an extensive parametric study of structures with different geometrical configurations, different loading (near fault or far fault ground motions), boundary conditions and alternative materials. The finite elements models may also be used to investigate different retrofit schemes for unreinforced masonry infill walls and RC frames.
- 3) In this research, the unreinforced masonry infill walls were modeled with a single diagonal strut. This model has the drawback of not being able to model the interaction with the bounding frame and the presences of openings (Asteris et al., 2011) and special treatment is required in order to cover this deficiencies (Asteris et al., 2012). Therefore, further works of consideration of this deficiencies are highly recommended.
- 4) Repeating a large number of time-history analyses is significant loss of computing time and effort. Therefore, a future line of research will focus on the use of reliability models (e.g. artificial neural network, response surface or others) for

probabilistic estimation of seismic performance to a structure. This approach allows seismic fragility curves to be effectively generated with a reasonable level of accuracy for making macro-level decisions because the simulation is performed not with a large number of nonlinear dynamic time-history analyses but with simple numerical equations. This also allows for flexible estimation of the seismic damage and fragility of arbitrarily selected structures of a given class.

- 5) The limit states functions may be defined in terms of other important engineering demand parameters such as column shear, or maximum floor acceleration for the fragility curves development.

University of Malaysia

REFERENCES

- Adnan, A. (2013). Seismic Hazard Assessment for Kuala Lumpur and Kedah: Structural Earthquake Engineering Research (SEER), University of Technology Malaysia.
- Applied Technology Council (ATC-40). (1996). Seismic evaluation and retrofit of concrete buildings. Report ATC-40. Redwood City (CA): Applied Technology Council
- Argyroudis, S., Kaynia, A. M., & Ptilakis, K. (2013). Development of fragility functions for geotechnical constructions: Application to cantilever retaining walls. *Soil Dynamics and Earthquake Engineering*, 50, 106-116.
- Assimaki, D., & Li, W. (2012). Site- and ground motion-dependent nonlinear effects in seismological model predictions. *Soil Dynamics and Earthquake Engineering*, 32, 143-151.
- Asteris, P. G., Antoniou, S. T., Sophianopoulos, D. S., & Chrysostomou, C. Z. (2011). Mathematical macromodeling of infilled frames: State of the Art. *Journal of Structural Engineering*, 137(12), 1508-1517.
- Asteris, P. G., Giannopoulos, I. P., & Chrysostomou, C. Z. (2012). Modeling of infilled frames with openings. *The Open Construction and Building Technology Journal*, 6((Suppl 1-M6)), 81-91.
- Baker, J., & Cornell, C. A. (2005). A vector-valued ground motion intensity measure consisting of spectral acceleration and epsilon. *Earthquake Engineering & Structural Dynamics*, 34, 1193-1217.
- Banon, H., Biggs, J. M., & Irvine, H., M. (1981). Seismic damage in reinforced concrete frames. *Journal of Structural Engineering*, 107, 1713-1729.
- Bilgin, H. (2013). Fragility-based assessment of public buildings in Turkey. *Engineering Structures*, 56, 1283-1294.
- Bommer, J. J., & Acevedo, A. (2004). The use of real earthquake accelerograms as input to dynamic analysis. *Journal of Earthquake Engineering*, 8(1), 43-91.
- Bommer, J. J., & Martinez-Pereira. (1999). The effective duration of earthquake strong motion. *Journal of Earthquake Engineering*, 3, 127-172.

- Bommer, J. J., & Scott, S. G. (2000). The feasibility of using real accelerograms for seismic design Implications of recent earthquakes on seismic risk (pp. 115-126).
- Boore, D. M., & Atkinson, G. M. (2008). Ground-motion prediction equations for the average horizontal component of PGA, PGV, and 5%-damped PSA at spectral periods between 0.01s and 10.0s. *Earthquake Spectra*, 24, 99-138.
- Borzi, B., Pinho, R., & Crowley, H. (2008). Simplified pushover-based vulnerability analysis for large-scale assessment of RC buildings. *Engineering Structures*(30), 804-820.
- Brandenberg, S., Bellana, N., & Shantz, T. (2010). Shear wave velocity as function of standard penetration test resistance and vertical effective stress at California bridge sites. *Soil Dynamics and Earthquake Engineering*, 30(10), 1026-1035.
- Calvi, G. M. (1999). A displacement-based approach for vulnerability evaluation of classes of buildings. *Journal of Earthquake Engineering*, 3, 411-438.
- Chiou, J.-S., Chiang, C.-H., Yang, H.-H., & Hsu, S.-Y. (2011). Developing fragility curves for a pile-supported wharf. *Soil Dynamics and Earthquake Engineering*, 31(5-6), 830-840.
- Chrysostomou, C. Z., & Asteris, P. G. (2012). On the in-plane properties and capacities of infilled frames. *Engineering Structures*, 41, 385-402.
- Chung, Y. S., Meyer, C., & Shinozuka, M. (1987). Seismic assessment of reinforced concrete members, NCEER-87-0022: National Center for Earthquake Engineering Research, State University of New York at Buffalo.
- Consortium of Organizations for Strong Motion Observation Systems (COSMOS). Retrieved 21 November 2013
- Cosenza, E., Manfredi, G., & Ramasco, K. (1990). An evaluation of the use of damage functionals in earthquake-resistant design. Paper presented at the Proceeding of the 9th European Conference on Earthquake Engineering, Moscow.
- Darendeli, M. B. (2001). Development of a new family of normalized modulus reduction and material damping curves. The University of Texas at Austin.

- Deodatis, G. (1999). Non-stationary stochastic vector processes: seismic ground motion applications. *Probabilistic Engineering Mechanics*, 11, 149-167.
- Dhakal, P. R., Mander, B. J., & Mashiko, N. (2006). Identification of critical ground motions for seismic performance assessment of structures. *Earthquake Engineering & Structural Dynamics*, 35, 989-1008.
- Dhakal, R. P., & Maekawa, K. (2002). Path-dependent cyclic stress-strain relationship of reinforcing bar including buckling. *Engineering Structures*, 24, 1383-1396.
- DiPasquale, E., & Cakmak, A. S. (1990). Seismic damage assessment using linear models. *Soil Dynamics and Earthquake Engineering*, 9, 194-215.
- Elnashai, A. S. (2006). Assessment of seismic vulnerability of structures. *Journal of Constructional Steel Research*, 62, 1134-1147.
- Engineering Seismology and Earthquake Engineering Research (ESEER). (2013). *Seismic hazard assessment of Kuala Lumpur and Kedah*. Skudai, Johor: University of Technology Malaysia.
- Erberik, M. A. (2008). Fragility-based assessment of typical mid-rise and low-rise RC buildings in Turkey. *Engineering Structures*, 30, 1360-1374.
- FEMA. (2003). *Multi-hazard loss estimation methodology. HAZUS-MH MR4 Technical Manual*. Washington, D. C.
- Fiore, A., Netti, A., & Monaco, P. (2012). The influence of masonry infill on the seismic behaviour of RC frame buildings. *Engineering Structures*, 44, 133-145.
- Fotopoulou, S. D., & Pitilakis, K. D. (2013). Vulnerability assessment of reinforced concrete buildings subjected to seismically triggered slow-moving earth slides. *Landslides*, 10(5), 563-582.
- Goda, K., & Yoshikawa, H. (2013). Incremental dynamic analysis of wood-frame houses in Canada: Effects of dominant earthquake scenarios on seismic fragility. *Soil Dynamics and Earthquake Engineering*, 48, 1-14.
- Güneyisi, E. M., & Altay, G. (2008). Seismic fragility assessment of effectiveness of viscous dampers in R/C buildings under scenario earthquakes. *Structural Safety*, 30, 461-480.

- Hashemi, A., & Mosalam, K. M. (2007). Seismic evaluation of reinforced concrete buildings including effects of masonry infill walls PEER report 2007/100 Pacific Earthquake Engineering Research Center. College of Engineering, University of California, Berkeley.
- Hassan, A. F., & Sozen, M. A. (1997). Seismic vulnerability assessment of low-rise buildings in regions with infrequent earthquakes. American Concrete Institute Structural Journal: Technical Paper.
- Heidary-Torkamani, H., Bargi, K., Amirabadi, R., & McClough, N. J. (2014). Fragility estimation and sensitivity analysis of an idealized pile-supported wharf with batter piles. *Soil Dynamics and Earthquake Engineering*, 61-62, 92-106.
- Idriss, I. M., & Sun, J. I. (1992). SHAKE91: a computer program for conducting equivalent linear seismic response analyses of horizontally layered soil deposits. Davis, California: University of California.
- Jeong, S.-H., & Elnashai, A. S. (2007). Probabilistic fragility analysis parameterized by fundamental response quantities. *Engineering Structures*, 29(66), 1238-1251.
- Kadysiewski, S., & Mosalam, K. M. (2009). Modeling of unreinforced masonry infill walls considering in-plane and out-of-plane interaction. PEER report 2008/102 Pacific Earthquake Engineering Research Center College of Engineering. Berkeley: University of California.
- Katsanos, E. I., Sextos, A. G., & Manolis, G. D. (2010). Selection of earthquake ground motion records: A state-of-the-art review from a structural engineering perspective. *Soil Dynamics and Earthquake Engineering*, 30, 157-169.
- Kayhan, A. H., Korkmaz, K. A., & Irfanoglu, A. (2011). Selecting and scaling real ground motion records using harmony search algorithm. *Soil Dynamics and Earthquake Engineering*, 31, 941-953.
- Kent, D. C., & Park, R. (1971). Flexural members with confined concrete. *Journal of the Structural Division*, 97, 1969-1990.
- Kircil, M. S., & Polat, Z. (2006). Fragility analysis of mid-rise R/C frame buildings. *Engineering Structures*, 28, 1335-1345.
- Kiureghian, A. D., Haukaas, T., & Fujimura, K. (2006). Structural reliability software at the University of California, Berkeley. *Structural Safety*, 28, 44-67.

- Koutromanos, I., Stavridis, A., Shing, P. B., & Willam, K. (2011). Numerical modeling of masonry infilled RC frames subjected to seismic loads. *Computers and Structures*, 89, 1026-1037.
- Kwon, O.-S., & Elnashai, A. (2006). The effect of material and ground motion uncertainty on the seismic vulnerability curves of RC structure. *Engineering Structures*, 28(2), 289-303.
- Kwon, O.-S., & Kim, E. (2010). Case study: Analytical investigation on the failure of a two-story RC building damaged during the 2007 Pisco-Chincha earthquake. *Engineering Structures*, 32(7), 1876-1887.
- Lagaros, N. D., & Papadrakakis, M. (2012). Neural network based prediction schemes of the non-linear seismic response of 3D buildings. *Advances in Engineering Software*, 44(1), 92-115.
- Iervolino, I., & Cornell, C. A. (2005). Record selection for nonlinear seismic analysis of structures. *Earthquake Spectra*, 21, 685-713.
- Li, Z., & Hatzigeorgiou, G. D. (2012). Seismic damage analysis of RC structures using fiber beam-column elements. *Soil Dynamics and Earthquake Engineering*, 32(1), 103-110.
- Liauw, T. C., & Kwan, K. H. (1985). Unified plastic analysis for infilled frames. *Journal of Structural Engineering*, 111, 1427-1448.
- Matasović, N., & Vucetic, M. (1993). Cyclic characterization of liquefiable sands. *Journal of Geotechnical Engineering*, 119, 1805-1822.
- Mazzoni, S., McKenna, F., Scott, M. H., & Fenves, G. L. (2007). *OpenSees command language manual – version 2.0*. Berkeley: University of California.
- McKenna, F., & Fenves, G. L. (2001). *The OpenSees command language manual - version 1.2*. Pacific Earthquake Engineering Research Centre: Berkeley: University of California.
- Menegotto, M., & Pinto, P. E. (1973). Method of analysis for cyclically loaded reinforced concrete plane frames including changes in geometry and non-elastic behavior of elements under combined normal force and bending. *IABSE symposium on resistance and ultimate deformability of structures acted on by well defined repeated loads*, 15-22.

- Mitropoulou, C. C., & Papadrakakis, M. (2011). Developing fragility curves based on neural network IDA predictions. *Engineering Structures*, 33(12), 3409-3421.
- Mork, K. J. (1992). Stochastic analysis of reinforced concrete frames under seismic excitation. *Soil Dynamics and Earthquake Engineering*, 11, 145-161.
- NEHRP. (2001). NEHRP recommended provisions for seismic regulations for new buildings and other structures. Washington, DC, USA: Building Seismic Safety Council.
- Pagliaroli, A., & Lanzo, G. Selection of real accelerograms for the seismic response analysis of the historical town of Nicastro (Southern Italy) during the March 1638 Calabria earthquake. *Engineering Structures*, 30, 2211-2222.
- Papaspiliou, M., Kontoe, S., & Bommer, J. J. (2012). An exploration of incorporating site response into PSHA-part 1: Issues related to site response analysis methods. *Soil Dynamics and Earthquake Engineering*, 42, 302-315.
- Park, J., Towashiraporn, P., Craig, J. I., & Goodno, B. J. (2009). Seismic fragility analysis of low-rise unreinforced masonry structures. *Engineering Structures*, 31, 125-137.
- Park, Y.-J., & Ang, A. H.-S. (1985a). Mechanistic seismic damage model for reinforced concrete. *Journal of Structural Engineering*, 111(4), 722-739.
- Park, Y. J., & Ang, A. H.-S. (1985b). Seismic damage analysis of reinforced concrete buildings. *Journal of Structural Engineering*, 111, 740-757.
- Park, Y. J., Ang, M., & Wen, Y. K. (1987). Damage-limiting aseismic design of buildings. *Earthquake Spectra*, 3, 1-25.
- Paulay, T., & Priestley, M. J. N. (1992). *Seismic design of reinforced concrete and masonry buildings*: John Wiley & Sons, Inc.
- Perera, R. (2005). Performance evaluation of masonry-infilled RC frames under cyclic loading based on damage mechanics. *Engineering Structures*, 27, 1278-1288.
- Petersen, M. D., Dewey, J., Hartzell, S., Mueller, C., Harmsen, S., Frankel, A. D., & Rukstales, K. (2004). Probabilistic seismic hazard analysis for Sumatra, Indonesia and across the Southern Malaysian Peninsula. *Tectonophysics*, 390(1-4), 141-158.

- Pujol, S., & Fick, D. (2010). The test of a full-scale three-story RC structure with masonry infill walls. *Engineering Structures*, 32, 3112-3121.
- Rabinovitch, O., & Madah, H. (2011). Finite element modeling and shake-table testing of unidirectional infill masonry walls under out-of-plane dynamic loads. *Engineering Structures*, 33, 2683-2696.
- Risk Engineering. (2013). EZ-FRISK, Software for Earthquake Ground motion: User's Manual: Risk Engineering Inc.
- Roh, H., & Reinhorn, A. M. (2009). Analytical modeling of rocking elements. *Engineering Structures*, 25, 1241-1263.
- Rossetto, T., & Elnashai, A. (2003). Derivation of vulnerability functions for European-type RC structures based on observational data. *Engineering Structures*, 25, 1241-1263.
- Rossetto, T., & Elnashai, A. (2005). A new analytical procedure for the derivation of displacement-based vulnerability curves for populations of RC structures. *Engineering Structures*, 27, 397-409.
- Roufaiel, M. S. L., & Meyer, C. (1987). Reliability of concrete frames damaged by earthquakes. *Journal of Structural Division ASCE*, 113, 445-457.
- Sawada, T., Hirao, K., & Yamamoto, H. (1992). Relation between maximum amplitude ratio (a/v , ad/v^2) and spectral parameters of earthquake ground motion. *Earthquake Engineering*. Paper presented at the Tenth World Conference © Balkema, Rotterdam.
- Schnabel, P. B., Lysmer, J., & Seed, H. B. (1972). SHAKE: a computer program for earthquake response analysis of horizontally layered sites Report no. EERC72-12. Berkeley: University of California.
- Scott, B. D., Park, R., & Priestley, M. J. N. (1982). Stress-strain behavior of concrete confined by overlapping hoops at low and high strain rates. *American Concrete Institute Structural Journal: Technical Paper*.
- Seed, H. B., & Idriss, I. M. (1981). Evaluation of liquefaction potential sand deposits based on observation of performance in previous earthquakes. *ASCE National Convention (MO)*, 481-544.

- Shahrouzi, M., & Sazjini, M. (2012). Refined harmony search for optimal scaling and selection of accelerograms. *Scientia Iranica*, 19, 218-224.
- Shantz, T. J. (2006). Selection and scaling of earthquake records for nonlinear dynamic analysis of first mode dominate bridge structures. Paper presented at the 8th U.S. national conference on earthquake engineering, San Francisco, CA.
- Shome, N., Cornell, C. A., Bazzurro, P., & Carballo, J. E. (1998). Earthquakes, records and nonlinear responses. *Earthquake Spectra*, 14, 469-500.
- Sorabella, S., Baise, G. L., & Hines, M. E. (2006). Ground motion suite for Boston, Massachusetts. Paper presented at the Proceedings of the 8th national conference on earthquake engineering.
- Stewart, J. P., Chiou, S.-J., Bray, J. D., Graves, R. W., & Somerville, P. G. (2001). Ground Motion Evaluation Procedures for Performance-Based Design. PEER Report 2001/09. University of California, Berkeley: Pacific Earthquake Engineering Research Center.
- Su, L., & Shi, J. (2013). Displacement-based earthquake loss assessment methodology for RC frames infilled with masonry panels. *Engineering Structures*, 48, 430-441.
- Taucer, F. F., Spacone, E., & Filippou, F. C. (1991). A fiber beam-column element for seismic response analysis of reinforced concrete structures Report No. UCB/EERC-91/17 Earthquake Engineering Research Center. College of Engineering, University of California, Berkeley.
- Trifunac, M. D. (1971). A method for synthesizing realistic strong motion. *Bulletin of Seismological Society of America*, 61, 1739-1753.
- Trifunac, M. D., & Brady, A. G. (1975). A study on the duration of strong earthquake ground motion. *Bulletin of the Seismological Society of America*, 65, 581-626.
- Tu, Y. H., Chuang, T. H., Liu, P. M., & Yang, Y. S. (2010). Out-of-plane shaking table tests on unreinforced masonry panels in RC frames. *Engineering Structures*, 32, 3925-3935.
- Uva, G., Porco, F., & Fiore. (2012). Appraisal of masonry infill walls effect in the seismic response of RC framed buildings: A case study. *Engineering Structures*, 34, 514-526.
- Williams, M. S., & Sexsmith, R. G. (1995). Seismic damage indices for concrete structures: a state-of-the-art review. *Earthquake Spectra*, 11(2), 319-349.

Yu, Y.-J., Tsai, K.-C., Weng, Y.-T., Lin, B.-Z., & Lin, J.-L. (2010). Analytical studies of a full-scale steel building shaken to collapse. *Engineering Structures*, 32, 3418-3430.

University of Malaya

LIST OF PUBLICATIONS AND PAPER REPRESENTED

The findings of this dissertation were published or are currently under revision to be published in several international journals and conference proceedings. Below is a list of these publications:

Tan, Kok. Tong., Razak, H. A., Lu, D., Li, Y. (2015). Seismic response of a four-storey RC school building with masonry-infilled walls. *Natural Hazards*, 78, 141-153.

Tan, Kok. Tong., Hashim, H., Khair, N. M., Razak, H. A., Suhatriil, M., Lu, D., (2015). Damage assessment using modal parameters of a masonry-infilled reinforced concrete building subjected to seismic loadings. *Construction & Building Materials*, (Under review, Q1, IF: 2.296).

Tan, Kok. Tong., Razak, H. A., Suhatriil, M., Lu, D. (2015). Vulnerability analysis of a 3-storey RC framed building in low to moderate seismicity zones using site specific ground motions. *Earthquake Spectra*, (Under review, Q2, IF: 1.000)

Tan, Kok. Tong., Razak, H. A., Suhatriil, M., Lu, D. (2015). Effects of site soil conditions on vulnerability of RC framed buildings subjected to far-fault ground motions. *Engineering Structures*, (Under review, Q1, IF: 1.767)

Tan, Kok. Tong., Suhatriil, M., Razak, H. A., Lu, D. (2015). Seismic vulnerability assessment of a typical 3-story RC framed building in Malaysia. *Journal of Earthquake Engineering*, (Under review, Q3, IF: 0.905)

Tan, Kok. Tong., Suhatriil, M., Razak, H. A., Lu, D. (2015). Seismic fragility analysis of a four-storey RC school building in low seismicity zone. *Earthquakes and Structures*, (Under review, Q2, IF: 1.138)

Tan, Kok. Tong., Razak, H. A., Suhatriil, M., Lu, D. (2014). Fragility curves of a RC frame building subjected to seismic ground motions. *Journal of Civil Engineering Research*, 4, 159-163. (Open source)

APPENDIX A: LOGNORMAL PROBABILITY PLOT OF MAXIMUM DRIFT RATIO

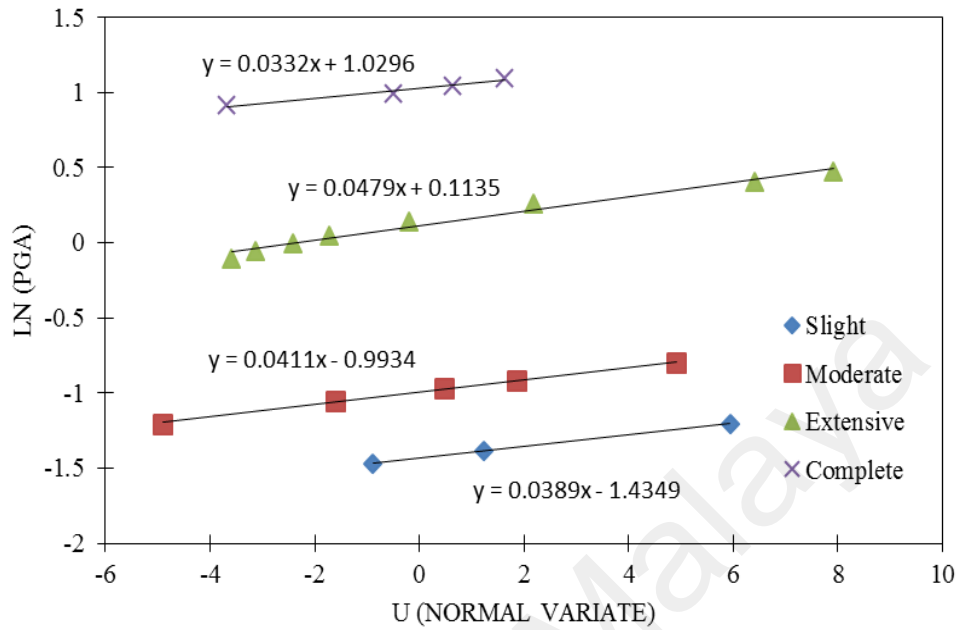


Figure. A1: Maximum drift ratio plot for 3-storey RC framed building at soil type C.

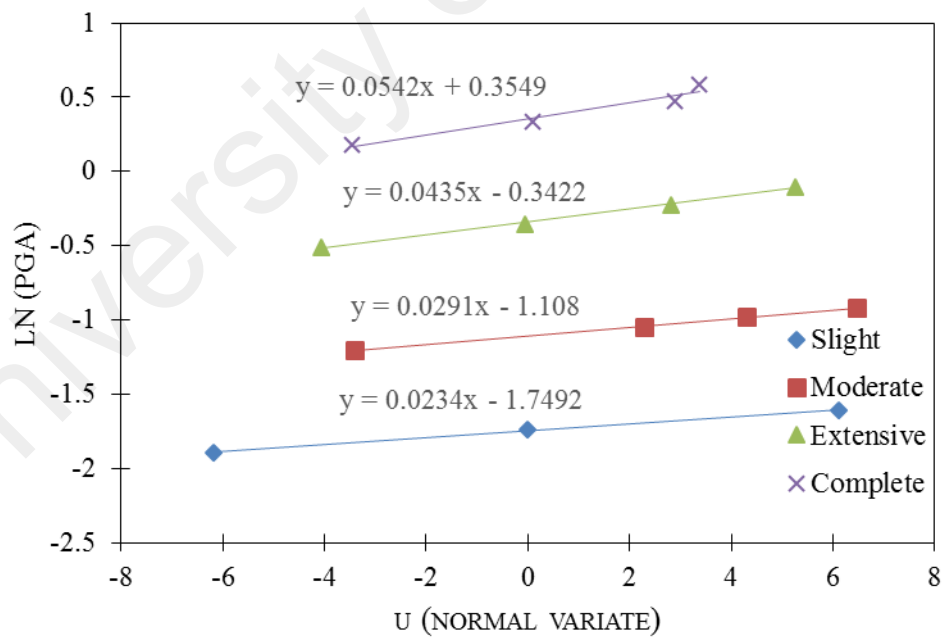


Figure. A2: Maximum drift ratio plot for 4-storey RC school building at soil type D.

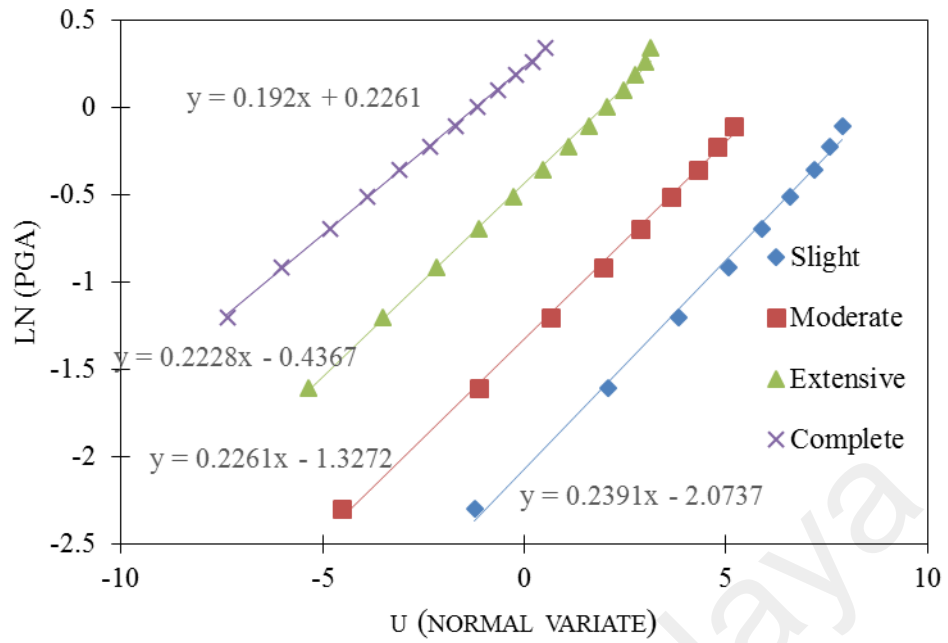


Figure. A3: Maximum drift ratio plot for 4-storey RC school building at soil type E.

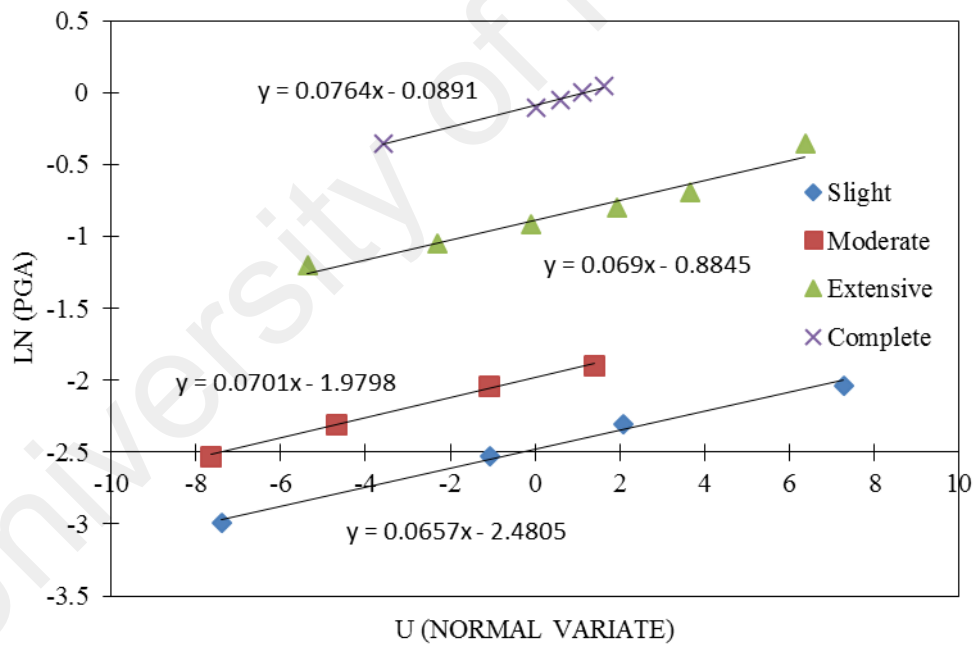


Figure. A4: Maximum drift ratio plot for 7-storey RC framed building at soil type C.

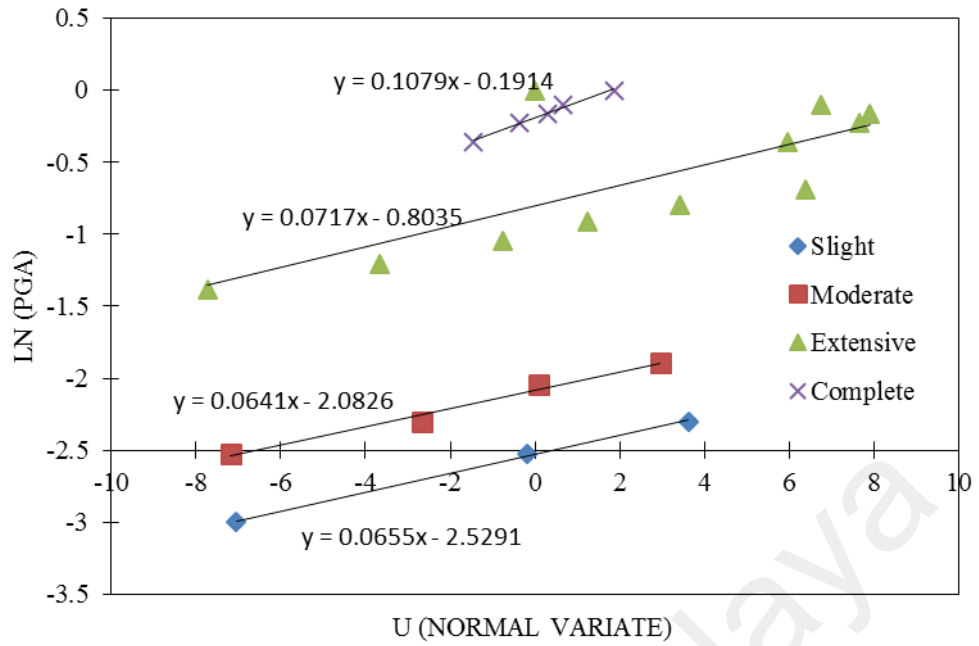


Figure. A5: Maximum drift ratio plot for 7-storey RC framed building at soil type D.

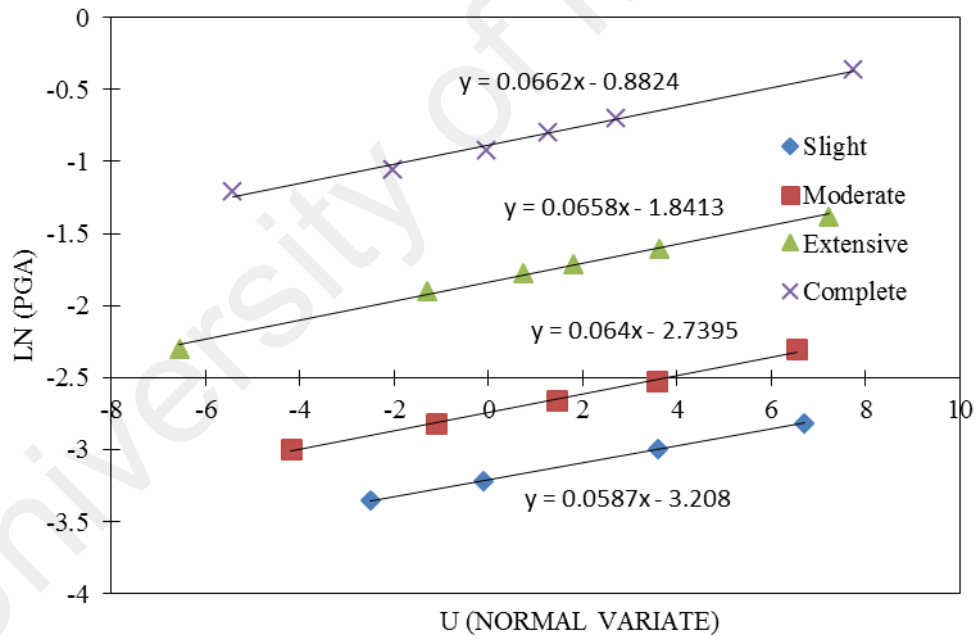


Figure. A6: Maximum drift ratio plot for 11-storey RC framed building at soil type C.

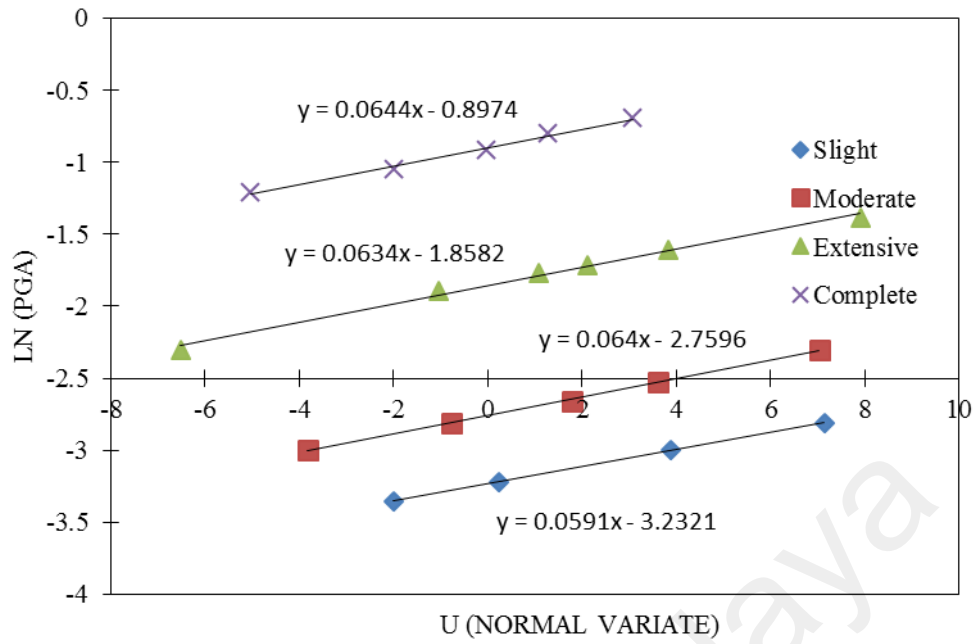


Figure. A7: Maximum drift ratio plot for 11-storey RC framed building at soil type D.

University of Malaya

APPENDIX B: PROBABILITY TABULATIONS FOR DIFFERENT EAARTHQUAKE LEVELS

Table B1. Probability tabulation for 3-storey RC framed building at soil type C.

PHGA	0.001	0.04	0.08	0.2	0.23	0.25	0.3	0.35	0.38	0.4	0.45	0.5	0.7	0.9	0.95	1	1.05	1.15	1.3	1.5	1.6	1.7	1.8	2.5	2.7	2.85	3	3.1	3.2	3.3
Slight	0	0	2.5E-173	3.6E-06	0.185665	0.894259	1	1	1	1	1	1	1	1	1	1	1	1	1	1	1	1	1	1	1	1	1	1	1	1
Moderate	0	0	1.6E-304	4.3E-51	2.36E-31	5.92E-22	1.5E-07	0.084907	0.735039	0.969682	1	1	1	1	1	1	1	1	1	1	1	1	1	1	1	1	1	1	1	1
Extensive	0	0	0	1E-283	7.4E-240	1.7E-215	8E-167	1.4E-130	4.3E-113	8E-103	4E-81	6.19E-64	4.82E-23	2.45E-06	0.00029	0.008906	0.088358	0.708245	0.999058	1	1	1	1	1	1	1	1	1	1	1
Complete	0	0	0	0	0	0	0	0	0	0	0	0	0	2E-256	8.3E-233	1.9E-211	4.1E-192	1.5E-158	1.9E-118	3.83E-79	4.8E-64	2.36E-51	1.05E-40	0.000321	0.136796	0.703227	0.981177	0.998916475	0.999971	1

Table B2. Probability tabulation for 3-storey RC framed building at soil type D.

PHGA	0.001	0.04	0.08	0.1	0.15	0.18	0.2	0.25	0.28	0.3	0.35	0.4	0.45	0.5	0.7	0.75	0.8	0.85	0.9	1	1.05	1.3	1.5	1.6	1.7	1.8	1.9	2	2.1
Slight	0	5E-267	1.2E-81	6E-45	8.6E-07	0.26404	0.96156	1	1	1	1	1	1	1	1	1	1	1	1	1	1	1	1	1	1	1	1	1	1
Moderate	0	0	6E-238	5E-161	5.9E-60	9.8E-31	2E-18	0.00276	0.58828	0.9797	1	1	1	1	1	1	1	1	1	1	1	1	1	1	1	1	1	1	1
Extensive	0	0	6E-221	1E-182	2E-122	2E-99	3.3E-87	5.2E-64	1.3E-53	9E-48	6E-36	4E-27	2E-20	3E-15	0.0003	0.0058	0.04599	0.18549	0.44061	0.88957	0.96858	1	1	1	1	1	1	1	1
Complete	0	0	0	0	0	0	0	3E-259	2E-229	3E-212	3E-176	1E-147	1E-124	8E-106	5E-56	9E-48	1.1E-40	1.49E-34	2.9E-29	1E-20	2.8E-17	3.3E-06	0.02783	0.22829	0.63825	0.9176	0.99108	0.9995	1

Table B3. Probability tabulation for 4-storey RC framed building at soil type D.

PGA	0.001	0.04	0.08	0.1	0.15	0.175	0.2	0.3	0.35	0.375	0.4	0.5	0.6	0.7	0.8	0.9	1.2	1.4	1.6	1.8	1.9	2
Slight	0	0	8.9E-242	6.1E-124	1.296E-10	0.604984	1	1	1	1	1	1	1	1	1	1	1	1	1	1	1	1
Moderate	0	0	0	0	3.06E-162	7.5E-106	7.7E-67	0.000487	0.977209	0.999994	1	1	1	1	1	1	1	1	1	1	1	1
Extensive	0	0	0	0	3.92E-280	8.4E-228	7.1E-187	1.2E-87	8.44E-60	4.26E-49	4.54E-40	3.58E-16	5.3E-05	0.369659	0.996899	1	1	1	1	1	1	1
Complete	0	0	0	0	0	0	6.5E-288	3.3E-182	2.1E-148	2.1E-134	6.1E-122	1.32E-83	9.89E-58	1.13E-39	7.42E-27	1.02E-17	0.000726	0.36693	0.983152	0.999991	1	1

Table B4. Probability tabulation for 4-storey RC framed building at soil type E.

PHGA	0.001	0.04	0.08	0.1	0.2	0.3	0.4	0.5	0.6	0.7	0.8	0.9	1	1.1	1.2	1.3	1.4	1.6	1.8	2	2.2	2.4	2.6	2.8	3	3.2	3.5
Slight	3.419E-91	8.359E-07	0.029343	0.169214	0.973914	0.99986	0.999999	1	1	1	1	1	1	1	1	1	1	1	1	1	1	1	1	1	1	1	1
Moderate	8.39E-135	2.967E-17	5.76E-08	8.02E-06	0.105963	0.70713	0.96542	0.997479	0.999847	0.999991	0.999999	1	1	1	1	1	1	1	1	1	1	1	1	1	1	1	1
Extensive	9.1E-186	4.377E-36	3.42E-21	2.77E-17	7.06E-08	0.00029	0.015677	0.124862	0.36968	0.640269	0.831098	0.931514	0.975005	0.991526	0.997268	0.999148	0.99974	0.999976	0.999998	1	1	1	1	1	1	1	1
Complete	1.79E-302	2.742E-72	6.86E-47	6.51E-40	5.88E-22	4.7E-14	1.34E-09	8.43E-07	6.2E-05	0.001202	0.009647	0.042142	0.119477	0.247873	0.409818	0.574905	0.717305	0.898017	0.970203	0.992503	0.998299	0.99964	0.999927	0.999986	0.999997	0.999999	1

Table B5. Probability tabulation for 7-storey RC framed building at soil type C.

PHGA	0.001	0.05	0.01	0.025	0.05	0.08	0.1	0.13	0.15	0.2	0.25	0.3	0.35	0.4	0.45	0.5	0.7	0.9	0.95	1	1.05	1.1	1.2	1.3	1.5	1.6	
Slight	0	2.214E-15	9.91E-230	7.56E-76	2.214E-15	0.2455968	0.9966154	1	1	1	1	1	1	1	1	1	1	1	1	1	1	1	1	1	1	1	1
Moderate	0	6.745E-48	2.81E-307	1.4E-131	6.745E-48	3.4078E-15	2.066E-06	0.1943648	0.8808921	1	1	1	1	1	1	1	1	1	1	1	1	1	1	1	1	1	1
Extensive	0	6.59E-206	0	0	6.59E-206	2.336E-125	3.696E-94	2.852E-63	4.616E-49	4.04E-26	1.77E-13	1.83E-06	0.008288	0.322494	0.893666	0.997225	1	1	1	1	1	1	1	1	1	1	1
Complete	0	0	0	0	0	1.667E-223	7.35E-185	3.71E-144	4.12E-124	2.05E-88	5.88E-65	1.57E-48	1.45E-36	1.28E-27	8.05E-21	1.32E-15	0.000231	0.415728	0.689648	0.878239	0.964451	0.992105	0.999809	0.999998	1	1	

Table B6. Probability tabulation for 7-storey RC framed building at soil type D.

PHGA	0.02	0.04	0.048	0.05	0.08	0.1	0.13	0.15	0.2	0.25	0.3	0.35	0.4	0.45	0.5	0.7	0.8	0.85	0.9	1	1.2	1.4			
Slight	3E-99	3.111E-26	4.69E-15	5.236E-13	0.5205249	0.999728	1	1	1	1	1	1	1	1	1	1	1	1	1	1	1	1	1		
Moderate	1.86E-179	1.307E-70	2.148E-50	2.393E-46	2.371E-12	0.0003	0.7457392	0.998096	1	1	1	1	1	1	1	1	1	1	1	1	1	1	1	1	
Extensive	4.11E-304	4.84E-181	5.49E-154	3.12E-148	5.698E-90	1.87E-67	3.241E-45	5.19E-35	1.34E-18	1.27E-09	0.000108	0.036758	0.446324	0.907342	0.995733	1	1	1	1	1	1	1	1	1	
Complete	5.6E-292	2.78E-194	6.61E-172	4.37E-167	1.4E-116	8.13E-96	4.736E-74	2.2E-63	1.63E-44	3.07E-32	9.68E-24	1.27E-17	4.08E-13	9.57E-10	3.3E-07	0.04672	0.355813	0.588662	0.78346	0.965305	0.999842	1	1	1	1

Table B7. Probability tabulation for 11-storey RC framed building at soil type C.

PHGA	0.005	0.12	0.02	0.025	0.035	0.04	0.05	0.06	0.07	0.08	0.1	0.15	0.17	0.18	0.2	0.25	0.3	0.35	0.4	0.45	0.5	0.7	
Slight	4.87E-278	1	1.92E-33	1.283E-16	0.0069451	0.42650545	0.99985049	1	1	1	1	1	1	1	1	1	1	1	1	1	1	1	1
Moderate	0	1	2.83E-75	4.412E-50	5.011E-22	3.4372E-14	3.1189E-05	0.1240749	0.8950335	0.999581	1	1	1	1	1	1	1	1	1	1	1	1	1
Extensive	0	1.12E-05	1.12E-217	8.91E-174	5.2E-117	1.2639E-97	3.2727E-69	1.082E-49	8.87E-36	1.22E-25	1.19E-12	0.198128	0.854024	0.97273	0.999787	1	1	1	1	1	1	1	1
Complete	0	2.529E-78	0	0	5.38E-305	3.604E-273	6.312E-224	2.37E-187	5.4E-159	2.5E-136	2.1E-102	2.48E-53	1.82E-41	1.47E-36	2.32E-28	1.35E-14	5.94E-07	0.005719	0.304345	0.897468	0.997874	1	1

Table B8. Probability tabulation for 11-storey RC framed building at soil type D.

PHGA	0.005	0.01	0.02	0.025	0.035	0.04	0.05	0.06	0.07	0.08	0.1	0.15	0.17	0.18	0.2	0.25	0.3	0.35	0.4	0.45	0.5	0.6	
Slight	4.35E-268	1.06E-119	6.252E-31	5.423E-15	0.0208925	0.5885277	0.99996826	1	1	1	1	1	1	1	1	1	1	1	1	1	1	1	1
Moderate	0	3.68E-183	8.645E-73	4.526E-48	9.9745E-21	3.584E-13	0.00011232	0.20023211	0.9415375	0.999871	1	1	1	1	1	1	1	1	1	1	1	1	1
Extensive	0	0	1.63E-230	1.23E-183	4.11E-123	1.77E-102	2.7638E-72	1.3467E-51	6.768E-37	3.18E-26	1.198E-12	0.269647	0.913133	0.988147	0.999956	1	1	1	1	1	1	1	1
Complete	0	0	0	0	0	7.48E-285	3.594E-233	8.238E-195	4.33E-165	2.4E-141	7.55E-106	1.2E-54	2.63E-42	3.25E-37	1.02E-28	1.58E-14	9.66E-07	0.008971	0.384633	0.937681	0.999242	1	1

APPENDIX C: THE LOCAL AND GLOBAL RESPONSES FOR 11-STOREY RC BUILDING

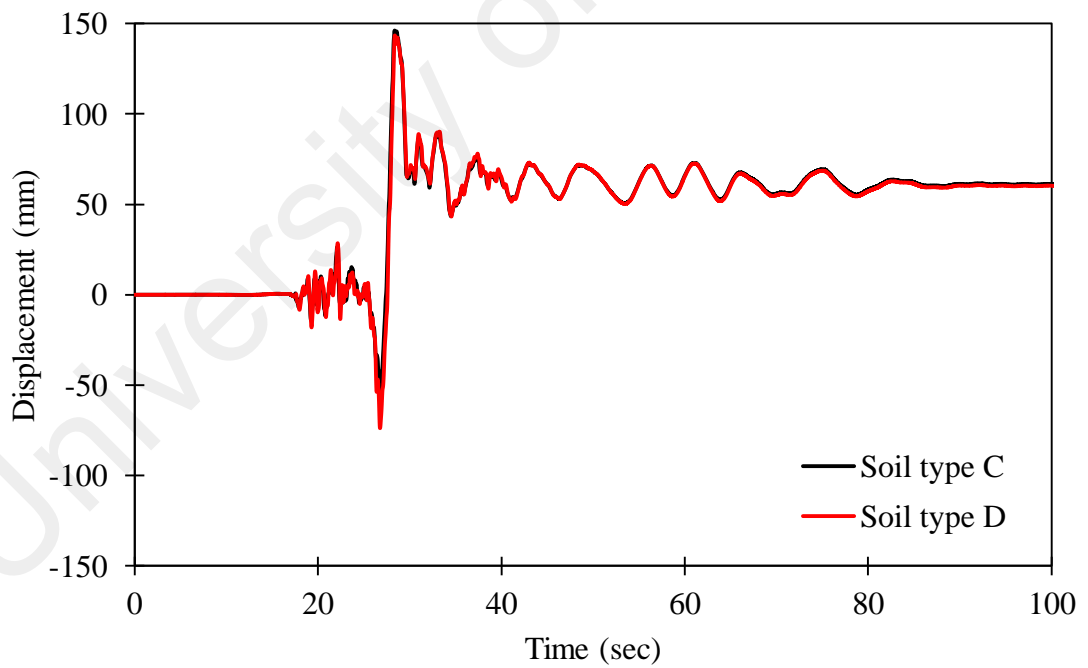
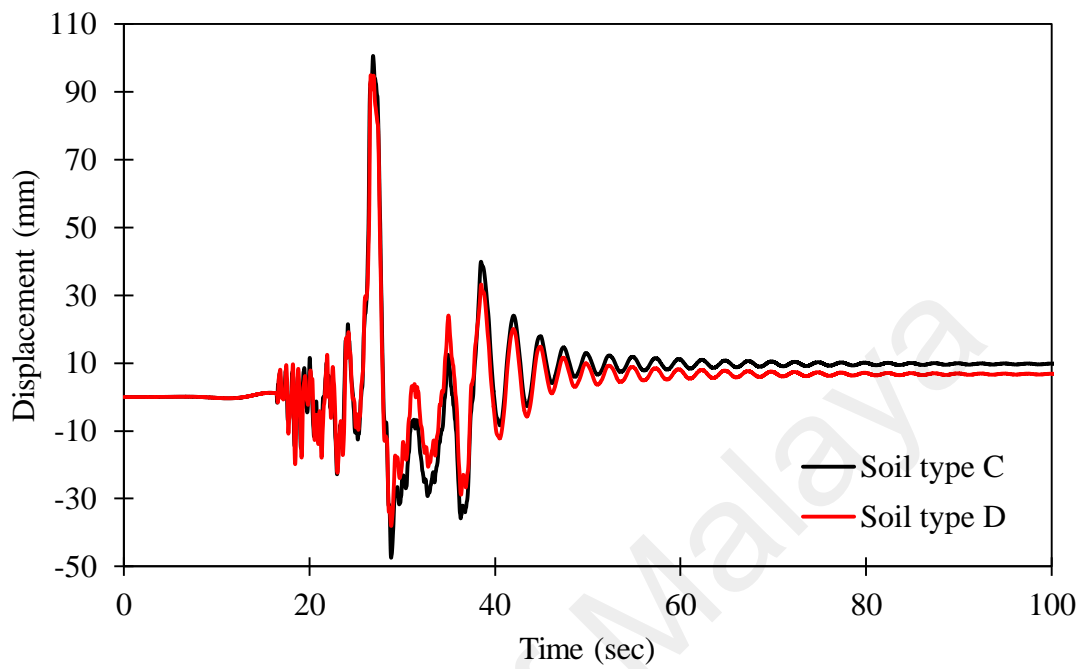


Figure. C1. Displacement time history for 11-story RC building at soft rock and stiff soil.

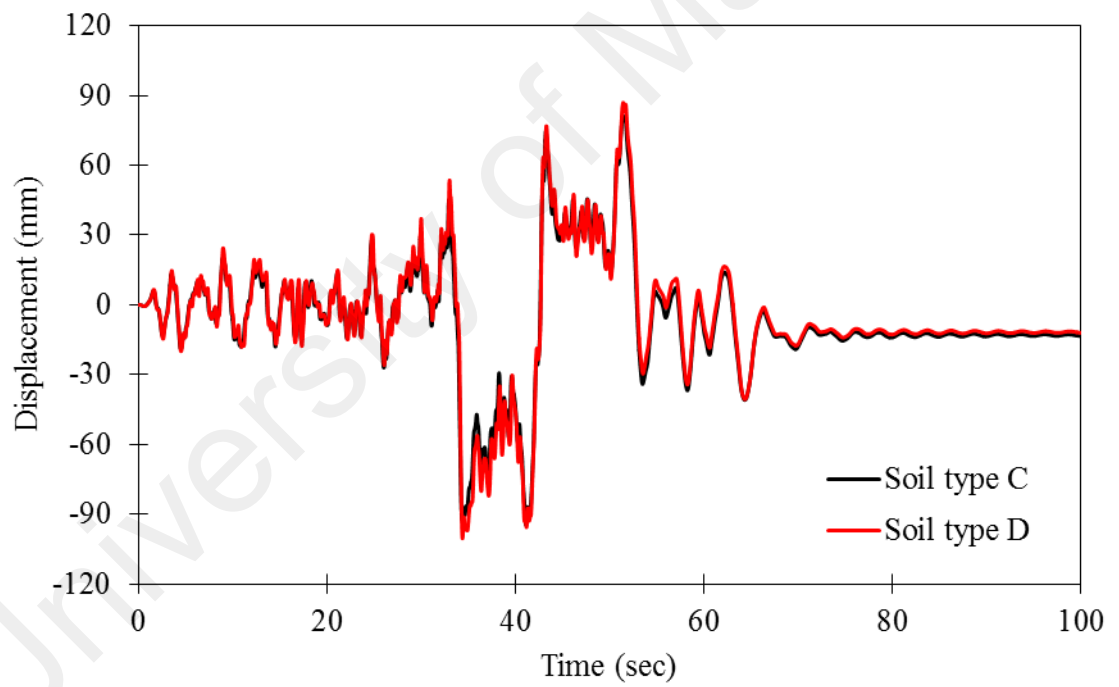
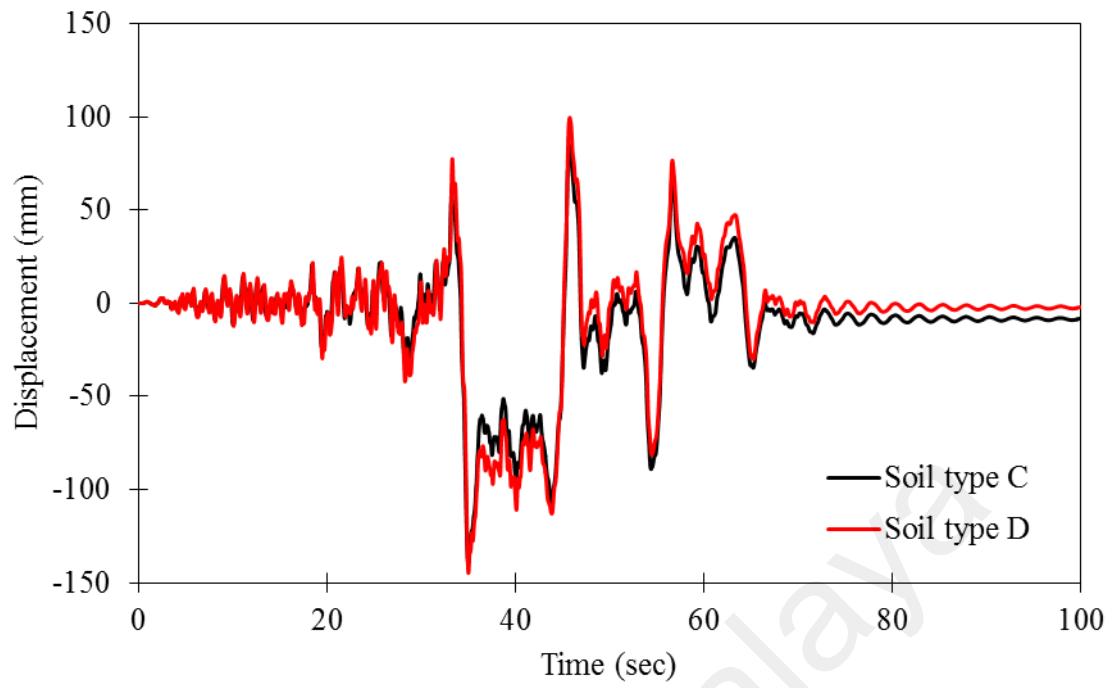


Figure. C1. Continuation.

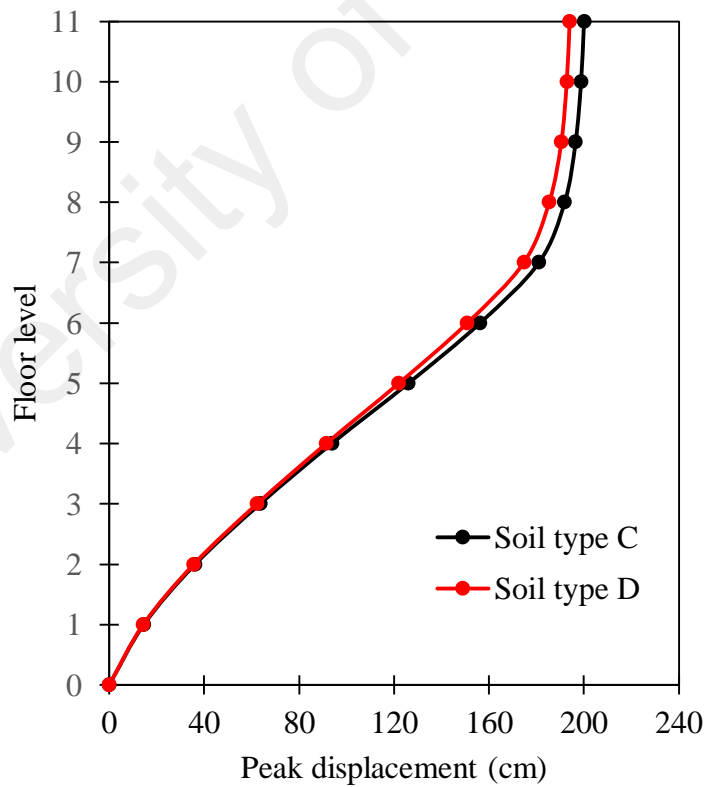
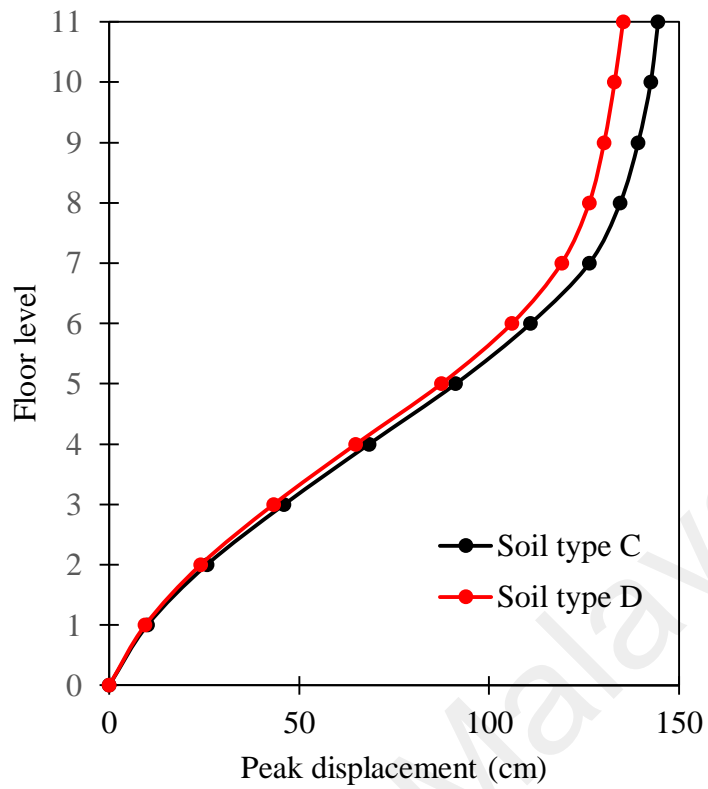


Figure. C2. Peak lateral displacement for 11-story RC building at soft rock and stiff soil.

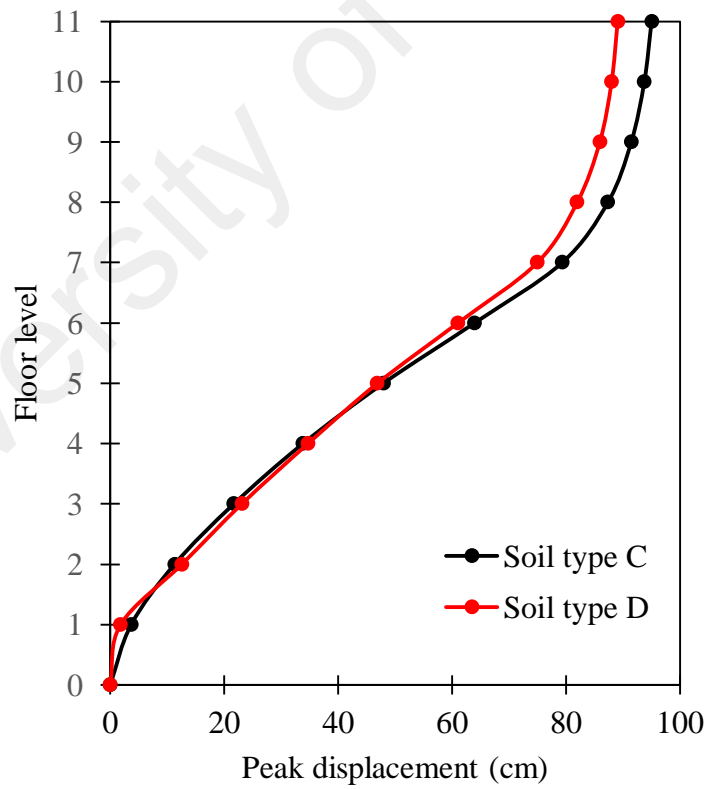
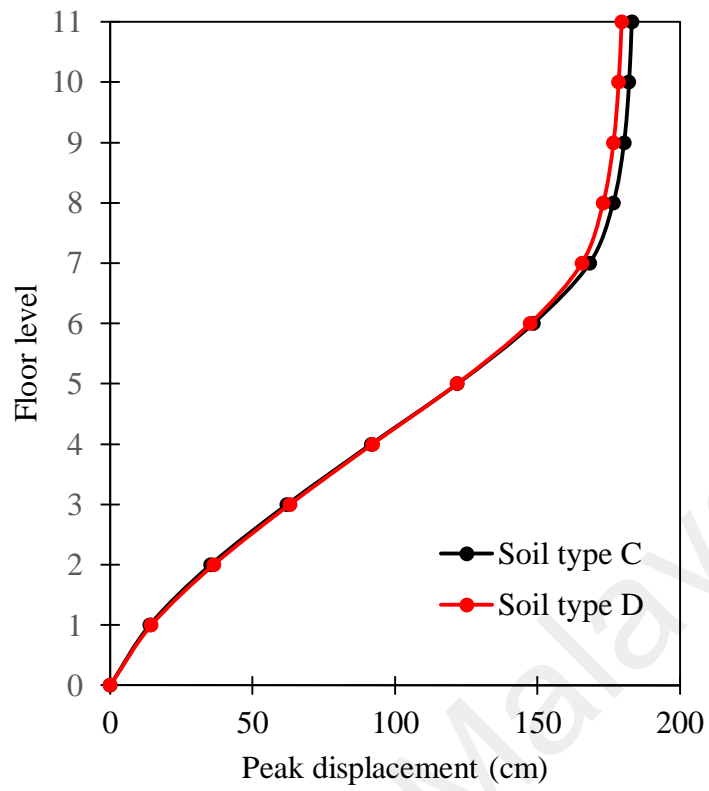


Figure. C2. Continuation.

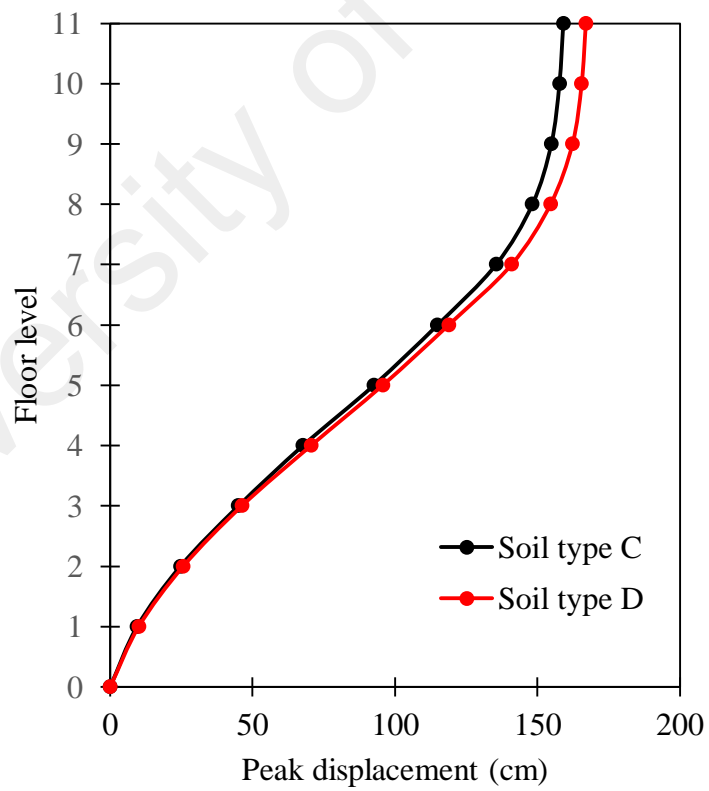
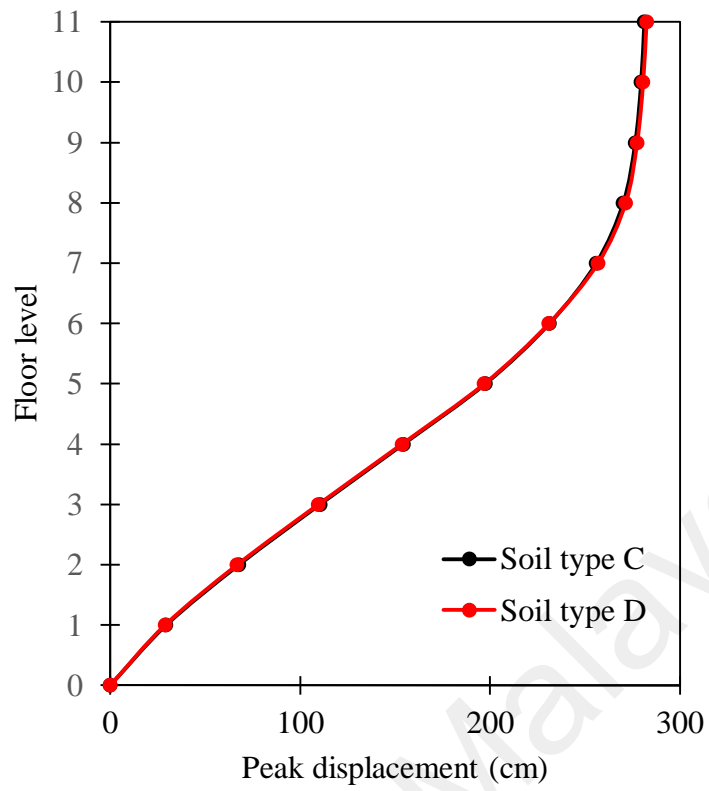


Figure. D2. Continuation.

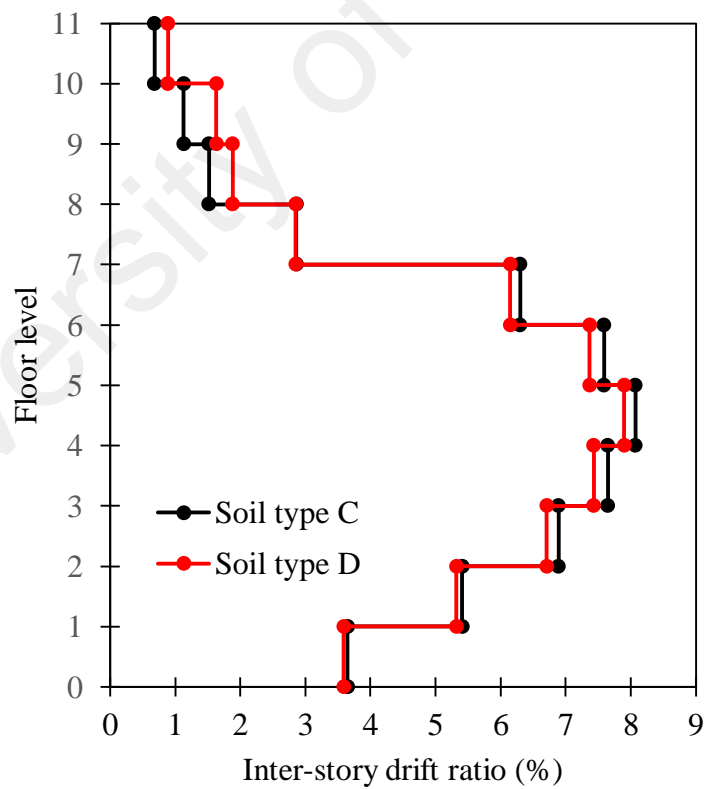
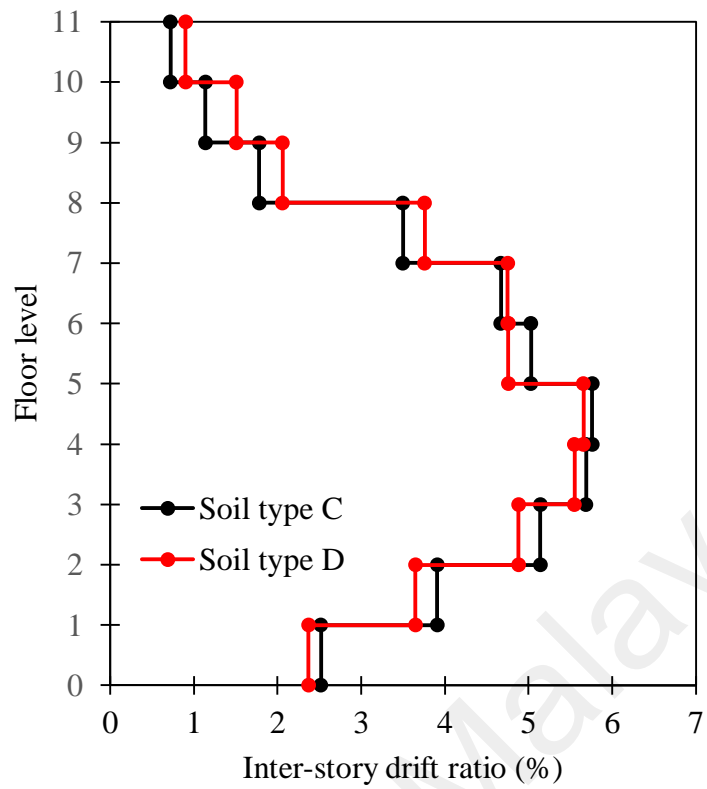


Figure. C3. Maximum interstory drift ratio for 11-story RC building at soft rock and stiff soil.

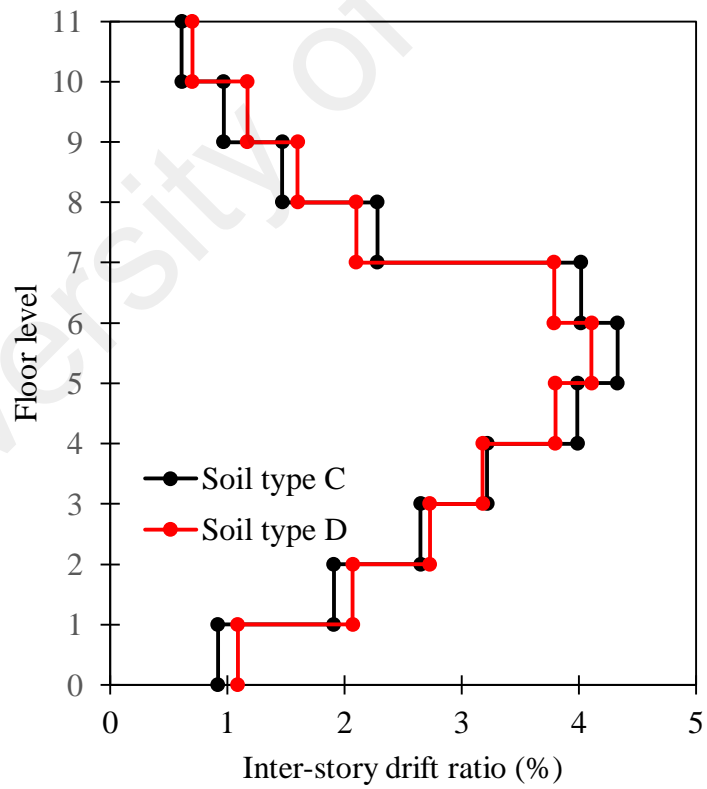
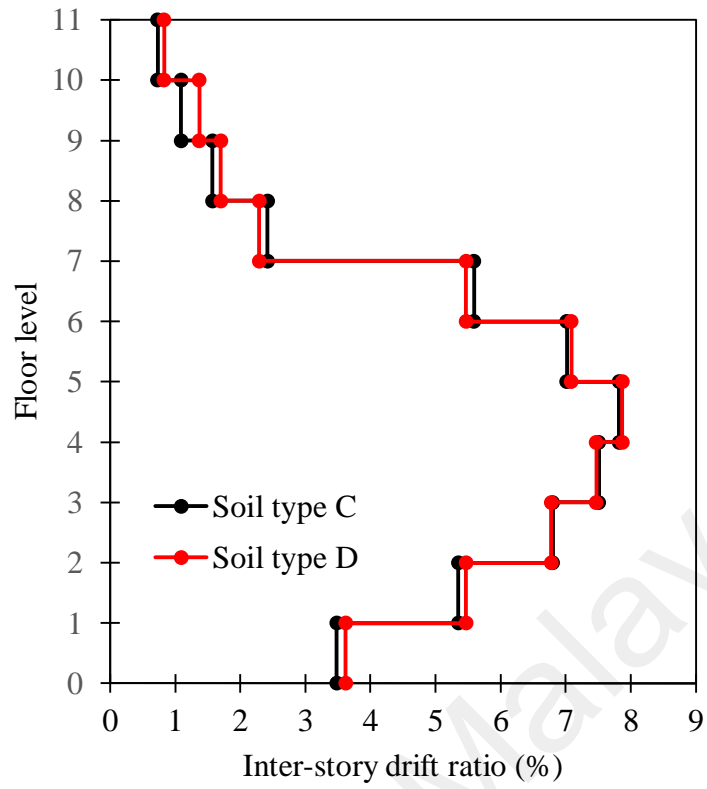


Figure. C3. Continuation.

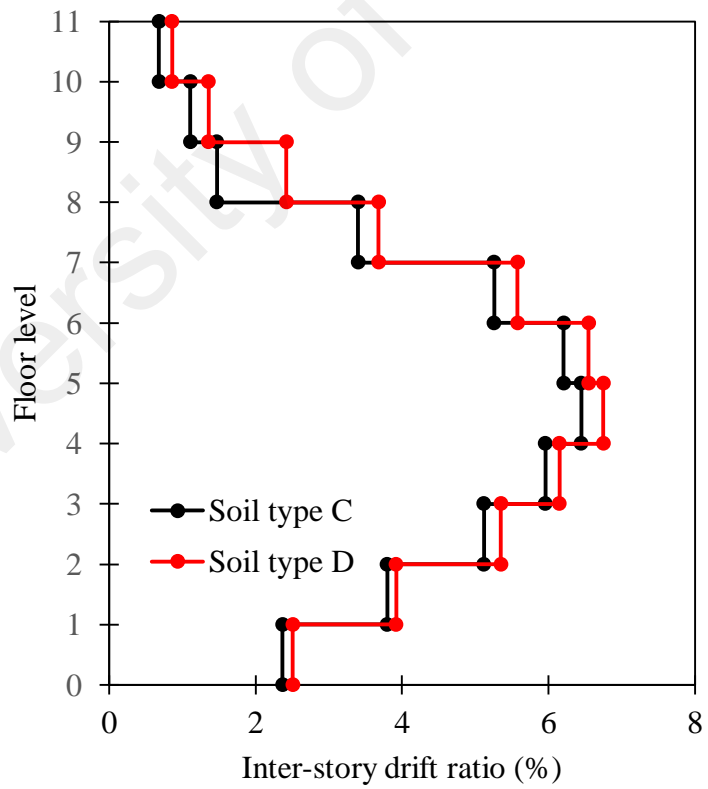
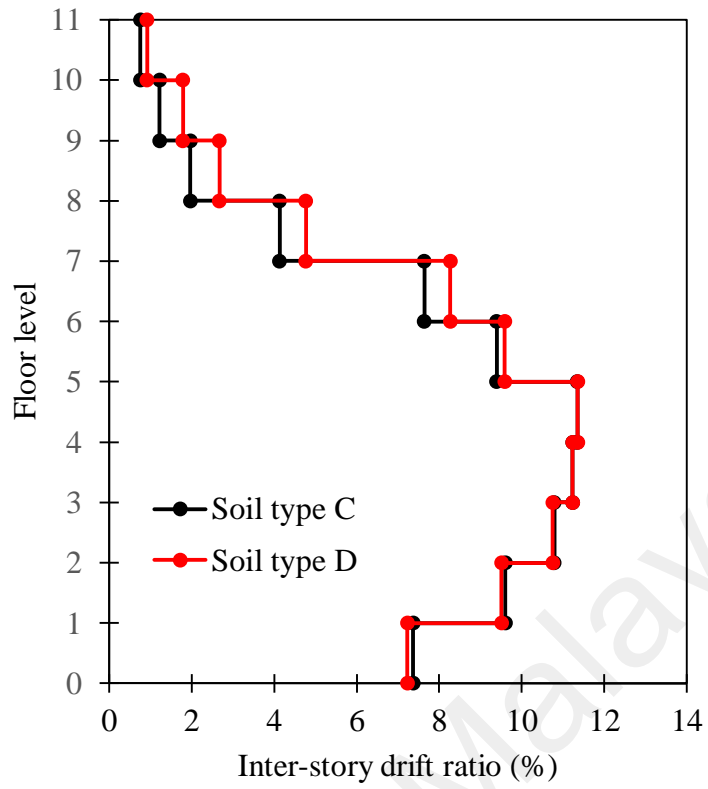


Figure. C3. Continuation.

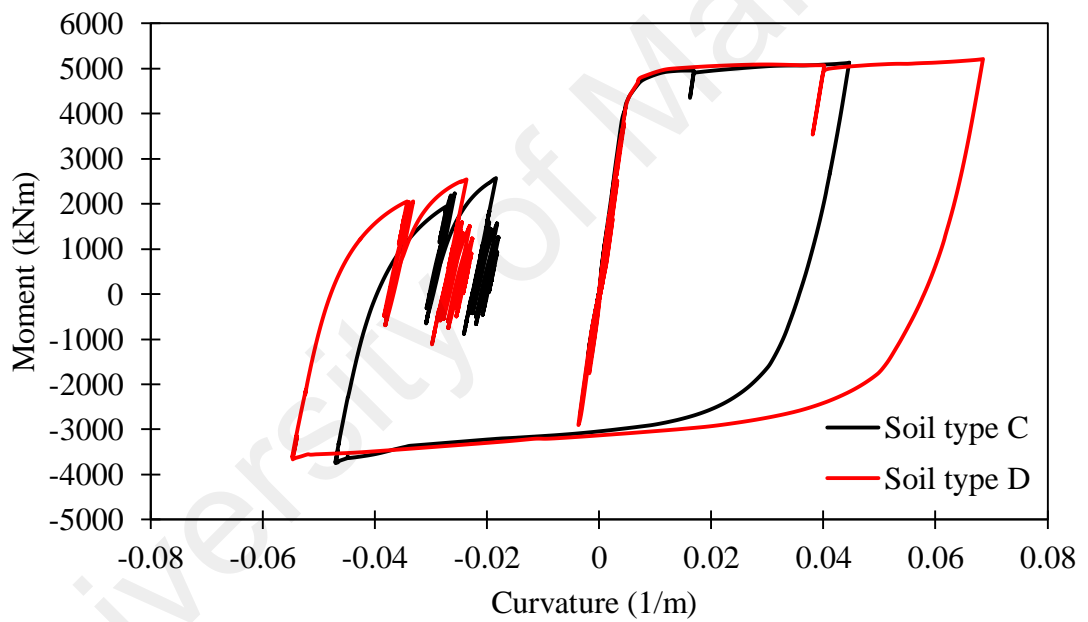
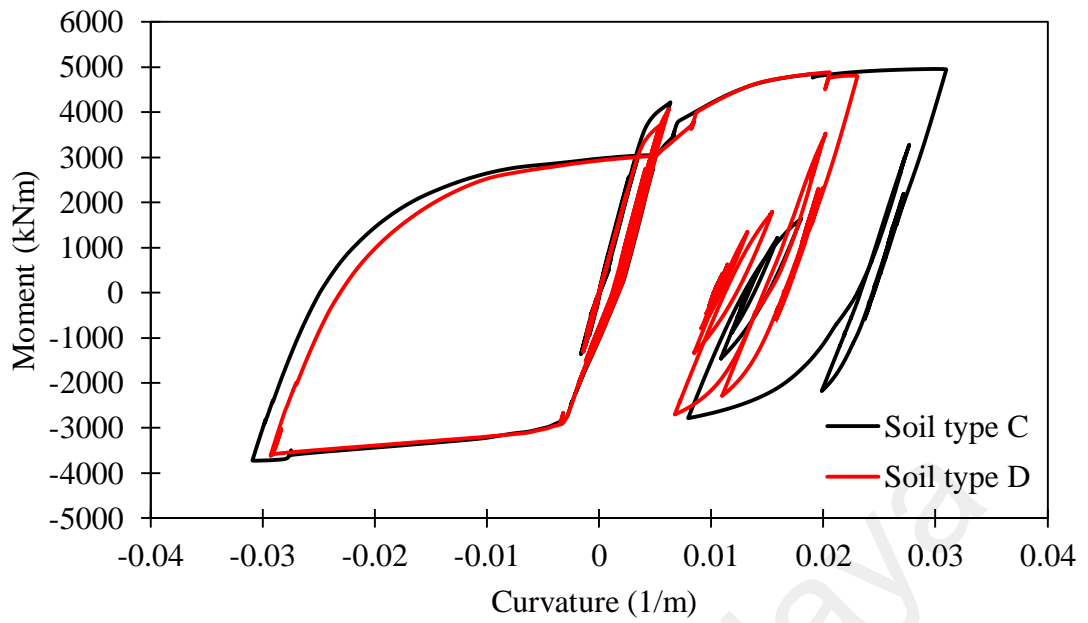


Figure. C4. The section moment curvature responses for leftmost first story column of 11-story RC building at soft rock and stiff soil.

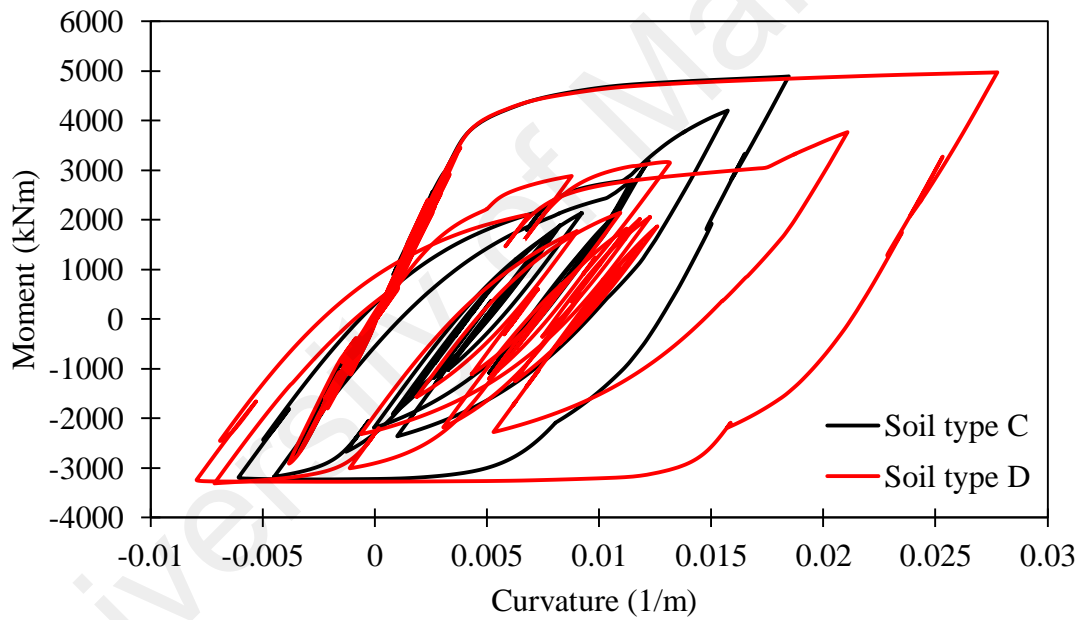
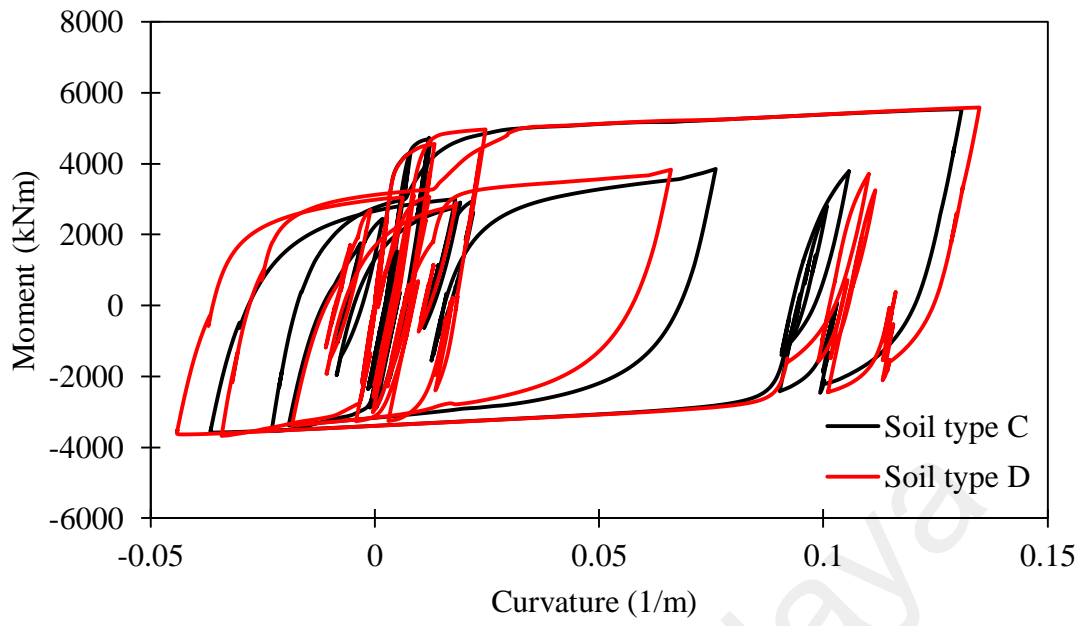


Figure. C4. Continuation.

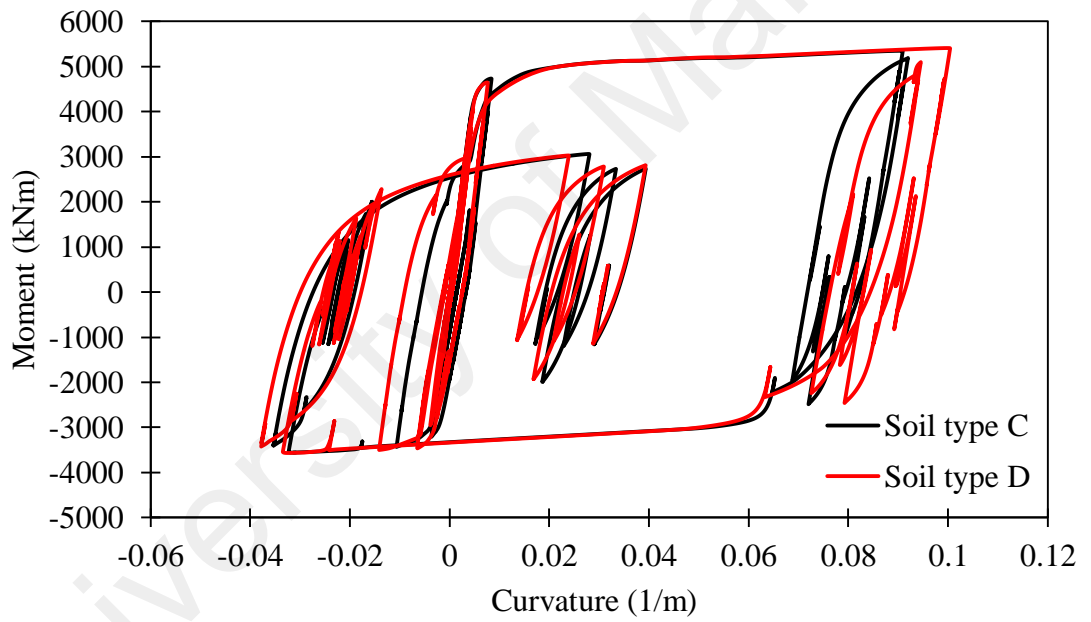
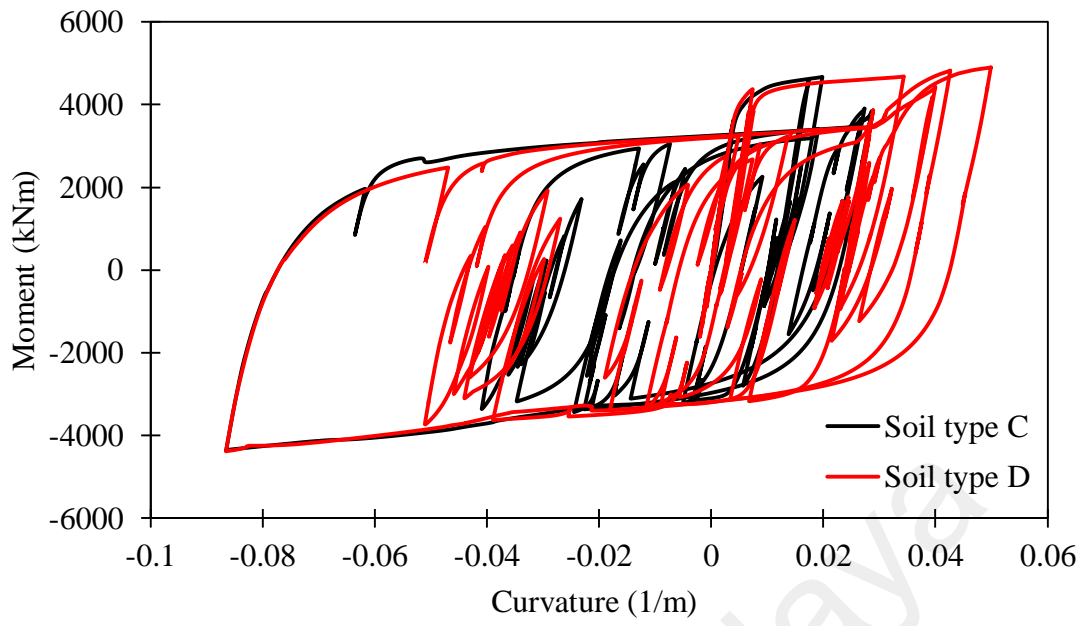


Figure. C4. Continuation.